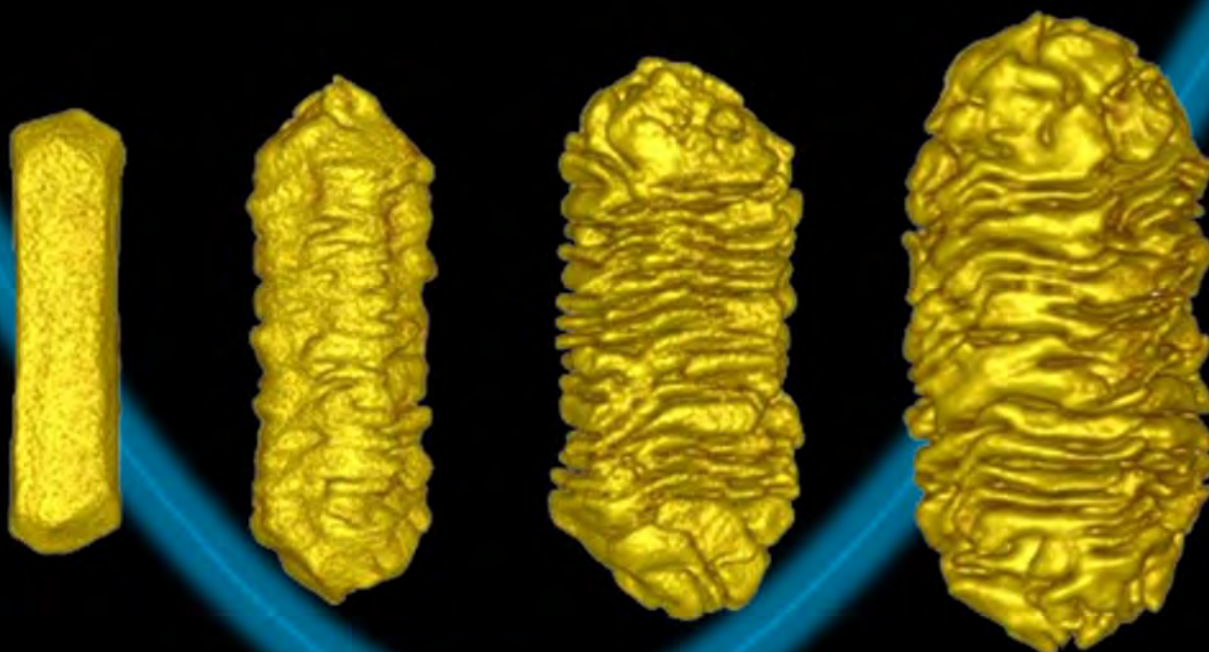


Mechanistic investigation of the seeded growth on chiral **gold** nanoparticles

A PhD Thesis
by
Kyle Douglas Van Gordon

Supervised by Prof. Luis M. Liz-Marzán

Donostia-San Sebastián, 2024



eman ta zabal zazu



Universidad del País Vasco Euskal Herriko Unibertsitatea

DOCTORAL THESIS

Department of Applied Chemistry

Department of Polymer Science and Technology

Mechanistic investigation of the seeded growth of chiral gold nanoparticles

by

Kyle Douglas Van Gordon

To achieve a PhD in Applied Chemistry and Polymeric Materials by The University of Basque Country

Supervised by:

Prof. Luis M. Liz-Marzán (Bionanoplasmonics Lab, CIC biomaGUNE)

Donostia-San Sebastián, 2024

CICbiomaGUNE

MEMBER OF BASQUE RESEARCH
& TECHNOLOGY ALLIANCE

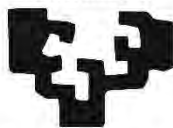


eman ta zabal zazu



Universidad del País Vasco Euskal Herriko Unibertsitatea

eman ta zabal zazu



Universidad del País Vasco Euskal Herriko Unibertsitatea

DOCTORAL THESIS

Department of Applied Chemistry

Department of Polymer Science and Technology

Mechanistic investigation of the seeded growth of chiral gold nanoparticles

by

Kyle Douglas Van Gordon

To achieve a PhD in Applied Chemistry and Polymeric Materials by The University of Basque Country

Supervised by:

Prof. Luis M. Liz-Marzán (Bionanoplasmonics Lab, CIC biomaGUNE)

Donostia-San Sebastián, 2024

CICbiomaGUNE

MEMBER OF BASQUE RESEARCH
& TECHNOLOGY ALLIANCE



eman ta zabal zazu



Universidad del País Vasco Euskal Herriko Unibertsitatea

**TESI ZUZENDARIAREN BAIMENA
TESIA AURKEZTEKO**

**AUTORIZACIÓN DEL/LA DIRECTORA/A
DE TESIS PARA SU PRESENTACIÓN**

Zuzendariaren izen-abizenak /Nombre y apellidos del/la director/a: Luis Manuel Liz-Marzan

IFZ /NIF: 33304170D

Tesiaren izenburua / Título de la tesis:

Mechanistic investigation of the seeded growth on chiral gold nanoparticles

Doktorego programa / Programa de doctorado: Química Aplicada y Materiales Poliméricos

Doktoregaiaren izen-abizenak / Nombre y apellidos del/la doctorando/a: Kyle Douglas Van Gordon

Unibertsitateak horretarako jartzen duen tresnak emandako ANTZEKOTASUN TXOSTENA ikusita, baimena ematen dut goian aipatzen den tesia aurkez dadin, horretarako baldintza guztiak betetzen baititu.

Visto el INFORME DE SIMILITUD obtenido de la herramienta que a tal efecto pone a disposición la universidad, autorizo la presentación de la tesis doctoral arriba indicada, dado que reúne las condiciones necesarias para su defensa.

Tokia eta data / Lugar y fecha:

LIZ MARZAN
LUIS
MANUEL -
33304170D

Firmado digitalmente
por LIZ MARZAN LUIS
MANUEL -
33304170D
Fecha: 2024.09.04
14:03:25 +02'00'

Sin. / Fdo.: Tesiaren zuzendaria / El/La director/a de la tesis

**AUTORIZACION DEL TUTOR/A DE TESIS
PARA SU PRESENTACION**

Dr/a. Miren Ostra Beldarrain, como Tutor/a de la Tesis Doctoral: Mechanistic investigation of the seeded growth on chiral gold nanoparticles realizada en el Programa de Doctorado Química Aplicada y Materiales Poliméricos por el Doctorando Don/ña. Kyle Douglas Van Gordon, y dirigida por el Dr./a Luis M. Liz Marzan autorizo la presentación de la citada Tesis Doctoral, dado que reúne las condiciones necesarias para su defensa.

En Donostia a 9 de septiembre de 2024

LA TUTORA DE LA TESIS

MIREN OSTR
BELDARRAIN
- 72449374H

Firmado digitalmente
por MIREN OSTR
BELDARRAIN -
72449374H
Fecha: 2024.09.09
12:12:17 +02'00'

Fdo.: Miren Ostra Beldarrain

AUTORIZACIÓN DE LA COMISIÓN ACADÉMICA DEL PROGRAMA DE DOCTORADO

La Comisión Académica del Programa de Doctorado en Química Aplicada y Materiales Poliméricos en reunión celebrada el día 9 de septiembre de 2024, ha acordado dar la conformidad a la presentación de la Tesis Doctoral titulada: Mechanistic investigation of the seeded growth on chiral gold nanoparticles, dirigida por el/la Dr/a. Luiz M. Liz-Marzán y presentada por Don/Dña. Kyle Douglas Van Gordon adscrito o adscrita al Departamento Química Aplicada.

En Donostia a 9 de septiembre de 2024

LA RESPONSABLE DEL PROGRAMA DE DOCTORADO

MIREN OSTRÁ Firmado digitalmente por
MIREN OSTRÁ
BELDARRAIN - BELDARRAIN - 72449374H
72449374H Fecha: 2024.09.09
12:13:02 +02'00'

Fdo.: Miren Ostra Beldarrain

ACTA DE GRADO DE DOCTOR O DOCTORA

ACTA DE DEFENSA DE TESIS DOCTORAL

DOCTORANDO/A DON/DÑA. Kyle Douglas Van Gordon

TITULO DE LA TESIS: Mechanistic investigation of the seeded growth on chiral gold nanoparticles

El Tribunal designado por la Comisión de Postgrado de la UPV/EHU para calificar la Tesis Doctoral arriba indicada y reunido en el día de la fecha, una vez efectuada la defensa por el/la doctorando/a y contestadas las objeciones y/o sugerencias que se le han formulado, ha otorgado por _____ la calificación de: *unanimidad ó mayoría*

SOBRESALIENTE / NOTABLE / APROBADO / NO APTO

Idioma/s de defensa (en caso de más de un idioma, especificar porcentaje defendido en cada idioma):

Castellano _____

Euskera _____

Otros Idiomas (especificar cuál/cuales y porcentaje) _____

En _____ a _____ de _____ de _____

EL/LA PRESIDENTE/A,

EL/LA SECRETARIO/A,

Fdo.:

Fdo.:

Dr/a: _____

Dr/a: _____

VOCAL 1º,

VOCAL 2º,

VOCAL 3º,

Fdo.:

Fdo.:

Fdo.:

Dr/a: _____

Dr/a: _____

Dr/a: _____

EL/LA DOCTORANDO/A,

Fdo.: _____

Acknowledgements

I was sitting in the passenger seat of my grandfather's cherry-red Toyota during an elk hunting expedition near Sumpter, Oregon. I was an undergrad then and filled with pride about one of my first real research positions at a protein crystallography lab working on parasites, notably those that cause malaria. I don't recall my grandfather having said anything, only the way he looked at me as I spoke, causing my rapid, bright description of the work to slow and eventually stop entirely. My grandfather stared back. He was losing his wife, my grandmother, too slowly and too steadily to Alzheimer's. I was in principle able to do something about it—why wasn't I doing something about it? My grandfather is no fool. He knew that I had no control, the circumstances, but it didn't matter. Sometimes as a scientist you are just helpless, even for those you love the most.

I shared this story as Luis and I sat in a restaurant in Seoul, enjoying a tall beer and bowls of seolleongtang, a flavorful bone broth with strips of beef and noodles. To my surprise and lament, he shared a similar story right back. At the conclusion, a familiar expression of vengeance, heartache, and determination crossed his face. I smirked. Luis knows more than most about my background and hired me anyway; the mental impetus in me to prove his decision right will never completely fade. But in a field that often gives over to cold professionalism, I am most grateful for a supervisor that is so much more. I am eager to continue work with him in the near future and beyond.

I was welcomed to use the rich resources present at CIC biomaGUNE, and I deeply thank administration for getting me quickly up to speed. Of essential note are Marco Moller and Marta Gallego Gonzalez, a microscopy team without peer. Though I am often regarded as reserved in the office and laboratory, neither Marco nor Marta would know it—I cherish the discussions shared in the spaces between specimen exchanges, respect the extreme degree of technical expertise they effortlessly demonstrate daily, and am grateful for our fast-formed friendship. This institute is also blessed with a team of optical technicians of an extremely high caliber, without whom I would simply be lost. Judith Langer and Irantzu Llarena are brilliant, accommodating, friendly, and absolutely critical to efficient operation of the spectrophotometers I poured untold hours into during my studies. Beyond my little world, these technicians keep the sky from falling for so many students and post-docs that their significance to the institute and to science becomes very hard to quantify. I am humbled by their continued passion and consistently positive outlook that brightens up our workplace by an amount that is too easily taken for granted.

When I arrived at CIC biomaGUNE, the first person to greet me was David Vila-Liarte, a person I recognized immediately would become a close friend and confidant in the lab. This patient gentleman with a wide smile and hair down to his lower back presented a sharp and necessary counterpoint to my impersonal and frenetic energy, encouraging me to slow down and proceed deliberately through the early days of my doctoral studies. I was the latest in a grand set of distractions from David's doctoral studies—he had persevered through the pandemic and research stays riddled with bureaucracy, and yet he devoted a substantial amount of his time to instructing and supplying me with the necessary background. Together briefly with Xiaolu Zhuo, we became a formidable team taking on all things chiral. I owe them both a substantial deal for the scientific, organizational, and personal growth made during these past few years. Instead of allowing his

creative talents to wither on the vine, David actively pursued his musical interests in a way that clearly makes him happy. As of writing, I will have him tomorrow at my apartment as a guest for dinner—I hope to maintain a friendship with this singularly charming young man.

Like much of my time in Europe, the Bionanoplasmonics Group has constantly challenged me in the best possible way. Being in proximity to such a diverse array of talent and colorful personalities has driven me to better myself as a scientist and as a person. I admit seeking to impress my peers at every opportunity, a motivation that fills my voice with confidence when presenting data or asking questions, and inspires bravery when speaking to higher-ups or passionately advocating for improved scientific communication. I likely don't impress my group with my Spanish, nor my general inability to absorb European culture, both of which I can generously label “work in progress”... and yet. I still feel as embraced by this group as I ever could, knowing myself, knowing my tendency to press my nose into the grindstone until my peripheral vision is blocked, still when I finally rear my head the members of this group never shun, and instead smile my way, and clink glasses. To Laura, Paula P., Paula V., Ben, Manuel, Gail, Pablo, Marita, Lara, Manuel, Paco, Kevin, Clara, Isabel, Malou, Ada, Lucia and Martina—cheers; thank you all.

Though outside collaborators contributing to this work are referenced throughout this thesis, they will get an additional mention here for their tireless efforts leading to several publications in a short time. First, the EMAT/NanoLab advanced microscopy group at the University of Antwerp, under the supervision of Prof. Sara Bals. I had the pleasure of meeting Sara in person at a conference in Massachusetts, but I don't think I adequately offered my thanks for her caring direction and ambition towards excellence that has made our many projects together so successful. I have enjoyed many discussions with members of her unspeakably talented team, including Dr. Mikhail Mychinko, Dr. Robin Girod, Wouter Heyvaert, and Evgenii Vlasov. They each have often

gone out of their way to maintain communication channels irrespective of time zone or work load, and inspire me with their commitment, compassion and camaraderie. I am also fortunate to have worked with a skilled team at CICA (Centro Interdisciplinar de Química e Biología; part of Universidade da Coruña), including Dr. Jesús Mosquera, Dr. Alejandro Criado, and Sandra Baúlde Álvarez. Their foundational (and often thankless) synthetic work to create the novel chiral inducers used throughout this thesis cannot go overlooked. Though I seldom interacted with them directly, the vital computational modelling and light simulations performed by Manuel Obelleiro-Liz (Universidade de Vigo), Fernando Obelleiro (Universidade de Vigo), and José Manuel Taboada (Universidad de Extremadura) must be highlighted. Their work inspired my research stay at the University of Michigan this year, to be discussed promptly.

Working abroad is a necessary part of any international PhD, but these opportunities were to me welcomed and essential towards further expanding my horizons, worldview, and network as a progressing scientist. With the objective of exploring the critically important computational approaches that I had not previously delved into during my time as a synthetic chemist, I was offered the chance to work at the University of Michigan as a visiting scholar. My sincere thanks to Prof. Nicholas Kotov and his chemical engineering group for organizing the stay and enabling me to produce particle models and light simulations of my own—the knowledge gained in the process is invaluable towards expanding understanding of all the concepts laid out in this work. I need to spotlight Julia Zaher's contribution to science here; as my landlord and unofficial transportation administrator during my time in Saline, Michigan, the research stay would simply not be possible without her. Beyond this, she is a terrific human being and I will miss our political sparring. Another wildly productive research stay—organized earlier in the same year—was to Seoul National University in South Korea. Enormous thanks to Prof. Ki Tae Nam and SNU for the

invitation and accommodation, making what could have been a difficult transition into a new environment a happily trivial affair. From the densely skilled research group to the densely wondrous city complete with densely layered food, it all made for an unbelievable, unforgettable experience. To call In Han Ha simply my lab partner during this time would be a gross understatement—I consider him my brother, a ravenously ambitious young man who would (and did) put everything aside for the sake of a guest. I have never met another so brilliant and yet so humble, so fast and yet so error-averse, so determined and yet so kind. I miss him terribly.

I hereby give my father permission to white-out my first name and use this document at his discretion. When I came home again, he crushed me in a hug that lasted just a moment too long, and gave the game away—and all the tears rushed out of my face. They didn't stop after a truly memorable summer week with him—where he exhibited all the spots in Central Oregon he knew were beautiful—as the miles crept behind my rental car, an endless flood cut through the tough-guy banter and joking and postering from before. Years ago, he gave me his support to do the hard thing: to leave family, friends, all my connections and all sense of comfort, to pursue something greater in Europe. He doesn't always know what I am doing. But he asks, and he trusts me. That's enough. Thank you, Dad.

While I spin my wheels with nonsense that means so much to us few, my sister works in Phoenix, Oregon as an advocate for victims of sexual assault. I remain in awe of her: her growing maturity, her growing life, her growing influence. I am thankful for her patient, funny, and often mediative discussions with me, and I wish her continued success and happiness.

My mother and I have had a contentious relationship for a long time. Someday we'll likely get over ourselves. Who I was, how I progressed, who I am: I owe much to her. I miss the simpler times at hers between shifts at a casino during the height of COVID. Those were simpler times?

Through it all, Silvia Collavini has been there. She was there with me in Seoul, an oasis of adventure, photographs and soju after six weeks and untold hours of my trying in vain to keep up with the Korean students at work. She was there at CIC biomaGUNE, immediately and kindly introducing me to a whole new set of colorful personalities in the Prato group, and always advising me to take breaks and care after myself, even when she was tired and with her eyes set on a different path. Upon her leaving to pursue a new career, she garnered support from old talent to new arrivals and all in between, so profound was her positive impact on everyone around her. She was there consoling me as I accelerated away from Oregon, holding my hand, knowing how hard it is to be away from home. She is with me now, after another sleepless night burning my eyes out looking at this screen, loving me anyway. Her, a real Renaissance woman, armed with a half-dozen languages, able to interact with and— what's more— charm anyone and everyone she meets. Me, a white-hot stubborn block of American steel filled with marshmallow—we have, and we still do, make an excellent team. I intend to marry her next year and I hope she remains with me always.

To you, Grandpa—where God and country fail to motivate, I found a reason to fight from you.

If you think that's twisted, well, that's my specialty...

Table of Contents

Summary	pg. 23
Chapter 0 – Scope and Objectives	pg. 28
Chapter I – Introduction	pg. 33
1.1 Nanotechnology	pg. 34
1.2 Plasmonics	pg. 35
1.2a Plasmonics Theory: Thin Films	pg. 36
1.2b Plasmonics Theory: Sub-Wavelength Nanoparticles	pg. 39
1.2c Composition and Synthesis of Plasmonic Nanomaterials	pg. 42
1.2d Colloidal Synthesis of Plasmonic Nanomaterials: Nucleation and Growth	pg. 43
1.2e Colloidal Synthesis of Plasmonic Nanomaterials: Gold Nanorods	pg. 46
1.3 Chirality and Light: Circular Dichroism	pg. 49
1.4 Chiral Plasmonics	pg. 52
1.5 Production and Analysis of Inherently Chiral Plasmonic Nanomaterials	pg. 54
1.5a Electron Tomography and Helicity Analysis	pg. 55
1.5b Computational Modeling and Electromagnetic Simulations	pg. 57
1.5c Chemically-Induced Chiral Growth	pg. 58
1.5d Micelle-Directed Chiral Growth	pg. 63
1.6 Summary	pg. 68
1.7 References	pg. 69
Chapter II – Tuning the Growth of Chiral Gold Nanoparticles Through Rational Design of a Chiral Molecular Inducer	pg. 85
2.1 Introduction	pg. 86
2.2 Bridging Chiral Mechanisms with LipoCYS	pg. 89
2.3 Computational Modeling and Electromagnetic Simulations	pg. 97
2.4 High-Resolution Facet Analysis of Chiral Nanorods	pg. 99
2.5 Conclusions	pg. 105
2.6 References	pg. 106
Chapter III – Single Crystal and Pentatwinned Gold Nanorods Result in Chiral Nanocrystals with Reverse Handedness	pg. 111
3.1 Introduction	pg. 112
3.2 Rationalizing use of cystine vs. cysteine	pg. 114
3.3 Chemically-Induced Mechanism: Single-Step vs. Stepwise Growth	pg. 116
3.4 Micelle-Directed Chiral Growth	pg. 121
3.5 Electron Tomography and Helicity Analysis	pg. 123
3.6 Symmetry Characterization	pg. 129

3.7 Conclusions	pg. 133
3.8 References	pg. 135
Chapter IV – Time-resolved optical and structural characterization of chiral growth on gold nanorods	pg. 139
4.1 Introduction	pg. 140
4.2 Method Development: Chiral Product Stability in NaBH ₄	pg. 142
4.3 Method Development: Ceasing Chiral Reactions with NaBH ₄	pg. 143
4.4 Method Development: Comparison to <i>in situ</i> analysis	pg. 144
4.5 Time-resolved evolution of BINAMINE chiral products (SC-AuNRs)	pg. 146
4.6 Time-resolved evolution of BINAMINE chiral products (PT-AuNRs)	pg. 149
4.7 Conclusions	pg. 152
4.8 References	pg. 153
Chapter V – Outlook: Engineering Hierarchical, Multi-Scale Chirality	pg. 157
5.1 Introduction	pg. 158
5.2 Hierarchical chiral growth mediated by LipoCYS	pg. 161
5.3 Double-chirality: chiral growth using chiral nanoparticles as seeds	pg. 168
5.4 Conclusions	pg. 174
5.5 References	pg. 175
Chapter VI – Experimental Section	pg. 180
Synthesis of achiral nanomaterials	pg. 180
Chemicals	pg. 180
Methods	pg. 181
Synthesis of single-crystalline gold nanorods (SC-AuNRs)	pg. 181
Preparation of gold nanoclusters (AuNCs)	pg. 181
Preparation of gold mini-rods for use as seeds in AuNR synthesis	pg. 182
Preparation of high aspect ratio gold nanorods for chiral synthesis	pg. 182
Synthesis of pentatwinned gold nanorods (PT-AuNRs)	pg. 183
Preparation of pentatwinned gold seeds	pg. 183
Preparation of high aspect ratio gold nanorods for chiral synthesis	pg. 183
Synthesis of single-crystal octahedral gold nanoparticles (octa-AuNPs)	pg. 184
Preparation of CTAC-stabilized gold nanoclusters (AuNCs)	pg. 184
Preparation of octahedral gold nanoparticles (octa-AuNPs)	pg. 184
Synthesis of cubic single-crystal gold nanoparticles (cube-AuNPs)	pg. 185
Preparation of CTAB-stabilized gold nanoclusters (AuNCs)	pg. 185
Preparation of gold cubic nanoparticles (cube-NPs)	pg. 185
Synthesis of inherently chiral nanoparticles	pg. 186
Chemicals	pg. 186
Methods	pg. 186
Seeded chiral growth in the presence of LipoCYS	pg. 186

<u>Estimation of relative LipoCYS concentration</u>	pg. 187
<u>Seeded hierarchical chiral growth in the presence of LipoCYS</u>	pg. 188
<u>Single-step seeded chiral growth in the presence of <i>L</i>-2cys</u>	pg. 188
<u>Multi-step seeded chiral growth in the presence of <i>L</i>-2cys</u>	pg. 188
<u>Seeded chiral growth in the presence of BINAMINE</u>	pg. 189
<u>Time-resolved synthesis of inherently chiral nanoparticles</u>	pg. 189
<u>Optical Characterization, Electron Tomography, and Computational Analysis</u>	pg. 190
<u>Optical Characterization</u>	pg. 190
<u>Electron Tomography</u>	pg. 191
<u>Surface helicity analysis</u>	pg. 191
<u>Numerical Solution of Maxwell's Equations</u>	pg. 192
<u>Nanoparticle Models</u>	pg. 193
<u>Synthesis of LipoCYS</u>	pg. 194
<u>Chemicals</u>	pg. 194
<u>Methods</u>	pg. 195
<u>Synthesis of N-Boc-(<i>R</i>)-Cys(Trt)-Decan</u>	pg. 195
<u>NMR Spectra of N-Boc-(<i>R</i>)-Cys(Trt)-Decan</u>	pg. 196
<u>Synthesis of N-Boc-(<i>S</i>)-Cys(Trt)-Decan</u>	pg. 197
<u>NMR Spectra of N-Boc-(<i>S</i>)-Cys(Trt)-Decan</u>	pg. 198
<u>Synthesis of (<i>R</i>)-LipoCYS</u>	pg. 199
<u>NMR Spectra of (<i>R</i>)-LipoCYS</u>	pg. 200
<u>Synthesis of (<i>S</i>)-LipoCYS</u>	pg. 201
<u>NMR Spectra of (<i>S</i>)-LipoCYS</u>	pg. 202
<u>References</u>	pg. 203
<u>Chapter VII – Conclusions</u>	pg. 206
<u>Appendix</u>	pg. 212

Summary

The field of chiral nanoplasmonics is sprawling and multifaceted, and the theme that connects the objectives of the projects comprising this thesis is the colloidal synthesis of chiral plasmonic nanomaterials. Using gold as the building block, a synthetic chemist can construct in water a vast array of nanoparticle morphologies and sizes that shine intensely in the entire visible spectrum and beyond. This easily accessible phenomenon has been harnessed to make advances in optical displays, metamaterials, and biosensors; for decades before the recent pandemic burned a red control line into the public's consciousness, plasmonic technology had been familiar to anyone who had used a pregnancy test. On the other hand, the building blocks of life are chiral, and the typically weak optical signal from chiral substances is greatly intensified in the proximity of plasmonic nanomaterials. Introduction of a chiral molecule into a colloidal synthesis of plasmonic nanomaterials grants access to exponentially more complicated twisted particle morphologies and correspondingly more interesting optical signatures. However, the mechanisms by which chiral growth occurs are not as well established as those for growth into achiral morphologies. The aim of this thesis is to explore this less well-trodden aspect of colloidal chemistry by systematically testing different synthetic variables that may influence chiral growth, and pushing the methodological boundaries for both the investigation and production of new chiral morphologies.

In Chapter I, we begin with an introduction to plasmonics, the background theory, and the progression of “bottom-up” synthetic strategies to produce plasmonic nanomaterials. This is followed by a discussion about chirality in the context of light, and how chirality will be quantified

in the chapters to come. We can then proceed with earnest to the field of chiral plasmonics in the context of “bottom-up” colloidal synthesis; we introduce the prevailing mechanistic theory for chiral growth on nanoparticles, which depends heavily on the choice of chiral inducer.

In Chapter II, we considered established chiral growth inducers, split into two categories based on how they influence chiral growth: those directly interacting with the gold surface, usually via a thiol-Au bond, and those forming micelles in solution that template the gold surface. We then developed and tested a novel chiral inducer, LipoCYS, designed with elements from both categories: a polar cysteine-like head and a long aliphatic tail, intended to bridge both growth mechanisms. Remarkably, solely depending on the concentration of LipoCYS used in the chiral synthesis, the chiroptical signature of products was observed to widely shift and vary in intensity. Further characterization by electron tomography revealed that products synthesized with a low concentration of LipoCYS appeared smooth and twisted, like those obtained using inducers that directly interact with the gold surface; at a high concentration of LipoCYS, products possessed distinct surface wrinkles, like those obtained using inducers that form a micellar template on the gold surface. A similar chiroptical and structural evolution was observed even when the starting material in the synthesis was changed from nanorods of a high aspect ratio to nano-cubes and octahedrons. However, at low concentrations of LipoCYS, the chiroptical signature from cubes and octahedrons were observed to be inverted with respect to each other, suggesting that starting seed geometry was a highly influential variable for the products of chiral syntheses.

In Chapter III, we delved more deeply into the influence of starting seed geometry by using both well-established (chemically-induced or micelle-directed) growth mechanisms and contrasting the chiral products from similarly-sized single-crystalline and pentatwinned achiral nanorods, respectively. The chiroptical signatures and structural handedness of the products were found to

be inverted, though this was more apparent for products from the micelle-directed mechanism, owing to the highly regular and defined helical wrinkles that formed regardless of achiral seed used. From careful analysis of the wrinkle orientation about the particle surface it was observed the symmetry present in the seeds was conserved after the chiral reaction: chiral products from single-crystal seeds maintained their four-fold symmetry, and chiral products from pentatwinned seeds maintained their five-fold symmetry.

To better understand how these chiral structures could develop whilst preserving the symmetry of the starting seed, we endeavored in Chapter IV to study the structural evolution of these products in real time. A method using sodium borohydride was developed to cease chiral reactions in progress, enabling the isolation and characterization of products from varying time intervals of growth. A time-resolved series prepared and analyzed in this way displayed the evolving chiroptical signature much like *in situ* measurements, but with the added advantage of being able to characterize the products under an electron beam and display the evolving structural features as well. This was demonstrated using single-crystal and pentatwinned achiral seeds and the micelle-directed growth mechanism, which was revealed to proceed faster than previously thought, especially when pentatwinned achiral seeds were used; their growth far outpacing that on single-crystal achiral seeds. Furthermore, the growth on the tips of single-crystal and pentatwinned rods evolved differently; the former appeared far more rounded than the latter, potentially contributing to their inverted chiroptical signatures.

In Chapter V, using lessons learned from observations made in previous chapters, we attempted to produce structures with multi-scale chirality that more closely resembled how chirality is expressed in nature. Our approach was two-fold. First, noting that LipoCYS could produce wrinkled dumbbell-like structures under certain synthetic conditions, and that gentler synthetic

conditions to slow a chemically-induced chiral reaction produces helicoid-like particles, we used LipoCYS in the context of a helicoid synthetic methodology and observed the products. While the lack of particles evaluated by electron tomography stymied our conclusions, promising corkscrew-like chiral features that grew to dominate the handedness of certain particles (as the concentration of LipoCYS was raised) were observed. In our second approach, we exploited the observation that symmetry is conserved during the course of a chiral reaction to prepare particles with multi-scale chirality. Using geometrically twisted yet smooth products of a chemically-induced chiral reaction as the seeds in a subsequent micelle-directed chiral reaction, geometrically twisted and wrinkled products were formed. This was done at a range of gold salts : chiral seeds ratios in order to contrast differing extents of growth.

In Chapter VI and VII, we outline the materials and methods used throughout the projects described above, and summarize our conclusions from each chapter, respectively.

Chapter Ø – Scope and Objectives

This thesis was completed under Grant PRE2021-097588, entitled “Design of Chiral Plasmonic Nanostructures for Theranostics”, under the supervision of Prof. Luis Liz-Marzan (CIC biomaGUNE). Capitalizing off early success that revealed a sufficiently broad set of experimental avenues to explore with regards to synthesis, the project was gradually focused into an incisive investigation of chiral growth mechanics. The primary aims were to 1) optimize colloidal syntheses of nanoparticles with chiral geometry and their associated optical response, and 2) comprehend the growth mechanism of chiral inducer-mediated growth on these nanoparticles.

Both goals were pursued in the context of the emerging field of novel chiral inducers. Working in close collaboration with Prof. Jesús Mosquera (Universidade da Coruña), newly synthesized chiral molecules (by Sandra Baúlde, Universidade da Coruña), were used in a variety of syntheses of chiral products. In all cases, chirality transfer from novel chiral inducers to achiral nanomaterials was accomplished through an overgrowth reaction: chiral growth is directed by the rapid reduction of gold salts around the achiral seeds, kept stable in solution by the presence of a surfactant. Special attention was given to the products’ chiroptical signature and dissymmetry factor, evaluated using a circular dichroism (CD) instrument. The chiroptical signature of the products could be tuned according to the relative proportion of chemicals used in the synthesis, among other variable experimental parameters; the corresponding changes to yielded particle structure were evaluated using high-angle annular dark-field scanning transmission electron microscopy (HAADF-STEM). Production, optical and structural characterization of chiral products was carried out at CIC biomaGUNE.

Establishing structural-optical relationships of chiral products and how they relate to synthetic variables is foundational to the ongoing research projects of the Bionanoplasmonics Group. When more detailed structural information is required, the research group supervised by Prof. Sara Bals, and their sophisticated electron tomography lab at the University of Antwerp have been an invaluable resource. Through this collaboration, 3D reconstructions of particles representative of those observed in HAADF-STEM images can be acquired. Subsequent helicity measurements, among additional topographical characterization, provided more context to structural observations made in this work. This was especially relevant for exploring the concept of multi-scale chirality, using chiral products made in-house and by a collaborator (Prof. Bing Ni, University of Michigan) as seeds for further chiral overgrowth reactions. Taken as a whole, this approach revealed critical information regarding the relationship between products' structural characteristics and their optical properties.

Further to this are contributions from EM3Works, an offshoot of the University of Vigo and the University of Extremadura. Particle models and corresponding simulated optical data provided by Manuel Obelleiro-Liz, Fernando Obelleiro, and José Manuel Taboada were utilized to contrast against experimental data acquired at CIC biomaGUNE. For hands-on experience with applicable software and expertise regarding particle modelling and light simulations, a research stay at the University of Michigan under the supervision of Prof. Nicholas Kotov was coordinated.

The size, shape, and crystallinity of the achiral nanomaterials used as seeds in chiral syntheses are known to have a strong influence on the properties of yielded chiral materials. The use of single-crystal (SC) achiral gold nanorods (AuNRs) in the early stages of this thesis, and the reproducible production of monodisperse pentatwinned (PT) achiral AuNRs of similar dimensions by an in-house collaborator (Francisco Bevilacqua, CIC biomaGUNE) provided an opportunity to isolate

the variable of these seeds' different crystal facets and directly contrast properties of the yielded chiral products. Additionally, part of this project was carried out at Seoul National University, with an aim during the research stay being the contrast of chiral products yielded when using different achiral seeds. Specifically, working alongside a group led by Prof. Ki Tae Nam, octahedral and cubic achiral seeds were used in chiral syntheses alongside a common inducer, and the optical and structural properties of yielded chiral products were compared.

As the thesis progressed, the ability to track the structural and optical evolution of chiral products in a time-resolved fashion gained greater attention. Being able to show where particle growth was occurring during the course of a chiral reaction would provide insights onto how the chiral inducers (and other reagents) are interacting with the surface of the particles, and how factors like crystallinity of the achiral seeds influences the attained morphology after chiral growth. The development of a synthetic protocol for the time-resolved preparation and characterization of chiral products was informed by previous literature derived from the Bionanoplasmonic group. A previous method for real-time analysis, chiroptical measurements performed *in situ*, was valuable as a comparative approach to the eventual time-resolved protocol. Through the rapid reduction of excess gold salts via sodium borohydride, a progressing chiral reaction could be ceased; this was a method common to much synthetic literature inside and outside this research group but used for a unique purpose.

In summary, the thesis can be separated into four distinct objectives:

1. Testing of novel chiral inducers

- Seed-mediated synthesis of chiral AuNRs using 2-amino-N-decyl-3-mercaptopropanamide (LipoCYS) as the chiral inducer and single-crystal high aspect ratio AuNRs as the starting achiral seeds
- Investigate [LipoCYS]-mediated chiroptical and structural evolution of chiral products

2. Facet-directed syntheses

- Synthesis of chiral AuNRs using cystine and 1,1'-binaphthyl-2,2'-diamine (BINAMINE), contrasting the chiral growth mediated by each chiral inducer using single-crystal and pentatwinned achiral nanorods as the starting achiral seeds
- Investigate opposing handedness of chiral products yielded using SC or PT achiral seeds, and corresponding chiroptical inversion

3. Time-resolved analysis of chiral growth

- Demonstrate efficacy of technique using sodium borohydride to cease BINAMINE-mediated chiral growth on single-crystal high aspect ratio AuNRs
- Investigate structural and chiroptical properties of chiral products at different time points; generate time-resolved reaction series of chiral AuNRs, contrasting progressing growth on single-crystalline and pentatwinned achiral nanorods used as seeds

4. **Production of nanomaterials with multi-scale chirality**

- Use LipoCYS and octahedral or cubic achiral seeds in established protocol designed to produce helicoids; evaluate particles for multi-scale chirality
- Use chiral products of cystine-mediated overgrowth reaction as seeds in a subsequent chiral synthesis using BINAMINE; evaluate contrasting “core-shell” helical features

Chapter I – Introduction

The field of chiral plasmonics lies at a convergence of scientific disciplines, including physics, synthetic chemistry, and biochemistry. As with many young scientific fields, the future of chiral plasmonics depends on both the careful application of established theory and the discovery of innovative approaches and techniques. For example, the preparation of metal nanomaterials dates back to the mid-19th century, but their applications in the context of forming plasmonic chiral arrangements remain cutting-edge: advanced optics, molecular sensing, and immunotherapy, to name a few. The true promise of chiral plasmonics is tunability enabled at the synthetic level; historically, control over the structural and optical properties of nanomaterials has been asserted to yield products in a variety of shapes and sizes. Owing to the ease and advancement of seed-mediated over one-pot nucleation and growth methods, anisotropy may be engineered into particle populations with a very high degree of homogeneity. However, the underlying growth mechanisms, especially for the synthesis of inherently chiral nanomaterials, remain insufficiently understood. Understanding this subject requires a deep background regarding surface plasmon resonance, chirality in natural and synthetic contexts, strategies for the production of colloidal metal nanomaterials, and how these all intersect and lend themselves to theranostic applications. In this chapter, we introduce the concept of plasmonics, provide a general overview of chirality in nature and chemistry, and explain how the two connect with regards to circularly polarized light and colloidal synthesis of gold nanorods. Then, we contrast putative mechanisms for chiral growth, and describe approaches to characterize the products of chiral reactions to help the understanding of the underlying mechanisms become more complete.

1.1 Nanotechnology

Nanotechnology encompasses any material in the nano-size range ($1 \times 10^{-9} \text{ m} - 1 \times 10^{-7} \text{ m}$)¹ and is ubiquitous in modern life. From antimicrobial gym clothing infused with nano-silver, to solar cells engineered with carbon nanotubes, to sunscreen containing nanoparticles comprised of tin oxide, the applications of nanotechnology are as numerous as its many forms. Nanoparticles in particular possess unique physical characteristics, including the ability to be dispersed as a stable colloidal suspension, a high surface area to volume ratio, and, in the case of Nobel-prize winning semiconductor nanocrystals (quantum dots), size-dependent optoelectronic properties.^{2,3} The surface of nanoparticles is a versatile platform for interesting catalysis and electrochemistry, as well as for conjugated ligands or antibodies for active targeting and anti-fouling techniques meant to evade the body's various defense mechanisms.⁴⁻⁶ Varying widely in composition, nanoparticle systems have been developed for commercial use. For medicinal purposes, polymeric micelles, liposomes, and drug-polymer and protein-polymer conjugates function as nanocarriers, meant to protect, direct and control the distribution of DNA or small molecules into a biological system.^{7,8} For electronics and diagnostic purposes, inorganic "hard" nanoparticles (i.e. copper, iron oxide, lanthanides, etc.) function as semiconductors for sensors and telecommunication, and as contrast agents for magnetic resonance imaging.^{9,10} The size, shape, and interfacial properties of nanoparticles are intrinsically linked to the viability of a given nanosystem and its desired application; many nanomaterial syntheses including those in this work optimize these parameters for success. Taken as a whole, the morphology of nanoparticles making up a nanosystem and their surface chemistry can be exploited to enable the production of advanced optics and metamaterials, and for biological applications like triggers for specific immune responses and targets for photothermal and photoacoustic therapies.^{11,12}

1.2 Plasmonics

The same phenomenon that facilitates the function of pregnancy test kits and rapid antigen detection strips for COVID-19 was also observed for hundreds of years prior to these technologies in the form of stained glass.¹³ Though there is evidence of stained glass made in ancient Egypt, the most dramatic early example of plasmonic properties in common culture is found in the Lycurgus cup, a stunningly intact piece of dichroic glassware from the 4th century¹⁴ (**Figure 1.1**).

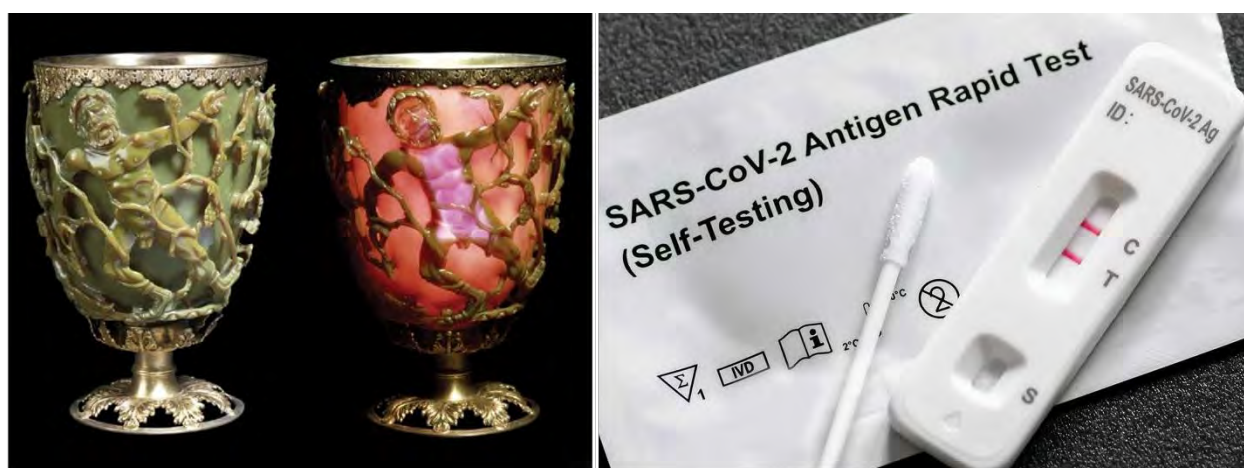


Figure 1.1. The Lycurgus Cup (left) reflects light in one color and transmits light in another due to gold and silver nanomaterials embedded in the glass. The indicative lines on lateral flow assays such as rapid antigen tests for SARS-CoV-2 (right) arise because of gold nanoparticles carrying the complementary antibody in the test strips. Photo credit: britishmuseum.org (left), uclahealth.org (right).

In all cases, these colorful applications are enabled by the interaction of light with metal nanomaterials; first documented in colloidal gold (and other metals) by Michael Faraday in 1857, and described in great detail with regards to spherical nanoparticles by Gustav Mie, fifty years later.^{15,16} Fifty years after that, pioneering thin-film research by R.H. Ritchie laid the foundation for the discovery of trapped light waves along metal surfaces called surface plasmon polaritons, also known as surface plasmons or surface plasmon resonances.¹⁷⁻¹⁹ Under specific conditions, the

surface plasmons of thin metallic films can be excited by incident light. The conditions for this excitement, known as surface plasmon resonance, are simplified when the metal is much smaller than the wavelength of the incident light (i.e. nanomaterials). Furthermore, this effect is confined to the nanomaterials resulting in vast near-field electromagnetic enhancements. Plasmon resonance-enhanced responses to light from embedded nanomaterials in modern lateral flow assays are responsible for the appearance of intense bands from trace sample present in mucus, saliva, or urine, making these tests faster and more easily interpreted.²⁰ As demonstrated by the multicolored stained glass of antiquity, this response can also change, which depends on the size, shape, and composition of the nanomaterial used. Harnessing the tunable potential of the plasmonic properties of metals is key to the success of downstream applications, to be discussed.

1.2a Plasmonics Theory: Thin Films

As with all periodic elements, on the scale of a single atom, the electrons of the alkali and noble metals are distributed into discrete orbitals; however, this electron configuration is less defined when there are many nuclei involved. The uncertainty about the position of electrons in solids resulting from the presence of many nuclei is called delocalization; in metals, the electrons are delocalized over the whole of the bulk material. An approximation of these so-called free electrons in metallic solids is given by the Drude-Sommerfeld model,²¹ which posits an encompassing idealized (Fermi) gas of electrons that helps to explain the high electrical and thermal conductivity observed in metals.²² In an electric field, polarization is induced between the delocalized Fermi gas and the positively charged nuclei of the metal; a Coulomb restoring force causes electronic (plasma) oscillations to occur, called plasmons. The concept of a material's plasma frequency was

theorized in great detail by Pines and Bohm before the term plasmon was coined, or indeed before this was considered in the context of nanomaterials.²³ The bulk plasma frequency of a material is dictated by the band structure, which is itself determined by the electron configuration into discrete orbitals. Further displacement of the Fermi gas from the positively charged nuclei can be induced with incident light above the plasma frequency; plasmons excited by light in this way are called polaritons. The significance of this intrinsic property of metals is expanded by theory conceptualized by Ritchie and supporting subsequent experiments by Powell and Swan.²⁴ It is well established that upon interaction of an electron beam with a material, energy is lost to nuclear scattering, ionization, and radiative emission, as well as to excitation of the plasmons in the bulk material.²⁵⁻²⁸ However, this expected loss in energy could not account for the total amount of energy lost for thin metallic films, which was found by Powell and Swan to be dependent on the film material. Furthermore, they theorized this additional loss was occurring at the metal-air interface, which was evidenced by evolution of the signal as the film surface was oxidized.¹⁷ This serves as the foundational evidence for surface plasmon polaritons (SPPs); despite resulting from the interaction of light with metals, they are simplified in the nomenclature to surface plasmons. The nature of surface plasmons in a thin film can be understood through an optical method to excite them, called attenuated total reflection (ATR). Demonstrated in different configurations by Otto, Kretschmann and Raether in 1968, decaying evanescent waves are generated by light passing through a prism of high refractive index and under the conditions of total internal reflection (**Figure 1.2**).²⁹⁻³¹

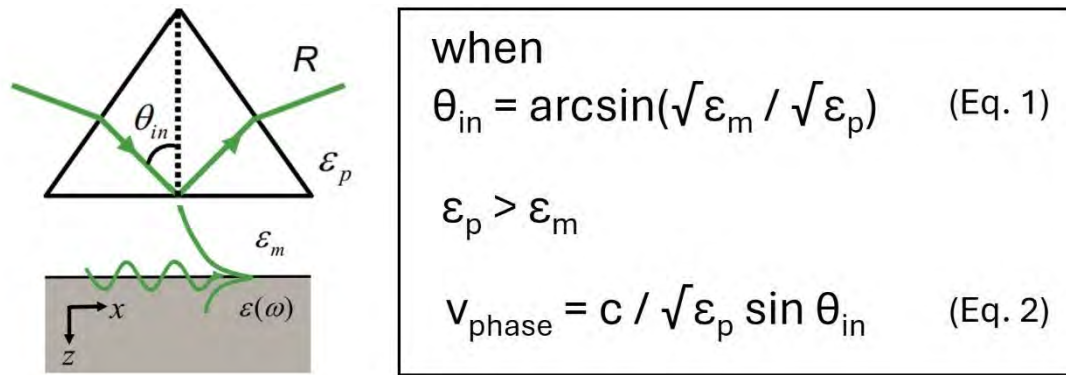


Figure 1.2. When the conditions for total internal reflection are met (Equation 1), a light beam passing through a prism of high refractive index (related to dielectric constant, ϵ_p) will generate an evanescent wave at the interface with a material of low refractive index (ϵ_m). When the prism is sufficiently close to a metal surface, the phase velocity of this evanescent wave will match that of the SPPs (Equation 2), causing coupling and an excited evanescent wave that propagates along the dielectric-metal interface. Adapted from ref. 18 (© IOP Publishing Ltd, 2012).

When this prism is placed near a thin metallic film, these evanescent waves propagate in a direction parallel to the film surface;³² the observation that the decay length of these waves is extended along metallic films suggests coupling with waves of a similar nature at the surface, originating from surface plasmons. Understanding the evanescent nature of surface plasmon oscillations in thin films and taking advantage of the conditions to make them resonate with incident light is fundamental to the function of modern surface plasmon resonance (SPR) biosensors, which are largely unchanged from their originally conceived configuration.³³

1.2b Plasmonics Theory: Sub-Wavelength Nanoparticles

In stark contrast to thin metallic solids, the resonance conditions for surface plasmons of nanomaterials are much easier to achieve. As discussed previously, surface plasmon resonance in thin films relies on the generation of evanescent waves by a prism, which depends on satisfying Maxwell equations that are relevant at this scale.³⁴ For particles considerably smaller than the wavelength of visible light, the electrostatic approximation applies: essentially, the electromagnetic field that a given particle experiences is uniform.^{18,35} Owing to the curved surface of spheres, the electric polarization modes are simplified to the point of a dipole across the sphere called the Fröhlich mode.³⁶ This mode can resonate with the frequency of incident light; the coherent oscillations of conduction electrons are localized to each of the small metal particles, giving rise to localized surface plasmon resonance (LSPR).^{37,38} The LSPR-induced strong electric field in the near vicinity of metal nanoparticles strongly enhances the scattering and absorption (**Figure 1.3**).³⁹⁻⁴¹ Furthermore, the formation of inter-particle areas of extreme optical enhancement can occur when two or more metal nanoparticles are in close proximity,⁴²⁻⁴⁴ giving rise to coupled plasmon modes; these “hot-spots” can be exploited for the sensing of molecular drugs, biomarkers, or other small molecules in extremely trace quantities.⁴⁵

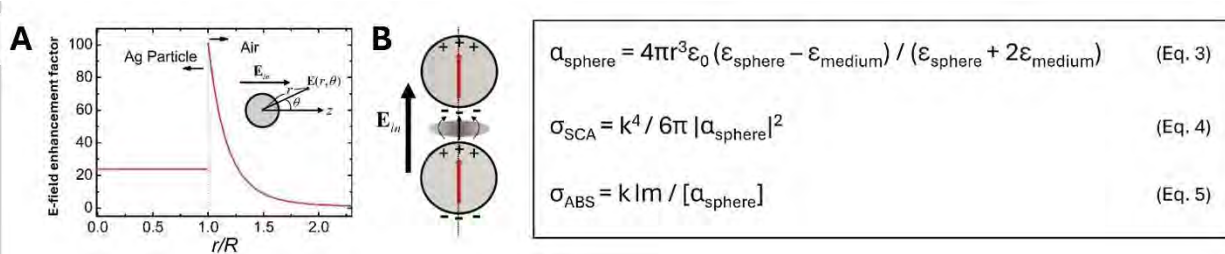


Figure 1.3. Under Fröhlich mode resonance and the electrostatic approximation, the polarization α (Equation 3) and electric field across a spherical metal nanoparticle are uniform, with a large field enhancement localized at the particle surface (A). The optical properties can be quantified via the scattering and absorption cross-sections (Equations 4 and 5), where k is the wave vector (related to the refractive index, frequency and speed of light in a vacuum). The dipolar plasmonic modes of two metal nanoparticles within the coupling limit ($5r$) will hybridize in a distance-dependent manner analogous to molecular orbital theory, giving rise to shifting of the resonance peak and large enhancements to the electric field in the gap (B). Adapted from ref. 18 (© IOP Publishing Ltd, 2012).

This is relevant to the subject of surface-enhanced Raman scattering (SERS) spectroscopy. Raman spectroscopy measures the difference in energy between incident photons and those inelastically scattered off a target molecule; the difference in energy is characteristic to the target molecule because it derives from the vibrational energy transferred by inelastic scattering.³⁵ When the molecule is adsorbed onto a plasmonic nanoparticle, an enhancement to the Raman scattering cross-section of the molecule takes place because of the electromagnetic near-field enhancement described above.⁴⁶ Fabricated nanosystems for SERS are designed to take advantage of the further field enhancement provided by “hot-spots”.^{47,48}

In practice, colloidal gold nanoparticles analyzed using a spectrophotometer will yield LSPR peak(s) on the absorbance spectrum at wavelength(s) where plasmon resonance(s) occur. Localized surface plasmon resonance frequencies depend on factors intrinsic to the nanoparticles, including size, shape, and polarizability, as well as on extrinsic factors, such as the dielectric properties of the surrounding medium.⁴⁰ For the purposes of the work presented here, the most

important takeaway is that the LSPR peaks from colloidal nanomaterials can vary according to the morphology of the nanoparticles. For instance, plasmonic nanorods experience LSPR on either the transverse or longitudinal axis, depending on their orientation with respect to the electromagnetic field, and thus when characterized in a colloidal dispersion possess two LSPR bands at specific frequencies depending on the particles' dimensions⁴⁹ (**Figure 1.4**). Effectively tuning the wavelength of the LSPR bands by simply changing the particle aspect ratio (length : width) has been consistently demonstrated.⁵⁰⁻⁵² This effect has been explored theoretically using the Mie theory (an analytical solution to Maxwell's equations describing electromagnetic scattering from particles with spherical symmetry),^{16,53} Gans theory (a modification of Mie theory applicable to ellipsoids),^{54,55} and numerical methods such as the discrete dipole approximation (which enable computational quantification of scattering from particles of arbitrary geometry).⁵⁶⁻⁵⁸ In this way, relationships between the LSPR peak position, aspect ratio of the particles, and dielectric constant of the medium have been derived, which compare well with experimentally obtained data.

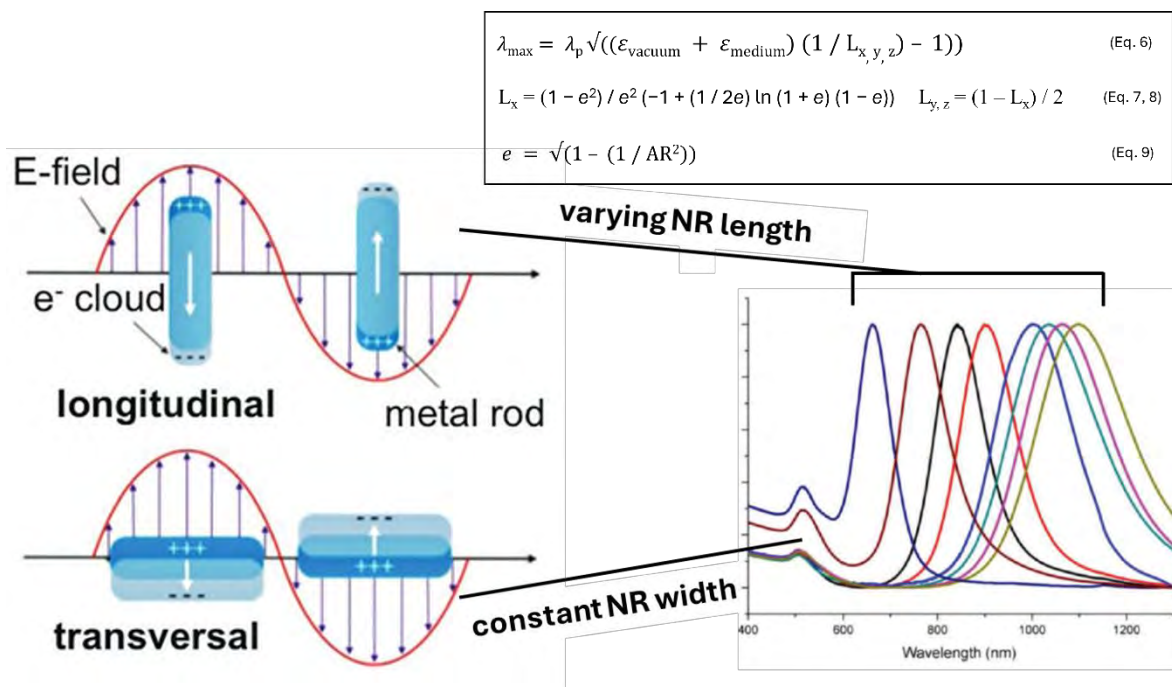


Figure 1.4. Metal nanorods in an electromagnetic field (light) experience coherent oscillations of their conduction electrons along the longitudinal and transverse axes (left). A colloid of these nanorods under spectrophotometric analysis will yield LSPR peaks representative of these, at wavelengths dependent on the average dimensions of the nanorods. The positions of these peaks can be estimated using relations derived from Gans theory (Equation 6),⁵⁹ where λ_p refers to the characteristic plasma frequency of the metal, and L refers to the depolarization factor for each axis of the ellipse (Equation 7 and 8),⁵⁹ which is related to the ellipse aspect ratio (Equation 9).⁶⁰ Adapted from ref. 49 (© RSC 2017).

As a result, LSPR enhancement phenomena can be applied to the entire visible spectrum and into the near-infrared (near-IR) range. The latter is foundational to surface-enhanced infrared absorption spectroscopy (SEIRA), which enables the structural and conformational analysis of minute amounts of molecules by observing changes in their plasmon-enhanced IR spectra.⁶¹ Since extinction and absorption of light by skin tissue is reduced in the near-IR range, high LSPR intensities in the near-IR range are also paramount to biological applications.⁶² All told, advancements in plasmonics have led to recent innovations in molecular sensing,⁶³ photovoltaics,⁶⁴ photothermal therapy,⁶⁵ and advanced optics.⁶⁶

1.2c Composition and Synthesis of Plasmonic Nanomaterials

Tailoring the properties of metal nanomaterials to optimize LSPR-enhanced effects is crucial to their application. To this end, noble metals have been embraced by the plasmonics community for their chemical stability and biocompatibility, high electrical conductivity, and high near-field electromagnetic enhancement. Silver and gold in particular are attractive choices for plasmonic nanostructures, owing to their comparatively low damping rates deriving from scattering interactions of conduction electrons, as dictated by the Drude-Lorentz model.⁶⁷ Copper, though more reactive, is also widely used for electrochemistry and catalysis applications.^{68,69} Although there are hundreds of syntheses using all three aforementioned materials, gold has enjoyed a very long history of use for plasmonic nanostructures thanks to being a nonreactive yet versatile material for synthesis, enabling the focus to be on the control of nucleation and growth instead of the avoidance of side reactions and the formation of undesired chemical byproducts. Additionally, gold is an excellent platform for surface conjugation because of the well-documented strong interaction between gold and thiols.⁷⁰⁻⁷² Reproducible protocols using gold to produce nanoparticles with a plethora of shapes and variable degrees of anisotropy have been developed.^{73,74} A distinction here should be made between the two main categories of strategies to produce nanomaterials. In “top-down” approaches, milling, etching, or laser ablation are employed to convert bulk material into nanomaterials.⁷⁵ “Bottom-up” approaches concern the synthesis of nanomaterials from smaller components, derived from nature or commercial sources. In a colloidal synthesis of nanomaterials, the modification of chemical variables (reagent concentration,⁷⁶ choice of surfactant⁷⁷ or reducing agent⁷⁸) and experimental variables (temperature,⁷⁹ time⁸⁰) can lead to a wide variety of predictable morphologies with excellent monodispersity. Being synthesized in both aqueous and organic media, and in an array of size-mediated colors, colloidal gold

nanomaterials are among the most common and instantly recognizable products on a synthetic chemist's workbench.

1.2d Colloidal Synthesis of Plasmonic Nanomaterials: Nucleation and Growth

The fundamentals of gold nanoparticle synthesis have not shifted greatly since the first documented report by Michael Faraday.⁸¹ Essentially, solvated gold salts (HAuCl_4 ; Au^{3+}) are reduced in the presence of surfactants or protecting surface ligands, which promote colloidal stability during the course of the reaction. A protocol using sodium citrate as a dual-function molecule to reduce and stabilize gold nanospheres was introduced by Turkevich, and later experimentation by Frens revealed the average size of these materials could be modified by simply changing the concentration of sodium citrate involved in the synthesis.^{82,83} On the other hand, the understanding of the growth mechanics for nanoparticles has evolved significantly, with updates continuously suggested over the last twenty years. The classic mechanistic theory was introduced by LaMer *et. al.* in 1950 to explain the formation of uniform sulfur sols (colloidal particulate) by dissolving sodium hydrogen thiosulfate in hydrochloric acid. An instantaneous nucleation event was proposed to occur to relieve a supersaturated solution of solvated unstable species,⁸⁴ and further growth would proceed according to the rate of diffusion of the precursor to the newly formed particle surface. LaMer theory presented nucleation as a kinetically driven process, via “stepwise bimolecular additions” as stated in an update to the original manuscript.⁸⁵ On the other hand, it was proposed that particle growth was a thermodynamically driven process; to explain the observed monodispersity of the sols, Reiss (working closely with LaMer) submitted mathematically the diffusion-mediated faster growth of smaller particles compared to that of larger

ones.⁸⁶ Though LaMer theory features prominently in modern literature describing the syntheses of different nanosystems, inconsistencies were observed as early as Turkevich's work (published less than a year after LaMer) with colloidal gold and sodium citrate. The rate of nucleation was found to be dependent on temperature (which would complicate a mechanism based on supersaturation), and the rate of growth of gold nanoparticles was proposed to proceed exponentially, proportional to the diameter. Turkevich hypothesized an alternative "organizer" mechanism for nucleation mediated by copolymeric assemblies of gold and reducing agent that rearrange into larger particles. Remarkably, with the benefit of advanced electron microscopy apparatus and techniques, this was revisited in work more than fifty years later by Pong, et. al.;⁸⁷ the nucleation event was observed to be indicated by the formation of a citrate-stabilized network of nanowires which then coalesce into larger spherical particles, closely resembling Turkevich's written predictions. Noting the decreased applicability of the LaMer mechanism outside of the system where it was first applied, Finke and Watsky in their proposed mechanism sought to correct for kinetic incompatibilities by describing the nucleation step as slow and continuous, and occurring alongside autocatalyzed growth.⁸⁸ Though nucleation here (concerning the formation of iridium nanoclusters in this work) is still suggested to be kinetically controlled, the rate determining step for growth was strongly suggested to derive not from diffusion but from surface addition, enthalpically driven by the coordination of metal atoms to the particle surface. A commonality between this and the aforementioned mechanisms is agglomerative growth,⁸⁹ a concept universal to colloid science that takes place through nanocluster aggregation or Ostwald ripening (the maximization of crystal growth at the expense and dissolution of smaller particles).⁹⁰ These universal processes are known to be thermodynamically favored since a molecule in the interior volume of a material is more stable than on the surface, and the surface area to volume

ratio decreases as the particles increase in size. The work by Murphy, et. al. should be recognized here for elucidating the role of surfactant and a stepwise seeded approach on the growth of gold nanoparticles,^{91,92} to be discussed in the next section. While there is still much debate whether agglomerative growth is helping or hindering the monodispersity of a given colloidal synthesis of nanoparticles, the use of seeds and several growth steps has enabled the production of monodisperse products of many geometries. Whereas a deeper examination of these mechanisms is beyond the scope of this thesis, the prevailing theory for nanomaterial nucleation and growth can be summarized as exactly this: nucleation *and* growth, as two distinct events.⁹³ The controlled separation of nucleation and growth, influenced by the presence of additives, surfactants, and breaking up the process into several growth steps, must be considered when engineering particles with anisotropy.

1.2e Colloidal Synthesis of Plasmonic Nanomaterials: Gold Nanorods

Introduced and optimized by Murphy et. al., seed-mediated growth has been found to be an excellent approach to increase the monodispersity of anisotropic nanomaterials at a variety of shapes, sizes, and crystallinities.⁹⁴ A familiar synthetic approach inside and outside of this research group starts with the aqueous production of single-crystalline gold nanoclusters (approximately 1-2 nm in diameter) based on a method first established by Jana, et. al. in 2001;⁹⁵ gold salts are quickly reduced from Au³⁺ to Au⁰ by sodium borohydride in the presence of a high concentration of surfactant(s) to restrict the particle size. A modified version of this method involving thermal treatment promotes twinning of these gold nanoclusters into a stabilized pentagonal geometry.⁹⁶ In a subsequent growth step, the above pre-formed “seeds” are transferred into a fresh solution

with similar surfactant(s) and a weaker reducing agent to reduce additional gold salts from Au^{3+} to Au^+ , with reduction to Au^0 catalyzed at the surface of the seeds.^{94,97} When cetyltrimethylammonium bromide (CTAB) is used as the surfactant for the synthesis of seeds, as is the case in this thesis, the redox potential of Au^+ is changed by the formation of CTA- Au^+ complexes and halide ions in solution, further influencing the reduction and addition of gold to the seed surface.^{98,99} Furthermore, CTAB forms micelles in aqueous solution, which can sequester excess gold.¹⁰⁰ In this way, secondary nucleation is discouraged and the formation of larger products is promoted. Using the products of the previous growth step as seeds for the next growth step is the basis of the seed-mediated growth method, and further steps may be added to achieve anisotropic nanorods of an extreme aspect ratio.¹⁰¹ The geometry and corresponding surface facets of nanorods produced in a seed-mediated approach are dependent on the crystallinity of the starting seeds,¹⁰²⁻¹⁰⁴ whether single-crystalline (nanorods characterized by an octagonal cross-section) or penta-twinned (nanorods characterized by a pentagonal cross-section). An important concept to understand for success here is symmetry breaking; essentially the removal of symmetric elements in the early stages of the reaction to promote nanomaterial growth in a specific direction.^{76,97} Compared to the geometry present in penta-twinned seeds (see **Figure 1.5**), single-crystalline nanoclusters possess a much more indistinct geometry, and thus necessitates a means for symmetry breaking when anisotropy is the objective. Silver fulfills this role by promoting reduction at the tips of single-crystal particles, truncating their geometry and encouraging asymmetric growth.^{97,105} This same effect will hamper the anisotropic growth of penta-twinned nanorods; for this reason many penta-twinned syntheses are silver-free,^{94,95,101} which will be important when these products are used in downstream chiral syntheses, to be discussed below.

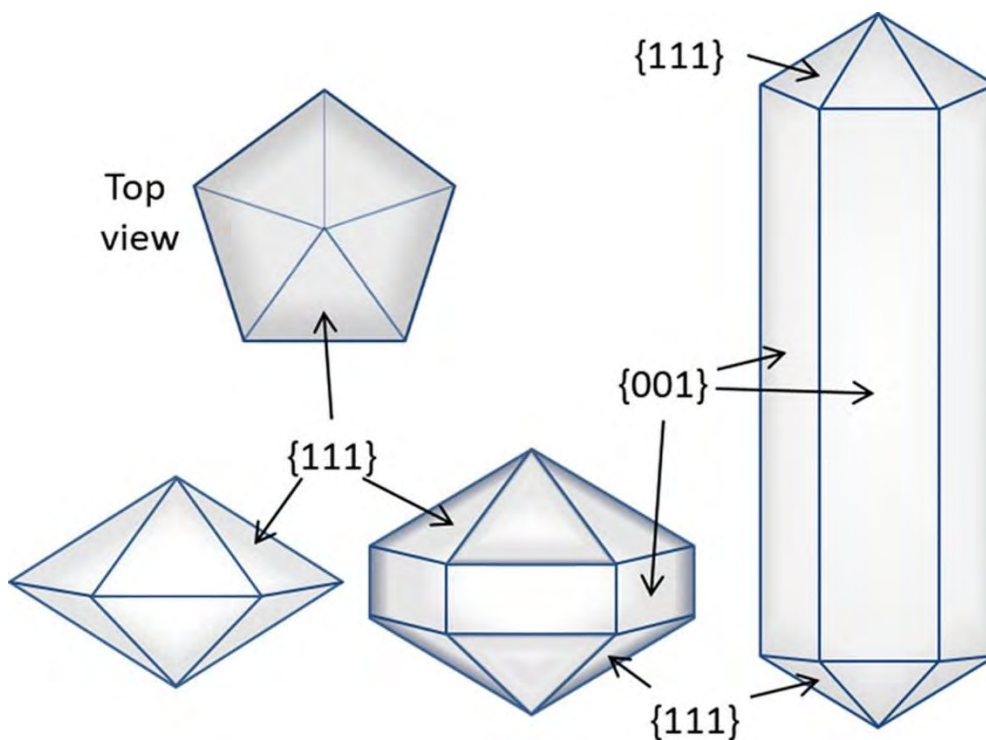


Figure 1.5. The sharp intersecting crystal facets of penta-twinned starting seeds (bottom left) quickly truncate into a more energetically favorable arrangement, breaking symmetry and promoting directional elongation of the newly formed low-index facets. Adapted from ref. 96 (© ACS 2017).

For anisotropic growth past the early stages of the synthesis, it is believed that a combination of surface passivation and facet-selective stabilization are occurring, enabled by interactions of surfactant(s) and additives like silver ions (in the case of single-crystal nanorods) with the growing gold surface.¹⁰⁶ Specifically, high-index facets may be blocked by underpotential deposition of silver,¹⁰⁷ or they may be blocked by surfactant aggregates, hindering the growth of gold in that direction^{97,108,109} (**Figure 1.6**).

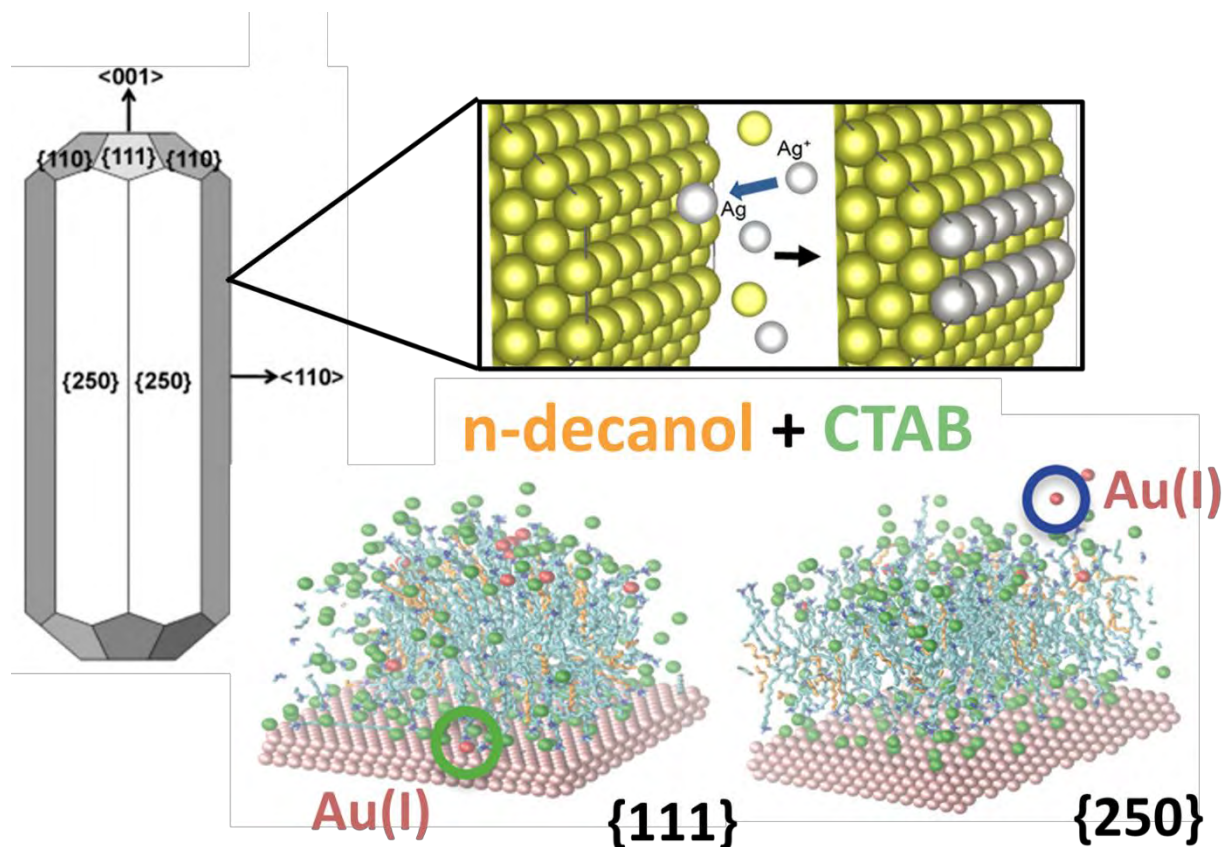


Figure 1.6. High-index facets on a growing single-crystal nanorod (left) may be selectively passivated by underpotential deposition of silver (top) or blocked by aggregates of cetyltrimethylammonium bromide and *n*-decanol (bottom), promoting further anisotropic growth and the production of high-aspect ratio gold nanorods. Adapted from ref. 76 (© ACS 2019) and ref. 108 (© Wiley-VCH 2010).

As stated above, cetyltrimethylammonium halides form micelles in aqueous solution, owing to their aliphatic tail and polar head group. However, they may rearrange into a bilayer on the surface of gold nanocrystal facets, which can prohibit the addition of gold ions depending on the crystal facet and additives that influence the chemistry and rigidity of the bilayer.^{76,109,110} The organization of cetyltrimethylammonium bromide (CTAB) about gold surfaces on the scale of a single particle is still under contention, with recent observations suggesting the formation of a dynamic micellar shell.¹¹¹ Notably, *n*-decanol has been observed to intercalate and stabilize the organization of

CTAB on gold nanocrystal facets, increasing the reproducibility of single-crystalline syntheses.⁷⁶ Anisotropic growth can also be influenced by reaction kinetics dictated via temperature, or the reductive potential of the reducing agent, which itself is dependent on the pH of the reaction mixture.⁷⁹ By virtue of the ease at which these syntheses may be repeated and refined, and with a thorough understanding of seed-mediated approaches, symmetry breaking, and methods to promote controlled anisotropic growth, nanorods at a given desired aspect ratio may be obtained with a very high degree of homogeneity.

1.3 Chirality and Light: Circular Dichroism

From amino acids to pharmacological eutomers, the shells of snails, to your own hands, encompassing the shape of galaxies themselves, chirality is inescapable at nearly every conceivable scale. If an object lacks internal symmetry planes and therefore cannot be superimposed onto its own mirror image, that object is chiral. First observed in sodium ammonium tartrate by Louis Pasteur in 1848,¹¹² molecular chirality embedded itself in the public consciousness upon discovery that an enantiomer of thalidomide, commonly used in the late 1950s for morning sickness, caused severe birth defects in thousands of children.¹¹³ Beyond this example, molecules that constitute the building blocks of life, such as amino acids, carbohydrates, and nucleic acids, are all chiral. Placing a chiral object in the path of a linearly polarized light field will result in the plane of the light being rotated, compared to its original orientation.¹¹⁴ Chiral molecules are denoted as **D** (*dextro*-rotatory) or **L** (*levo*-rotatory) based on their ability to rotate the plane of light polarization in a clockwise (to the right side) or counterclockwise (to the left side) manner when viewed along the direction facing the in-coming beam, as defined by IUPAC.¹¹⁵

The efficiency of a chiral molecule to rotate linearly polarized light is called optical rotatory dispersion (ORD); this example is helpful to visualize linearly polarized light as the sum of equal measures of left-handed and right-handed circularly polarized light.¹¹⁶ Circularly polarized light is produced by shifting the horizontal and vertical components of linearly polarized light $\frac{1}{4} \lambda$ out of phase with respect to each other; this may be simply achieved by passing linearly polarized light through a quarter-phase plate. Circularly polarized light is considered to be chiral as well, and each handedness is differently absorbed when passing through a chiral substance. This phenomenon is called circular dichroism (CD) and is foundational to the field of nanoscale chiroptics, which is concerned with the analysis and characterization of chiral nanostructures, each of which has its own particular CD signature.¹¹⁷ It should be noted that circular dichroism in practice, as a characterization method, is the function of the ellipticity produced by summing unequally absorbed (unequally transmitted) circularly polarized light; this signal is typically measured in mdeg (thousandths of degrees away from perfectly circular). Chirality is quantified via the dissymmetry factor (*g*-factor), which for a given sample is given as a percentage of the differential extinction of left- or right-handed light, out of the total extinction¹¹⁸ (as defined in **Figure 1.5**). Hence, the *g*-factor is a concentration-independent quantity, and can be easily compared between differently prepared samples. A positive CD signal (*g*-factor) at a given wavelength will mean that the sample primarily absorbed left-handed circularly polarized light, while a negative magnitude means that the sample primarily absorbed right-handed circularly polarized light. As the position of the chiroptical band approaches that of the overall absorbance, the magnitude of the *g*-factor goes to zero and inverts, according to the Cotton effect.¹¹⁹ This is due to the combination of unequal absorption (dichroism) and refraction (birefringence) of circularly polarized light at the optically active region for a material.

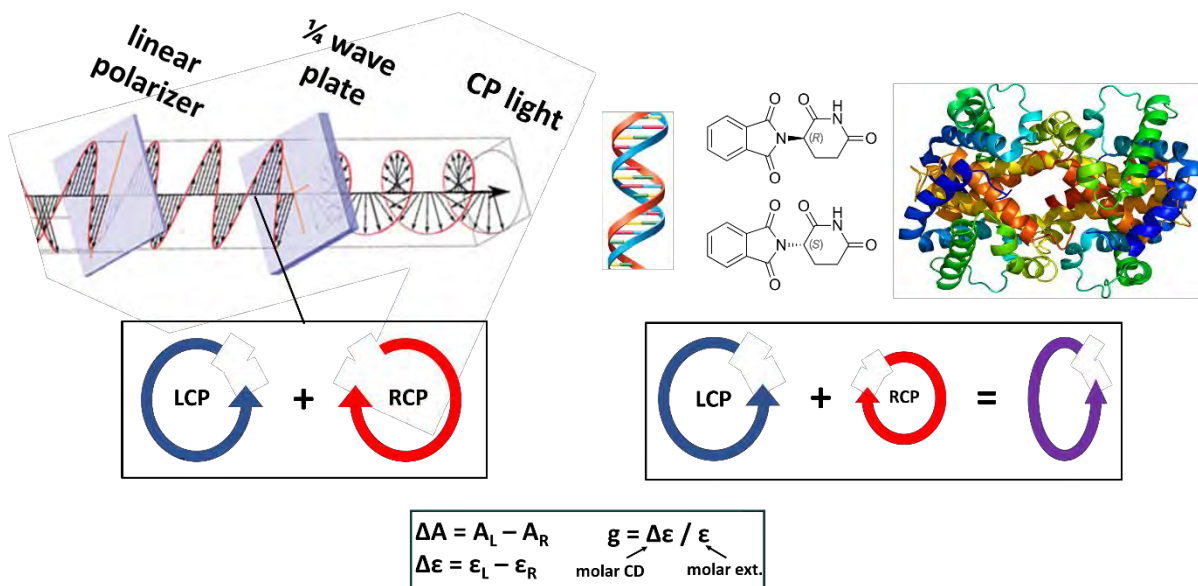


Figure 1.7. Passing linearly polarized light through a quarter-phase plate will circularly polarize it; technically, linearly polarized light can be considered the sum of equal measures of left- and right- circularly polarized light. When circularly polarized light interacts with a chiral material, there is a differential absorption of left- versus right- circularly polarized light, depending on the handedness of the chiral material analyzed. An elliptical superposition of left- and right- circularly polarized light of different magnitudes is measured by the detector of a circular dichroism (CD) spectrophotometer. Chirality is quantified using *g*-factor, a fraction of the CD signal over the total extinction of a given sample. Adapted from ref. 116 (publ. Oxford University Press).

It is worth stressing here that different handedness can be perceived from different perspectives, even though the absolute handedness is unchanged. This is true for chiral objects as well as for circularly polarized light. For the sake of consistency, one must be overly cautious and explicit when using handedness conventions. Turning to IUPAC definitions once again, left or right circularly polarized light is counter-clockwise or clockwise when viewed against the direction of propagation.¹²⁰ Circular dichroism is built from a fundamental understanding of chirality and how it applies to light-matter interactions, and has applications that include macromolecular characterization and chiral nanoplasmonics, the latter of which will be the focus of this work.

1.4 Chiral Plasmonics

Characterization by circular dichroism (CD) spectroscopy reveals much about a chiral substance's conformation and can enable delineation of the secondary and even tertiary structure of biomacromolecules. However, the generally weak optical response of chiral molecules places a practical limit on analysis. The true potential of this method is unlocked when combined with nanoplasmonics, as the near-field electromagnetic enhancement effects afforded by localized surface plasmons will be extended to the circular dichroism of a chiral analyte. The strongest chiral optical (chiroptical) signatures will derive from the collective modes of a chiral arrangement of plasmonic material. The surface plasmons of an inherently chiral nanoparticle or chiral configuration of achiral nanoparticles will also be chiral, and their resonances are capable of coupling collectively across the entire assembly. The overlapping and coherence of electromagnetic dipole moments originating from the surface plasmons of a chiral structure gives rise to the enhanced circular dichroism.¹²¹⁻¹²³ The arrangement of plasmonic material into a chiral configuration is a challenge met with a familiar two-pronged scientific approach. In "top-down" approaches, advanced lithographic techniques such as direct laser writing and glancing angle deposition have been employed to fabricate chiral structures to an extremely precise degree. However, "top-down" products like these are difficult to achieve in solution at a large scale. In "bottom-up" approaches, achiral components may be placed in an assembly with a certain handedness (configurational chirality) or arranged about a tetrahedron (constitutional chirality).¹²⁴ This is most easily accomplished using a chiral template, which can be isolated from natural sources (DNA, proteins, amino acids) or synthesized (liquid crystals, silica nanohelices, polydimethylsiloxane films).¹²⁵ In previous work at our research group, achiral Au nanorods were demonstrated to assemble about amyloid fibrils into chiral structures; the resultant CD signal

(weaker for AuNRs and monomeric α -synuclein or healthy brain samples) could be seen as an indicator for Parkinson's or other degenerative diseases.¹²⁶ Another example of a “bottom-up” approach to chiral plasmonics is the seed-mediated synthesis of inherently chiral nanoparticles, to be discussed in the next section. Regardless of how they are produced, the origin of the chiroptical signature of these structures can be explained by describing the plasmonic modes extended over chiral nanomaterials. As explained previously, a small spherical nanoparticle will have only a dipolar plasmon mode. It stands to reason that higher-order plasmon resonance modes (quadrupole, octupole, etc.) can be achieved through slight variations in the nanostructure and its surrounding environment.¹²⁷ For the more complicated geometries of chiral nanomaterials, the chiroptical signature is a product of the plasmon modes coupling over the entire surface of these structures.¹²⁸ The properties of chiral nanomaterials with novel morphologies have been exploited in recent innovations to molecular sensing,¹²⁹ photovoltaics,¹³⁰ photothermal therapy,¹³¹ and advanced optics.¹³² The challenge lies in constructing chiral gold nanostructures and interpreting the resulting CD spectra to attempt to understand the structure and underlying growth mechanisms. The focus of this body of work is on inherently chiral plasmonic nanostructures, particles with a twisted geometry or topology, typically synthesized and stabilized in a colloid dispersion.

1.5 Production and Analysis of Inherently Chiral Plasmonic Nanomaterials

The engineering of chiral nanomaterials has been recognized in the scientific community as extraordinarily challenging and extraordinarily rewarding in equal measure. As “bottom-up” synthetic strategies have become more advanced, the production of inherently chiral plasmonic nanostructures has become possible. The challenges to engineer inherently chiral nanomaterials

are recognizable as common challenges to “bottom-up” colloidal synthesis: a practical understanding of seed-mediated growth, gradual stabilization of selected crystal facets, and structural evolution at the atomic level are all relevant here as well.^{133,134} The majority of approaches maintain a focus at the synthetic level to assert control over chiral growth and enhance chiroptical activity; common to the approaches discussed here is the presence of a chiral molecule which induces chiral growth, and an overgrowth reaction where chiral growth is directed by the controlled reduction of gold salts around the achiral starting seeds, kept stable in solution by the presence of a surfactant (**Figure 1.8**). As such, the morphologies of chiral products are sensitive to the relative concentrations of reducing agent, surfactant, and chiral inducer in comparison to the available surface on the achiral seeds. Beyond reaction kinetics, chiral morphologies are also influenced by the chemical nature of the chiral inducer (**Chapter II**), the crystallinity of the starting seeds (**Chapter III**), and whether the reaction was prematurely terminated (**Chapter IV**).

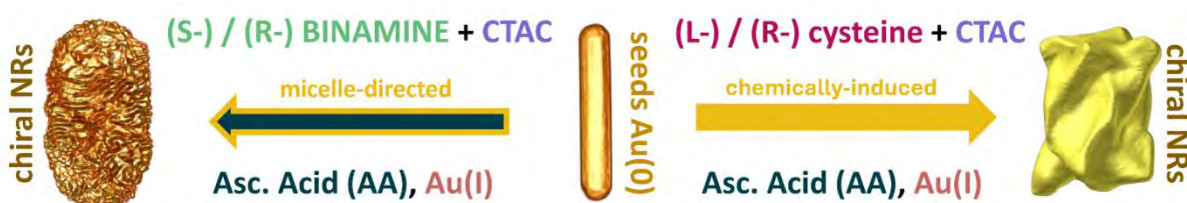


Figure 1.8. Mechanistic overview of chiral overgrowth reactions on gold nanorod starting seeds. Depending on the chiral inducer and synthetic conditions, chiral growth can progress very differently, resulting in products with intricate morphologies and intense chiroptical signatures. Adapted from ref. 163 (publ. Wiley-VCH GmbH 2022) and ref. 173 (publ. Science 2020).

Circularly polarized light has also been effectively used as an external stimulus to promote the formation of chiral structures and has great potential when used in conjunction with synthetic strategies (see **Chapter V**). In any case, a deep understanding of the growth mechanisms and chemical interactions is vital to the efficient optimization and engineering of viable products. In the following discussion, two different approaches to promote enantioselective growth of gold

nanomaterials are distinguished based on differing synthetic conditions and the resulting particle morphology. Establishing connections between the structure of chiral products from each approach and their chiroptical properties is fundamental to revealing the underlying growth mechanisms. The following section will briefly discuss the analytical strategies used in this work to this end.

1.5a Electron Tomography and Helicity Analysis

Scanning transmission electron microscopy (STEM) transmits a focused and raster-scanning electron beam through a thin specimen; these electrons are diffracted or scattered depending on the distribution of electron density present in the specimen. An annular (ring) detector may be used to detect only those electrons that are scattered at a high angle (via Rutherford or inelastic scattering), which are more numerous when the specimen encountered by the beam is comprised of elements of a high atomic number (i.e. gold).¹³⁵ The background (field), typically comprised of amorphous carbon, will therefore appear dark. Thus, high-angle annular dark-field STEM (HAADF-STEM) can display the finer structures of chiral gold nanoparticles with atomic resolution and great contrast.^{136,137} However, this technique is limited by the 2D nature of the produced images. The basis of electron tomography (ET) is the tilting of a sample with respect to the electron beam and the collection of a series of images projected over a wide range of tilt angles; these images are then combined using a computerized algorithm into a 3D reconstruction.^{138,139} Aided by a three-dimensional perspective, the handedness of structural features on chiral nanoparticles is more clearly apparent. Quantifying morphological chirality by its strict definition is possible by measuring the degree of coincidence of superimposed mirrored objects using the so-called Hausdorff chirality measure.^{140,141} The two objects are arranged in a fashion that minimizes

the greatest distance from a given point in one object to the closest point in its mirror (Hausdorff distance); the degree of chirality is interpreted as a ratio of the minimum Hausdorff distance over the diameter of the object.¹⁴² For objects with complex morphologies like those observed in chiral nanoparticles, the amount of points to consider for this calculation makes it prohibitively demanding to compute. Therefore, in this work morphological chirality is indirectly quantified by a measure of the helicity. Relating the structures of chiral nanoparticles to a helix is advantageous because geometrical properties of the latter can be simply applied to the former. By aligning a particle (such as a 3D reconstruction obtained from ET) along the central axis of a helix, the helicity of chiral features can be quantified and plotted as a function of the radius ρ and inclination angle α (see **Figure 1.9**).^{143,144}

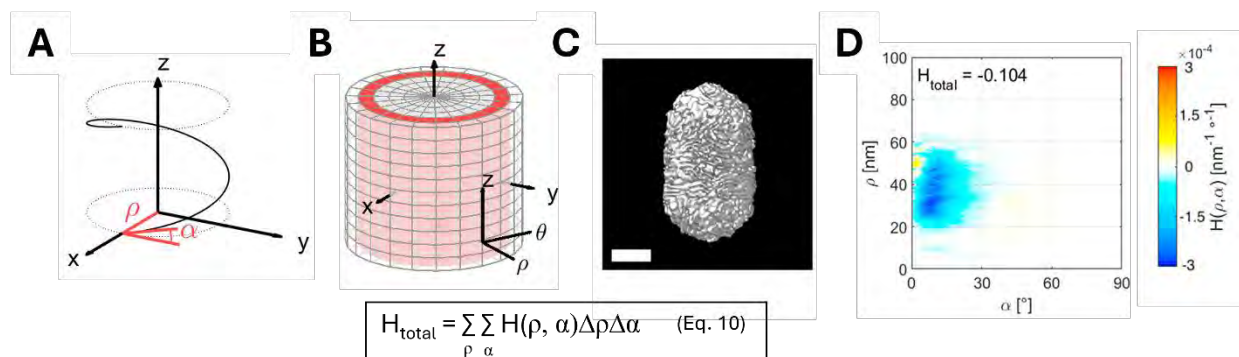


Figure 1.9. Method for quantifying the helicity of chiral particles, designed by Heyvaert, *et al.* The longitudinal symmetry axis of an ET reconstruction becomes the z axis of a cylindrical coordinate system (A,B), where the helicity of chiral features are evaluated voxel by voxel as a function of ρ and α . For a chiral particle (even with complex surface geometry (C; scale bar = 50 nm), a helicity plot is generated for all combinations of ρ and α (D). Total helicity (inset, D) for an analyzed nanoparticle is given by integrating the helicity function (Equation 8).¹⁴³ Adapted from ref. 143 (© ACS 2022).

Unlike other approaches for quantifying morphological chirality, quantifying helicity reports the directionality of morphological features: positive helicity values correspond to right-handedness and negative helicity values correspond to left-handedness.¹⁴³⁻¹⁴⁷ Furthermore, this helicity

function can be easily applied to computer models of chiral nanoparticles and compared to simulated electromagnetic spectra for the efficient investigation of structural-chiroptical relationships.

1.5b Computerized Modelling and Electromagnetic Simulations

Describing the intricacies of the many tools to simulate molecular dynamics and interactions of an electromagnetic field with small particles is beyond the scope of this thesis. However, these methods represent an important approach for understanding how chiral inducers influence the surface of achiral seeds and establishing relationships between structural features on chiral nanoparticles and the resulting optical signature (especially when compared to experimental data). In particular, the iterative nature of particle modelling and electromagnetic simulation enables morphology-driven investigation at a speed and resolution impossible for synthetic approaches. For example, changing a set of crystal facets on a nanoparticle as one would change a variable in an experiment (while keeping everything else constant) might take dozens of syntheses to perfect; this process is dramatically simplified using 3D modelling software on a computer. Generally, simulations relevant to the context of this work fall into one of two categories.^{148,149} Volumetric approaches (e.g. discrete-dipole approximation, finite difference time-domain)⁵⁶ use simplified electromagnetic solutions applied to representative points across the whole structure; the computational time scales with the simulated volume, thus becoming increasingly impractical to run for larger structures. Boundary approaches like SIE-MoM (surface integral equations method of moments)^{145,150,151} only solve for 2D interfaces of the simulated object, and thus computational time is not wasted on simulating the space inside or surrounding the object; these methods are

more efficient than volumetric approaches. In any case, the careful design of 3D models (or directly imported data from electron tomography reconstructions) and electromagnetic simulations provide an additional tool for further understanding chiral growth mechanisms.

1.5c Chemically-Induced Chiral Growth

The first chiral growth strategy relies on the use of thiolated chiral molecules during seeded growth on gold nanomaterials with selected morphologies. Chiral molecules such as glutathione, cysteine–phenylalanine, and adenine oligomers have shown great promise in inducing chiral growth,¹⁵²⁻¹⁵⁴ the following is a discussion of the chemisorption strategy in the context of cysteine, which is the most widely used inducer for this purpose.¹⁵⁵⁻¹⁵⁸ Cysteine is unique among amino acids in a pair of important aspects. The only amino acid possessing a thiol group, cysteine is favored to coordinate gold surfaces during a synthetic step and influence the growth of nanomaterials. Secondly, the thiolated side chain of cysteine is prioritized over the carboxylic acid on the backbone according to the Cahn-Ingold-Prelog (CIP) rules.¹⁵⁹ This has an important and nonintuitive ramification for the associated nomenclature: whereas natural amino acids are all **L**-type and are thus expected to align with the **S**-type CIP notation, natural cysteine does not. In other words, this means that natural (**L**-) cysteine is of the right-handed (**R**-) configuration, as opposed to synthetic (**D**-) cysteine, which is of the left-handed (**S**-) configuration. When introduced during a synthetic step, cysteine can guide the growth of gold nanomaterials into an array of different shapes and surface geometries. This process is typically conducted at a relatively low concentration of chiral inducer (compared to that of the surfactant and available Au surface), suggesting that weakly-binding functional groups that would be less relevant at high concentration are important

for optimal chiral growth.¹⁶⁰⁻¹⁶² The extent of chiral growth can be controlled by modifying the concentrations of gold precursor and reducing agent, as well as the temperature or time of reaction. The variety of chiral nanostructures achieved using cysteine as the chiral inducer suggests a complex and incompletely understood growth mechanism.¹⁶³⁻¹⁶⁵ Chiral growth on gold nanomaterials mediated by cysteine has been proposed to evolve through the gradual removal of mirror planes present in the initial seeds, yielding dissymmetric final products. At a very early stage in a typical chiral reaction, the formation of high-Miller-index facets at the nanoscale corresponds to the arrangement of chiral facets at the atomic scale.¹⁶⁶ Specifically, chiral facets can be seen as the resulting clockwise (**R**) or counterclockwise (**S**) arrangement of small low-index terraces, from the most densely to the least densely packed terraces, i.e., from (111) to (100) and (110). The enantioselective adsorption of cysteine to these chiral facets, or “kink sites”, causes the gradual removal of mirror planes from nanomaterials as they grow, resulting in products with a twisted geometry.^{162,163} A pair of publications by Nam and co-workers demonstrate the reliance of this mechanism on the symmetry of the starting materials.^{160,161} Nanocuboids with a strong chiroptical signature were synthesized using the same enantiomer of cysteine, and differing starting seeds: cubes became stellated octahedrons (termed Helicoid I) and cuboctahedrons became rhombic dodecahedrons (termed Helicoid IV). An unstated observation in these publications was that the chiroptical signatures for Helicoid I and Helicoid IV are inverted with respect to one another, despite using the same enantiomer of cysteine in both syntheses (**Figure 1.10**). Though the conclusions of these publications emphasized the importance of the timing of introducing cysteine into each reaction mixture, the unstated influence of the starting seed crystallinity on the final product geometry and corresponding chiroptical signature should not be ignored. Helicoidal products like these are also observed to possess chiral features of opposing directionality

depending on the viewing direction: for example, the faces of Helicoid I when oriented along the [100] axis show a right-handed twist, whilst corners with a left-handed twist can be observed when orienting along the [111] axis (**Figure 1.10B**, inset). This contrast is even more apparent in the features on the faces and corners of Helicoid IV (**Figure 1.10E**, inset). Exploring and optimizing the multi-scale chiral features appearing on the same particle will be the focus of a later chapter.

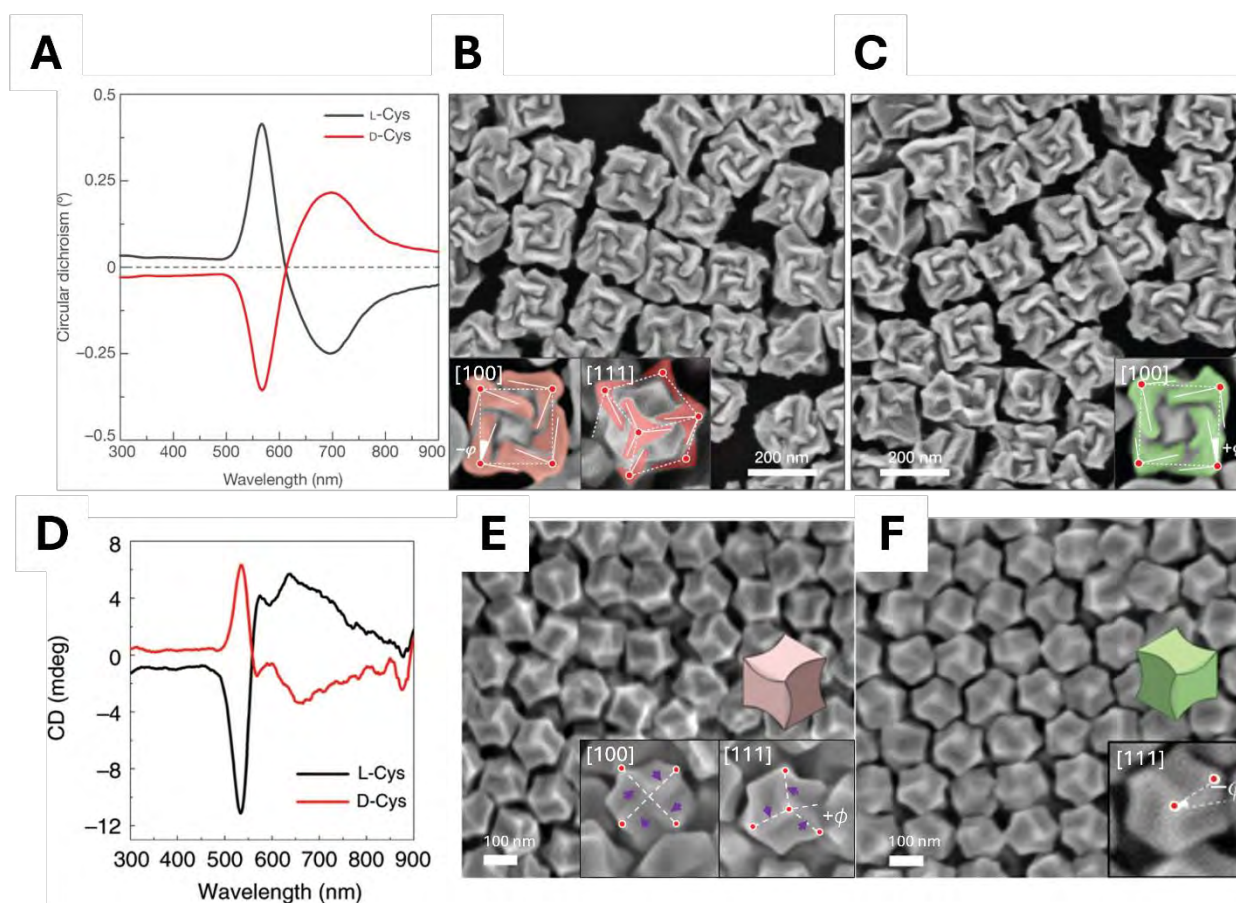


Figure 1.10. Circular dichroism spectra and SEM images of chiral particles synthesized with *L*-cysteine or *D*-cysteine, respectively for Helicoids I (A-C) and IV (D-F). Note the opposing chiroptical signatures of Helicoid I and Helicoid IV, prepared identically except the starting achiral seeds: the Helicoid I synthesis used cubes, whereas the Helicoid IV synthesis used cuboctahedrons. Adapted from ref. 160 (publ. Nature 2018) and ref. 161 (publ. Nature Comm. 2020).

It has been proposed that the structural evolution occurring at either protruding facets or particle tips is disproportionately important to the chiroptical signature and final geometry of yielded particles.¹⁶⁷ The influence of tip morphology on the chiroptical signature has been modelled by Liu, et al., who showed through simulations that chiroptical spectra for nanocube models with high-Miller-index chiral facets were dramatically shifted—and inverted—compared to those from nanorod models possessing similar chiral facets (**Figure 1.11**).¹⁶⁸ It should be noted, however, that no conclusive experimental evidence was provided to support this hypothesis.

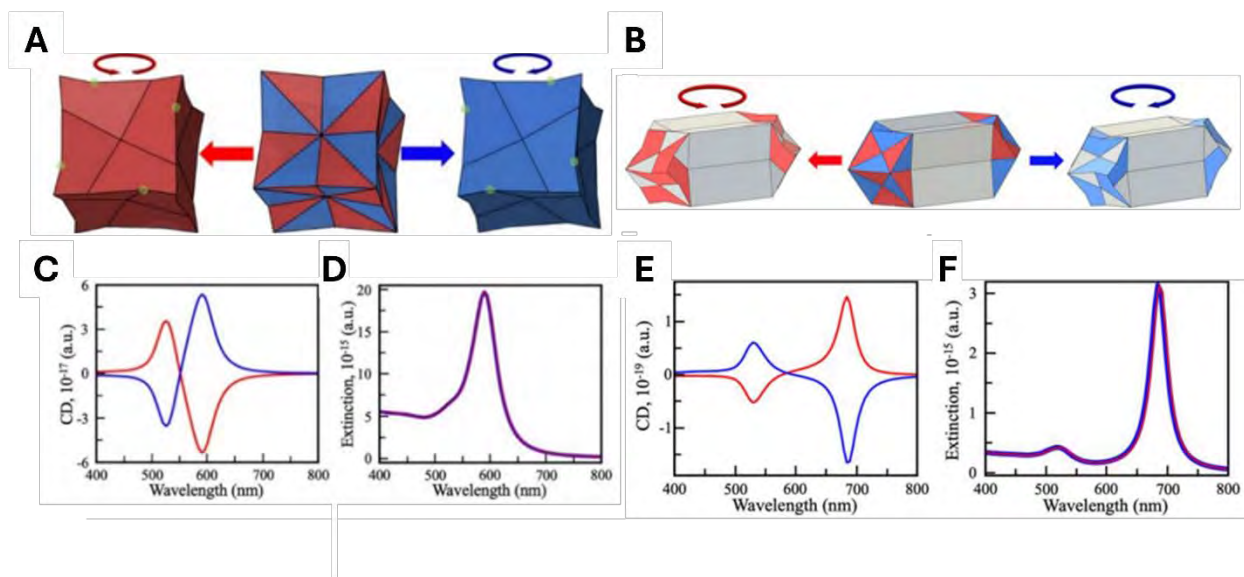


Figure 1.11. Schematics indicating putative chiral facets on (A) nanocubes and (B) nanorods, and computed CD (C, E for nanocubes, nanorods, respectively) and computed extinction spectra (D, F for nanocubes, nanorods, respectively). Note that the computed CD magnitudes of nanocubes and nanorods are opposite of each other, regardless of particle handedness (red spectrum = **S**, blue spectrum = **R**). Adapted from ref. 168 (© ACS 2023).

Additional factors, including concentration and conformation of the chiral inducer at the particle surface, how gold salts are introduced, and the influence of additives, should be considered when further investigating this mechanism.¹⁶⁹⁻¹⁷¹ Our research team reported a cysteine-mediated multistep growth method, enabling the synthesis of fourfold-twisted gold nanorods with a clearly apparent geometrical handedness and enhanced *g*-factor.¹⁶³ Gradual enantioselective growth

thanks to the stepwise addition of gold salts as the reaction progressed resulted in nanoparticles with a more defined twist and enhanced *g*-factor compared to other chiral products using this growth mechanism. In contrast, X. Wu et al. achieved the fabrication of helical plasmonic nanorods through the synergistic combination of cysteine and the achiral molecule 4-aminothiophenol, in the presence of a significant amount of Ag^+ ions, yielding a *g*-factor of 0.04.¹⁷² However, the specific role of additives like silver ions is yet to be determined. Precise characterization of chiral products via electron tomography,^{138,139} ideally during time-resolved experiments to track chiral growth during the course of each reaction, are critical to expanding our understanding of the underlying mechanism.

1.5d Micelle-Directed Chiral Growth

As discussed previously, cetyltrimethylammonium micelles are important to the formation of anisotropic nanoparticles. The observation that these micelles, and the subsequent crystal growth, could be influenced by changing the chemistry of these micelles using additives is foundational to the discovery of this chiral growth mechanism. This culminated in the use of cosurfactants such as 1,1'-bi(2-naphthol) (BINOL) and 1,1'-binaphthyl-2,2'-diamine (BINAMINE) to influence chiral growth.^{173,174} Unlike cysteine, these molecules do not possess point chirality, and are theorized to coordinate to Au nanostructures through the formation of large worm-like micelles comprised of the co-surfactant and CTAC.¹⁷⁵ As experimentation with this mechanism progressed, BINAMINE was favored, as its amine groups were proposed to adsorb more strongly to the Au surface during growth, thereby reinforcing a potential templating effect. The axial chirality present in BINAMINE denotes directionality to these micelles, depending on the handedness of the BINAMINE

enantiomer. As with the chemisorption mechanism, the chiral reaction is triggered on achiral seeds (Au^0) by an overgrowth step, which entails the fast reduction of gold salts (Au^{3+}) by ascorbic acid; as a result, protruding wrinkles form on seeds as the gold crystal grows between the spaces of the adsorbed micelles. Because of this, this mechanism is often referred to as chiral micelle templating or micelle-directed chiral growth. It has been shown that the incubation of achiral seeds with BINAMINE and CTAC, as well as the fast reduction of gold salts via quick addition of ascorbic acid, are vital factors to reaction success. Products obtained using BINAMINE and high-aspect gold nanorods as seeds have been observed to possess intense chiroptical magnitudes (up to 0.20 or even higher in the NIR), hypothesized to originate from the high degree of local directionality and definition of these wrinkles. In collaboration with the group of Prof. Sara Bals (EMAT, University of Antwerp), a method was devised to quantitatively evaluate the helicity of wrinkles produced on nanorods synthesized with BINAMINE, based on image reconstructions from particle characterization by electron tomography.¹⁴³ It was observed that the helicity and corresponding chiroptical signature of these particles are correlated with the thickness of the wrinkled features in the "chiral shell" surrounding the nanorod seed. Interestingly, both directionalities of this wrinkled morphology were identified in subregions of particles synthesized with either enantiomer of BINAMINE (**Figure 1.12**). The dominating handedness of the wrinkles present matched the handedness of BINAMINE used, which corresponded to the overriding magnitude of the total helicity.

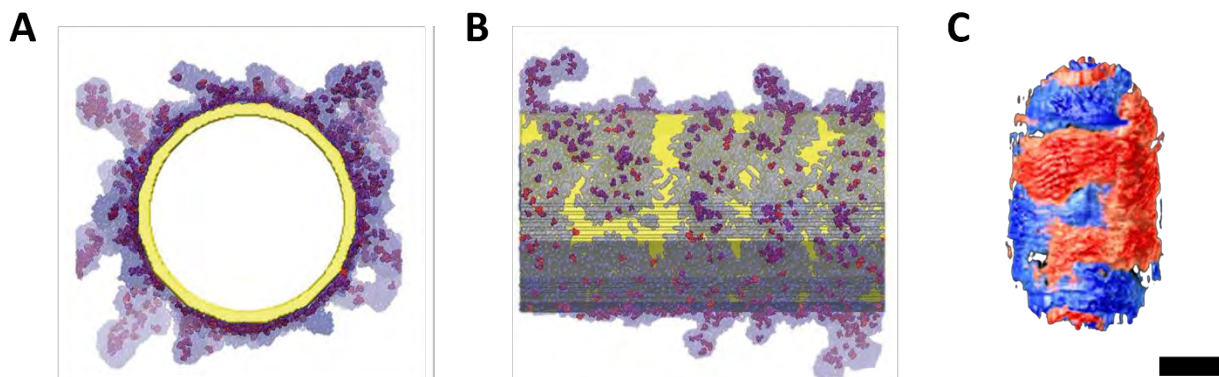


Figure 1.12. Molecular dynamics simulations of chiral micelles adsorbed onto a gold nanorod model (A, B). During a chiral reaction, growth occurs in the gaps in the micellar coverage, which results in well-defined wrinkles with a directionality dependent on the handedness of the chiral inducer used. However, wrinkles of both directionalities are present in products of micelle-directed chiral reactions, regardless of enantiomer used (C; red indicates right-handed wrinkles; blue indicates left-handed wrinkles, scale bar = 50 nm). Adapted from ref. 173 (publ. Science 2020) and ref. 143 (© ACS 2022).

Though limited by the small amount of particles assessed in this study, this work is invaluable towards investigating the products of micelle-directed chiral growth and the relationship between structure and chiroptical response. To further delve into the underlying mechanisms of micelle-directed chiral growth, it is important to track products as they grow from achiral seeds to chiral particles. Zhuo, et. al. presented a pair of approaches to monitor the products of micelle-directed chiral growth induced by BINAMINE.¹⁵¹ The first approach involved preparing a synthesis and tracking its chiroptical signature in real-time inside a CD instrument. From this work came the observation of a critical transition that occurs within the first minute of the reaction, and an abnormal increase in absorption with respect to scattering as chiral wrinkles form. The corresponding appearance of three distinct CD bands occurring within the first minute of the growth reaction, which progressively red-shift and typically reach their maximum magnitude within less than ten minutes, was also observed (**Figure 1.13A,B**). However, this approach was limited by the maximum scan speed and spectral resolution of the instrument; the fact that

increasing one of these factors decreases the other puts a practical limit on how fine the intervals in a real-time spectroscopic analysis can be. Additionally, the products of a specific time interval in an *in situ* preparation cannot be characterized in isolation because the chiral reaction continues to completion. There are methods to circumvent this, such as quenching the growing products in an excess of water or another non-reacting solvent to effectively stop chiral growth, but it is uncertain whether quenching occurs sufficiently fast, and whether these methods can reproducibly isolate small products from a large volume of liquid. Therefore, a second approach established a series of chiral growth reactions with increasing gold salt-to-seed ratio, to study the gradual formation of chiral features on the Au NR seed surface (**Figure 1.13C-F**).

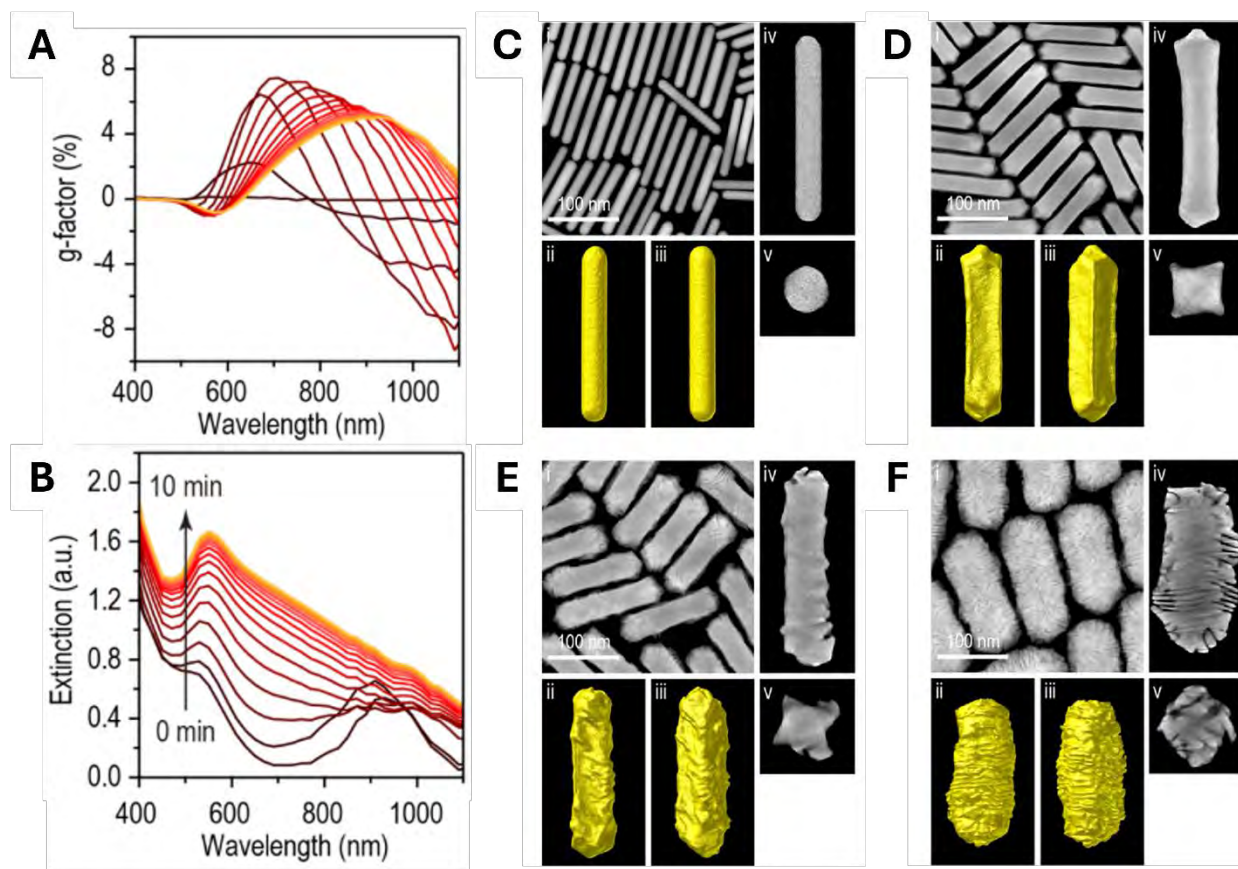


Figure 1.13. Comparison of methods to analyze products of micelle-directed chiral growth in progress. Chiroptical (A) and extinction (B) spectra of reactions prepared *in situ* indicate that the maximum chiroptical signature is quickly achieved, but these products are impossible to isolate since the reaction continues to completion. Thus, products were prepared with different amounts of gold salts available for the overgrowth reaction (HAADF-STEM images and electron tomography reconstructions, C-F), allowing study of intermediates since the reaction would terminate after the gold salts were exhausted. This revealed the formation of an elongated octahedra geometry, which promoted the growth of deep directional wrinkles as the reaction progresses. Adapted from ref. 151 (© ACS 2022).

This approach showed interesting information about intermediate morphologies that are important for chiral growth; specifically, an elongated octahedral intermediate was observed to be critical as a platform for the formation of distinct directional wrinkles. It should be noted that such a series is not a representation of an optimized reaction in progress, which was reproducibly achieved using a large excess of gold salts to achiral seeds. All told, there is a mandate for the time-resolved optical

and structural characterization of chiral nanomaterials, with a focus on finer time points, which especially concerns chiral syntheses like these that complete more quickly.

1.6 Summary

In “bottom-up” colloidal syntheses, nanoparticles can be engineered with directional, tunable morphologies dependent on the chemical parameters of the reaction. These reactions involve the transfer of chirality across different size scales and materials, from molecular to the nanoscale. Because stereochemistry has different forms at different scales, different handedness conventions have been historically used, and therefore care must be taken when using them. Currently, we can distinguish two main synthesis strategies toward synthesis of inherently chiral nanoparticles. In both cases, the underlying mechanism involves elimination of mirror planes present in the morphology of the employed seed particles. In the first strategy, thiolated chiral molecules such as amino acids or peptides are used as chiral inducers that affect nanomaterial surface energies, which in turn gradually translate into chiral and twisted facets in the resulting nanoparticle. As it happens for most nanomaterial growth methods, the obtained chiral shapes strongly depend on the concentrations of precursors and chiral inducers, as well as on the starting symmetry of the seeds. This is true also for the second main synthesis strategy discovered and discussed here: micelle-directed chiral growth. Here, BINAMINE, possessing axial chirality, is used as a co-surfactant with CTAC, forming large chiral micelles that adsorb to gold nanorods and act as a template for chiral growth. In addition to these strategies, external factors such as circularly polarized light can effectively modulate directional growth, resulting in materials with optical activities enhanced over that realized with chiral inducers alone. This approach will be discussed in greater detail in

the outlook. Chirality quantification has already demonstrated an immense potential in establishing structure-optical relationships and has been accomplished through approaches guided by information from electron tomography, such as mapping helicity on the surface of nanomaterials at the nanometer scale. Although the synthetic toolboxes are quite rich, large outstanding questions remain, i.e. how chiral inducers modulate growth on the atomic level, the contribution of seed crystallinity and protruding facets like particle tips to the chiroptical signature, and how chiral growth progresses in real-time. For the preparation of other kinds of inherently chiral plasmonic nanomaterials, a major bottleneck is in the discovery of novel and effective chiral inducers. As discussed in the forthcoming chapter, the judicious design and selection of a host of chiral inducers can bring about unprecedented structures and intense chiroptical activities. Furthermore, this approach is important towards expanding our understanding of the underlying growth mechanisms and optimizing future syntheses of chiral plasmonic nanomaterials.

1.7 References

1. Vert, M.; Doi, Y.; Hellwich, K.-H.; Hess, M.; Hodge, P.; Kubisa, P.; Rinaudo, M.; Schué, F., Terminology for Biorelated Polymers and Applications (IUPAC Recommendations 2012). **2012**, *84*, 377-410.
2. Liz-Marzán, L. M.; Artzi, N.; Bals, S.; Buriak, J. M.; Chan, W. C. W.; Chen, X.; Hersam, M. C.; Kim, I.-D.; Millstone, J. E.; Mulvaney, P.; Parak, W. J.; Rogach, A.; Schaak, R. E., Celebrating a Nobel Prize to the “Discovery of Quantum Dots, an Essential Milestone in Nanoscience”. *ACS Nano* **2023**, *17*, 19474-19475.
3. Khan, I.; Saeed, K.; Khan, I., Nanoparticles: Properties, Applications and Toxicities. *Arabian Journal of Chemistry* **2019**, *12*, 908-931.
4. Masel, R. I.; Liu, Z.; Yang, H.; Kaczur, J. J.; Carrillo, D.; Ren, S.; Salvatore, D.; Berlinguette, C. P., An Industrial Perspective on Catalysts for Low-Temperature CO₂ Electrolysis. *Nature Nanotechnology* **2021**, *16*, 118-128.

5. Wang, M.; Thanou, M., Targeting Nanoparticles to Cancer. *Pharmacol. Res.* **2010**, *62*, 90-99.
6. Sun, L.; Liu, H.; Ye, Y.; Lei, Y.; Islam, R.; Tan, S.; Tong, R.; Miao, Y.-B.; Cai, L., Smart nanoparticles for cancer therapy. *Signal Transduction and Targeted Therapy* **2023**, *8*, 418.
7. Barenholz, Y., Doxil® — The First FDA-Approved Nano-Drug: Lessons Learned. *J. Controlled Release* **2012**, *160*, 117-134.
8. Jia, Y.; Jiang, Y.; He, Y.; Zhang, W.; Zou, J.; Magar, K. T.; Boucetta, H.; Teng, C.; He, W. Approved Nanomedicine Against Diseases *Pharmaceutics* [Online], 2023.
9. Pierre, V. C.; Allen, M. J.; Caravan, P., Contrast Agents for MRI: 30+ Years and Where are we Going? *JBIC Journal of Biological Inorganic Chemistry* **2014**, *19*, 127-131.
10. Al-Hakkani, M. F., Biogenic Copper Nanoparticles and their Applications: A Review. *SN Applied Sciences* **2020**, *2*, 505.
11. Xu, L.; Wang, X.; Wang, W.; Sun, M.; Choi, W. J.; Kim, J.-Y.; Hao, C.; Li, S.; Qu, A.; Lu, M.; Wu, X.; Colombari, F. M.; Gomes, W. R.; Blanco, A. L.; de Moura, A. F.; Guo, X.; Kuang, H.; Kotov, N. A.; Xu, C., Enantiomer-Dependent Immunological Response to Chiral Nanoparticles. *Nature* **2022**, *601*, 366-373.
12. de la Encarnación, C.; Jimenez de Aberasturi, D.; Liz-Marzán, L. M., Multifunctional Plasmonic-Magnetic Nanoparticles for Bioimaging and Hyperthermia. *Advanced Drug Delivery Reviews* **2022**, *189*, 114484.
13. Zayats, A. V., Perspective: A Glint of the Future. *Nature* **2013**, *495*, S7-S7.
14. Leonhardt, U., Invisibility Cup. *Nature Photonics* **2007**, *1*, 207-208.
15. Montanarella, F.; Kovalenko, M. V., Three Millennia of Nanocrystals. *ACS Nano* **2022**, *16*, 5085-5102.
16. Mie, G., Beiträge zur Optik trüber Medien, speziell kolloidaler Metallösungen. *Annalen der Physik* **1908**, *330*, 377-445.
17. Ritchie, R. H., Plasma Losses by Fast Electrons in Thin Films. *Physical Review* **1957**, *106*, 874-881.
18. Hayashi, S.; Okamoto, T., Plasmonics: Visit the Past to Know the Future. *J. Phys. D: Appl. Phys.* **2012**, *45*, 433001.
19. Gray, S. K., Theory and Modeling of Plasmonic Structures. *The Journal of Physical Chemistry C* **2013**, *117*, 1983-1994.

20. Quesada-González, D.; Merkoçi, A., Nanoparticle-based Lateral Flow Biosensors. *Biosens. Bioelectron.* **2015**, *73*, 47-63.
21. Sommerfeld, A., Zur Elektronentheorie der Metalle auf Grund der Fermischen Statistik. *Zeitschrift für Physik* **1928**, *47*, 1-32.
22. Fermi, E., Zur Quantelung des Idealen Einatomigen Gases. *Zeitschrift für Physik* **1926**, *36*, 902-912.
23. Pines, D.; Bohm, D., A Collective Description of Electron Interactions: II. Collective vs. Individual Particle Aspects of the Interactions. *Physical Review* **1952**, *85*, 338-353.
24. Powell, C. J.; Swan, J. B., Origin of the Characteristic Electron Energy Losses in Aluminum. *Physical Review* **1959**, *115*, 869-875.
25. Marucho, M.; Garcia Canal, C. A.; Fanchiotti, H., The Landau Distribution for Charged Particles Traversing Thin Films. *International Journal of Modern Physics C* **2006**, *17*, 1461-1476.
26. Fermi, E., The Ionization Loss of Energy in Gases and in Condensed Materials. *Physical Review* **1940**, *57*, 485-493.
27. Sung, C. C.; Ritchie, R. H., The Energy-Loss Spectra of Fast Charged Particles Passing Through a Thin Metallic Film. *Journal of Physics C: Solid State Physics* **1981**, *14*, 2409.
28. Bethe, H.; Heitler, W., On the Stopping of Fast Particles and on the Creation of Positive Electrons. *Proceedings of the Royal Society of London. Series A, Containing Papers of a Mathematical and Physical Character* **1934**, *146*, 83-112.
29. Otto, A., Excitation of Nonradiative Surface Plasma Waves in Silver by the Method of Frustrated Total Reflection. *Zeitschrift für Physik A Hadrons and nuclei* **1968**, *216*, 398-410.
30. Kretschmann, E.; Raether, H., Notizen: Radiative Decay of Non Radiative Surface Plasmons Excited by Light. **1968**, *23*, 2135-2136.
31. Raether, H., Surface Plasmons on Smooth Surfaces. In *Surface Plasmons on Smooth and Rough Surfaces and on Gratings*, Raether, H., Ed. Springer Berlin Heidelberg: Berlin, Heidelberg, 1988; pp 4-39.
32. Parsoua, A. S.; Mojtaba, K., Principles and Applications of Nanoplasmonics in Biological and Chemical Sensing: A Review. In *Recent Advances in Nanophotonics*, Mojtaba, K.; Parsoua, A. S., Eds. IntechOpen: Rijeka, 2020; p Ch. 1.

33. Nguyen, H. H.; Park, J.; Kang, S.; Kim, M. Surface Plasmon Resonance: A Versatile Technique for Biosensor Applications *Sensors* [Online], 2015, p. 10481-10510.
34. Jiang, N.; Zhuo, X.; Wang, J., Active Plasmonics: Principles, Structures, and Applications. *Chem. Rev.* **2018**, *118*, 3054-3099.
35. Maier, S., *Plasmonics: Fundamentals and Applications*. 2007.
36. Fröhlich, H., *Theory of Dielectrics; Dielectric Constant and Dielectric Loss*. Clarendon Press: Oxford, 1949.
37. Agrawal, A.; Cho, S. H.; Zandi, O.; Ghosh, S.; Johns, R. W.; Milliron, D. J., Localized Surface Plasmon Resonance in Semiconductor Nanocrystals. *Chem. Rev.* **2018**, *118*, 3121-3207.
38. Jana, J.; Ganguly, M.; Pal, T., Enlightening Surface Plasmon Resonance Effect of Metal Nanoparticles for Practical Spectroscopic Application. *RSC Adv.* **2016**, *6*.
39. Goerlitzer, E. S. A.; Puri, A. S.; Moses, J. J.; Poulikakos, L. V.; Vogel, N., The Beginner's Guide to Chiral Plasmonics: Mostly Harmless Theory and the Design of Large-Area Substrates. *Advanced Optical Materials* **2021**, *9*, 2100378.
40. Kelly, K. L.; Coronado, E.; Zhao, L. L.; Schatz, G. C., The Optical Properties of Metal Nanoparticles: The Influence of Size, Shape, and Dielectric Environment. *The Journal of Physical Chemistry B* **2003**, *107*, 668-677.
41. Fan, X.; Zheng, W.; Singh, D. J., Light Scattering and Surface Plasmons on Small Spherical Particles. *Light: Science and Applications* **2014**, *3*, 14.
42. Nordlander, P.; Oubre, C.; Prodan, E.; Li, K.; Stockman, M. I., Plasmon Hybridization in Nanoparticle Dimers. *Nano Lett.* **2004**, *4*, 899-903.
43. Funston, A. M.; Novo, C.; Davis, T. J.; Mulvaney, P., Plasmon Coupling of Gold Nanorods at Short Distances and in Different Geometries. *Nano Lett.* **2009**, *9*, 1651-1658.
44. Rechberger, W.; Hohenau, A.; Leitner, A.; Krenn, J. R.; Lamprecht, B.; Aussenegg, F. R., Optical Properties of Two Interacting Gold Nanoparticles. *Optics Communications* **2003**, *220*, 137-141.
45. Severoni, E.; Maniappan, S.; Liz-Marzán, L. M.; Kumar, J.; García de Abajo, F. J.; Galantini, L., Plasmon-Enhanced Optical Chirality through Hotspot Formation in Surfactant-Directed Self-Assembly of Gold Nanorods. *ACS Nano* **2020**, *14*, 16712-16722.
46. Willets, K. A.; Van Duyne, R. P., Localized Surface Plasmon Resonance Spectroscopy and Sensing. *Annu. Rev. Phys. Chem.* **2007**, *58*, 267-297.

47. Abalde-Cela, S.; Hermida-Ramón, J. M.; Contreras-Carballada, P.; De Cola, L.; Guerrero-Martínez, A.; Alvarez-Puebla, R. A.; Liz-Marzán, L. M., SERS Chiral Recognition and Quantification of Enantiomers through Cyclodextrin Supramolecular Complexation. *ChemPhysChem* **2011**, *12*, 1529-1535.
48. Jimenez de Aberasturi, D.; Henriksen-Lacey, M.; Litti, L.; Langer, J.; Liz-Marzán, L. M., Using SERS Tags to Image the Three-Dimensional Structure of Complex Cell Models. *Adv. Funct. Mater.* **2020**, *30*, 1909655.
49. Reguera, J.; Langer, J.; Jiménez de Aberasturi, D.; Liz-Marzán, L. M., Anisotropic Metal Nanoparticles for Surface Enhanced Raman Scattering. *Chem. Soc. Rev.* **2017**, *46*, 3866-3885.
50. Huang, X.; Neretina, S.; El-Sayed, M. A., Gold Nanorods: From Synthesis and Properties to Biological and Biomedical Applications. *Adv. Mater.* **2009**, *21*, 4880-4910.
51. Smitha, S. L.; Gopchandran, K. G.; Smijesh, N.; Philip, R., Size-Dependent Optical Properties of Au Nanorods. *Progress in Natural Science: Materials International* **2013**, *23*, 36-43.
52. Kumar, R.; Binetti, L.; Nguyen, T. H.; Alwis, L. S. M.; Agrawal, A.; Sun, T.; Grattan, K. T. V., Determination of the Aspect-Ratio Distribution of Gold Nanorods in a Colloidal Solution using UV-visible Absorption Spectroscopy. *Scientific Reports* **2019**, *9*, 17469.
53. Jain, P. K.; Lee, K. S.; El-Sayed, I. H.; El-Sayed, M. A., Calculated Absorption and Scattering Properties of Gold Nanoparticles of Different Size, Shape, and Composition: Applications in Biological Imaging and Biomedicine. *The Journal of Physical Chemistry B* **2006**, *110*, 7238-7248.
54. Yan, B.; Yang; Wang, Y., Comment on “Simulation of the Optical Absorption Spectra of Gold Nanorods as a Function of Their Aspect Ratio and the Effect of the Medium Dielectric Constant”. *The Journal of Physical Chemistry B* **2003**, *107*, 9159-9159.
55. Gans, R., Über die Form Ultramikroskopischer Goldteilchen. *Annalen der Physik* **1912**, *342*, 881-900.
56. Brioude, A.; Jiang, X. C.; Pileni, M. P., Optical Properties of Gold Nanorods: DDA Simulations Supported by Experiments. *The Journal of Physical Chemistry B* **2005**, *109*, 13138-13142.
57. DeVoe, H., Optical Properties of Molecular Aggregates. I. Classical Model of Electronic Absorption and Refraction. *The Journal of Chemical Physics* **1964**, *41*, 393-400.

58. Myroshnychenko, V.; Rodríguez-Fernández, J.; Pastoriza-Santos, I.; Funston, A. M.; Novo, C.; Mulvaney, P.; Liz-Marzán, L. M.; De Abajo, F. J. G., Modelling the Optical Response of Gold Nanoparticles. *Chem. Soc. Rev.* **2008**, *37*, 1792-1805.
59. Pérez-Juste, J.; Pastoriza-Santos, I.; Liz-Marzán, L. M.; Mulvaney, P., Gold Nanorods: Synthesis, Characterization and Applications. *Coord. Chem. Rev.* **2005**, *249*, 1870-1901.
60. Hong, Y.; Huh, Y.-M.; Yoon, D. S.; Yang, J., Nanobiosensors Based on Localized Surface Plasmon Resonance for Biomarker Detection. *Journal of Nanomaterials* **2012**, *2012*, 759830.
61. Wagner, M.; Seifert, A.; Liz-Marzán, L. M., Towards Multi-Molecular Surface-Enhanced Infrared Absorption using Metal Plasmonics. *Nanoscale Horizons* **2022**, *7*, 1259-1278.
62. Smith, A. M.; Mancini, M. C.; Nie, S., Second Window for *in vivo* Imaging. *Nature Nanotechnology* **2009**, *4*, 710-711.
63. Ma, H.; Xu, L.; Tian, Y.; Jiao, A.; Zhang, M.; Li, S.; Chen, M., Design of a Thermally Stable and Highly Active SERS Optical Sensor for the Ultrasensitive Detection of Dye Molecules at High-Temperature. *Optical Materials Express* **2021**, *11*, 2001-2015.
64. Ali, A.; El-Mellouhi, F.; Mitra, A.; Aïssa, B., Research Progress of Plasmonic Nanostructure-Enhanced Photovoltaic Solar Cells. *Nanomaterials (Basel)* **2022**, *12*.
65. Espinosa, A.; Reguera, J.; Curcio, A.; Muñoz-Noval, Á.; Kuttner, C.; Van de Walle, A.; Liz-Marzán, L. M.; Wilhelm, C., Janus Magnetic-Plasmonic Nanoparticles for Magnetically Guided and Thermally Activated Cancer Therapy. *Small* **2020**, *16*, 1904960.
66. Kong, X.-T.; Besteiro, L. V.; Wang, Z.; Govorov, A. O., Plasmonic Chirality and Circular Dichroism in Bioassembled and Nonbiological Systems: Theoretical Background and Recent Progress. *Adv. Mater.* **2020**, *32*, 1801790.
67. West, P. R.; Ishii, S.; Naik, G. V.; Emani, N. K.; Shalaev, V. M.; Boltasseva, A., Searching for Better Plasmonic Materials. *Laser & Photonics Reviews* **2010**, *4*, 795-808.
68. Indhu, A. R.; Dharanya, C.; Dharmalingam, G., Plasmonic Copper: Ways and Means of Achieving, Directing, and Utilizing Surface Plasmons. *Plasmonics* **2024**, *19*, 1303-1357.
69. Zhou, L.; Swearer, D. F.; Zhang, C.; Robotjazi, H.; Zhao, H.; Henderson, L.; Dong, L.; Christopher, P.; Carter, E. A.; Nordlander, P.; Halas, N. J., Quantifying Hot Carrier and Thermal Contributions in Plasmonic Photocatalysis. *Science* **2018**, *362*, 69-72.
70. Xue, Y.; Li, X.; Li, H.; Zhang, W., Quantifying Thiol–Gold Interactions Towards the Efficient Strength Control. *Nature Communications* **2014**, *5*, 4348.

71. Pacchioni, G., A Not-So-Strong Bond. *Nature Reviews Materials* **2019**, *4*, 226-226.
72. Wang, Y.; Serrano, A. B.; Sentosun, K.; Bals, S.; Liz-Marzán, L. M., Stabilization and Encapsulation of Gold Nanostars Mediated by Dithiols. *Small* **2015**, *11*, 4314-4320.
73. Novikov, S. M.; Sánchez-Iglesias, A.; Schmidt, M. K.; Chuvilin, A.; Aizpurua, J.; Grzelczak, M.; Liz-Marzán, L. M., Gold Spiky Nanodumbbells: Anisotropy in Gold Nanostars. *Particle & Particle Systems Characterization* **2014**, *31*, 77-80.
74. Barbosa, S.; Agrawal, A.; Rodríguez-Lorenzo, L.; Pastoriza-Santos, I.; Alvarez-Puebla, R. A.; Kornowski, A.; Weller, H.; Liz-Marzán, L. M., Tuning Size and Sensing Properties in Colloidal Gold Nanostars. *Langmuir* **2010**, *26*, 14943-14950.
75. Baig, N.; Kammakam, I.; Falath, W., Nanomaterials: A Review of Synthesis Methods, Properties, Recent Progress, and Challenges. *Materials Advances* **2021**, *2*, 1821-1871.
76. Gonzalez-Rubio, G.; Kumar, V.; Llombart, P.; Diaz-Nunez, P.; Bladt, E.; Altantzis, T.; Bals, S.; Pena-Rodriguez, O.; Noya, E. G.; MacDowell, L. G.; Guerrero-Martinez, A.; Liz-Marzan, L. M., Disconnecting Symmetry Breaking from Seeded Growth for the Reproducible Synthesis of High Quality Gold Nanorods. *Acs Nano* **2019**, *13*, 4424-4435.
77. Zhang, J.; Langille, M. R.; Personick, M. L.; Zhang, K.; Li, S.; Mirkin, C. A., Concave Cubic Gold Nanocrystals with High-Index Facets. *JACS* **2010**, *132*, 14012-14014.
78. Li, J.; Wu, J.; Zhang, X.; Liu, Y.; Zhou, D.; Sun, H.; Zhang, H.; Yang, B., Controllable Synthesis of Stable Urchin-like Gold Nanoparticles Using Hydroquinone to Tune the Reactivity of Gold Chloride. *The Journal of Physical Chemistry C* **2011**, *115*, 3630-3637.
79. Sanchez-Iglesias, A.; Jenkinson, K.; Bals, S.; Liz-Marzan, L. M., Kinetic Regulation of the Synthesis of Pentatwinned Gold Nanorods below Room Temperature. *Journal of Physical Chemistry C* **2021**, *125*, 23937-23944.
80. Wadams, R. C.; Fabris, L.; Vaia, R. A.; Park, K., Time-Dependent Susceptibility of the Growth of Gold Nanorods to the Addition of a Cosurfactant. *Chem. Mater.* **2013**, *25*, 4772-4780.
81. Faraday, M., X. The Bakerian Lecture. —Experimental Relations of Gold (and Other Metals) to Light. *Philosophical Transactions of the Royal Society of London* **1857**, *147*, 145-181.
82. Turkevich, J.; Stevenson, P. C.; Hillier, J., A Study of the Nucleation and Growth Processes in the Synthesis of Colloidal Gold. *Discussions of the Faraday Society* **1951**, *11*, 55-75.
83. Frens, G., Controlled Nucleation for the Regulation of the Particle Size in Monodisperse Gold Suspensions. *Nature Physical Science* **1973**, *241*, 20-22.

84. LaMer, V. K.; Dinegar, R. H., Theory, Production and Mechanism of Formation of Monodispersed Hydrosols. *JACS* **1950**, *72*, 4847-4854.
85. LaMer, V. K., Nucleation in Phase Transitions. *Industrial & Engineering Chemistry* **1952**, *44*, 1270-1277.
86. Reiss, H., The Growth of Uniform Colloidal Dispersions. *J. Chem. Phys.* **1951**, *19*, 482-487.
87. Pong, B.-K.; Elim, H. I.; Chong, J.-X.; Ji, W.; Trout, B. L.; Lee, J.-Y., New Insights on the Nanoparticle Growth Mechanism in the Citrate Reduction of Gold(III) Salt: Formation of the Au Nanowire Intermediate and Its Nonlinear Optical Properties. *The Journal of Physical Chemistry C* **2007**, *111*, 6281-6287.
88. Watzky, M. A.; Finke, R. G., Transition Metal Nanocluster Formation Kinetic and Mechanistic Studies. A New Mechanism When Hydrogen Is the Reductant: Slow, Continuous Nucleation and Fast Autocatalytic Surface Growth. *JACS* **1997**, *119*, 10382-10400.
89. Lin, M. Y.; Lindsay, H. M.; Weitz, D. A.; Ball, R. C.; Klein, R.; Meakin, P., Universality in Colloid Aggregation. *Nature* **1989**, *339*, 360-362.
90. Ostwald, W., Studien über die Bildung und Umwandlung fester Körper. *1. Abhandlung: Übersättigung und Überkaltung* **1897**, *22U*, 289-330.
91. Dreaden, E. C.; Alkilany, A. M.; Huang, X.; Murphy, C. J.; El-Sayed, M. A., The Golden Age: Gold Nanoparticles for Biomedicine. *Chem. Soc. Rev.* **2012**, *41*, 2740-79.
92. Johnson, C. J.; Dujardin, E.; Davis, S. A.; Murphy, C. J.; Mann, S., Growth and Form of Gold Nanorods Prepared by Seed-Mediated, Surfactant-Directed Synthesis. *J. Mater. Chem.* **2002**, *12*, 1765-1770.
93. Suárez-López, R.; Puentes, V. F.; Bastús, N. G.; Hervés, C.; Jaime, C., Nucleation and Growth of Gold Nanoparticles in the Presence of Different Surfactants. A Dissipative Particle Dynamics Study. *Scientific Reports* **2022**, *12*, 13926.
94. Jana, N. R.; Gearheart, L.; Murphy, C. J., Seed-Mediated Growth Approach for Shape-Controlled Synthesis of Spheroidal and Rod-like Gold Nanoparticles Using a Surfactant Template. *Adv. Mater.* **2001**, *13*, 1389-1393.
95. Jana, N. R.; Gearheart, L.; Murphy, C. J., Seeding Growth for Size Control of 5–40 nm Diameter Gold Nanoparticles. *Langmuir* **2001**, *17*, 6782-6786.

96. Sánchez-Iglesias, A.; Winckelmans, N.; Altantzis, T.; Bals, S.; Grzelczak, M.; Liz-Marzán, L. M., High-Yield Seeded Growth of Monodisperse Pentatwinned Gold Nanoparticles through Thermally Induced Seed Twinning. *JACS* **2017**, *139*, 107-110.
97. Walsh, M. J.; Tong, W.; Katz-Boon, H.; Mulvaney, P.; Etheridge, J.; Funston, A. M., A Mechanism for Symmetry Breaking and Shape Control in Single-Crystal Gold Nanorods. *Acc. Chem. Res.* **2017**, *50*, 2925-2935.
98. Lohse, S. E.; Burrows, N. D.; Scarabelli, L.; Liz-Marzán, L. M.; Murphy, C. J., Anisotropic Noble Metal Nanocrystal Growth: The Role of Halides. *Chem. Mater.* **2014**, *26*, 34-43.
99. Rodríguez-Fernández, J.; Pérez-Juste, J.; Mulvaney, P.; Liz-Marzán, L. M., Spatially-Directed Oxidation of Gold Nanoparticles by Au(III)-CTAB Complexes. *The Journal of Physical Chemistry B* **2005**, *109*, 14257-14261.
100. Scarabelli, L.; Sánchez-Iglesias, A.; Pérez-Juste, J.; Liz-Marzán, L. M., A “Tips and Tricks” Practical Guide to the Synthesis of Gold Nanorods. *The Journal of Physical Chemistry Letters* **2015**, *6*, 4270-4279.
101. Jana, N. R.; Gearheart, L.; Murphy, C. J., Wet Chemical Synthesis of High Aspect Ratio Cylindrical Gold Nanorods. *The Journal of Physical Chemistry B* **2001**, *105*, 4065-4067.
102. Park, K.; Hsiao, M.-S.; Koerner, H.; Jawaid, A.; Che, J.; Vaia, R. A., Optimizing Seed Aging for Single Crystal Gold Nanorod Growth: The Critical Role of Gold Nanocluster Crystal Structure. *The Journal of Physical Chemistry C* **2016**, *120*, 28235-28245.
103. Liu, M.; Guyot-Sionnest, P., Mechanism of Silver(I)-Assisted Growth of Gold Nanorods and Bipyramids. *The Journal of Physical Chemistry B* **2005**, *109*, 22192-22200.
104. Carbó-Argibay, E.; Rodríguez-González, B.; Pacifico, J.; Pastoriza-Santos, I.; Pérez-Juste, J.; Liz-Marzán, L. M., Chemical Sharpening of Gold Nanorods: The Rod-to-Octahedron Transition. *Angew. Chem. Int. Ed.* **2007**, *46*, 8983-8987.
105. Tong, W.; Walsh, M. J.; Mulvaney, P.; Etheridge, J.; Funston, A. M., Control of Symmetry Breaking Size and Aspect Ratio in Gold Nanorods: Underlying Role of Silver Nitrate. *The Journal of Physical Chemistry C* **2017**, *121*, 3549-3559.
106. Langille, M. R.; Personick, M. L.; Zhang, J.; Mirkin, C. A., Defining Rules for the Shape Evolution of Gold Nanoparticles. *JACS* **2012**, *134*, 14542-14554.
107. Personick, M. L.; Langille, M. R.; Zhang, J.; Mirkin, C. A., Shape Control of Gold Nanoparticles by Silver Underpotential Deposition. *Nano Lett.* **2011**, *11*, 3394-3398.

108. Carbó-Argibay, E.; Rodríguez-González, B.; Gómez-Graña, S.; Guerrero-Martínez, A.; Pastoriza-Santos, I.; Pérez-Juste, J.; Liz-Marzán, L. M., The Crystalline Structure of Gold Nanorods Revisited: Evidence for Higher-Index Lateral Facets. *Angew. Chem. Int. Ed.* **2010**, *49*, 9397-9400.
109. Mosquera, J.; Wang, D.; Bals, S.; Liz-Marzán, L. M., Surfactant Layers on Gold Nanorods. *Acc. Chem. Res.* **2023**, *56*, 1204-1212.
110. Esumi, K.; Matsuhisa, K.; Torigoe, K., Preparation of Rodlike Gold Particles by UV Irradiation using Cationic Micelles as a Template. *Langmuir* **1995**, *11*, 3285-3287.
111. Pedraza-Tardajos, A.; Claes, N.; Wang, D.; Sánchez-Iglesias, A.; Nandi, P.; Jenkinson, K.; De Meyer, R.; Liz-Marzán, L. M.; Bals, S., Direct Visualization of Ligands on Gold Nanoparticles in a Liquid Environment. *Nature Chemistry* **2024**.
112. Jozwiak, K.; Lough, W. J.; Wainer, I. W., *Drug stereochemistry: Analytical methods and pharmacology*. CRC Press: 2012.
113. Davies, N. M.; Teng, X. W., Importance of Chirality in Drug Therapy and Pharmacy Practice: Implications for Psychiatry. *Advances in Pharmacy* **2003**, *1*, 242-252.
114. Bayley, P. M., The Analysis of Circular Dichroism of Biomolecules. *Prog. Biophys. Mol. Biol.* **1973**, *27*, 1-76.
115. Moss, G. P., Basic terminology of stereochemistry (IUPAC Recommendations 1996). *Pure Appl. Chem.* **1996**, *68*, 2193-2222.
116. Cronin, T. W., A Different View: Sensory Drive in the Polarized-light Realm. *Current Zoology* **2018**, *64*, 513-523.
117. Chen, Y.; Du, W.; Zhang, Q.; Ávalos-Ovando, O.; Wu, J.; Xu, Q.-H.; Liu, N.; Okamoto, H.; Govorov, A. O.; Xiong, Q.; Qiu, C.-W., Multidimensional Nanoscopic Chiroptics. *Nature Reviews Physics* **2022**, *4*, 113-124.
118. Berova, N.; Bari, L. D.; Pescitelli, G., Application of Electronic Circular Dichroism in Configurational and Conformational Analysis of Organic Compounds. *Chem. Soc. Rev.* **2007**, *36*, 914-931.
119. Kwon, J.; Park, K. H.; Choi, W. J.; Kotov, N. A.; Yeom, J., Chiral Spectroscopy of Nanostructures. *Acc. Chem. Res.* **2023**, *56*, 1359-1372.
120. Braslavsky, S. E., Glossary of terms used in photochemistry, 3rd edition (IUPAC Recommendations 2006). **2007**, *79*, 293-465.

121. Prodan, E.; Radloff, C.; Halas, N. J.; Nordlander, P., A Hybridization Model for the Plasmon Response of Complex Nanostructures. *Science* **2003**, *302*, 419-422.
122. Fan, Z.; Govorov, A. O., Plasmonic Circular Dichroism of Chiral Metal Nanoparticle Assemblies. *Nano Lett.* **2010**, *10*, 2580-2587.
123. Goerlitzer, E. S. A.; Zapata-Herrera, M.; Ponomareva, E.; Feller, D.; Garcia-Etxarri, A.; Karg, M.; Aizpurua, J.; Vogel, N., Molecular-Induced Chirality Transfer to Plasmonic Lattice Modes. *ACS Photonics* **2023**, *10*, 1821-1831.
124. Hentschel, M.; Schäferling, M.; Duan, X.; Giessen, H.; Liu, N., Chiral Plasmonics. *Science Advances* **2017**, *3*, e1602735.
125. Vila-Liarte, D.; Kotov, N. A.; Liz-Marzán, L. M., Template-Assisted Self-Assembly of Achiral Plasmonic Nanoparticles into Chiral Structures. *Chemical Science* **2022**, *13*, 595-610.
126. Kumar, J.; Eraña, H.; López-Martínez, E.; Claes, N.; Martín, V. F.; Solís, D. M.; Bals, S.; Cortajarena, A. L.; Castilla, J.; Liz-Marzán, L. M., Detection of Amyloid Fibrils in Parkinson's Disease using Plasmonic Chirality. *Proceedings of the National Academy of Sciences* **2018**, *115*, 3225-3230.
127. Frank, B.; Yin, X.; Schäferling, M.; Zhao, J.; Hein, S. M.; Braun, P. V.; Giessen, H., Large-Area 3D Chiral Plasmonic Structures. *ACS Nano* **2013**, *7*, 6321-6329.
128. Movsesyan, A.; Muravitskaya, A.; Castilla, M.; Kostcheev, S.; Proust, J.; Plain, J.; Baudrion, A.-L.; Vincent, R.; Adam, P.-M., Hybridization and Dehybridization of Plasmonic Modes. *The Journal of Physical Chemistry C* **2021**, *125*, 724-731.
129. Tadgell, B.; Liz-Marzán, L. M., Probing Interactions Between Chiral Plasmonic Nanoparticles and Biomolecules. *Chemistry – A European Journal* **2023**, *n/a*, e202301691.
130. Zhou, S.; Li, J.; Lu, J.; Liu, H.; Kim, J.-Y.; Kim, A.; Yao, L.; Liu, C.; Qian, C.; Hood, Z. D.; Lin, X.; Chen, W.; Gage, T. E.; Arslan, I.; Travesset, A.; Sun, K.; Kotov, N. A.; Chen, Q., Chiral Assemblies of Pinwheel Superlattices on Substrates. *Nature* **2022**, *612*, 259-265.
131. Peng, Z.; Yuan, L.; XuHong, J.; Tian, H.; Zhang, Y.; Deng, J.; Qi, X., Chiral Nanomaterials for Tumor Therapy: Autophagy, Apoptosis, and Photothermal Ablation. *Journal of Nanobiotechnology* **2021**, *19*.
132. Thiel, M.; Rill, M. S.; von Freymann, G.; Wegener, M., Three-dimensional Bi-chiral Photonic Crystals. *Adv. Mater.* **2009**, *21*, 4680-4682.

133. Urban, M. J.; Shen, C.; Kong, X.-T.; Zhu, C.; Govorov, A. O.; Wang, Q.; Hentschel, M.; Liu, N., Chiral Plasmonic Nanostructures Enabled by Bottom-Up Approaches. *Annu. Rev. Phys. Chem.* **2019**, *70*, 275-299.
134. Zheng, J.; Boukouvala, C.; Lewis, G. R.; Ma, Y.; Chen, Y.; Ringe, E.; Shao, L.; Huang, Z.; Wang, J., Halide-Assisted Differential Growth of Chiral Nanoparticles with Threefold Rotational Symmetry. *Nature Communications* **2023**, *14*, 3783.
135. Van Tendeloo, G.; Bals, S.; Van Aert, S.; Verbeeck, J.; Van Dyck, D., Advanced Electron Microscopy for Advanced Materials. *Adv. Mater.* **2012**, *24*, 5655-5675.
136. Sohlberg, K.; Pennycook, T. J.; Zhou, W.; Pennycook, S. J., Insights into the Physical Chemistry of Materials from Advances in HAADF-STEM. *Physical Chemistry Chemical Physics* **2015**, *17*, 3982-4006.
137. Zhang, Y.; Bals, S.; Van Tendeloo, G., Understanding CeO₂-Based Nanostructures through Advanced Electron Microscopy in 2D and 3D. *Particle & Particle Systems Characterization* **2019**, *36*, 1800287.
138. Hovden, R.; Muller, D. A., Electron Tomography for Functional Nanomaterials. *MRS Bull.* **2020**, *45*, 298-304.
139. Albrecht, W.; Bals, S., Fast Electron Tomography for Nanomaterials. *The Journal of Physical Chemistry C* **2020**, *124*, 27276-27286.
140. Buda, A. B.; Mislow, K., A Hausdorff Chirality Measure. *JACS* **1992**, *114*, 6006-6012.
141. Yewande, E. O.; Neal, M. P.; Low, R., The Hausdorff Chirality Measure and a Proposed Hausdorff Structure Measure. *Mol. Phys.* **2009**, *107*, 281-291.
142. Birsan, T.; Tiba, D. In *One Hundred Years Since the Introduction of the Set Distance by Dimitrie Pompeiu*, System Modeling and Optimization, Boston, MA, 2006; Ceragioli, F.; Dontchev, A.; Futura, H.; Marti, K.; Pandolfi, L., Eds. Springer US: Boston, MA, 2006; pp 35-39.
143. Heyvaert, W.; Pedraza-Tardajos, A.; Kadu, A.; Claes, N.; González-Rubio, G.; Liz-Marzán, L. M.; Albrecht, W.; Bals, S., Quantification of the Helical Morphology of Chiral Gold Nanorods. *ACS Materials Letters* **2022**, *4*, 642-649.
144. Spaeth, P.; Adhikari, S.; Heyvaert, W.; Zhuo, X.; García, I.; Liz-Marzán, L. M.; Bals, S.; Orrit, M.; Albrecht, W., Photothermal Circular Dichroism Measurements of Single Chiral Gold Nanoparticles Correlated with Electron Tomography. *ACS Photonics* **2022**, *9*, 3995-4004.

145. Van Gordon, K.; Baúlde, S.; Mychinko, M.; Heyvaert, W.; Obelleiro-Liz, M.; Criado, A.; Bals, S.; Liz-Marzán, L. M.; Mosquera, J., Tuning the Growth of Chiral Gold Nanoparticles Through Rational Design of a Chiral Molecular Inducer. *Nano Lett.* **2023**, *23*, 9880-9886.
146. Van Gordon, K.; Ni, B.; Girod, R.; Mychinko, M.; Bevilacqua, F.; Bals, S.; Liz-Marzán, L. M., Single Crystal and Pentatwinned Gold Nanorods Result in Chiral Nanocrystals with Reverse Handedness. *Angew. Chem. Int. Ed.* **2024**, *63*, e202403116.
147. Vlasov, E.; Heyvaert, W.; Ni, B.; Van Gordon, K.; Girod, R.; Verbeeck, J.; Liz-Marzán, L. M.; Bals, S., High-Throughput Morphological Chirality Quantification of Twisted and Wrinkled Gold Nanorods. *ACS Nano* **2024**, *18*, 12010-12019.
148. Solís, D. M.; Taboada, J. M.; Landesa, L.; Rodríguez, J. L.; Obelleiro, F. In *Squeezing Maxwell's Equations into the Nanoscale*, 2015.
149. Solís, D. M.; Taboada, J. M.; Obelleiro, F.; Liz-Marzán, L. M.; García de Abajo, F. J., Toward Ultimate Nanoplasmonics Modeling. *ACS Nano* **2014**, *8*, 7559-7570.
150. Obelleiro-Liz, M.; Martín, V. F.; Solís, D. M.; Taboada, J. M.; Obelleiro, F.; Liz-Marzán, L. M., Influence of Geometrical Parameters on the Optical Activity of Chiral Gold Nanorods. *Advanced Optical Materials* **2023**, *11*, 2203090.
151. Zhuo, X.; Mychinko, M.; Heyvaert, W.; Larios, D.; Obelleiro-Liz, M.; Taboada, J. M.; Bals, S.; Liz-Marzán, L. M., Morphological and Optical Transitions during Micelle-Seeded Chiral Growth on Gold Nanorods. *ACS Nano* **2022**, *16*, 19281-19292.
152. Lee, Y. Y.; Cho, N. H.; Im, S. W.; Lee, H.-E.; Ahn, H.-Y.; Nam, K. T., Chiral 432 Helicoid II Nanoparticle Synthesized with Glutathione and Poly(T)20 Nucleotide. *ChemNanoMat* **2020**, *6*, 362-367.
153. Cho, N. H.; Kim, Y. B.; Lee, Y. Y.; Im, S. W.; Kim, R. M.; Kim, J. W.; Namgung, S. D.; Lee, H.-E.; Kim, H.; Han, J. H.; Chung, H. W.; Lee, Y. H.; Han, J. W.; Nam, K. T., Adenine Oligomer Directed Synthesis of Chiral Gold Nanoparticles. *Nature Communications* **2022**, *13*, 3831.
154. Cho, N. H.; Byun, G. H.; Lim, Y.-C.; Im, S. W.; Kim, H.; Lee, H.-E.; Ahn, H.-Y.; Nam, K. T., Uniform Chiral Gap Synthesis for High Dissymmetry Factor in Single Plasmonic Gold Nanoparticle. *ACS Nano* **2020**, *14*, 3595-3602.
155. Cho, N. H.; Lee, H.-E.; Ahn, H.-Y.; Lee, Y. Y.; Im, S. W.; Kim, H.; Nam, K. T., Cysteine Induced Chiral Morphology in Palladium Nanoparticle. *Particle & Particle Systems Characterization* **2019**, *36*, 1900062.

156. Gao, X.; Zheng, Q.; Li, H.; Zhang, C.; Cai, R.; Ji, Y.; Hu, Z.; Wu, X., Modulation of Plasmonic Chiral Shell Growth on Gold Nanorods via Nonchiral Surfactants. *Nanoscale* **2023**, *15*, 10651-10660.
157. Zhang, S.; Zhou, H.; Kong, N.; Wang, Z.; Fu, H.; Zhang, Y.; Xiao, Y.; Yang, W.; Yan, F., L-cysteine-Modified Chiral Gold Nanoparticles Promote Periodontal Tissue Regeneration. *Bioactive Materials* **2021**, *6*, 3288-3299.
158. Ni, B.; Vivod, D.; Avaro, J.; Qi, H.; Zahn, D.; Wang, X.; Cölfen, H., Reversible Chirality Inversion of an AuAg_x-cysteine Coordination Polymer by pH Change. *Nature Communications* **2024**, *15*, 2042.
159. Cahn, R. S.; Ingold, C. K.; Prelog, V., The Specification of Asymmetric Configuration in Organic Chemistry. *Experientia* **1956**, *12*, 81-94.
160. Lee, H.-E.; Ahn, H.-Y.; Mun, J.; Lee, Y. Y.; Kim, M.; Cho, N. H.; Chang, K.; Kim, W. S.; Rho, J.; Nam, K. T., Amino-Acid and Peptide-Directed Synthesis of Chiral Plasmonic Gold Nanoparticles. *Nature* **2018**, *556*, 360-365.
161. Lee, H.-E.; Kim, R. M.; Ahn, H.-Y.; Lee, Y. Y.; Byun, G. H.; Im, S. W.; Mun, J.; Rho, J.; Nam, K. T., Cysteine-Encoded Chirality Evolution in Plasmonic Rhombic Dodecahedral Gold Nanoparticles. *Nature Communications* **2020**, *11*, 263.
162. Morales-Vidal, J.; López, N.; Ortuño, M. A., Chirality Transfer in Gold Nanoparticles by l-Cysteine Amino Acid: A First-Principles Study. *The Journal of Physical Chemistry C* **2019**, *123*, 13758-13764.
163. Ni, B.; Mychinko, M.; Gómez-Graña, S.; Morales-Vidal, J.; Obelleiro-Liz, M.; Heyvaert, W.; Vila-Liarte, D.; Zhuo, X.; Albrecht, W.; Zheng, G.; González-Rubio, G.; Taboada, J. M.; Obelleiro, F.; López, N.; Pérez-Juste, J.; Pastoriza-Santos, I.; Cölfen, H.; Bals, S.; Liz-Marzán, L. M., Chiral Seeded Growth of Gold Nanorods Into Fourfold Twisted Nanoparticles with Plasmonic Optical Activity. *Adv. Mater.* **2023**, *35*, 2208299.
164. Song, Q.; Liu, B., Uniform Colloidal Synthesis of Highly Branched Chiral Gold Nanoparticles. *Chem. Commun.* **2024**, *60*, 5602-5605.
165. Cho, N. H.; Kim, H.; Kim, J. W.; Lim, Y.-C.; Kim, R. M.; Lee, Y. H.; Nam, K. T., Chiral Inorganic Nanomaterials for Biomedical Applications. *Chem* **2024**, *10*, 1052-1070.
166. Im, S. W.; Ahn, H.-Y.; Kim, R. M.; Cho, N. H.; Kim, H.; Lim, Y.-C.; Lee, H.-E.; Nam, K. T., Chiral Surface and Geometry of Metal Nanocrystals. *Adv. Mater.* **2020**, *32*, 1905758.
167. Zhang, N.-N.; Shen, Z.-L.; Gao, S.-Y.; Peng, F.; Cao, Z.-J.; Wang, Y.; Wang, Z.; Zhang, W.; Yang, Y.; Liu, K.; Sun, T., Synthesis and Plasmonic Chiroptical Properties of Double-Helical Gold Nanorod Enantiomers. *Advanced Optical Materials* **2023**, *11*, 2203119.

168. Liu, H.; Vladár, A. E.; Wang, P.-P.; Ouyang, M., Tuning Geometric Chirality in Metallic and Hybrid Nanostructures by Controlled Nanoscale Crystal Symmetry Breaking. *JACS* **2023**, *145*, 7495-7503.
169. Wan, J.; Sun, L.; Sun, X.; Liu, C.; Yang, G.; Zhang, B.; Tao, Y.; Yang, Y.; Zhang, Q., Cu²⁺-Dominated Chirality Transfer from Chiral Molecules to Concave Chiral Au Nanoparticles. *JACS* **2024**, *146*, 10640-10654.
170. Rodríguez-Zamora, P.; Salazar-Angeles, B.; Buendía, F.; Cordero-Silis, C.; Fabila, J.; Bazán-Díaz, L.; Fernández-Díaz, L. M.; Paz-Borbón, L. O.; Díaz, G.; Garzón, I. L., Revisiting the Conformational Adsorption of *L*- and *D*-cysteine on Au Nanoparticles by Raman Spectroscopy. *Journal of Raman Spectroscopy* **2020**, *51*, 243-255.
171. Golze, S. D.; Porcu, S.; Zhu, C.; Sutter, E.; Ricci, P. C.; Kinzel, E. C.; Hughes, R. A.; Neretina, S., Sequential Symmetry-Breaking Events as a Synthetic Pathway for Chiral Gold Nanostructures with Spiral Geometries. *Nano Lett.* **2021**, *21*, 2919-2925.
172. Chen, J.; Gao, X.; Zheng, Q.; Liu, J.; Meng, D.; Li, H.; Cai, R.; Fan, H.; Ji, Y.; Wu, X., Bottom-Up Synthesis of Helical Plasmonic Nanorods and Their Application in Generating Circularly Polarized Luminescence. *ACS Nano* **2021**, *15*, 15114-15122.
173. González-Rubio, G.; Mosquera, J.; Kumar, V.; Pedraza-Tardajos, A.; Llombart, P.; Solís, D. M.; Lobato, I.; Noya, E. G.; Guerrero-Martínez, A.; Taboada, J. M.; Obelleiro, F.; MacDowell, L. G.; Bals, S.; Liz-Marzán, L. M., Micelle-Directed Chiral Seeded Growth on Anisotropic Gold Nanocrystals. *Science* **2020**, *368*, 1472-1477.
174. Zhuo, X.; Vila-Liarte, D.; Wang, S.; Jimenez de Aberasturi, D.; Liz-Marzán, L. M., Coated Chiral Plasmonic Nanorods with Enhanced Structural Stability. *Chem. Mater.* **2023**, *35*, 5689-5698.
175. Ito, T. H.; Salles, A. G.; Priebe, J. P.; Miranda, P. C. M. L.; Morgon, N. H.; Danino, D.; Mancini, G.; Sabadini, E., Generation of a Chiral Giant Micelle. *Langmuir* **2016**, *32*, 8461-8466.

Chapter II – Tuning the Growth of Chiral Gold Nanoparticles Through Rational Design of a Chiral Molecular Inducer

As mentioned in the previous chapter, the “bottom-up” preparation of inherently chiral colloidal nanomaterials holds great potential for the advancement of biosensing and nano-optics, which has been reproducibly demonstrated using cosurfactants or chiral molecules such as thiolated amino acids. Lending to the adaptable nature of plasmonic nanoparticle synthesis methods and the wide range of chiral inducers, several types of plasmonic nanoparticles have been reported and a wider variety is expected. Further expansion of downstream applications largely depends on our ability to tailor the chiral intricacy of the nanomaterial and to understand its influence on the resulting optical activity and spectral range. Thus, tunable control over particle growth, as well as the prominence of absorption or scattering on the optical response, are highly relevant. However, the underlying growth mechanisms for these nanomaterials remain insufficiently understood. We introduce herein a purpose-devised small molecule, a cysteine modified with a hydrophobic chain, as a versatile chiral inducer. The amphiphilic and chiral features of this molecule provide control over the chiral morphology and the chiroptical signature of the obtained nanoparticles by simply varying the concentration of chiral inducer. These results are supported by circular dichroism measurements and electromagnetic modeling, as well as electron tomography to analyze structural evolution at the facet scale. Our observations suggest expanded roles for the factors involved in chiral synthesis: the chemical nature of the chiral inducers and the influence of cosurfactants.

2.1 Introduction

As discussed in **Chapter I**, the relevant “bottom-up” synthetic techniques of plasmonic nanomaterials thus far developed are sufficiently common to be readily reproduced, but also possess a depth that allows for a high level of flexibility and variability in the syntheses.¹⁻³ A challenging obstacle has been the engineering of chiral morphology at the single-particle level, and applying it to colloidal nanomaterials while maintaining a high degree of monodispersity.⁴⁻⁶ This has typically been achieved via a seeded overgrowth reaction mediated by a chiral inducer, which allows for the chiral arrangement of gold atoms about achiral starting gold nanoparticles (seeds) via the rapid reduction of gold ions. Regardless of the chiral inducer used, the outcome of the overgrowth process is significantly influenced by the experimental conditions employed. Variables such as temperature and the concentration of applicable reagents can be optimized to maximize the dissymmetry factor (*g*-factor) of the products.⁷⁻⁹ The geometry and crystallinity of the achiral seeds also play an important role in determining the final morphology of the chiral products, which is a topic that will be discussed at length in the following chapter.^{8,10-12} The variable of focus for this chapter is the chemical nature of the chiral inducer; depending on this factor, chiral seeded growth on gold nanomaterials can be achieved through several alternative pathways. One reported synthetic pathway results in the formation of plasmonic nanorods with twisted geometry (**Figure 2.1a**).¹³ This method was initially applied to other achiral seed morphologies, using thiolated molecules (such as cysteine or glutathione) or short polypeptides comprised of the same amino acid as the chiral inducers.^{10,11,14,15} Asymmetric growth on the plasmonic seeds has been claimed to be induced by the enantioselective adsorption of chiral inducers on high-index facets with atomic-scale chirality.¹⁶⁻¹⁸ This preferential interaction promotes the kinetic growth of crystallographic facets with a handedness corresponding to the

enantiomer of the chiral inducer used, ultimately resulting in the formation of twisted shapes. The same strategy has been applied to prepare several types of twisted gold nanorods (Au NRs), using achiral Au NRs as seeds.^{13,19} A second generic synthetic protocol is known as micelle-directed chiral growth, in which large helical micelles formed in solution wrap around achiral Au NR seeds; such helical micelles act as templates during seeded growth, resulting in a dense array of quasi-helical wrinkles around a central nanorod (**Figure 2.1b**).^{20,21} Despite the wide variety of chiral co-surfactants that could potentially act under this mechanism, only one example has been reported so far, using 1,1'-bi(2-naphthylamine) (BINAMINE) as the chiral inducer, alongside a primary surfactant (cetyltrimethylammonium chloride, CTAC), to induce chiral seeded growth. BINAMINE is a molecule with axial chirality, containing an aromatic hydrophobic region that can be inserted into CTAC micelles, and two amino groups that assist binding onto the Au surface.^{22,23} On this basis, it has been postulated that BINAMINE plays a dual role, inducing both the formation of chiral worm-like micelles and a stronger interaction between the elongated micelle and the seed surface through amine groups. This interaction between the elongated micelles and the seed is required for the formation of a micellar template that can promote the growth of steep wrinkles and the stabilization of such morphological features.

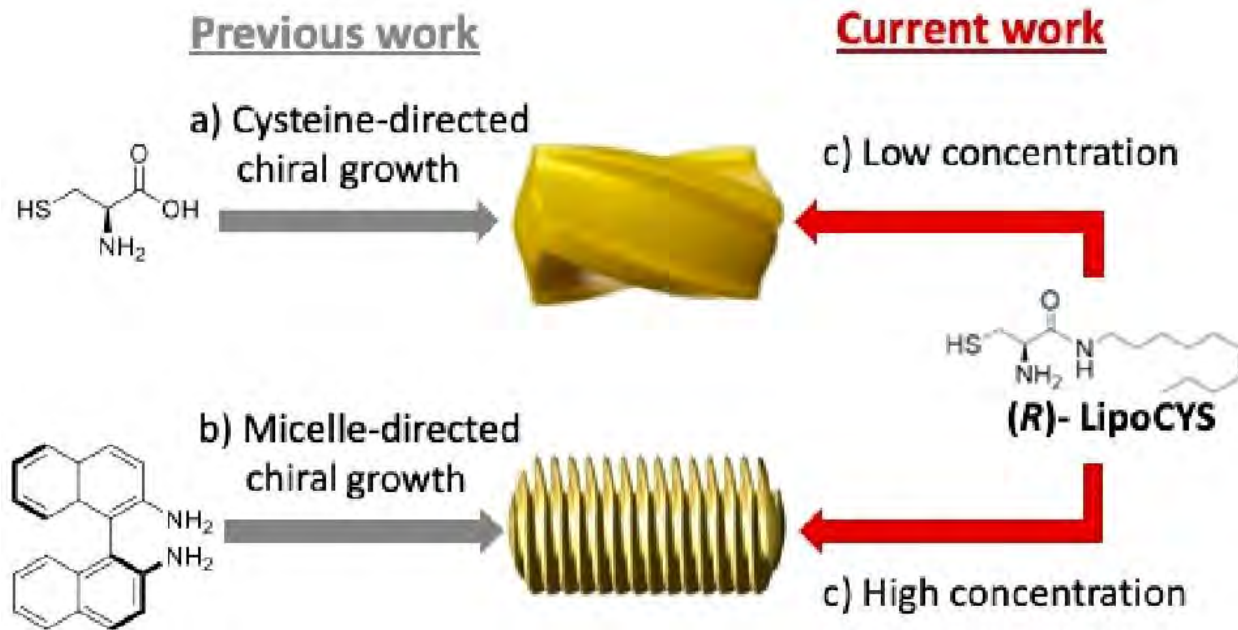


Figure 2.1. Schematic view of the mechanisms for seeded growth of chiral nanorods. (a) Cysteine as a chirality inducer, resulting in twisted nanorods. (b) Chiral growth directed by micelles containing BINAMINE as cosurfactant, resulting in a wrinkled particle structure. The use of LipoCYS (c) is proposed to bridge both growth mechanisms.

In this chapter, we describe the use of a purposely synthesized molecule possessing elements from chiral inducers used in the aforementioned chiral mechanisms (i.e. a thiolated functional group and a hydrophobic aliphatic tail), in seeded chiral overgrowth reactions (**Figure 2.1c**). Because achiral seeds of a high aspect ratio were found in previous work to be more efficient in terms of chiral growth and optical activity,^{20,21,24} the investigation of the growth mechanism mediated by this new chiral molecule was carried out using single-crystal gold NRs as seeds, and later expanded to octahedral and cubic seeds, to investigate whether similar structural and chiroptical trends would be observed. The development and testing of new chiral molecules to induce directional growth on gold nanomaterials is a subject that has great potential for the fine-tuning of the resulting particle morphologies and eventually the creation of novel ones, as well as the better understanding of the aforementioned chiral growth mechanisms.

2.2 Bridging Established Chiral Mechanisms with LipoCYS

Emboldened by the success of chiral synthesis using amino acids, and inspired by the putative micellar template growth mechanism, we explored the role of a purposely devised chiral molecule consisting of a modified cysteine: 2-amino-N-decyl-3-mercaptopropanamide (synthesized by Sandra Baúlde and Jesús Mosquera at Universidade da Coruña (CICA), see **Chapter VI** for details), which we term LipoCYS, as the chiral inducer for the seeded growth of gold nanorods.²⁵ The presence of a cysteine-like head group and a longer hydrophobic tail was foreseen to provide a dual function, allowing high affinity for both the gold surface and the micellar system. Chiral products were prepared using a method developed by González-Rubio *et. al.*²⁰: achiral seeds are dispersed in a solution containing surfactant, gold salts, and the chiral inducer, and the overgrowth reaction is triggered by the rapid addition of excess ascorbic acid, immediately followed by vigorous shaking to rapidly combine the mixture (see **Chapter VI** for more details). The choice of gold nanorods as achiral seeds provides a larger surface area per particle for adsorption of the cysteine moiety on LipoCYS, while capitalizing on the potential for micelle formation, maximizing their elongation and promoting the growth of distinct chiral features. To evaluate the performance of LipoCYS as a chiral inducer, we implemented experimentally the overgrowth about pre-manufactured gold nanorods using CTAC as the surfactant, and ascorbic acid (AA) as the reducing agent. As a means to monitor the quality of the produced chiral NRs, circular dichroism (CD) spectroscopy was used to quantify the chiroptical response, i.e. the unequal extinction of left- and right-handed circularly polarized light.²⁶ Additionally, to characterize surface wrinkles and other geometrical features, high-angle annular dark-field scanning transmission electron microscopy (HAADF-STEM) was applied. Subsequently, acquisition of tomographic reconstructions by collaborators at the University of Antwerp (NANOLab Center of

Excellence; EMAT) permitted analysis of the morphology and structural features in 3D, which can hardly be discerned in conventional 2D HAADF-STEM images. Through the modification of experimental parameters, we aimed at maximizing the *g*-factor of chiral products (see **Chapter I** for definition), while monitoring the resulting structural evolution. To begin our investigation, the concentration of LipoCYS was kept constant while the concentration of other chemical factors was changed, one variable at a time in iterative syntheses. In this way, the impact of each variable on the chiroptical and structural properties of chiral products could be observed (see **Figure 2.2**). Increasing the concentration of ascorbic acid ([AA]) used in the synthesis led to significant enhancements in the peak *g*-factor of the products, which shifted little in wavelength; this corresponded to discreet changes in the surface wrinkles of the products, becoming incrementally more distinct. Changing the concentration of CTAC led to an even more noticeable shift: at very low CTAC concentration, an inversion of the chiroptical response was observed—the usually negative *g*-factor became positive. This could be attributed to the slightly bowed structure of these particles, perhaps possessing a microscale chirality that overwhelms the nanoscale chirality present in the wrinkles. Another example of surfactant-directed chiroptical inversion will be discussed in **Chapter V**, in the context of multi-scale chirality. Finally, changing the concentration of AuNR seeds (Au^0) involved in the chiral reaction resulted in a red-shift of the chiroptical signature, proportional to the ratio of gold salts to gold seeds ($[\text{Au}^{3+}] : [\text{Au}^0]$).

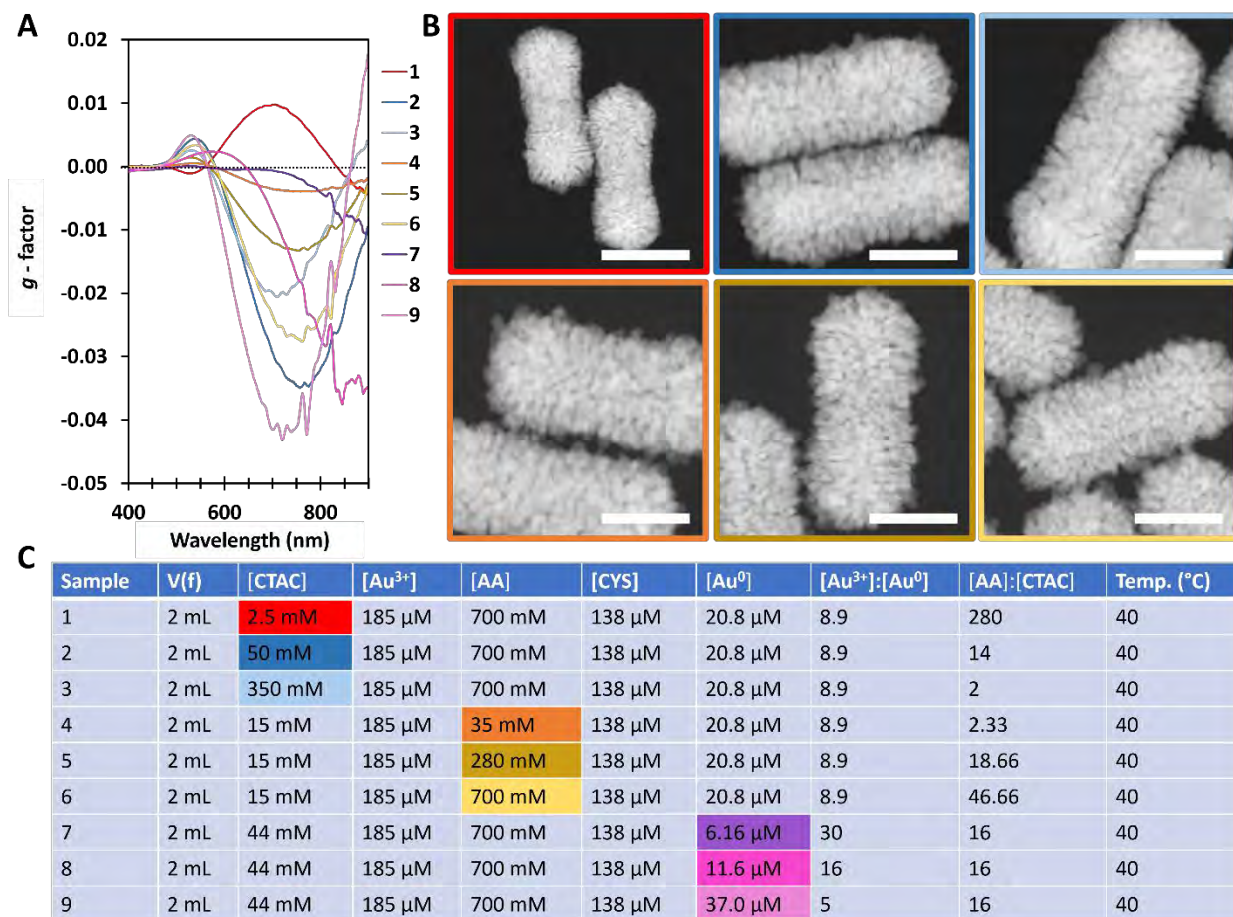


Figure 2.2. Circular dichroism (A) and HAADF-STEM (B) characterization of chiral gold nanomaterials prepared with novel chiral inducer (*R*)-LipoCYS. Image outlines are color-coded to match the legend of the plots. Scale bars = 100 nm. Highlighted columns in table (C) show sample sets where one chemical variable was modified, while all others were kept constant.

Taken as a whole, these results inform an optimal set of parameters for chiral syntheses with LipoCYS, yielding products with strong chiroptical signals and products with well-defined structural features. Carrying these optimized parameters forward in syntheses where [LipoCYS] is the variable will help us to further clarify the chiroptical and structural changes for the products of these reactions. With these observations in mind, we performed LipoCYS-mediated chiral growth reactions with a [Au³⁺]:[Au⁰] typical to the literature,^{13,20} a high excess of ascorbic acid (700 mM), and a moderate amount of surfactant (44 mM CTAC) to keep the colloid stable during the

reaction (see **Chapter VI** for more synthetic details). The rapid progression of these reactions (owing to the high concentration of ascorbic acid and elevated reaction temperature) is indicated by the appearance of a purple-pink color in the first few minutes after the addition of ascorbic acid to initiate the reaction. With the intent of yielding an evolving series of chiral products with a maximized chiroptical signature, we screened a wide range of LipoCYS concentrations under the aforementioned synthetic conditions. A gradual increase of the LipoCYS concentration (keeping all other variables constant) resulted in a spectral redshift of the chiroptical signature, and a corresponding change in particle morphology (**Figure 2.3**).

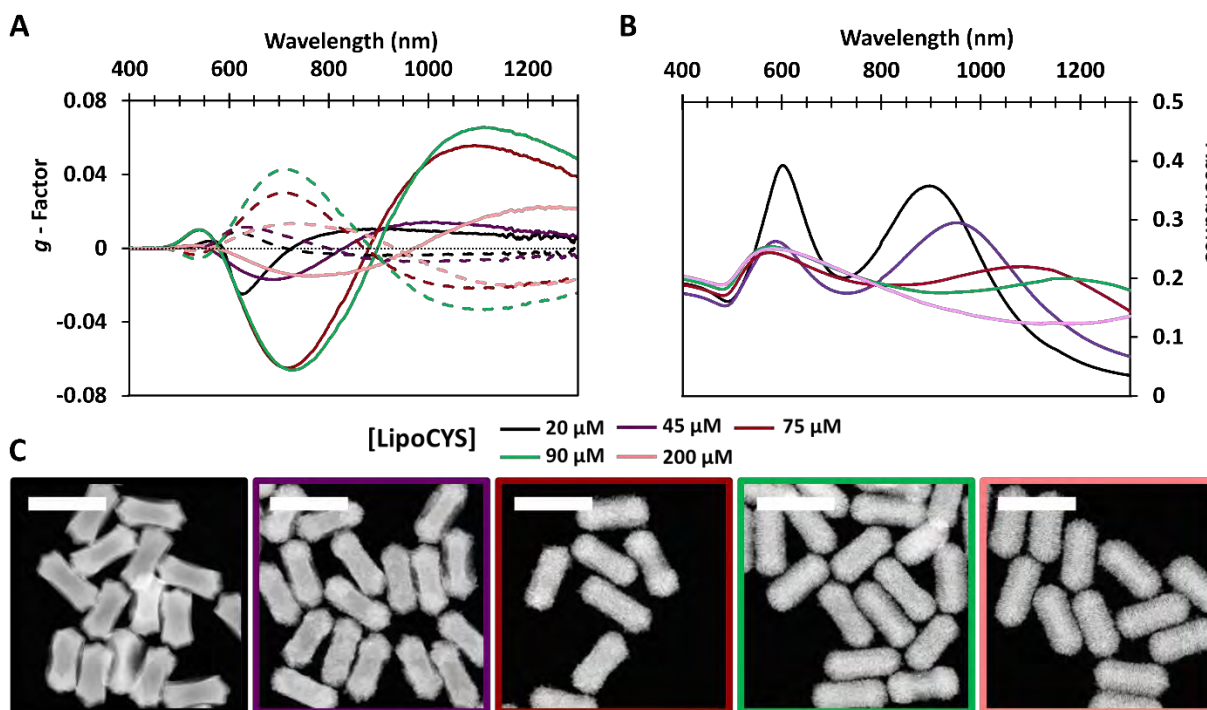


Figure 2.3. Circular dichroism (g -factor) spectra (A) and absorbance spectra (B) for chiral Au NR colloids prepared using different [LipoCYS], as labeled. Solid and dashed lines correspond to results from particles synthesized with the R and S enantiomers of LipoCYS, respectively. HAADF-STEM images of chiral particles synthesized with (R)-LipoCYS (C); image outlines are color-coded to match the legend of the plots. Scale bars: 200 nm.

Regarding the g -factors, the maximum value for NPs obtained at 20 μM of LipoCYS is observed at around 620 nm, with magnitudes of -0.025 for (*R*)-LipoCYS and 0.009 for (*S*)-LipoCYS. Larger g -factors were consistently achieved with the (*R*) enantiomer, which may be related to inherent challenges associated with thiolated molecules and their potential oxidation by atmospheric oxygen. The obtained chiroptical signature of greatest intensity was observed for wrinkled particles synthesized with 90 μM LipoCYS (equivalent to a ratio of 1:486 LipoCYS to CTAC molecules), with maximum g -factors (at 720 nm) of 0.066 for (*R*)-LipoCYS and 0.043 for (*S*)-LipoCYS. Three-dimensional reconstructions of the chiral products (obtained via electron tomography data acquired by Mikhail Mychinko and Wouter Heyvaert, EMAT) highlight the evolution from relatively smooth surfaces at a low LipoCYS concentration to densely wrinkled shapes at a high LipoCYS concentration (**Figure 2.4** and **Figure 2.5**). To elucidate the underlying mechanism governing chiral growth at high LipoCYS concentrations, it is crucial to emphasize that LipoCYS was synthesized with a specific design, aimed at facilitating interaction with both the CTAC micelles – through the incorporation of the aliphatic chain – and the gold surface – via the thiol group. On this basis, we hypothesize that a critical threshold exists, at which the local concentration of LipoCYS on the Au surface becomes sufficient to trigger the formation of worm-like micelles over the NP surface. In this scenario, the aliphatic tails of LipoCYS act as anchoring points for the micelles, directing crystal growth into wrinkles. Evaluated by HAADF-STEM (also performed at EMAT), the average length of wrinkles on particles synthesized with 90 μM was around 22 nm, with a distance between them of ~ 2 nm and a thickness of ~ 4 nm. Importantly, HAADF-STEM analysis of the intermediate samples, i.e. those synthesized with 45 and 75 μM LipoCYS, showed a lower density of wrinkles, because their thickness increases until ~ 7 nm (**Figure 2.5**). This result can also be elucidated through the earlier hypothesis, given that

hydrophobic forces drive LipoCYS toward clustering, thereby initiating the formation of elongated micelles. A lower amount of LipoCYS would thus yield a reduced number of wormlike micelles, leading to a correspondingly lower count of grooves and resulting in the formation of larger wrinkles.

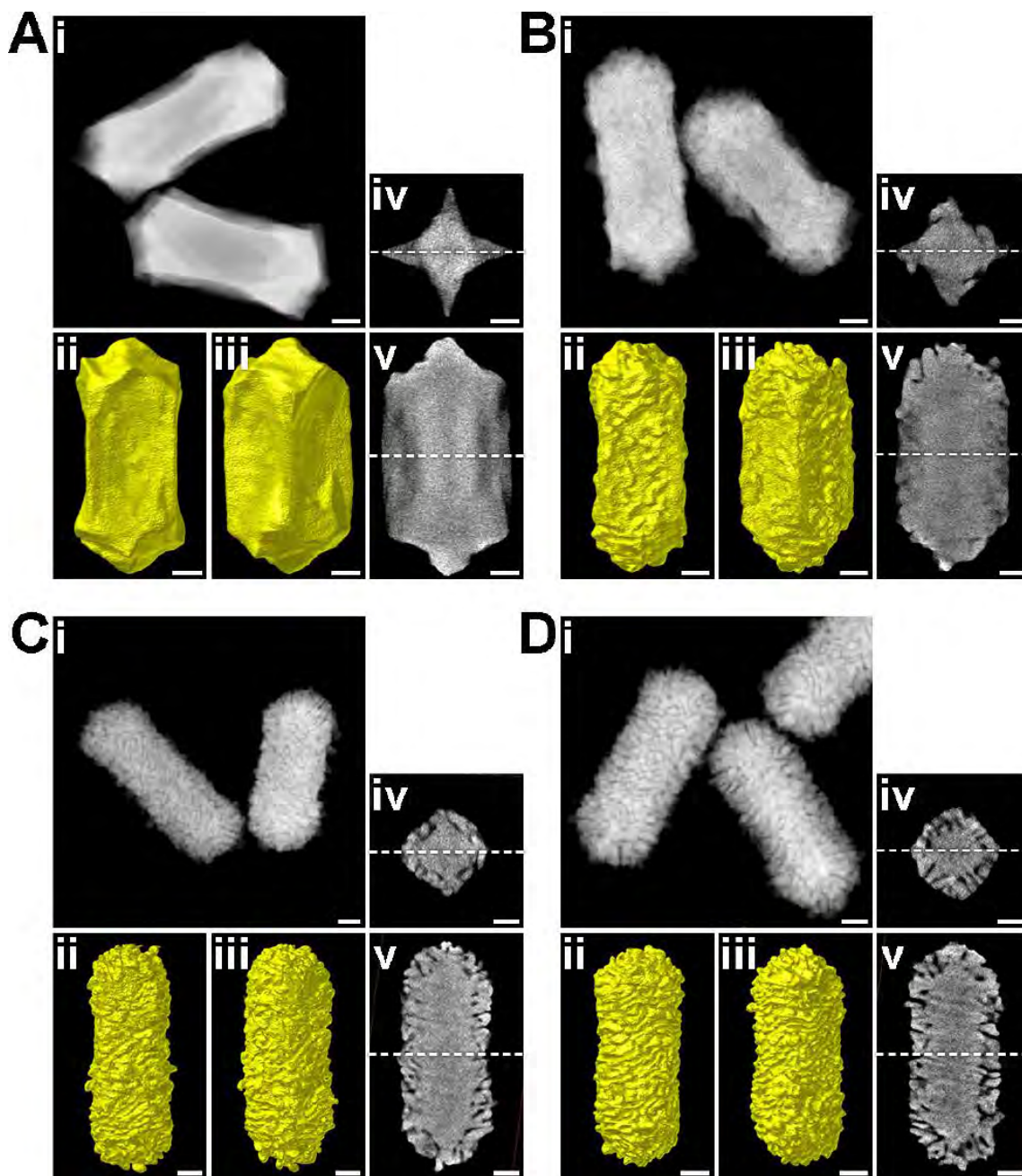


Figure 2.4. Morphological characterization of Au NPs obtained by increasing the concentration of (*R*)-LipoCYS (A, 20 μ M; B, 45 μ M; C, 75 μ M; D, 90 μ M) during chiral overgrowth. The morphological characterization for each sample includes (i) HAADF-STEM image of several representative nanoparticles, (ii, iii) Visualizations of the 3D reconstructions, presented along different viewing angles (oriented 45° relative to each other), and (iv, v) selected orthoslices extracted from the 3D reconstructions, perpendicular to the longitudinal and transverse axes, at the center of the NRs. White dashed lines represent the relative positions of slices shown in (iv) and (v). All scale bars are 25 nm.

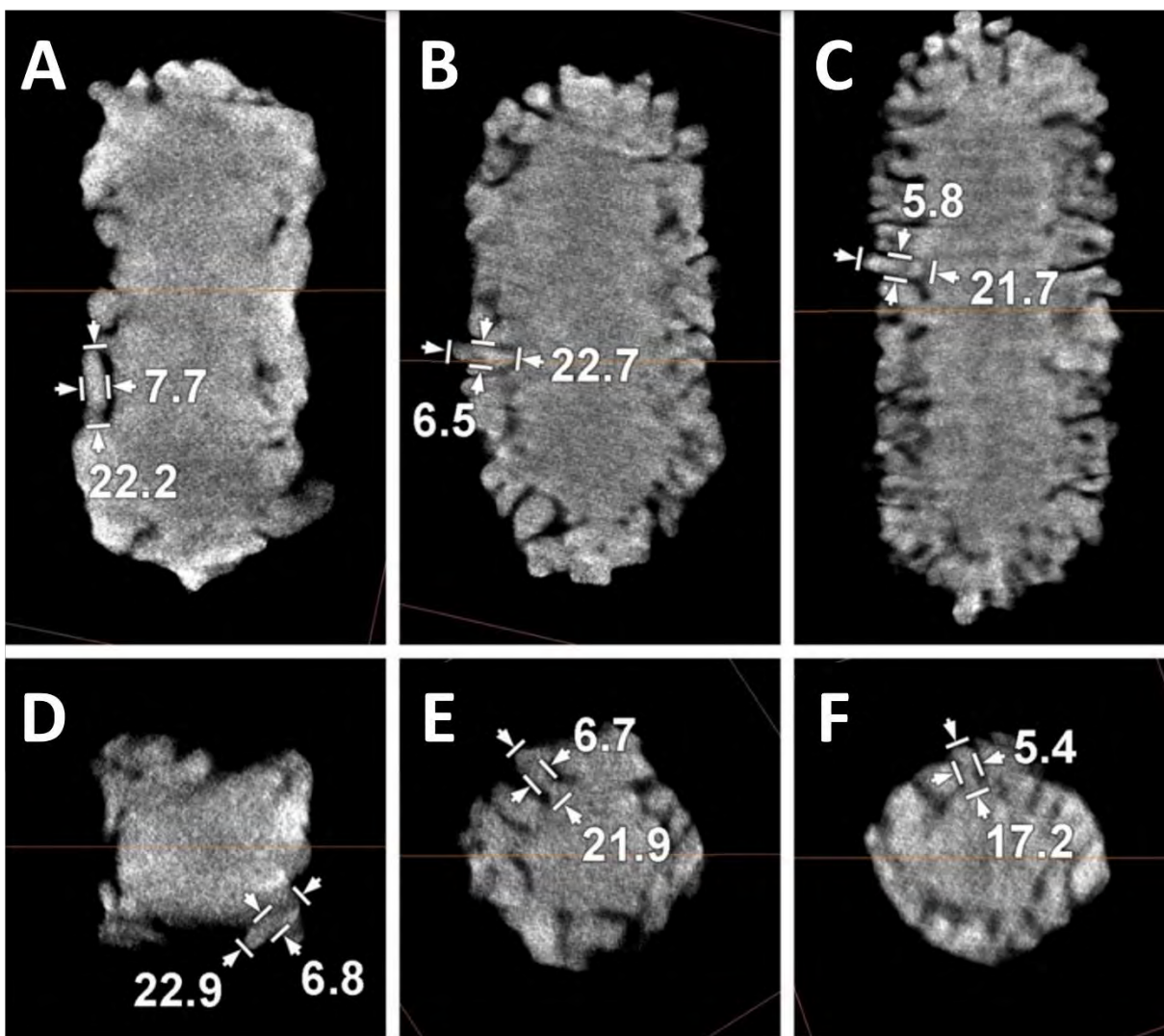


Figure 2.5. Selected orthoslices extracted from the 3D reconstructions, perpendicular to the longitudinal and transverse axes, at the center of chiral Au NRs prepared with different concentrations of (*R*)-LipoCYS (A,D: 45 μ M, B,E: 75 μ M, C,F: 90 μ M). All values are given in nm.

In summary, we show that LipoCYS is a versatile inducer that can produce both twisted and wrinkled chiral plasmonic nanoparticles, solely depending on its concentration. At relatively low concentrations, LipoCYS behaves similarly to cysteine and generates twisted gold nanorods. In contrast, high concentrations of LipoCYS lead to the formation of NPs with well-defined helical wrinkles, typically obtained through micelle-directed growth. The observed morphological

changes are also reflected in distinct optical features with varying intensity and spectral position. In the following sections, an equally discerning eye will be given to structural-optical relationships of the chiral products, and morphological changes induced by LipoCYS on a facet-specific level.

2.3 Modelling and Electromagnetic Simulations

For additional evidence behind the correlation between the obtained morphologies and the plasmonic optical activity, our collaborators at EM3Works (Manuel Obelleiro-Liz) carried out electromagnetic simulations based on the surface-integral equations (SIEs) discretized by the method of moments (MoM) (see **Chapter I** and **Chapter VI** for details).²⁷ We used 3D models, based on the electron tomography reconstructions in **Figure 2.4**, that resembled chiral NRs obtained with three different LipoCYS concentrations. The simulated CD spectra (**Figure 2.6**) were found to agree with the experimental trend, in terms of both wavelength and relative intensity of the plasmonic CD bands. The broadened and redshifted *g*-factor bands observed for increasing LipoCYS concentrations are related to the formation of well-defined wrinkles, in agreement with detailed computational analysis reported elsewhere.²⁸ A deviation in the agreement is seen for the intensity of the near-IR band in the simulated spectrum of the 90 μM LipoCYS model, which is less intense and more broadened in the experimental spectrum. This is likely due to the idealized nature of our particle models, in contrast with the complex wrinkled geometry in the particles. The effect of disorder in the wrinkled structure (for the highest LipoCYS concentrations) was also accounted for by simulating 3D models with randomized surface texture, indeed revealing loss of CD signal when the surface features are disordered (**Figure 2.7**).

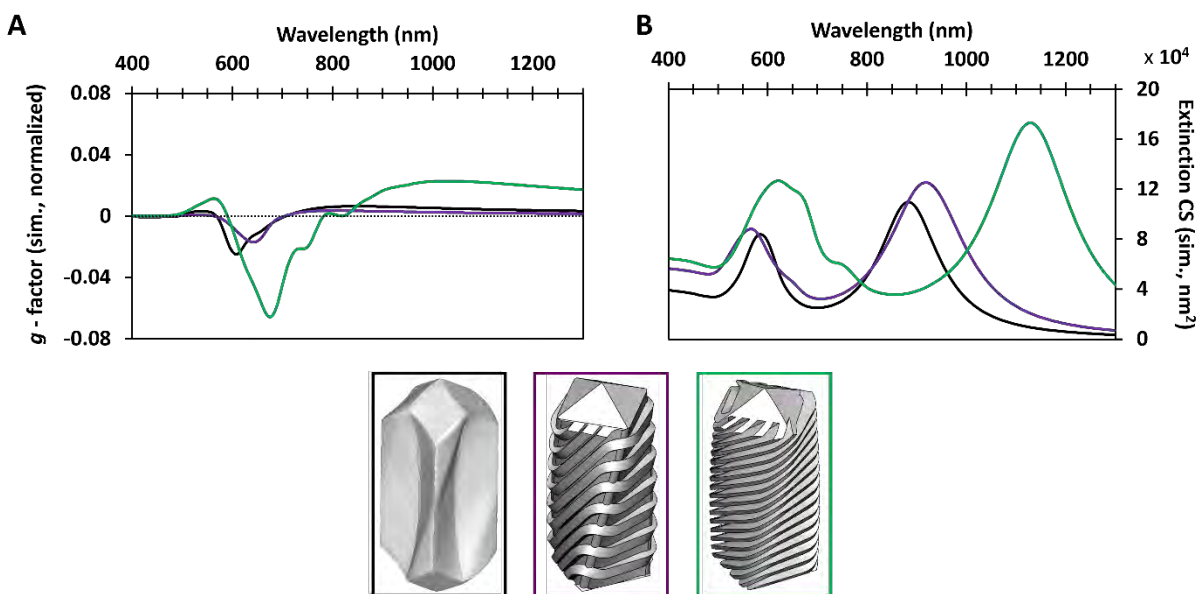


Figure 2.6. Simulated circular dichroism (A) and extinction (B) spectra for three 3D models made to resemble the observed morphology of selected experimental samples from **Figure 2.4** (black: 20 μM , purple: 45 μM , green: 90 μM). Simulations were based on SIE-MoM (see text and **Chapter VI** for details).

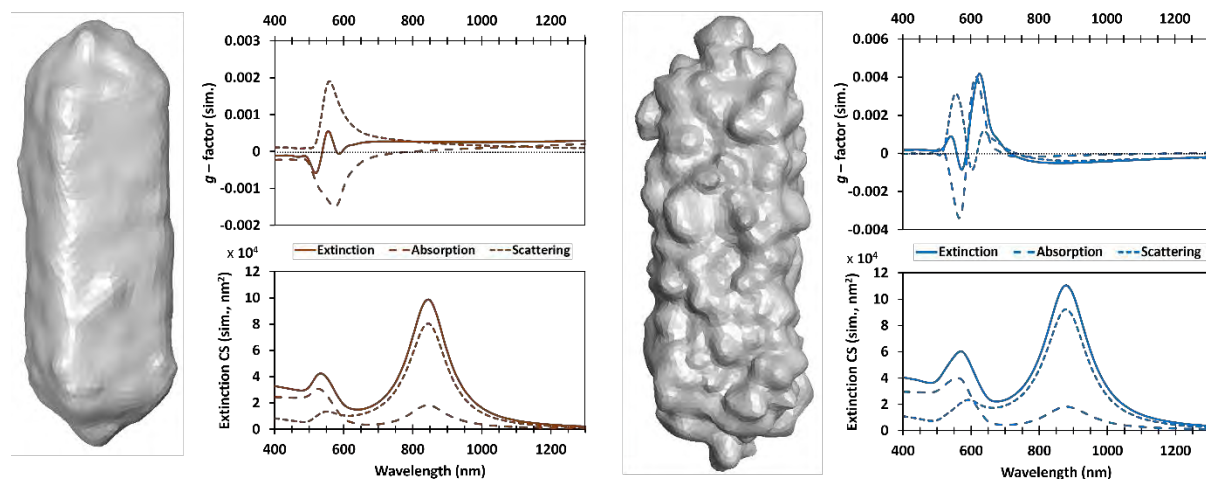


Figure 2.7. Electromagnetic simulations for 3D models of Au NRs with disordered surface features, resulting in strongly decreased g -factor. CD and extinction cross-section spectra are shown for randomly oriented distributions of nanorods, under illumination with left- and right-handed circularly polarized light (extinction cross-section spectra are shown as an average for left- and right- circular polarizations).

Further considerations should be made when contrasting simulated and experimental data: ultimately what is represented in simulations is a simplified perspective of the geometry of a single particle, in comparison with the variety of morphological details present in a colloid dispersion. Both examples from this work speak to the compromise and limitations innate to computerized modeling and light simulations: specifically, that a given simulation will only be as good as the model being simulated, and a nanoparticle model will never be a perfect representation of the myriad colloidal particles synthesized in a chiral reaction. The observation that the optical spectra obtained from real samples are remarkably similar to those derived from simulated models despite their inherent limitations is a testament to the validity of the results presented here. Advancements in modelling that directly incorporate the output from electron tomography characterization are helpful towards moving what is simulated ever closer to reality. The potential for computerized techniques is clear: the facet-directed investigation of structural-optical relationships of chiral nanoparticles often requires a brute-force approach that is much more time efficient with simulations than with syntheses.^{29,30}

2.4 High-Resolution Facet Analysis of Chiral Nanorods

To further investigate the chiral growth mechanism for low LipoCYS concentration, high resolution HAADF-STEM images were acquired by our collaborators at EMAT, which indicate that the tips are enclosed by {110} facets (**Figure 2.8**).

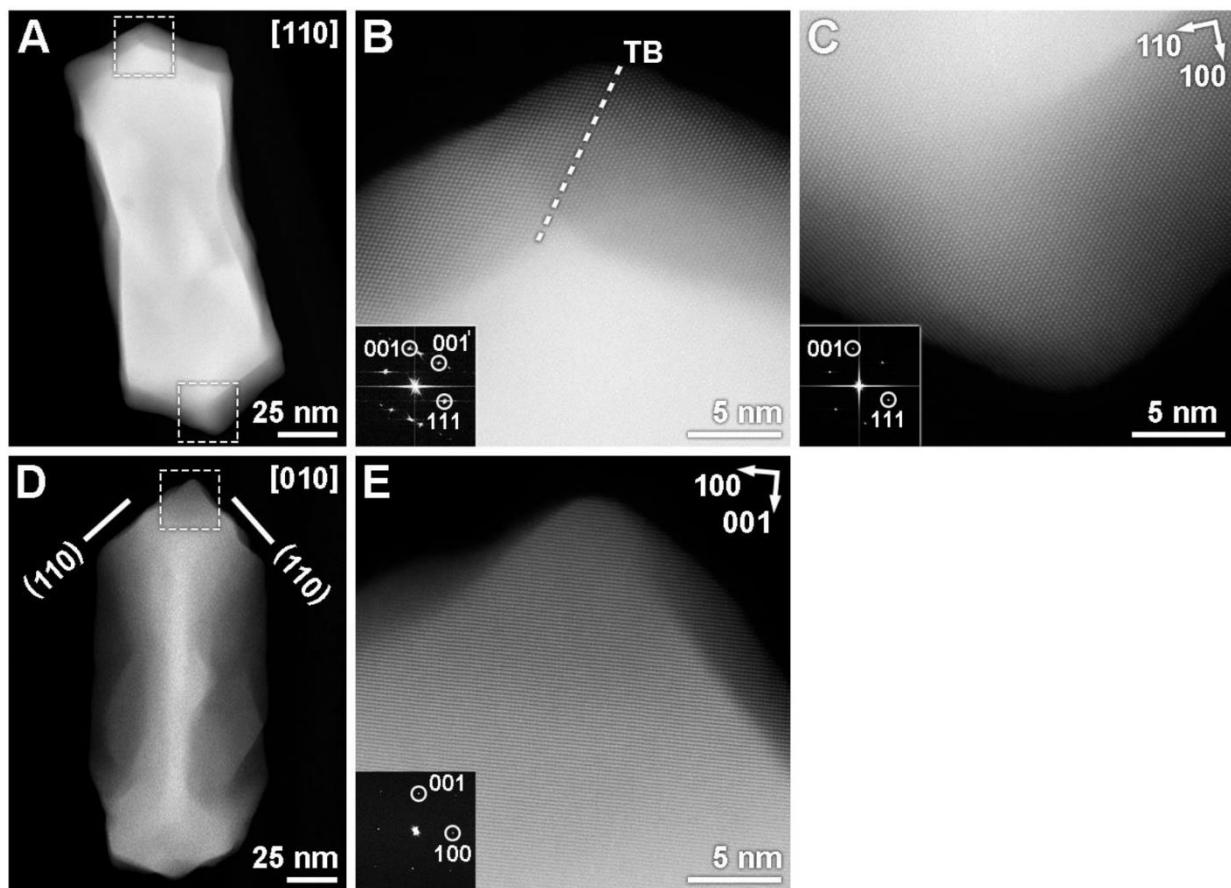


Figure 2.8. (A,D) HAADF-STEM images and (B,C,E) high resolution HAADF-STEM images of a chiral AuNR prepared with (*R*)-LipoCYS (similar to that in Figure 3A), taken along $\langle 110 \rangle$ and $\langle 100 \rangle$ zone axes. The insets in (B), (C) and (E) show fast Fourier transform (FFT) patterns along $[110]$ and $[100]$ directions for the fcc lattice of Au, which indicate that the tips are enclosed by $\{110\}$ facets.

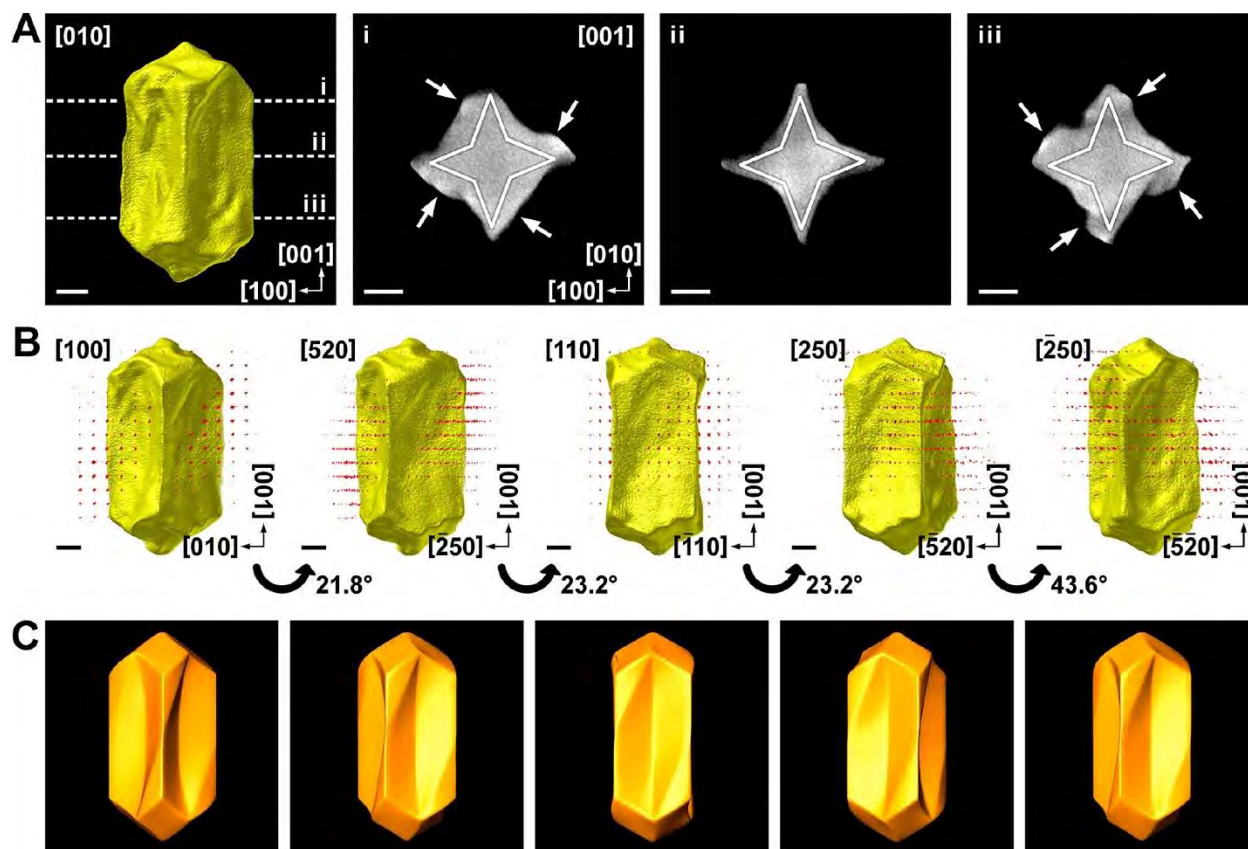


Figure 2.9. (A) 3D reconstruction and selected orthoslices of a twisted Au NR, obtained using 20 μM (*R*)-LipoCYS during chiral overgrowth. Solid white lines indicate the expected crystallographic orientations of [520] facets. White arrows indicate positions where chiral overgrowth occurs. (B) Combined HAADF-STEM tomography (real space) and electron diffraction tomography (reciprocal space) reconstructions of the same particle oriented along [100], [520], [110], [250], and $[-250]$, with rotation angles as indicated. (C) Idealized chiral model of the same nanoparticle, oriented along the same directions as the corresponding panels in (B). All scale bars correspond to 25 nm.

For nanoparticles as complex as those investigated here, 2D HAADF-STEM images do not enable a straightforward identification of the crystallographic nature of the overall surface structure, particularly the concave surfaces. Therefore, simultaneous HAADF-STEM and electron diffraction (ED) tomography was performed (at EMAT) on a selected NP obtained using 20 μM (*R*)-LipoCYS (**Figure 2.9**). Orthoslices orthogonal to the [001] direction (**Figure 2.9A**) of the HAADF-STEM reconstruction indicate that the particle has a square-like cross-section, albeit with

concave faces. Combination of tomography reconstructions in real and reciprocal space enables a detailed analysis of the various facets in the NP, by orienting it along a given zone axis and inspecting the corresponding part of the NP surface perpendicular to that direction (**Figure 2.9B**). Through the former analysis, we conclude that the observed concave faces mainly consist of two facets belonging to the $\{520\}$ family. Further inspection of the orthoslices near the NP tips (**Figure 2.9Ai,iii**) indicates selective overgrowth at the corners of the two-sided faces (indicated by white arrows), resulting in a seemingly twisted structure. In the case of (*R*)-LipoCYS, this selective overgrowth occurs on the top left and bottom right corners of each concave face, as also illustrated in the idealized model (**Figure 2.9C**). The concavity of the NR morphology in these regions can be expected to lead to local $\{521\}$ facets at the top left and bottom right corners of the lateral facets and $\{52-1\}$ facets at the top right and bottom left corners. Since these are chiral facets, the mechanism resulting in the final morphology would, therefore, be similar to that described in refs. 5 and 21. Finally, an inspection of the $\langle 111 \rangle$ and $\langle 011 \rangle$ corners indicates that they are twisted in a similar manner as the helicoids reported by Lee *et al.*, likely intertwined with the presence of chiral facets.¹¹ The resulting morphology is thus similar to the four-fold twisted gold nanorods described in previous work by Ni, *et. al.*¹³ Whereas cysteine was used there at a concentration of 75 nM, micromolar concentration (20 μM) is required for LipoCYS to induce chirality. We ascribe this difference to the absence of a carboxylate group in LipoCYS, reducing the affinity for the gold surface. This is in agreement with Chen, *et. al.*, where *g*-factor was significantly reduced when cysteine was replaced by an analogue containing a methylated carboxylate group.³¹ Based on the former morphological studies, it is obvious that at low concentration, LipoCYS follows an equivalent mechanism as that described for standard cysteine, inducing chiral growth upon symmetry breaking of chiral high-Miller-index facets. Additional wrinkling on particles at higher

LipoCYS concentration resulted in weaker chiroptical activity, which might be related to a lower degree of order in surface topography at higher concentrations, or a complex directional geometry developing at the particle tips. This hypothesis is supported by the results of a quantitative helicity analysis performed at EMAT (see **Chapters I and VI** for details) and based on HAADF-STEM tomography (**Figure 2.10**), which confirms the direct correlation between the handedness of the studied NPs and the type of enantiomer used during the synthesis. For the NRs prepared with the highest LipoCYS concentration (**Figure 2.10D**), a less defined helicity plot was obtained.

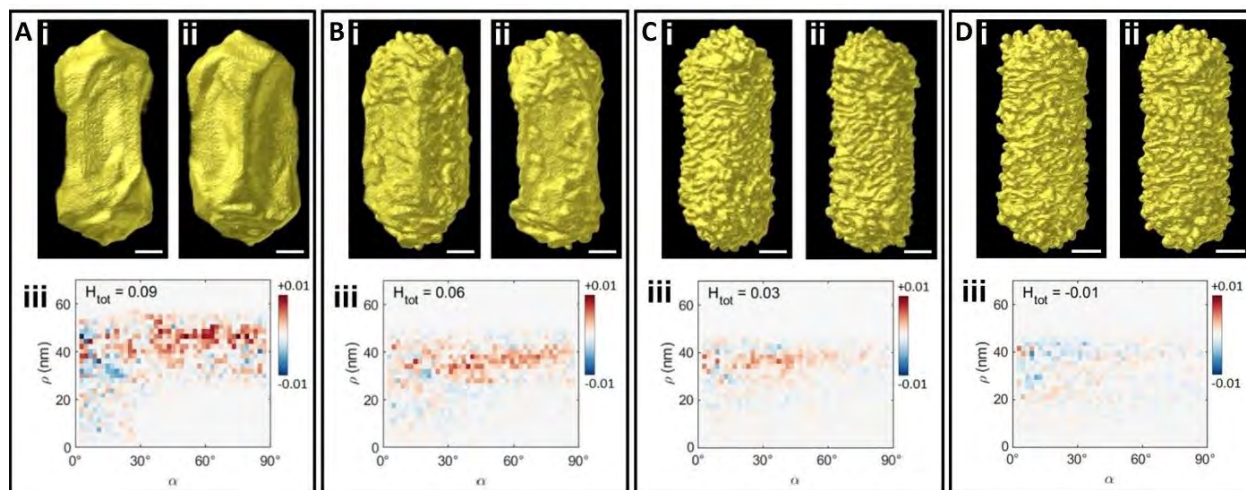


Figure 2.10. Isosurface visualizations of the 3D reconstructions (i, ii) for Au NRs obtained using different concentrations of (*R*)-LipoCYS (A: 20 μM; B: 45 μM; C: 90 μM; D: 200 μM). Presented images are made along different viewing angles (oriented 45° relatively to each other) for each particle. Plots of the corresponding helicity function (iii; red: right-handed; blue: left-handed) are provided for each 3D reconstruction. Technical details on how to compute these helicity functions are provided in **Chapter VI**. The AuNRs obtained by (*R*)-LipoCYS are found to yield a right-handed helicity (red). All scale bars are 25 nm.

A subsequent study using LipoCYS with different achiral seeds also supported the hypotheses described above. Using both cubic and octahedral achiral gold nanoparticles as seeds for chiral reactions at a similar range of LipoCYS concentrations, similar concentration-dependent chiroptical and structural evolutions of the chiral products were observed (**Figure 2.11**). Although

the chiroptical signal was found to decrease compared to similar syntheses using nanorods as seeds, the overall trend was replicated: a spectral redshift was observed as the concentration of LipoCYS was increased. These optical effects were confirmed to correspond to a morphological evolution from smooth to wrinkled particles, as described above. However, it should be noted that at low LipoCYS concentrations, the magnitude of the g -factor for chiral products synthesized from the two different seeds was inverted with respect to one another.

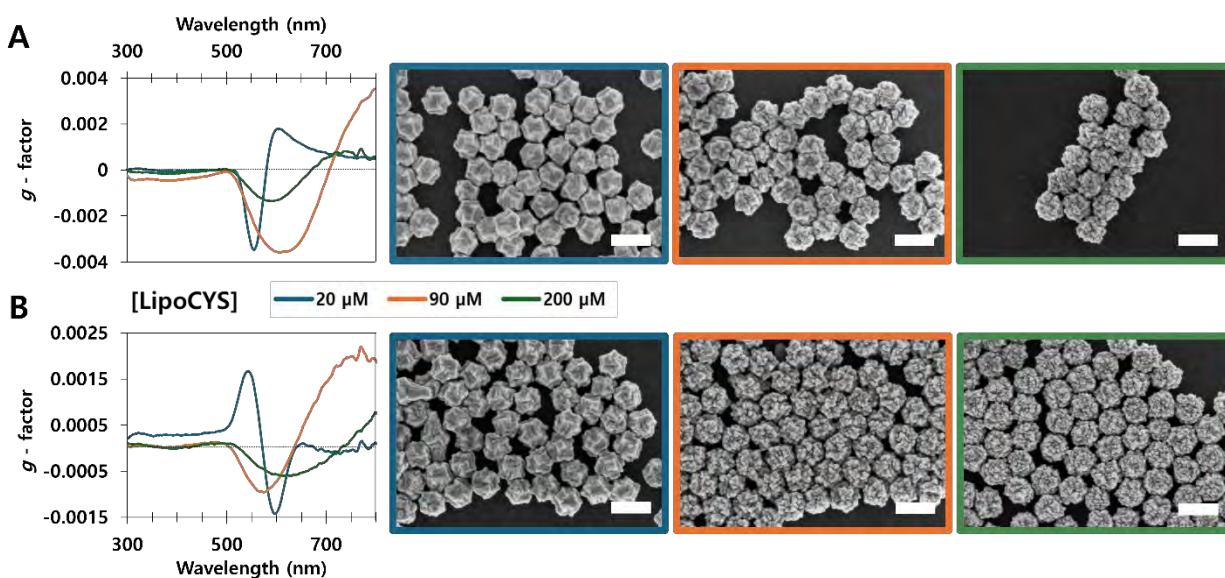


Figure 2.11. Chiroptical (g -factor) spectra and SEM images for chiral products obtained using octahedral (A) and cubic (B) achiral Au NPs as seeds, with different concentrations of (R) -LipoCYS. Image outlines are color-coded to match the legend of the plots; all scale bars are 200 nm. Note the redshifted chiroptical trend and structural evolution of products from smooth to wrinkled, as the LipoCYS concentration is increased.

It must be stressed that the achiral octahedral and cubic seeds used here were of comparable dimensions to each other, and subjected to identical conditions for the chiral growth reactions; the variable of concern here was in the differing geometries of the starting achiral seeds. A more dramatic example of this phenomenon will be explored in **Chapter III**. Efficient approaches for a systematic investigation of the influence of crystallinity in the initial achiral seeds,³² the

development of chiral facets,³³ as well as high-throughput characterization of helicity in chiral products,^{34,35} are critical to a deeper understanding of the underlying growth mechanisms.

2.5 Conclusions

We have contended in this work that chiral growth on gold nanorods can be modulated through rational control over the underlying growth mechanisms, which may provide valuable information toward the predictable synthesis of chiral plasmonic nanomaterials. We have demonstrated reproducible control over the obtained nanoparticle structure at different scales: both fine-detailed wrinkles and the larger overall particle geometry can be tailored through the synthesis conditions. Such a variation can be achieved by modifying a single parameter (the concentration of the chiral molecule, LipoCYS) on a given chiral synthesis. These results are supported by observations that the deposition of gold on the nanorod (seed) surface, and even the preference of facet growth, is heavily influenced by the presence of co-surfactants. It should be noted that, above a certain concentration of LipoCYS, the observed chiroptical response decreases significantly, as a result of the observed lower degree of order in the wrinkled structure. The relative contribution to the overall chiroptical signature of micelle-directed formation of wrinkles and stabilized facet-directed twisting of particle geometry warrants further investigation. An additional relevant finding of this study is related to the micellar template growth: to date, this synthetic protocol has been based on applying a very particular type of molecules with axial chirality as inducers of dissymmetry. Herein, we found that molecules with central chirality are also capable of giving rise to the same type of chiral morphology. Comparison of the chemical structure of LipoCYS and the previously used inducers suggest that micellar template growth requires chiral inducers with two different regions,

a polar head with high affinity for the gold surface and a hydrophobic part that endows affinity for the micelles. Taken together, these results suggest an expanded role for co-surfactants that can be applied for the preparation of nanomaterials with chiral morphology. The availability of a diverse range of gold seeds in various shapes and sizes further emphasizes the significance of these findings.

2.6 References

1. Urban, M. J.; Shen, C.; Kong, X.-T.; Zhu, C.; Govorov, A. O.; Wang, Q.; Hentschel, M.; Liu, N., Chiral Plasmonic Nanostructures Enabled by Bottom-Up Approaches. *Annu. Rev. Phys. Chem.* **2019**, *70*, 275-299.
2. Murphy, C. J.; Sau, T. K.; Gole, A. M.; Orendorff, C. J.; Gao, J.; Gou, L.; Hunyadi, S. E.; Li, T., Anisotropic Metal Nanoparticles: Synthesis, Assembly, and Optical Applications. *The Journal of Physical Chemistry B* **2005**, *109*, 13857-13870.
3. Gonzalez-Rubio, G.; Kumar, V.; Llombart, P.; Diaz-Nunez, P.; Bladt, E.; Altantzis, T.; Bals, S.; Pena-Rodriguez, O.; Noya, E. G.; MacDowell, L. G.; Guerrero-Martinez, A.; Liz-Marzan, L. M., Disconnecting Symmetry Breaking from Seeded Growth for the Reproducible Synthesis of High Quality Gold Nanorods. *Acs Nano* **2019**, *13*, 4424-4435.
4. Xing, Y.; Li, H.; Liu, Y.; Jiang, W., Chiral Assembly of Nanoparticles in Functional Inorganic Materials. *MRS Bull.* **2024**, *49*, 340-351.
5. Tadgell, B.; Liz-Marzán, L. M., Probing Interactions Between Chiral Plasmonic Nanoparticles and Biomolecules. *Chemistry – A European Journal* **2023**, *n/a*, e202301691.
6. Hao, C.; Wang, G.; Chen, C.; Xu, J.; Xu, C.; Kuang, H.; Xu, L., Circularly Polarized Light-Enabled Chiral Nanomaterials: From Fabrication to Application. *Nano-Micro Letters* **2023**, *15*, 39.
7. Liu, Y.; Fu, W.; Xu, Z.; Zhang, L.; Sun, T.; Du, M.; Kang, X.; Xiao, S.; Zhou, C.; Gong, M.; Zhang, D., pH-Driven Reversible Assembly and Disassembly of Colloidal Gold Nanoparticles. *Frontiers in Chemistry* **2021**, *9*.

8. Liu, H.; Vladár, A. E.; Wang, P.-P.; Ouyang, M., Tuning Geometric Chirality in Metallic and Hybrid Nanostructures by Controlled Nanoscale Crystal Symmetry Breaking. *JACS* **2023**, *145*, 7495-7503.
9. Liu, Q.; Zhang, M.; Xu, C.; Li, B., Tuning Chiral Morphology of Gold Nanoparticles with Reversed Chiral Signals by Adjusting the Reaction Temperature of the Seed-mediated Growth Process. *Journal of Materials Chemistry C* **2024**, *12*, 7667-7672.
10. Lee, H.-E.; Ahn, H.-Y.; Mun, J.; Lee, Y. Y.; Kim, M.; Cho, N. H.; Chang, K.; Kim, W. S.; Rho, J.; Nam, K. T., Amino-Acid and Peptide-Directed Synthesis of Chiral Plasmonic Gold Nanoparticles. *Nature* **2018**, *556*, 360-365.
11. Lee, H.-E.; Kim, R. M.; Ahn, H.-Y.; Lee, Y. Y.; Byun, G. H.; Im, S. W.; Mun, J.; Rho, J.; Nam, K. T., Cysteine-Encoded Chirality Evolution in Plasmonic Rhombic Dodecahedral Gold Nanoparticles. *Nature Communications* **2020**, *11*, 263.
12. Van Gordon, K.; Ni, B.; Girod, R.; Mychinko, M.; Bevilacqua, F.; Bals, S.; Liz-Marzán, L. M., Single Crystal and Pentatwinned Gold Nanorods Result in Chiral Nanocrystals with Reverse Handedness. *Angew. Chem. Int. Ed.* **2024**, *63*, e202403116.
13. Ni, B.; Mychinko, M.; Gómez-Graña, S.; Morales-Vidal, J.; Obelleiro-Liz, M.; Heyvaert, W.; Vila-Liarte, D.; Zhuo, X.; Albrecht, W.; Zheng, G.; González-Rubio, G.; Taboada, J. M.; Obelleiro, F.; López, N.; Pérez-Juste, J.; Pastoriza-Santos, I.; Cölfen, H.; Bals, S.; Liz-Marzán, L. M., Chiral Seeded Growth of Gold Nanorods Into Fourfold Twisted Nanoparticles with Plasmonic Optical Activity. *Adv. Mater.* **2023**, *35*, 2208299.
14. Lee, Y. Y.; Cho, N. H.; Im, S. W.; Lee, H.-E.; Ahn, H.-Y.; Nam, K. T., Chiral 432 Helicoid II Nanoparticle Synthesized with Glutathione and Poly(T)20 Nucleotide. *ChemNanoMat* **2020**, *6*, 362-367.
15. Rai, A.; Seena, S.; Gagliardi, T.; Palma, P. J., Advances in the Design of Amino Acid and Peptide Synthesized Gold Nanoparticles for their Applications. *Adv. Colloid Interface Sci.* **2023**, *318*, 102951.
16. Wu, F.; Tian, Y.; Luan, X.; Lv, X.; Li, F.; Xu, G.; Niu, W., Synthesis of Chiral Au Nanocrystals with Precise Homochiral Facets for Enantioselective Surface Chemistry. *Nano Lett.* **2022**, *22*, 2915-2922.
17. Im, S. W.; Ahn, H.-Y.; Kim, R. M.; Cho, N. H.; Kim, H.; Lim, Y.-C.; Lee, H.-E.; Nam, K. T., Chiral Surface and Geometry of Metal Nanocrystals. *Adv. Mater.* **2020**, *32*, 1905758.
18. Morales-Vidal, J.; López, N.; Ortuño, M. A., Chirality Transfer in Gold Nanoparticles by l-Cysteine Amino Acid: A First-Principles Study. *The Journal of Physical Chemistry C* **2019**, *123*, 13758-13764.

19. Zheng, G.; Bao, Z.; Pérez-Juste, J.; Du, R.; Liu, W.; Dai, J.; Zhang, W.; Lee, L. Y. S.; Wong, K.-Y., Tuning the Morphology and Chiroptical Properties of Discrete Gold Nanorods with Amino Acids. *Angew. Chem. Int. Ed.* **2018**, *57*, 16452-16457.
20. González-Rubio, G.; Mosquera, J.; Kumar, V.; Pedraza-Tardajos, A.; Llombart, P.; Solís, D. M.; Lobato, I.; Noya, E. G.; Guerrero-Martínez, A.; Taboada, J. M.; Obelleiro, F.; MacDowell, L. G.; Bals, S.; Liz-Marzán, L. M., Micelle-Directed Chiral Seeded Growth on Anisotropic Gold Nanocrystals. *Science* **2020**, *368*, 1472-1477.
21. Zhuo, X.; Mychinko, M.; Heyvaert, W.; Larios, D.; Obelleiro-Liz, M.; Taboada, J. M.; Bals, S.; Liz-Marzán, L. M., Morphological and Optical Transitions during Micelle-Seeded Chiral Growth on Gold Nanorods. *ACS Nano* **2022**, *16*, 19281-19292.
22. Ito, T. H.; Salles, A. G.; Priebe, J. P.; Miranda, P. C. M. L.; Morgon, N. H.; Danino, D.; Mancini, G.; Sabadini, E., Generation of a Chiral Giant Micelle. *Langmuir* **2016**, *32*, 8461-8466.
23. Zhuo, X.; Vila-Liarte, D.; Wang, S.; Jimenez de Aberasturi, D.; Liz-Marzán, L. M., Coated Chiral Plasmonic Nanorods with Enhanced Structural Stability. *Chem. Mater.* **2023**, *35*, 5689-5698.
24. Heyvaert, W.; Pedraza-Tardajos, A.; Kadu, A.; Claes, N.; González-Rubio, G.; Liz-Marzán, L. M.; Albrecht, W.; Bals, S., Quantification of the Helical Morphology of Chiral Gold Nanorods. *ACS Materials Letters* **2022**, *4*, 642-649.
25. Van Gordon, K.; Baúlde, S.; Mychinko, M.; Heyvaert, W.; Obelleiro-Liz, M.; Criado, A.; Bals, S.; Liz-Marzán, L. M.; Mosquera, J., Tuning the Growth of Chiral Gold Nanoparticles Through Rational Design of a Chiral Molecular Inducer. *Nano Lett.* **2023**, *23*, 9880-9886.
26. Berova, N.; Bari, L. D.; Pescitelli, G., Application of Electronic Circular Dichroism in Configurational and Conformational Analysis of Organic Compounds. *Chem. Soc. Rev.* **2007**, *36*, 914-931.
27. Solís, D. M.; Taboada, J. M.; Obelleiro, F.; Liz-Marzán, L. M.; García de Abajo, F. J., Toward Ultimate Nanoplasmonics Modeling. *ACS Nano* **2014**, *8*, 7559-7570.
28. Obelleiro-Liz, M.; Martín, V. F.; Solís, D. M.; Taboada, J. M.; Obelleiro, F.; Liz-Marzán, L. M., Influence of Geometrical Parameters on the Optical Activity of Chiral Gold Nanorods. *Advanced Optical Materials* **2023**, *11*, 2203090.
29. Kuznetsova, V.; Coogan, Á.; Botov, D.; Gromova, Y.; Ushakova, E. V.; Gun'ko, Y. K., Expanding the Horizons of Machine Learning in Nanomaterials to Chiral Nanostructures. *Adv. Mater.* **2024**, *36*, 2308912.

30. Googasian, J. S.; Skrabalak, S. E., Practical Considerations for Simulating the Plasmonic Properties of Metal Nanoparticles. *ACS Physical Chemistry Au* **2023**, *3*, 252-262.
31. Chen, J.; Gao, X.; Zheng, Q.; Liu, J.; Meng, D.; Li, H.; Cai, R.; Fan, H.; Ji, Y.; Wu, X., Bottom-Up Synthesis of Helical Plasmonic Nanorods and Their Application in Generating Circularly Polarized Luminescence. *ACS Nano* **2021**, *15*, 15114-15122.
32. Sun, X.; Sun, L.; Lin, L.; Guo, S.; Yang, Y.; Zhang, B.; Liu, C.; Tao, Y.; Zhang, Q., Tuning the Geometry and Optical Chirality of Pentatwinned Au Nanoparticles with 5-Fold Rotational Symmetry. *ACS Nano* **2024**, *18*, 9543-9556.
33. Zheng, J.; Boukouvala, C.; Lewis, G. R.; Ma, Y.; Chen, Y.; Ringe, E.; Shao, L.; Huang, Z.; Wang, J., Halide-Assisted Differential Growth of Chiral Nanoparticles with Threefold Rotational Symmetry. *Nature Communications* **2023**, *14*, 3783.
34. Vlasov, E.; Heyvaert, W.; Ni, B.; Van Gordon, K.; Girod, R.; Verbeeck, J.; Liz-Marzán, L. M.; Bals, S., High-Throughput Morphological Chirality Quantification of Twisted and Wrinkled Gold Nanorods. *ACS Nano* **2024**, *18*, 12010-12019.
35. Vlasov, E.; Skorikov, A.; Sánchez-Iglesias, A.; Liz-Marzán, L. M.; Verbeeck, J.; Bals, S., Secondary Electron Induced Current in Scanning Transmission Electron Microscopy: an Alternative Way to Visualize the Morphology of Nanoparticles. *ACS Materials Letters* **2023**, *5*, 1916-1921.

Chapter III – Single Crystal and Pentatwinned Gold Nanorods Result in Chiral Nanocrystals with Reverse Handedness

As discussed in the previous chapter, the chemical makeup of the chiral inducer can have profound effects on the structure and chiroptical signature of the inherently chiral products of “bottom-up” chiral reactions. A more basic example of this is common to chiral synthetic literature, where the handedness of the products is changed by selecting an enantiomer of the chiral inducer used in the reaction. It is typical to use both enantiomers of a given chiral inducer and report the yielded pair of chiral products with inverse chiroptical magnitudes and geometrical handedness. This information is important towards revealing the intricacies of chirality transfer at different scales, i.e. from a molecule to a crystal facet to a nanoparticle. We report that, even when using the same chiral inducer enantiomer, the handedness of chiral gold nanocrystals can be reversed by using achiral AuNR seeds with either single-crystalline or pentatwinned structure. This effect holds for chiral growth, both chemically induced by amino acid derivatives (e.g. cystine) and directed by chiral micelles (comprising BINAMINE and CTAC). Although the particles obtained from the former growth mechanism display irregular shapes that made the morphological handedness challenging to discern, in both cases the products formed using either single crystalline or pentatwinned achiral seeds showed circular dichroism bands of opposite sign. For the micelle-directed growth mechanism, the chiral products had more consistent geometries, nearly mirrored chiroptical signatures, along with quasi-helical wrinkles of inverted handedness. These results

expand the toolbox for chiral synthesis with an effect that might be exploited to yield a host of interesting morphologies with tunable optical properties.

3.1 Introduction

Chirality can be transferred from organic to inorganic substances, via assembly of achiral building blocks into a chiral arrangement, or by the preparation of nanostructures with chiral morphology.¹ This has been historically accomplished by directing amino acids or peptides to systems such as CaCO_3 ,^{2,3} Au,⁴⁻⁷ Ag,⁸ HgS,⁹ or Te,¹⁰ with more recent studies applying DNA or even circularly-polarized light to these systems, yielding a host of novel structures with interesting optical properties.¹¹ These processes, which enable new approaches to control the structure of nanomaterials,¹²⁻¹⁵ crucially depend on the inherent properties of the inorganic crystals, such as the crystal lattice,⁹ stabilization of certain chiral kinks,² or the presence of crystalline defects such as screw dislocations.¹⁰ As discussed in **Chapter I** and **Chapter II**, a few synthetic strategies for chirality transfer to Au nanoparticles have been successfully applied, typically by removing mirror planes from the geometry of achiral nanoparticle seeds during growth. This is mediated either by the presence of small chiral molecules such as amino acids (chemically-induced),⁴ or by using chiral micelles to wrap around nanocrystal seeds and template further growth (micelle-directed).¹⁶ In all cases, the crystal properties of the achiral seeds have been reported to influence the morphology and handedness of the final chiral products. As discussed in **Chapter I**, the formation and use of single-crystalline (SC) or penta-twinned (PT) Au nanoclusters determines the growth of either single-crystal AuNRs (grown from SC seeds in the presence of Ag^+ ions) with an octagonal cross section, or elongated pentagonal prisms (from PT seeds and Ag-free).¹⁷

Consequently, the crystallographic surface facets for both AuNR types are different, with SC-AuNRs displaying {520} lateral facets capped by {110} and {100} tips^{18,19} and PT-AuNRs yielding {100} sides and {111} tip facets.²⁰

A striking example of the impact of the initial crystallinity on the properties of chiral products was demonstrated by Nam and colleagues,^{4,21} in a synthesis of helicoid particles from cubic or octahedral achiral seeds, which has been discussed in **Chapter I**. Briefly, helicoids were synthesized in the presence of the same amino acid enantiomer but using different achiral seeds; comparison of the corresponding CD spectra revealed an inverted chiroptical response between the different chiral products.²² Although the mechanisms related to such geometrical and optical differences remain largely unknown, it is clear that morphological or crystalline details in the seeds play a crucial role during crystal growth. From the reported observations, it remains unclear whether it is the seed morphology or other structural aspects, like the crystalline index of surface facets, the presence of twin boundaries, or other crystalline defects that determine the resulting chiral morphology. Therefore, achiral SC- and PT-AuNR seeds with similar sizes (the latter prepared by lab partner Francisco Bevilacqua; see **Chapter VI** for synthesis details) were subjected to syntheses operating under the aforementioned chiral growth mechanisms: chemically-induced (using cystine as the chiral inducer) and micelle-directed (using BINAMINE as the chiral co-surfactant). Given the radically different morphological features (twisted vs. wrinkled) that contribute to the chiroptical activity of products from each of these mechanisms, the effects of varying the crystal habit from SC to PT were also expected to be significantly different. As mentioned in **Chapter I** and **Chapter II**, the complex morphological details of chiral AuNRs require high resolution characterization in three dimensions (3D) that can only be achieved by means of state-of-the-art electron tomography methods; this characterization also allows for

quantification of the chiral structure at the nano-scale.²³ Correlation between morphological and optical features is not straightforward, but the handedness of chiral structures are expected to correlate with the sign of CD bands in the corresponding spectra.²⁴

3.2 Rationalizing the use of cystine vs. cysteine

An important digression will be made here to rationalize the use of cystine in this work, as opposed to cysteine, which is far more commonly used as an inducer for the chemically-induced chiral growth mechanism. When exposed to oxygen, cysteine forms disulfide bonds with itself, forming a dimer called cystine. It was suggested by our collaborators at the University of A Coruña that cysteine oxidizes more rapidly than previously thought, and that proportions of cystine present in chiral syntheses with cysteine are disproportionately significant towards the chiroptical signature from yielded particles. To test this, two series of chiral particles were synthesized using achiral SC- AuNRs at increasing [*L*-cystine] and [*L*-cysteine], respectively, keeping all other variables constant (**Figure 3.1**).

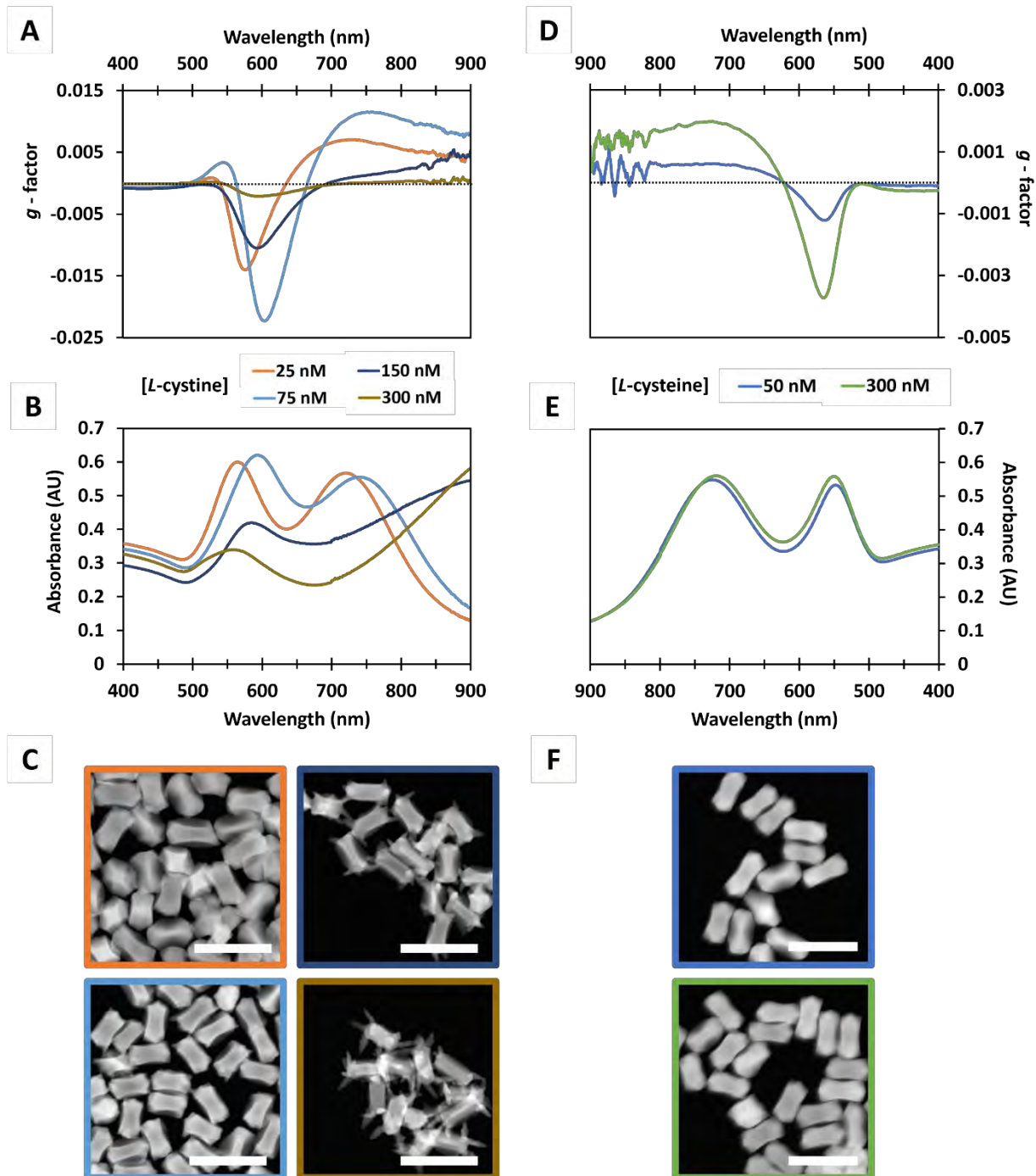


Figure 3.1. Circular dichroism spectra (A,D), absorbance spectra (B,E), and HAADF-STEM images (C,F) for chiral AuNRs synthesized with increasing [*L*-cystine] (left) and increasing [*L*-cysteine] (right); all other variables for chiral synthesis were held constant. Scale bars = 200 nm. Note the increased intensity of chiroptical signal and marked structural evolution for chiral products synthesized with cystine as opposed to cysteine.

The concentration-dependent structural evolution of the obtained particles is far more interesting when using *L*-cystine, as compared to an equivalent series of particles prepared with *L*-cysteine (taking care to use degassed reagents and minimizing exposure to oxygen). As [*L*-cystine] increases, the particles develop sharp protrusions, especially at the particle tips. This corresponds with an increase in *g*-factor up to 75 nM *L*-cystine, but above this concentration the absorbance spectra red-shift and the chiroptical signal starts to decrease. As [*L*-cysteine] increases, there is no observable evolution in particle geometry, and the chiroptical signature is lower in magnitude overall. Therefore, to increase the reproducibility of high *g*-factor chiral particles synthesized through the chemically-induced growth mechanism, we used cystine as the chiral inducer (referred to throughout as *L*-2cys).

3.3 Chemically-Induced Mechanism: Single-Step vs. Stepwise Growth

For initial investigation regarding the effect of different achiral seeds on chemically-induced chiral growth, a simplified protocol was implemented involving a single-step overgrowth reaction (see **Chapter VI** for synthetic details). Specifically, all gold salts to be involved in the chiral reaction were added at once and reduced together in the presence of the achiral seeds (PT- AuNRs: 122 ± 30.4 nm x 31.3 ± 6.5 nm; SC- AuNRs: 101 ± 17.3 nm x 29.0 ± 5.3 nm; $[\text{Au}^{3+}] : [\text{Au}^0] = 8.9$). Cystine (*L*-2cys) was used as the chiral inducer in these syntheses; a detailed rationale for usage of cystine over cysteine is provided in **Chapter VI**. Single-step growth in the presence of *L*-2cys resulted in remarkably different morphologies for PT- or SC-AuNRs. Whereas SC-AuNRs evolved into helical cuboid-like structures with obvious tip protrusions, PT-AuNRs evolved into complex structures (**Figure 3.2**).

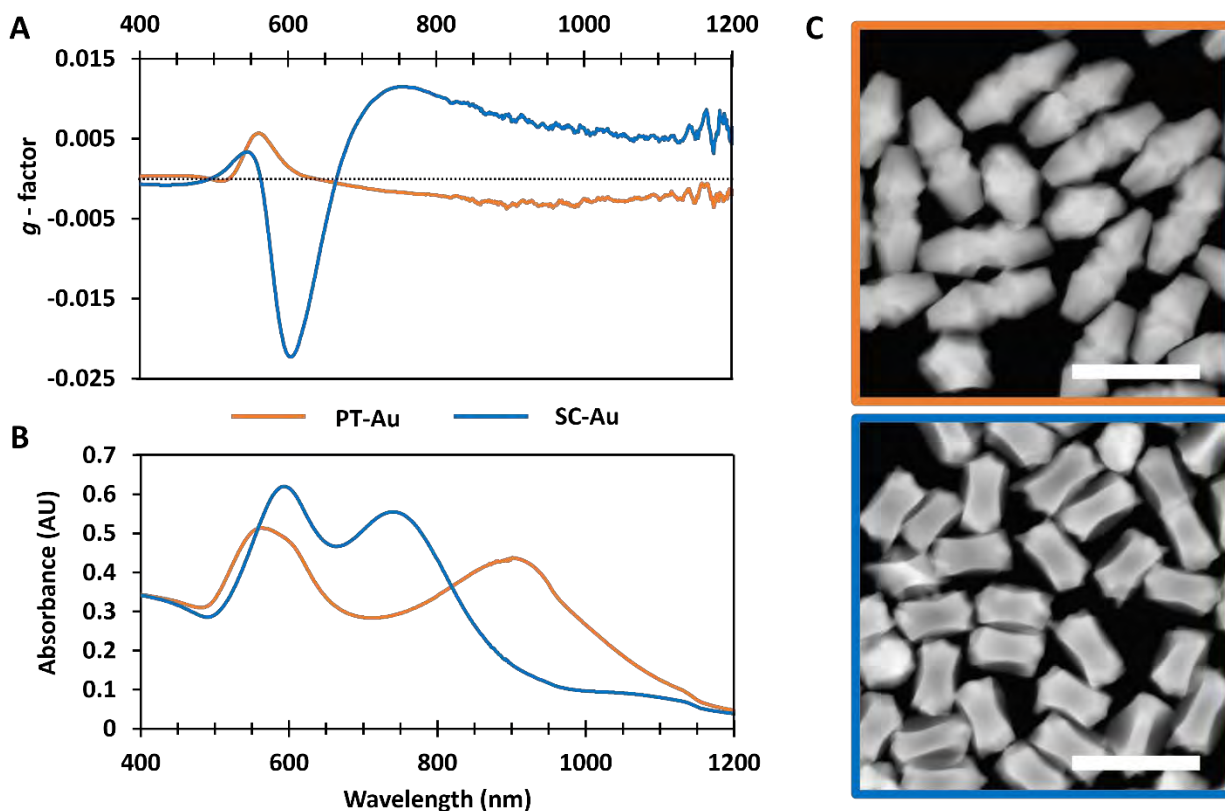


Figure 3.2. Chiroptical spectra (A) and absorbance spectra (B) for particles synthesized by a single-step growth protocol, using *L*-2cys and PT- or SC-AuNR seeds, as labeled. HAADF-STEM characterization of chiral products (C), image outlines are color-coded to match legend of plot; scale bars = 200 nm.

The linear optical response for both SC and PT products included a (transverse) extinction peak around 580-600 nm whereas the second (longitudinal) LSPR band was significantly redshifted for chiral PT-AuNRs, compared to chiral SC-AuNRs, in agreement with a larger measured aspect ratio for the former (PT- products: $198.9 \pm 5.4 \times 76.4 \pm 3.7$ nm (AR = 2.6); SC- products: $117.1 \pm 5.2 \times 57.4 \pm 3.4$ nm (AR = 2.0)). More remarkable differences were observed in the corresponding circular dichroism (CD) spectra (normalized to the g-factor), where the bands for SC- and PT-AuNRs seem to be inverted (opposite sign) and shifted: a negative peak at 595 nm and a positive plateau at the NIR region for chiral SC-AuNRs, whereas twisted PT-AuNRs featured a positive

peak at 563 nm and a negative plateau at the NIR region. A notable observation here is that, even though seeded growth was carried out in the presence of the same chiral inducer enantiomer, the sign of CD bands was inverted for NRs evolving from SC- and PT-AuNRs. However, the chiroptical magnitudes from products of single-step reactions are comparatively low, which corresponds to the yielded geometries lacking an apparent handedness. From our previous work,²⁵ we learned that multi-step seeded growth leads to better-defined twisted morphologies than those obtained in a single step. Therefore, our collaborator Dr. Bing Ni (University of Konstanz) followed a stepwise protocol to produce chiral products, including nine chiral growth steps, using both SC- and PT-Au NR seeds (PT-AuNRs: 90.9 ± 4.2 nm x 19.3 ± 1.3 nm; SC-AuNRs: 75.4 ± 6.3 nm x 15.6 ± 1.6 nm; $[\text{Au}^{3+}] : [\text{Au}^0] = 28.1$). This means that the gold salts to be involved in the chiral reaction were introduced fractionally (in nine portions) and reduced completely preceding each subsequent growth step, resulting in the gradual formation of a twisted morphology. Following the same chiroptical trend established in the single-step products, an intense negative peak at 590 nm (maximum *g*-factor of -0.036) and a positive plateau at longer wavelengths was observed for SC-AuNRs, but a weak negative peak at 535 nm and a more intense positive band centered at 660 nm (peak *g*-factor value of 0.020) for the product from growth on PT-AuNRs (**Figure 3.3A**). The linear optical spectra of the respective final products (**Figure 3.3B**) reveal significant differences. Two well-defined extinction bands of similar intensity, centered at 591 nm and 754 nm, were recorded for the particles obtained from SC-AuNRs, whereas growth on PT-AuNRs led to a weakly defined double band at shorter wavelengths (ranging from 550-750 nm) and an intense band around 1050 nm. Marked differences in the chiral products were also observed through electron microscopy. As previously reported, chiral particles grown in stepwise fashion

from SC-AuNRs in the presence of *L*-2cys showed a right-handed 4-fold twisted structure (Figure 3.3C), in agreement with the removal of mirror planes by *L*-2cys.²⁵

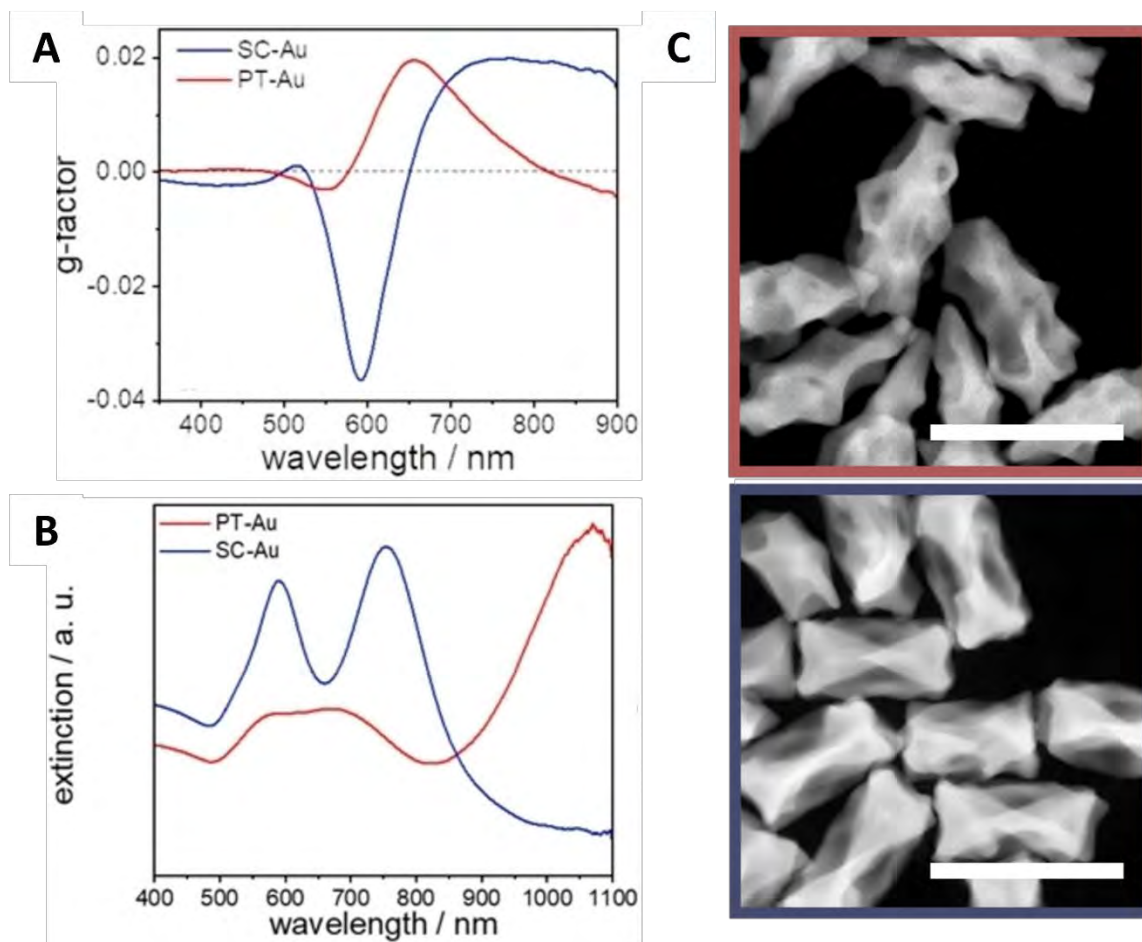


Figure 3.3. Chiroptical spectra (A) and extinction spectra (B) for particles synthesized by a multi-step growth protocol, using *L*-2cys and PT- or SC-AuNR seeds, as labeled. HAADF-STEM characterization of chiral products (C), image outlines are color-coded to match legend of plot; scale bars = 200 nm.

However, when growing PT-AuNRs under similar conditions, much more intricate structures were obtained, often containing cavities within highly twisted surfaces, somewhat resembling the shape of a conch shell.^{26,27} Along with differences in size, these major morphological irregularities are likely responsible for the observed discrepancies in the extinction spectra (PT-AuNRs: $179.5 \pm$

20.1 nm (accurate values for particle width not provided, given their ill-defined lateral morphologies); SC-AuNRs: 154.6 ± 11.5 nm x 77.9 ± 7.8 nm; AR = 1.98). These images also demonstrate strong inter-particle variability within the same batch compared to the products attained in a single growth step, which hinders interpretation of products attained via stepwise growth. Given the unexpected morphology obtained from chiral growth using PT-AuNRs, we tracked the morphological evolution upon various additions of growth solution (**Figure 3.4**). After 9 dissymmetric growth steps, the surface exhibited even more pronounced irregularities. These observations are significantly different compared to growth starting from SC-AuNR seeds, where smooth surfaces can be identified at early stages and well-defined handedness is observed in the final stage.²⁵

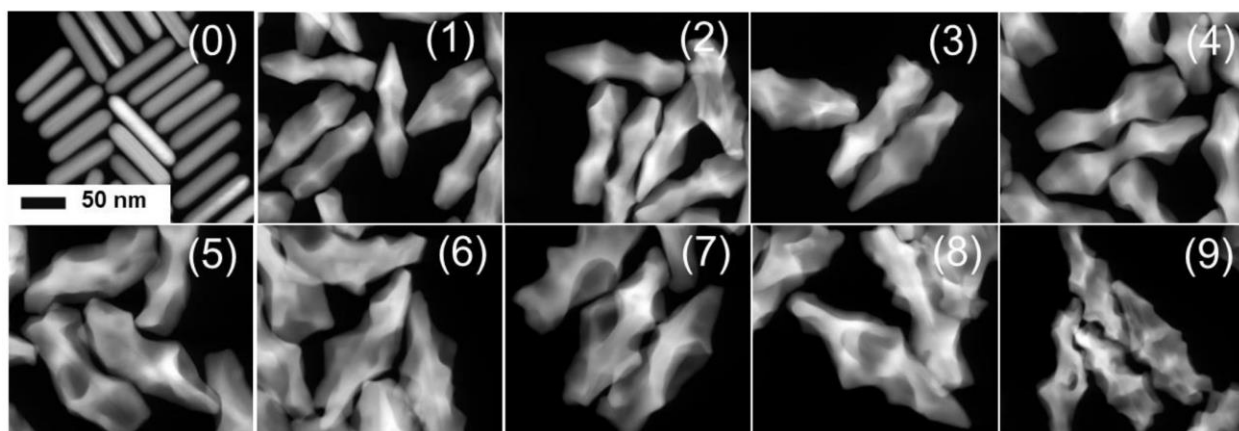


Figure 3.4. Representative HAADF-STEM images of the products obtained after different number of H₂AuCl₄ additions (as labeled) on PT-AuNRs in the presence of *L*-2cys. The scale bar applies to all images.

The above results suggest that chiral growth using PT-AuNR seeds yields chiral nanostructures with opposite optical handedness to that for chiral NRs grown from SC-AuNR seeds. We demonstrated this using the chemically-induced chiral mechanism and comparing a single-step and multi-step growth approach. Despite the simplified single-step growth approach yielding

products with low polydispersity, the intensity of the chiroptical signature was low as well, and the handedness of the structural features on these particles was not very apparent. Attempts to obtain better-defined twisted morphologies of chiral products and enhance the corresponding chiroptical signal via multi-step growth were successful; however, the wide variety of morphologies obtained using PT-AuNR seeds largely complicates the analysis and discussion of structural-optical relationships here.

3.4. Micelle-Directed Chiral Growth

While the products of chiral reactions under the chemically-induced growth mechanism are of disparate morphologies (even when produced using the same synthetic protocol, as shown above) the morphologies of micelle-directed chiral growth products are comparatively regular. We hypothesized that the micelle-directed chiral growth on PT- and SC-AuNR achiral seeds under identical conditions might also lead to an inversion in optical activity. Furthermore, we could obtain a clearer picture of the structural causes for this optical phenomenon by focusing on the predominant handedness of the wrinkles. The chiral growth reactions in this case involved BINAMINE and CTAC mixtures in a one-step overgrowth reaction, which had the added benefit of reducing the inter-particle morphological variability within each batch, as demonstrated in the previous section. As with the previous section, the enantiomer of the chiral inducer used was kept constant; the only variable in the reactions was the type of achiral AuNR used in the synthesis (PT-AuNRs: 122 ± 30.4 nm x 31.3 ± 6.5 nm; SC-AuNRs: 101 ± 17.3 nm x 29.0 ± 5.3 nm; $[\text{Au}^{3+}] : [\text{Au}^0] = 7.9$). Characterization of the obtained chiral products revealed similar absorbance spectra and wrinkled morphologies regardless of the crystallinity of the achiral AuNR seed employed in

the synthesis. The chiroptical signature of products grown from PT-AuNR seeds compared to that of products grown from SC-AuNR seeds were found to be nearly perfectly inverted (**Figure 3.5A**). Linear optical spectra for both chiral products feature a band peaking at 570 nm, which tails off into the NIR region (**Figure 3.5B**). As predicted, a similar wrinkled morphology formed on products according to the micelle-directed chiral growth mechanism, regardless of starting seed used (**Figure 3.5C**). As with the chiral growth products using PT-AuNRs as seeds mentioned above, these particles grew larger than their SC- counterparts under identical synthetic conditions (PT-products: 182.9 ± 11.2 nm x 76.2 ± 2.9 nm (AR = 2.4); SC-products: 134.4 ± 8.3 nm x 65.1 nm ± 5.6 nm (AR = 2.1)).

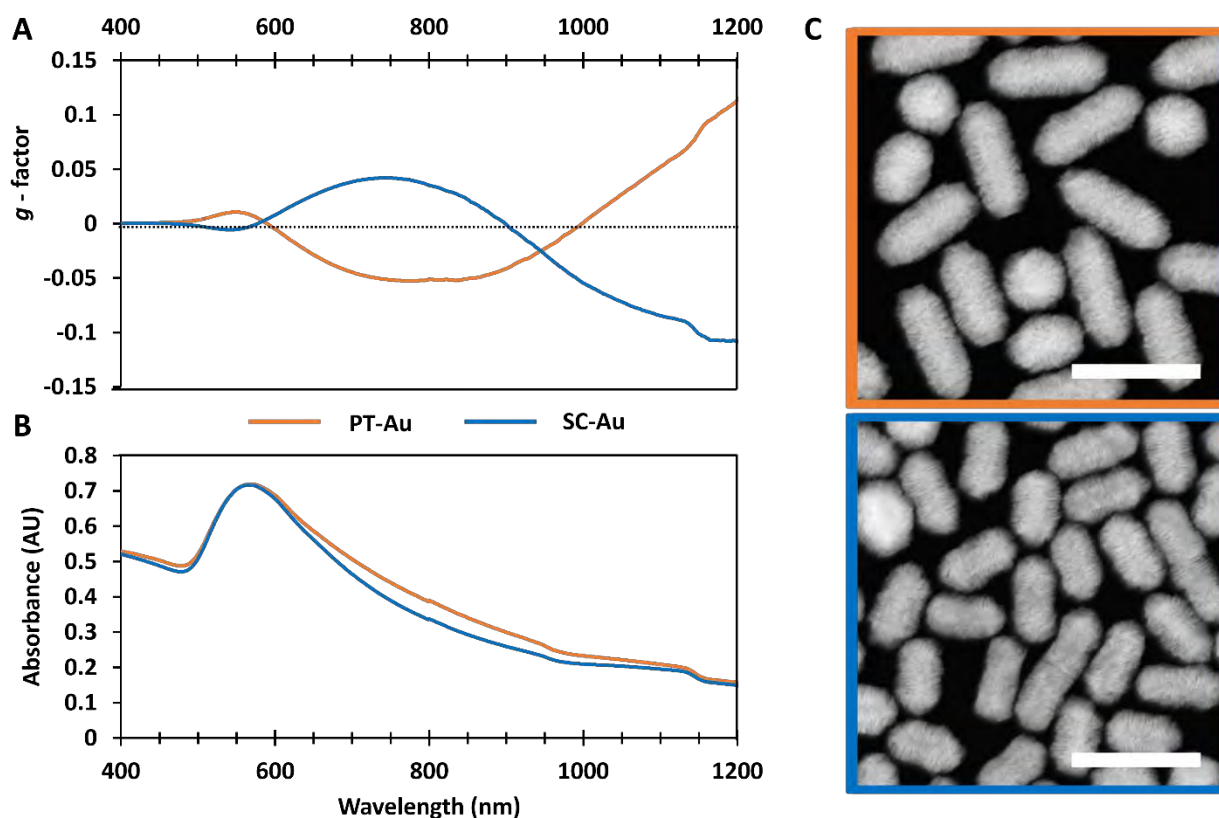


Figure 3.5. Chiroptical spectra (A) and absorbance spectra (B) for particles synthesized using *R*-BINAMINE and PT- or SC-AuNR seeds, as labeled. HAADF-STEM characterization of chiral products (C), image outlines are color-coded to match legend of plot; scale bars = 200 nm.

These observations hint at the handedness of the wrinkles to explain the CD sign reversal in the micelle-directed synthetic pathway, but, as with the *L*-2cys induced synthesis, other effects may co-exist. These effects include differences in growth kinetics, different intermediate structures, preferential interaction of the BINAMINE chiral molecules with the surface facets of these intermediates, subtle differences in tip protrusions and anisotropy, etc. The influence of tip morphology on the chiroptical signature has been explored by Liu, et al., who showed through simulations that chiroptical spectra for nanocube models with high-Miller-index chiral facets were dramatically shifted – and inverted – compared to those from nanorod models possessing similar chiral facets.²⁸ In summary, numerous factors may influence the morphology of AuNRs and in turn their chiroptical response. Disentangling these effects will require additional characterization and new descriptors for complex chiral structures, as well as chemical strategies to probe the growth pathway.

3.5 Electron Tomography and Helicity Analysis

To more thoroughly investigate the chiroptical inversion observed from chiral products of both growth mechanisms when using PT-AuNRs, we sought to better clarify and characterize structural features on these products via electron tomography, carried out by Dr. Robin Girod and Dr. Mikhail Mychinko, under the supervision of Prof. Sara Bals at the University of Antwerp (EMAT). Furthermore, to explore the relationship between the morphology of chiral particles and their chiroptical properties, our collaborators also conducted helicity analysis through a method specifically designed to quantify the handedness of surface features in electron tomography reconstructions.²³ This method is discussed in greater detail in **Chapter I**. Briefly, a 3D

reconstruction obtained from electron tomography is aligned along the central axis of an imaginary helix; the helicity of chiral features are plotted as a function of the radius ρ and inclination angle α , for all combinations of ρ and α in a cylindrical coordinate system. The resulting helicity plots show a histogram of right-handed (positive helicity values) or left-handed (negative helicity values) surface elements. Total helicity (H_{tot}) is calculated by integrating the entire surface of the reconstructions; this metric quantifies how close to a perfect helix a given geometry is, with the ideal case having a helicity of ± 1 , depending on handedness. As shown in **Figure 3.6**, using PT-AuNRs as the achiral seeds in a stepwise chemically-induced growth method yielded products with a mixture of right- and left-handed oriented surface features, reflecting their complex and varied structures. This was further confirmed by small total helicity values for PT- derived products, typically in a range of ± 0.03 . The inverted CD signal from these samples may arise from a predominance of optically active left-handed features that helicity cannot account for, i.e. a weakly helical yet chiral morphology.²⁹ In contrast, twisted chiral products yielded using SC-AuNR achiral seeds under identical synthetic conditions had mostly right-handed features and strongly positive helicity values, as previously reported.²⁵

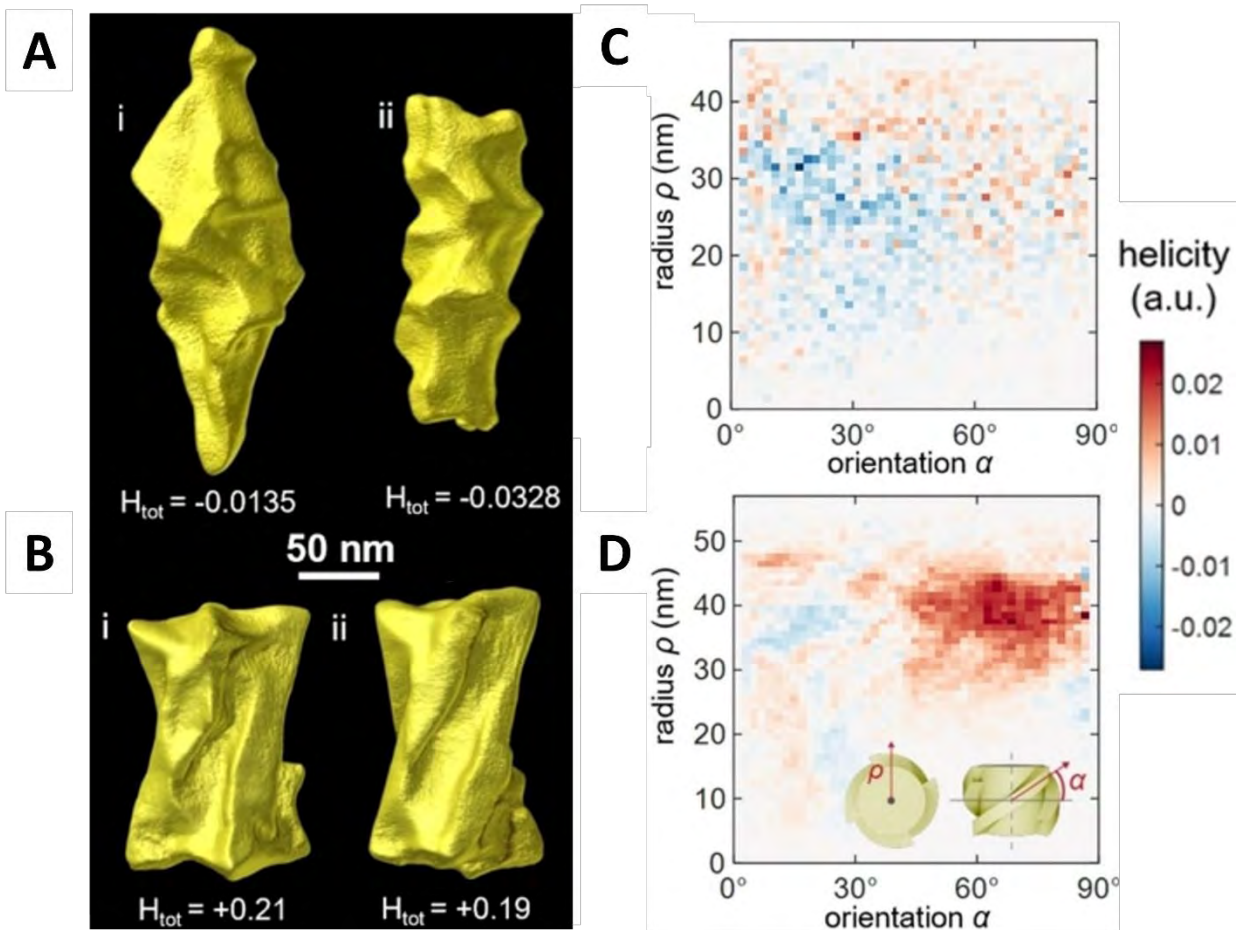


Figure 3.6. Characterization of chiral twisted AuNRs synthesized using PT- or SC- achiral seeds in the presence of *L*-2cys. Electron tomography reconstructions for typical chiral PT-AuNRs (A) and SC-AuNRs (B). Scale bar is valid for all images. Helicity plots for the chiral PT-AuNR shown in a-ii (C) and the chiral SC-AuNR shown in B-i (D). Insets in (D) show the definition of the orientation α and of the radius ρ (distance from central rotation axis) for a simple helix. Red dots indicate dominantly right-handed features, blue dots indicate dominantly left-handed features, the intensity scales with the number of similarly oriented surface elements. Total helicity (H_{tot}) was calculated for each particle by integrating the helicity plots.

It is difficult, due to the limited sample size and variability of the surface features, to attribute a dominant morphological handedness to the PT-derived products and to explain the inverted sign of the CD spectra based on this analysis. Interestingly, this also suggests that the origin of chirality in products derived from SC- and PT-AuNRs is fundamentally different, with the latter products possessing poorly defined structural helicity and nonobvious morphological handedness, despite

their clear chiroptical properties. A similar analysis was carried out on the helices of micelle-directed chiral products. As shown by electron tomography featured in **Figure 3.7**, it was apparent that the wrinkles on products yielded from SC-AuNRs preferentially tilted to the right, whereas wrinkles grown on PT-AuNRs preferentially tilted to the left. It is important to note that this was observed despite the same chiral inducer enantiomer being used in both cases. Quantification provided by helicity plots confirmed this observation, yielding a total helicity of -0.09 for PT-derived products, i.e., an overall left-handed helical structure, whereas a total helicity of $+0.10$ was determined for wrinkled SC-derived products, as expected for a right-handed structure.

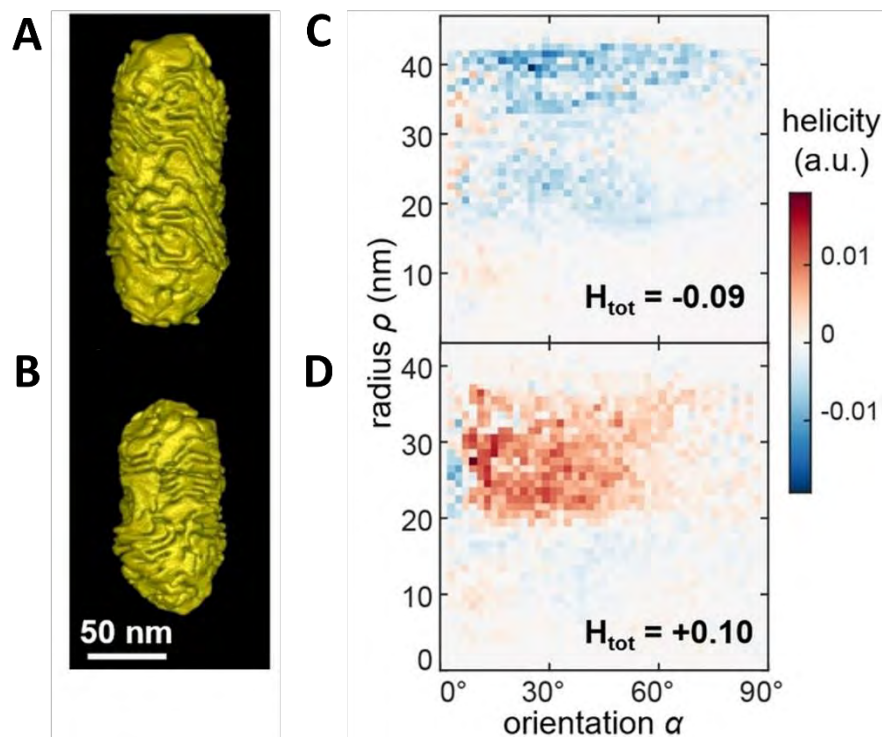


Figure 3.7. Characterization of chiral wrinkled AuNRs synthesized using pentatwinned or single-crystal achiral seeds, in the presence of *S*-BINAMINE/CTAC mixtures. Electron tomography reconstructions of a representative PT-AuNR (A) and a SC-AuNR (B). Scale bar is valid for both images. Helicity characterization of the particles in A (C) and B (D), respectively.

Detailed analysis of selected reconstructions revealed additional differences in the morphologies of wrinkled AuNRs obtained from SC- and PT-achiral seeds (**Figure 3.8**). Whereas the latter chiral products typically featured blunt tips, SC-AuNRs typically contained well-defined wrinkles, suggesting an influence of either the tip morphology or the type of crystal surface facets at the tips, on micelle adsorption and further growth. Notable differences were also found between wrinkles growing on the side facets of PT- or SC-AuNR seeds.

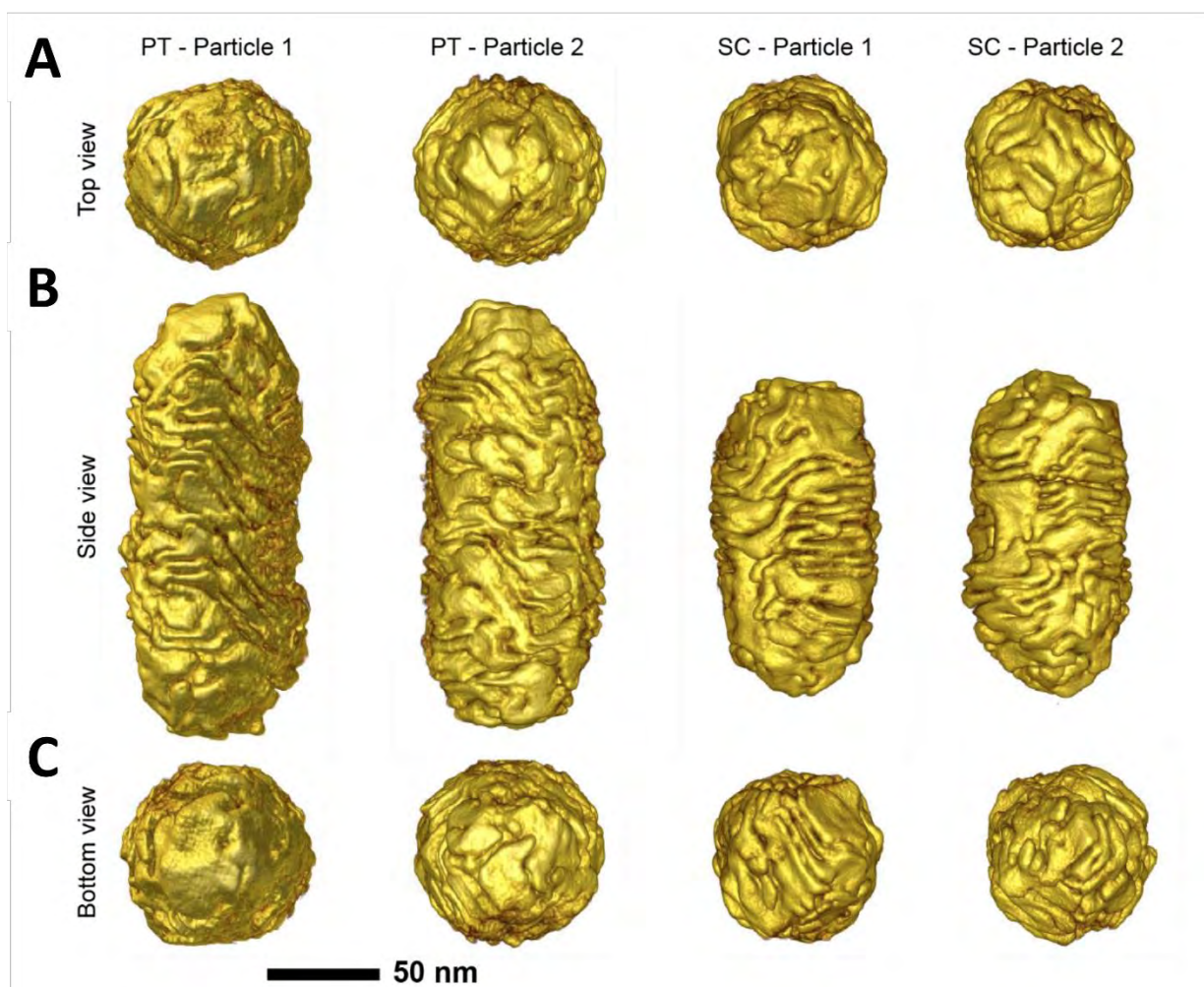


Figure 3.8. Overview of wrinkled chiral particles obtained from micelle-directed synthesis with *S*-BINANIME and PT- or SC-AuNRs as labeled on top. Surface views from (A) the top, (B) the side, (C) the bottom of the particles demonstrating the difference in wrinkle orientation and tip morphology. Note the typically wrinkled tips on SC particles. The scale bar is valid for all views and particles.

A firmer understanding of the relationship between the chiroptical signatures of products yielded using different achiral seeds and their corresponding particle morphologies can direct investigation into specific morphological features that may be disproportionately important to desired optical properties. The influence of protruding facets and particle tips was briefly discussed in **Chapter I**; further investigation into these features will likely have to proceed from a (similarly) computerized

approach, as the more prominent geometrical differences between particles synthesized for this work were of the surface wrinkles. Our focus for characterization in the next section is therefore directed at these more apparent chiral features.

3.6 Symmetry Characterization

Even though the quantitative evidence supplied by helicity analysis supports our hypotheses about the influence of the initial crystallinity of seeds on chiral products, a structural comparison of the achiral seeds and chiral products at the crystal facet level was implemented by our collaborators at EMAT to address how and why this phenomenon occurs. This approach was first applied to PT-derived products of chemically-induced stepwise chiral growth. We conducted atomic resolution tomography on a PT-AuNR isolated after the first addition of gold (**Figure 3.9**). Although the obtained reconstruction allowed us to identify crystallographic orientations, indexing the surface proved difficult because of its continuously varying curvature. This observation shows that PT-derived products under this chiral growth mechanism have less well-defined surface facets; in stark contrast to products of SC-AuNR seeds under the same mechanism, in which $\{521\}$ chiral facets are formed in the presence of chirality-inducing molecules of matching handedness. Close inspection of the images also revealed that the five-fold twinning of the PT-AuNR seed was preserved in the overgrown particle.

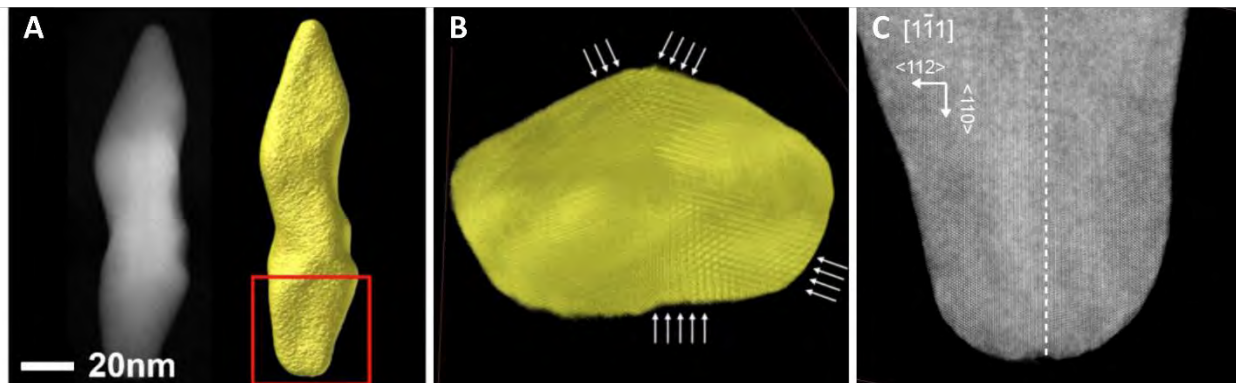


Figure 3.9. Detail of a PT-AuNR after one growth step. (A) HAADF image of the particle and its electron tomography (ET) results. The red square marks the area for atomic resolution ET measurement. (B) atomic-resolution ET reconstruction of the particle viewed from the bottom. The white arrows indicate the twin boundaries. (C) Orthoslice through the 3D reconstruction viewed along the $[1\bar{1}1]$ direction. Note that the crystallographic orientations are indicated for one side of the twin boundary (dashed line).

To expand on this observation, we then applied this approach to the products of micelle-directed chiral reactions. For clarity, we first establish two definitions to describe the geometry of wrinkles on rods, as shown in **Figure 3.10** and **Figure 3.11**: a wrinkle direction angle describes the angle of that wrinkle when visualized sideways or in cross-section (**Figure 3.10B**), and a wrinkle orientation angle describes the angle of that wrinkle when visualized in a front view through isosurface rendering (**Figure 3.10C**).

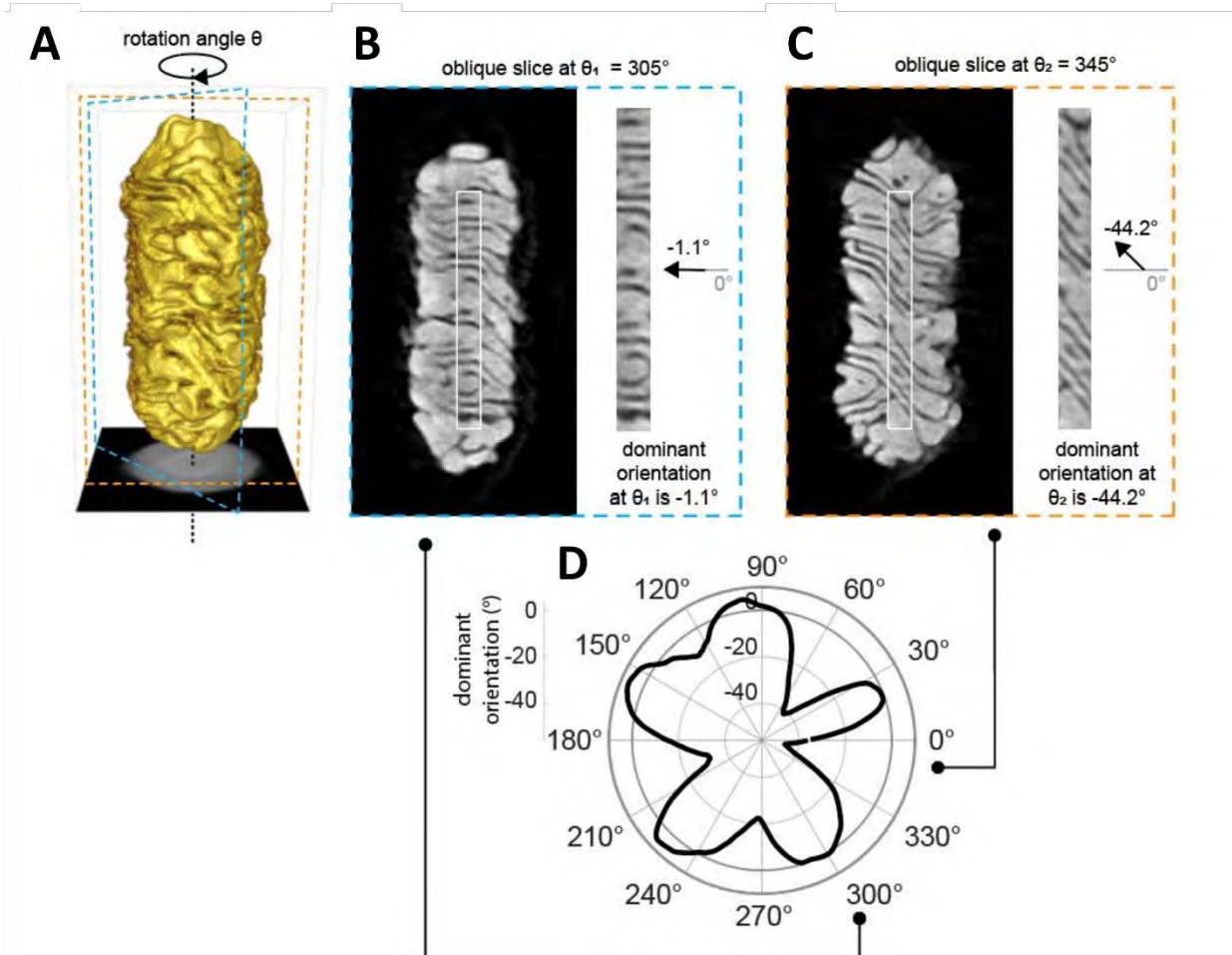


Figure 3.10. Method for tracking the dominant orientation of the wrinkles. The 3D reconstruction (A) is sliced through the wrinkle corona, 20-30 nm away from the center, for 360 rotation angles θ . The orange and blue dashed lines demonstrate two examples at (B) $\theta_1 = 305^\circ$ and (C) $\theta_2 = 345^\circ$. The dominant orientation is then computed in central areas (white rectangles in (B) and (C)) to prevent bias from the edges of the particle and ensure the metric is specific to a given rotation angle. Assembling the results for all 360 rotational slices yields the polar plots in (D).

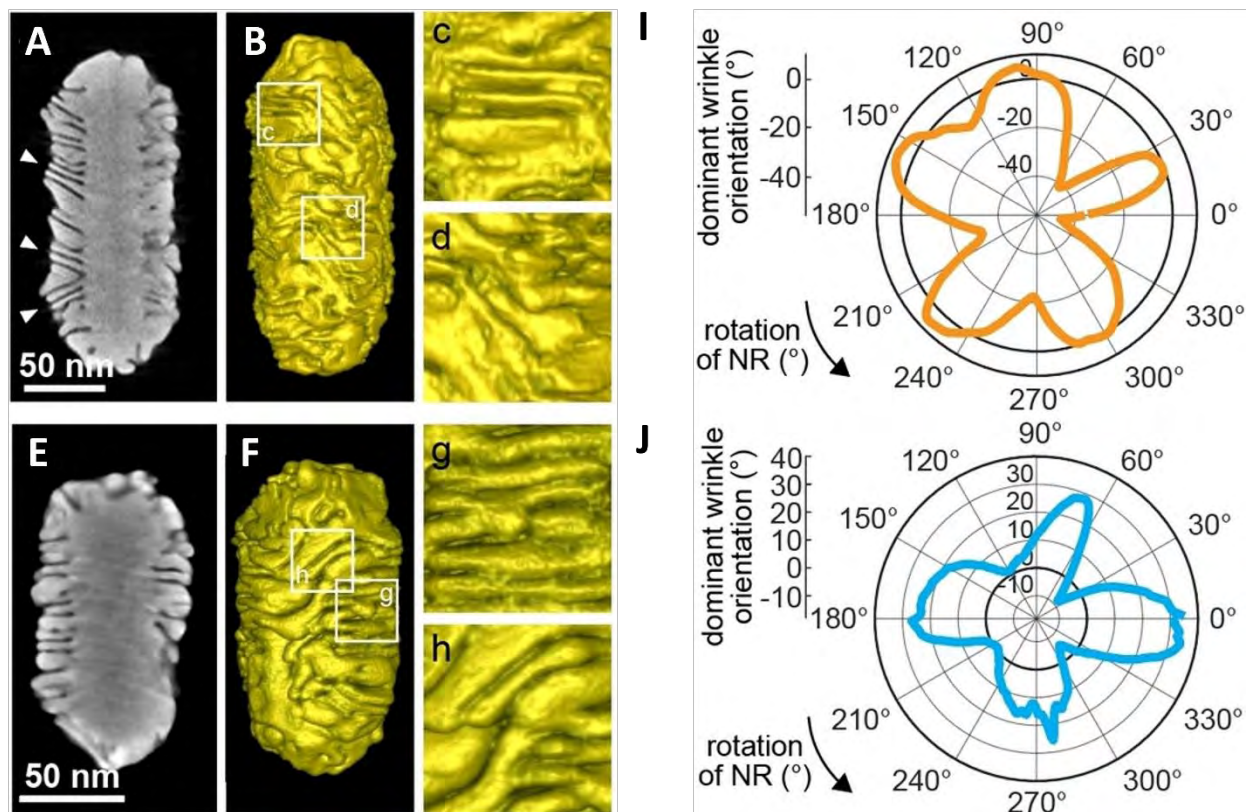


Figure 3.11. Morphology of wrinkles on chiral particles grown from PT- and SC-AuNRs using the micelle-templated synthesis with *S*-BINAMINE. Central orthoslice (A) showing the direction of growth (white arrows) and isosurface visualization of the 3D reconstruction (B) of a wrinkled PT-AuNR, with close-up views of the surface (c,d) demonstrating two main orientations of the wrinkles. Central orthoslice (E) and surface visualization (F) of a wrinkled SC-AuNR with close-up surface views (g,h). Polar plots of the dominant wrinkle orientation in the particles shown in B (I) and F (J) respectively, as a function of the rotation of each particle around its major axis.

On products obtained from PT-AuNR seeds, numerous wrinkles were seen to have a $\pm 25\text{-}30^\circ$ direction angle with respect to the normal direction of the surface. In contrast, most of the wrinkles on products obtained from SC-AuNR seeds were almost perpendicular to the lateral facets, occasionally with small but random direction angles. Apart from the growth direction, wrinkles were also observed to have different orientations. Specifically, two types of areas could be distinguished on the surfaces of wrinkled particles, in which wrinkles were either mostly flat (Figure 3.11c,g), or mostly tilted (Figure 3.11d,h). To understand the distribution of these areas

at the chiral NR surface, we tracked them by measuring the dominant wrinkle orientation when the NR was rotated along its major axis. As shown in **Figure 3.11I**, when rotating particles grown from PT-seeds, five areas were observed to contain mainly flat wrinkles (dominant orientation close to 0°), whereas five areas had wrinkles tilting to the left (negative orientation angle). Remarkably, these areas alternated, in agreement with the 5-fold symmetry of the achiral PT seeds being preserved. Particles grown from SC seeds also contained distinct areas of flat or tilted wrinkles (albeit with positive orientation angles, i.e., to the right), but in this case with a 4-fold rotational symmetry around the major axis of the NRs (**Figure 3.11J**). This symmetry is directly reminiscent of the intermediate morphologies that were reported to occur during achiral-to-chiral transitions, comprising a square cross-section with $\{110\}$ facets.²⁵ Given the different geometries (number of faces and corners or angles at corners) and surface facets between PT seeds and SC intermediates, our observations at the tips and sides of the wrinkled AuNRs strongly suggest that such geometrical and crystallographic considerations influence the growth of wrinkles and/or micelle adsorption.

3.7 Conclusions

We have identified a major influence of the crystallinity of achiral seeds on the handedness of AuNRs obtained using two different chiral growth methods on both SC- and PT-AuNRs, and always using the same enantiomer of the corresponding chiral inducer. When cystine was used as the chiral inducer, SC-AuNR seeds evolved into chiral NRs with a 4-fold twisted structure, whereas growth on PT-AuNR seeds led to more complex shapes. The overall optical handedness – as measured by CD spectroscopy – was inverted for these structures. However, although the

chiral products of SC-AuNRs showed a twisted right-handed morphology, particles grown from PT-AuNRs did not display an obvious left-handed twist, which suggests that the origin of their chiroptical properties may lie in a different type of geometrical chirality. Regarding chiral micelle-templated growth, similar rod-like structures surrounded by helical wrinkles were obtained, regardless of seed morphology (and thus facet crystallinity). In this case, inversion of the handedness for the wrinkled chiral products of SC- and PT-AuNRs was more evident, both in the optical (CD band inversion) and morphological (tilt angle inversion) characterization. Electron tomography analysis also allowed us to determine the 4-fold and 5-fold symmetries in SC- and PT-AuNRs respectively were still present in the corresponding chiral products using each type of achiral seed. These results reinforce the notion that wrinkle growth is not random but influenced by geometrical and/or crystallographic factors, thereby highlighting a previously neglected aspect of chiral syntheses that might be exploited to yield a host of interesting morphologies with tunable optical properties, depending on the starting symmetry of the achiral seed. In all cases, our conclusions here are limited by the small sample size of particles evaluated by electron tomography and helicity analysis. This is due in no small part to the exorbitant amount of time it takes to fully characterize chiral particles in this way using standard techniques. The tilt series and image reconstruction involved in electron tomography are particularly time-demanding (see **Chapter I** for details). A new technique developed by Evgenii Vlasov at EMAT exploits secondary electron-based electron beam-induced current (SEEBIC), which generates images of the surface topography of a specimen thanks to the “edge effect”: enhanced secondary electron intensities when they are emitted from protruding features on the particles.^{30,31} Using SEEBIC at low magnification, quantifying the helicity of a population of hundreds of particles can be accomplished in hours, instead of months via acquisition and processing of tilt series. As this

technique is optimized and more broadly applied, conclusions from similar work to that discussed in this chapter will be better supported. The development of yet another methodology to expand understanding of the aforementioned chiral growth mechanisms via the preparation, isolation, and characterization of intermediate morphologies will be detailed in the following chapter.

3.8 Conclusions

1. Wang, S.; Liu, X.; Mourdikoudis, S.; Chen, J.; Fu, W.; Sofer, Z.; Zhang, Y.; Zhang, S.; Zheng, G., Chiral Au Nanorods: Synthesis, Chirality Origin, and Applications. *ACS Nano* **2022**, *16*, 19789-19809.
2. Orme, C. A.; Noy, A.; Wierzbicki, A.; McBride, M. T.; Grantham, M.; Teng, H. H.; Dove, P. M.; DeYoreo, J. J., Formation of Chiral Morphologies Through Selective Binding of Amino Acids to Calcite Surface Steps. *Nature* **2001**, *411*, 775-779.
3. Addadi, L.; Weiner, S., Crystals, Asymmetry and Life. *Nature* **2001**, *411*, 753-755.
4. Lee, H.-E.; Ahn, H.-Y.; Mun, J.; Lee, Y. Y.; Kim, M.; Cho, N. H.; Chang, K.; Kim, W. S.; Rho, J.; Nam, K. T., Amino-Acid and Peptide-Directed Synthesis of Chiral Plasmonic Gold Nanoparticles. *Nature* **2018**, *556*, 360-365.
5. Lee, Y. Y.; Cho, N. H.; Im, S. W.; Lee, H.-E.; Ahn, H.-Y.; Nam, K. T., Chiral 432 Helicoid II Nanoparticle Synthesized with Glutathione and Poly(T)20 Nucleotide. *ChemNanoMat* **2020**, *6*, 362-367.
6. Wang, S.; Zheng, L.; Chen, W.; Ji, L.; Zhang, L.; Lu, W.; Fang, Z.; Guo, F.; Qi, L.; Liu, M., Helically Grooved Gold Nanoarrows: Controlled Fabrication, Superhelix, and Transcribed Chiroptical Switching. *CCS Chemistry* **2020**, *3*, 2473-2484.
7. Yang, S.; Li, H.; Liu, R.; Wang, C.; Yu, J.; Li, S.; Wang, Y.; Chen, H., Understanding the Evolution of Tunable Spiral Threads in Homochiral Au Nano-Screws. *Inorganic Chemistry Frontiers* **2022**, *9*, 4136-4141.
8. Ni, B.; Zhou, J.; Stolz, L.; Cölfen, H., A Facile and Rational Method to Tailor the Symmetry of Au@Ag Nanoparticles. *Adv. Mater.* **2023**, *35*, 2209810.
9. Wang, P.-p.; Yu, S.-J.; Govorov, A. O.; Ouyang, M., Cooperative Expression of Atomic Chirality in Inorganic Nanostructures. *Nature Communications* **2017**, *8*, 14312.

10. Ben-Moshe, A.; da Silva, A.; Müller, A.; Abu-Odeh, A.; Harrison, P.; Waelder, J.; Niroui, F.; Ophus, C.; Minor, A. M.; Asta, M.; Theis, W.; Ercius, P.; Alivisatos, A. P., The Chain of Chirality Transfer in Tellurium Nanocrystals. *Science* **2021**, *372*, 729-733.
11. Wang, Y.; Tay, A., Advances in Enantiomer-Dependent Nanotherapeutics. *ACS Nano* **2023**, *17*, 9850-9869.
12. Ma, W.; Xu, L.; de Moura, A. F.; Wu, X.; Kuang, H.; Xu, C.; Kotov, N. A., Chiral Inorganic Nanostructures. *Chem. Rev.* **2017**, *117*, 8041-8093.
13. Visheratina, A.; Kotov Nicholas, A., Inorganic Nanostructures with Strong Chiroptical Activity. *CCS Chemistry* **2020**, *2*, 583-604.
14. Ni, B.; Cölfen, H., Chirality Communications Between Inorganic and Organic Compounds. *SmartMat* **2021**, *2*, 17-32.
15. Kotov, N. A.; Liz-Marzán, L. M.; Weiss, P. S., Chiral Nanostructures: New Twists. *ACS Nano* **2021**, *15*, 12457-12460.
16. González-Rubio, G.; Mosquera, J.; Kumar, V.; Pedraza-Tardajos, A.; Llombart, P.; Solís, D. M.; Lobato, I.; Noya, E. G.; Guerrero-Martínez, A.; Taboada, J. M.; Obelleiro, F.; MacDowell, L. G.; Bals, S.; Liz-Marzán, L. M., Micelle-Directed Chiral Seeded Growth on Anisotropic Gold Nanocrystals. *Science* **2020**, *368*, 1472-1477.
17. Liu, M.; Guyot-Sionnest, P., Mechanism of Silver(I)-Assisted Growth of Gold Nanorods and Bipyramids. *The Journal of Physical Chemistry B* **2005**, *109*, 22192-22200.
18. Goris, B.; Bals, S.; Van den Broek, W.; Carbó-Argibay, E.; Gómez-Graña, S.; Liz-Marzán, L. M.; Van Tendeloo, G., Atomic-Scale Determination of Surface Facets in Gold Nanorods. *Nature Materials* **2012**, *11*, 930-935.
19. Carbó-Argibay, E.; Rodríguez-González, B.; Gómez-Graña, S.; Guerrero-Martínez, A.; Pastoriza-Santos, I.; Pérez-Juste, J.; Liz-Marzán, L. M., The Crystalline Structure of Gold Nanorods Revisited: Evidence for Higher-Index Lateral Facets. *Angew. Chem. Int. Ed.* **2010**, *49*, 9397-9400.
20. Johnson, C. J.; Dujardin, E.; Davis, S. A.; Murphy, C. J.; Mann, S., Growth and Form of Gold Nanorods Prepared by Seed-Mediated, Surfactant-Directed Synthesis. *J. Mater. Chem.* **2002**, *12*, 1765-1770.
21. Lee, H.-E.; Kim, R. M.; Ahn, H.-Y.; Lee, Y. Y.; Byun, G. H.; Im, S. W.; Mun, J.; Rho, J.; Nam, K. T., Cysteine-Encoded Chirality Evolution in Plasmonic Rhombic Dodecahedral Gold Nanoparticles. *Nature Communications* **2020**, *11*, 263.

22. Sun, X.; Yang, J.; Sun, L.; Yang, G.; Liu, C.; Tao, Y.; Cheng, Q.; Wang, C.; Xu, H.; Zhang, Q., Tunable Reversal of Circular Dichroism in the Seed-Mediated Growth of Bichiral Plasmonic Nanoparticles. *ACS Nano* **2022**, *16*, 19174-19186.
23. Heyvaert, W.; Pedraza-Tardajos, A.; Kadu, A.; Claes, N.; González-Rubio, G.; Liz-Marzán, L. M.; Albrecht, W.; Bals, S., Quantification of the Helical Morphology of Chiral Gold Nanorods. *ACS Materials Letters* **2022**, *4*, 642-649.
24. Obelleiro-Liz, M.; Martín, V. F.; Solís, D. M.; Taboada, J. M.; Obelleiro, F.; Liz-Marzán, L. M., Influence of Geometrical Parameters on the Optical Activity of Chiral Gold Nanorods. *Advanced Optical Materials* **2023**, *11*, 2203090.
25. Ni, B.; Mychinko, M.; Gómez-Graña, S.; Morales-Vidal, J.; Obelleiro-Liz, M.; Heyvaert, W.; Vila-Liarte, D.; Zhuo, X.; Albrecht, W.; Zheng, G.; González-Rubio, G.; Taboada, J. M.; Obelleiro, F.; López, N.; Pérez-Juste, J.; Pastoriza-Santos, I.; Cölfen, H.; Bals, S.; Liz-Marzán, L. M., Chiral Seeded Growth of Gold Nanorods Into Fourfold Twisted Nanoparticles with Plasmonic Optical Activity. *Adv. Mater.* **2023**, *35*, 2208299.
26. Knoll, P.; Wu, N.; Steinbock, O., Spiraling Crystallization Creates Layered Biomorphs. *Physical Review Materials* **2020**, *4*, 063402.
27. Kunz, W.; Kellermeier, M., Beyond Biomineralization. *Science* **2009**, *323*, 344-345.
28. Liu, H.; Vladár, A. E.; Wang, P.-P.; Ouyang, M., Tuning Geometric Chirality in Metallic and Hybrid Nanostructures by Controlled Nanoscale Crystal Symmetry Breaking. *JACS* **2023**, *145*, 7495-7503.
29. King, R. B., Chirality and Handedness: The Ruch ‘Shoe-Potato’ Dichotomy in the Right-Left Classification Problem. *Ann. N.Y. Acad. Sci.* **2003**, *988*, 158-170.
30. Vlasov, E.; Skorikov, A.; Sánchez-Iglesias, A.; Liz-Marzán, L. M.; Verbeeck, J.; Bals, S., Secondary Electron Induced Current in Scanning Transmission Electron Microscopy: an Alternative Way to Visualize the Morphology of Nanoparticles. *ACS Materials Letters* **2023**, *5*, 1916-1921.
31. Vlasov, E.; Heyvaert, W.; Ni, B.; Van Gordon, K.; Girod, R.; Verbeeck, J.; Liz-Marzán, L. M.; Bals, S., High-Throughput Morphological Chirality Quantification of Twisted and Wrinkled Gold Nanorods. *ACS Nano* **2024**, *18*, 12010-12019.

Chapter IV – Time-resolved optical and structural characterization of chiral growth on gold nanorods

As the library of particle morphologies produced from chiral growth reactions expands, the ability to track the associated structural evolution in a time-resolved fashion gains greater attention. Being able to show where particle growth occurs over time would provide insights into how the chiral inducers (and other reagents) are interacting with the surface of the particles, and how this influences the final morphology. Though this has been demonstrated with chemically-induced chiral reactions that can progress over a scale of hours, micelle-directed chiral growth is typically completed in a matter of minutes, and thus requires *in situ* characterization or tuning the supply of gold salts contributing to growth to estimate progression of the reaction. With both of these strategies proving unable to monitor the optical *and* structural evolution in a sufficiently time-resolved manner, an efficient method was devised to cease nanocrystal growth by addition of sodium borohydride. We hypothesize that NaBH_4 instantly reduces all of the excess gold salt present in a chiral growth mixture, leading to aggregation of the reduced gold, effectively ceasing gold nanoparticle overgrowth and preventing any further size or shape evolution. These intermediate (chiral) products could then be separated from the precipitate *via* centrifugation, permitting spectroscopic and morphological characterization of a so-called “kinetic series”, comprising the products of identically prepared chiral growth reactions ceased at different timepoints. In this chapter, we report on the preparation, analysis, and comparison of kinetic series

using achiral SC- and PT-AuNRs, and a range of chiral inducers, aiming to further elucidate the underlying growth mechanisms.

4.1 Introduction

A basic approach for the time-resolved analysis of chemically-induced chiral reaction products has been demonstrated in the literature from K.T. Nam's research group, where the synthesis of chiral helicoids, a process that typically takes hours to complete, is studied at regular time intervals.¹⁻⁴ By pulling aliquots from a single reaction every few minutes and rapidly centrifuging and quenching in an excess of water, a broad overview of the evolving structure was presented. An alternative method devised by Ahn, *et al.*, takes advantage of the various functional groups on cysteine to adsorb onto and quench the growth of metal nanomaterials.⁵ Through this approach, the intermediate structures of Au nanoplates, Pd nanosheets, and Ag nanoprisms could be characterized with a time resolution of seconds. Relevant to the work presented in this chapter are the products of micelle-directed chiral growth, which are directed by BINAMINE, or the more recent chiral inducer 2-amino-N-decyl-3-mercaptopropanamide (LipoCYS),⁶ working in conjunction with cetyltrimethylammonium chloride (CTAC). As covered in **Chapter II** and **Chapter III**, these co-surfactants are hypothesized to form large chiral micelles in solution, which effectively form a nanoscale template on achiral AuNRs that guides a subsequent overgrowth reaction, resulting in well-defined surface wrinkles with a quantifiable helicity and intense chiroptical signature.^{6,7} It has been observed that the structural evolution mediated by these co-surfactants occurs within a matter of minutes, and documenting particle growth as it progresses remains a difficult challenge. A pair of approaches⁸ to monitor the products of micelle-directed

chiral growth (induced by BINAMINE) were introduced in **Chapter I**. The first approach involved preparing and monitoring a chiral synthesis *in situ* using a CD instrument to track the chiroptical signature of a progressing reaction in real time. This approach is limited by the maximum scan speed and spectral resolution of the instrument; the fact that increasing one of these factors decreases the other puts a practical limit on how fine the intervals in a real-time spectroscopic analysis can be. Additionally, the products of a specific time interval in an *in situ* preparation cannot be characterized in isolation because the chiral reaction continues to completion. There are methods to circumvent this,⁹ such as quenching the growing products in an excess of water or another non-reacting solvent to effectively stop chiral growth, but it is uncertain whether quenching occurs sufficiently fast, and whether these methods can reproducibly isolate small products from a large volume of liquid. Thus, a second approach was used, in which a progression of chiral features was shown via the preparation of a series of growth reactions with a varying concentration of gold salt. Although this approach showed interesting information about the intermediate morphologies obtained by this category of chiral reaction, it should be noted that these results were not representative of optimized products (featured in the foundational manuscript¹⁰), obtained when using a large excess of gold salts to achiral seeds. In this chapter, we present a reproducible method that allows us to isolate chiral gold nanoparticles at different stages of the micelle-directed growth reaction by effectively terminating the reaction using sodium borohydride, which allows for product characterization at reaction time intervals resolved in a scale of tens of seconds. Sodium borohydride is a strong reducing agent, known to promote the fast reduction of metal salts including gold, silver, or platinum, and is typically used alongside surfactant in the preparation of small metal nanoclusters (approximately 1-2 nm in diameter), according to a method first established by Brust and Schiffrin in 1994.¹¹ We hypothesized that

addition of NaBH₄ solution to the reaction medium during chiral overgrowth should exhaust all remaining gold precursor, forming Au aggregates that could be readily separated from the intermediate chiral products by centrifugation, and permitting straightforward characterization of the isolated and stable particles. By ceasing chiral growth reactions at different time points and analyzing the products in a series, the chiroptical and structural evolution of a progressing reaction could be assessed. To demonstrate the overall reliability of this method, the chiroptical spectra of products from reactions ceased by NaBH₄ were compared to identical reactions prepared and measured *in situ* in a CD instrument. This was done for three reasons: i) to ensure that the optical signature of chiral products is not affected by treatment with NaBH₄; ii) to ensure that chiral growth is brought to a sudden stop upon NaBH₄ addition; and iii) to ensure that the time points from ceased reactions are representative of a reaction in progress.

4.2 Method Development: Chiral Product Stability in NaBH₄

First, it is important to check that chiral products are unaffected by the presence of NaBH₄. As it is a reducing agent capable of rapidly reducing gold salts to small gold NCs, the use of NaBH₄ here was limited to the amount required to accomplish this, which was established as 1.6x molar excess NaBH₄ to gold salts, following previous literature.¹² Identical reactions with BINAMINE were prepared in parallel and allowed to proceed for 30 minutes, a sufficient amount of time for the reaction to be completed.^{8,10} After treatment of one of the reactions with NaBH₄, the products were isolated from the reaction mixture *via* centrifugation and resuspended in water for characterization. The chiroptical responses from both products were found to be similar to each other (**Figure 4.1**), with a slight blue-shift and increase in intensity, consistent with surface

charging mediated by NaBH₄, as previously described in the literature for achiral Au NPs.^{13,14}

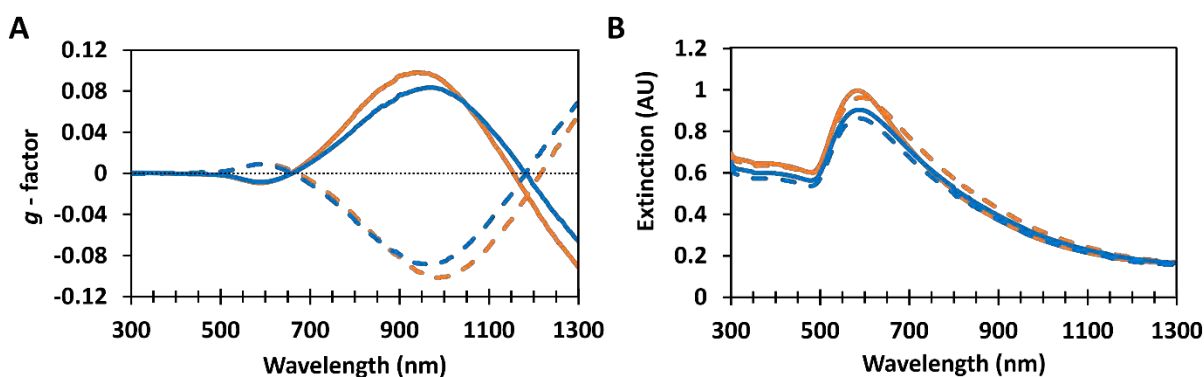


Figure 4.1. Dissymmetry factor (A) and extinction (B) spectra comparing the results of chiral growth in the presence of *S*-BINAMINE and achiral single-crystal AuNR seeds, untreated (blue lines) and treated (orange lines) with NaBH₄ after completion (reaction time: 30 minutes) The solid lines correspond to chiral reactions prepared with (*R*-) BINAMINE, and the dashed lines correspond to chiral reactions prepared with (*S*-) BINAMINE.

With this explained discrepancy between the optical spectra of NaBH₄-treated and untreated chiral products, and assuming that etching or reshaping of the chiral products would result in a more significant shift or reduction in intensity of the chiroptical signature,¹⁵ this indicates that chiral products are structurally unaffected by the NaBH₄ used in these experiments.

4.3 Method Development: Ceasing Chiral Reactions with NaBH₄

Second, we investigated whether chiral growth would stop immediately after addition of NaBH₄, at the desired time point. To demonstrate this, chiral reactions with BINAMINE were prepared *in situ* and continually scanned inside a CD instrument. As stated above, time zero of the reaction is represented by when ascorbic acid is added to initiate the overgrowth reaction, however there is an unavoidable delay between this event and the first scan of the CD instrument, which explains the observed chiroptical peak at time zero. Immediately following the first scan, and while the CD

instrument was preparing for a second scan, the reaction was quickly treated with NaBH_4 , shaken and returned to the instrument before the second CD spectrum was measured. The instrument was then left to continually scan for 15 scans in total, approximately 6.5 minutes. The chiroptical spectrum was observed not to evolve past that measured by the second scan, immediately following NaBH_4 addition (see **Figure 4.2A**). This experiment was performed thrice, at different stages of the reaction; in each case, after the CD scan following NaBH_4 addition, the chiroptical spectrum was observed not to evolve past that point (see **Figure 4.2B,C**). A rapid color change to dark brown after the addition of NaBH_4 indicated the fast reduction of gold salts to nanoclusters. This color change would be a good indicator for which stage the reaction was in as it progressed, to be discussed later.

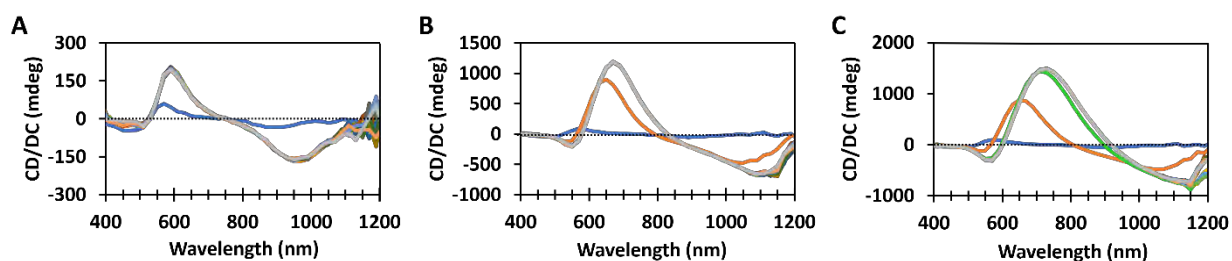


Figure 4.2. Chiroptical response from (*R*-) BINAMINE chiral reactions using achiral single-crystal AuNR seeds: prepared and measured *in situ* and treated with NaBH_4 after 1 scan (A; 1st scan in blue), 2 scans (B; 2nd scan in orange), and 3 scans (C; 3rd scan in green). The CD instrument scanned continuously, for 15 scans in total; note that the chiroptical signature does not evolve past the scan where NaBH_4 treatment occurs.

4.4 Comparison to *in situ* analysis

An important assessment of the method proposed here is that the chiroptical signatures from *in situ* measurements match those from NaBH_4 -ceased reactions at equivalent time points into the reaction. In this way, we could check that this protocol for ceasing chiral growth reactions works

as intended: that the reaction in progress is stopped completely and the products are unaffected by the presence of NaBH₄ or reduced gold at each desired time point. A series of identically prepared reactions, with BINAMINE as the chiral inducer, were ceased using NaBH₄ after 30, 60, 300, and 1800 seconds. The shade of brown these reactions would turn after NaBH₄ addition steadily decreased in intensity proportional to reaction time, indicating the gradual consumption of gold salt and their deposition onto the growing nanoparticles, forming chiral features as the reaction progresses. The products from each time point were then isolated *via* centrifugation and resuspended in pure water before spectral characterization. The chiroptical signatures of these products were compared to those obtained in real time from an identical reaction prepared *in situ* in a CD instrument. The signatures obtained at each time point for both strategies are remarkably similar (see **Figure 4.3**), which was true regardless of the enantiomer of chiral inducer used.

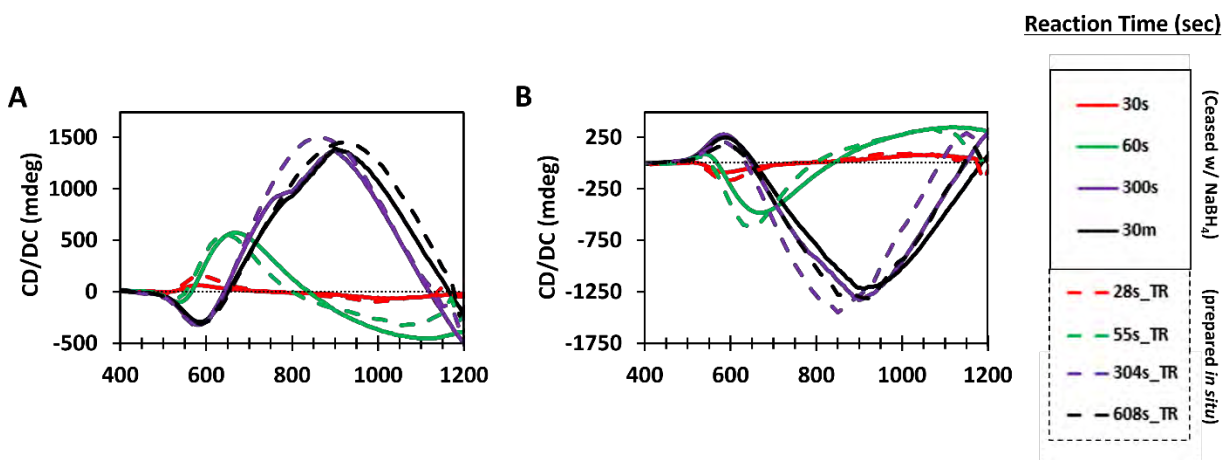


Figure 4.3. Comparison of chiroptical response from isolated chiral products upon ceasing the growth reaction by NaBH₄ (solid lines) vs. reactions progressing *in situ* (dashed lines). Reactions were prepared with single-crystal achiral seeds and *R*-BINAMINE (A) or *S*-BINAMINE (B).

As mentioned previously, a serious limitation of time-resolved measurements *in situ* is the scan speed of the CD instrument. Furthermore, the time zero of the reaction (when ascorbic acid is introduced to initiate seeded growth) will often not equal the time zero of *in situ* characterization

(when the instrument initializes the scanning process). The small differences in time between the spectra acquired from chiral reactions progressing in real time and those acquired from the products of reactions ceased by NaBH₄ at specific time points may account for the small discrepancies observed between the two strategies. An advantage of the latter strategy is the ability to cease and therefore monitor the products of a chiral reaction at time points inaccessible to the CD instrument. For example, the first time point acquired *in situ* (for a wavelength range of 400-1200 nm) was taken after 28 seconds, whereas the introduction of NaBH₄ may in principle cease chiral growth at any time. Whereas the former reaction will continue to completion, the latter will be suspended in place, permitting detailed characterization of chiral products at this time point, and enabling a broader analysis of a range of reaction time points. From these results, for a chiral reaction prepared with BINAMINE and allowed to progress for a given time interval, the products isolated after treatment with NaBH₄ have chiroptical signatures representative of identically prepared, untreated products.

4.5 Time-resolved evolution of BINAMINE chiral products (SC-AuNRs)

From the results in the previous section, it is notable that the chiroptical signature reaches its maximum magnitude between the first two to five minutes of the reaction. To investigate the structural factors responsible for this quickly achieved increase and subsequent decline in CD, it is desirable to probe the chiral features of colloidal products at each time point *via* electron microscopy techniques. However, *in situ* electron microscopy is limited by the complicated apparatus required for liquid phase characterization and low signal to noise ratios caused by the presence of the solvent and other electron-dense materials present in the reaction solution,

especially metal salts.^{16,17} Another advantage of ceasing chiral reactions using NaBH₄ is that products in a range of time points can be prepared, isolated from electron-dense reagents, and characterized under vacuum using HAADF-STEM. Samples prepared in this way were found to be remarkably stable under an electron beam. We present in **Figure 4.4** images of products synthesized with single-crystal achiral seeds in the presence of (*S*-) BINAMINE; alongside the corresponding chiroptical spectra, this shows a clear picture of optical and structural evolution as the reaction progressed. A red-shift and increase in intensity of the CD band as chiral features develop on the particles is consistent with observations made in previous literature.⁸ Noticeable surface texture and a detectable chiroptical signature are evident in products from a reaction ceased as early as the first 15 seconds into the reaction, with a more significant chiroptical intensity corresponding to the formation of distinct wrinkles (around 30 seconds past time zero). As the *g*-factor approaches its maximum after the two-minute time point, these wrinkles become more pronounced and present over the entire particle surface. Considering the sharp decrease in the CD band intensity after the typical 30 minute duration of this reaction, we can infer that the features contributing most to the chiral signature form early and subsequently get obscured by additional growth. These conclusions are supported by electron tomography reconstructions and helicity measurements acquired at critical time points (performed by Dr. Robin Girod at the University of Antwerp (EMAT), see **Figure 4.5A**). Wrinkling with a clear directionality can be observed at the 30s time point, and these wrinkles become more distinct on particles isolated 120s after time zero. Past this point, the chiral wrinkles become disordered by continued overgrowth, as can be seen at the 300s time point. Following a helicity analysis of the reconstructions (performed in a similar manner to that described in **Chapter II** and **Chapter III**), a clear connection between the maximum *g*-factor and total helicity at each time point was observed (**Figure 4.5B**).

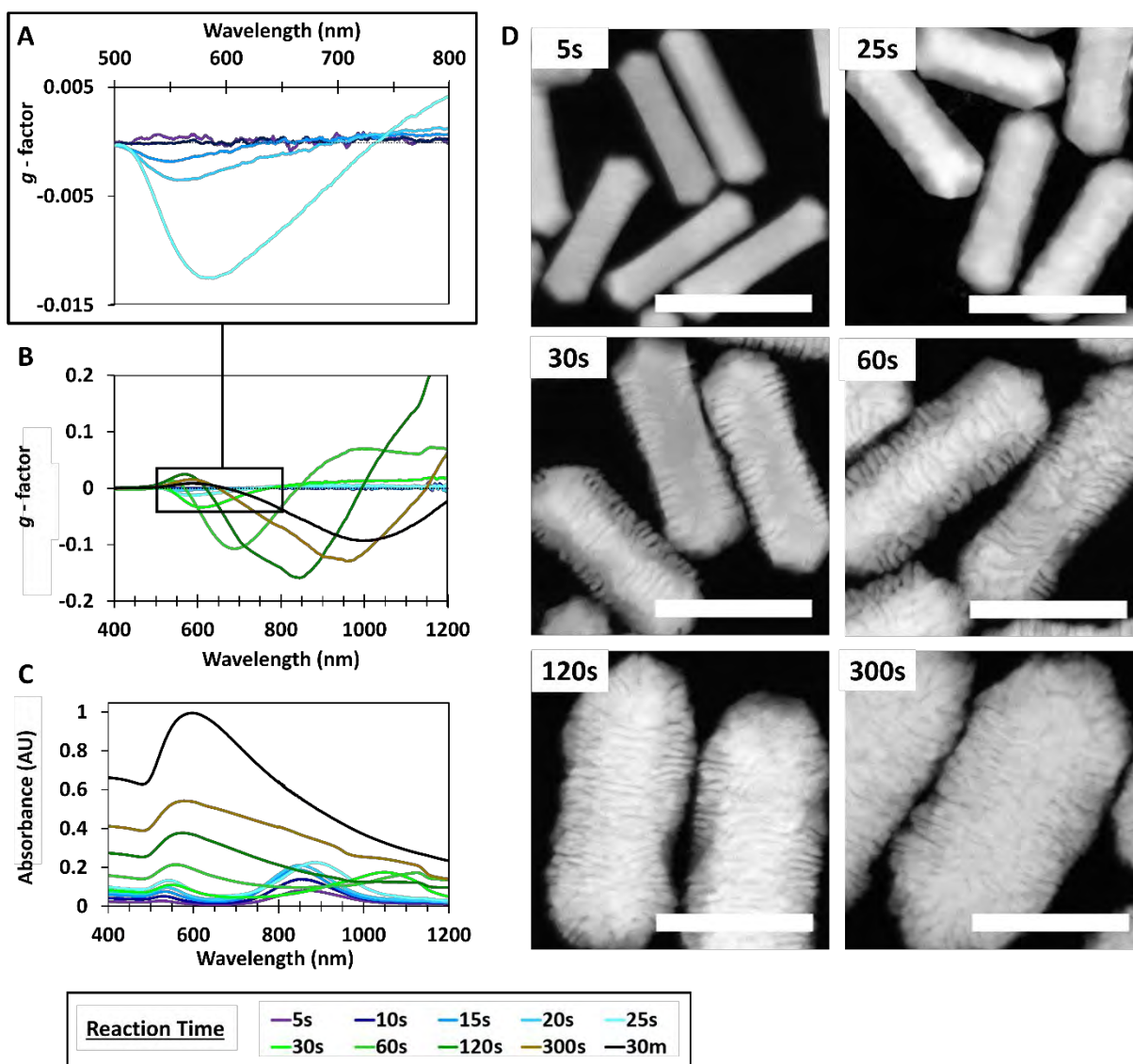


Figure 4.4. Dissymmetry factor (A,B) and extinction spectra (C) of isolated (*S*-) BINAMINE-induced chiral products, prepared using single-crystal achiral seeds and ceased by NaBH₄ at different time intervals after the reaction has been initiated. For dissymmetry factor plots, early time intervals (5s – 25s) are shown in (A), while the full range is shown in (B). HAADF-STEM images (D) correspond to spectra of NaBH₄-ceased chiral reactions; scale bars = 100 nm.

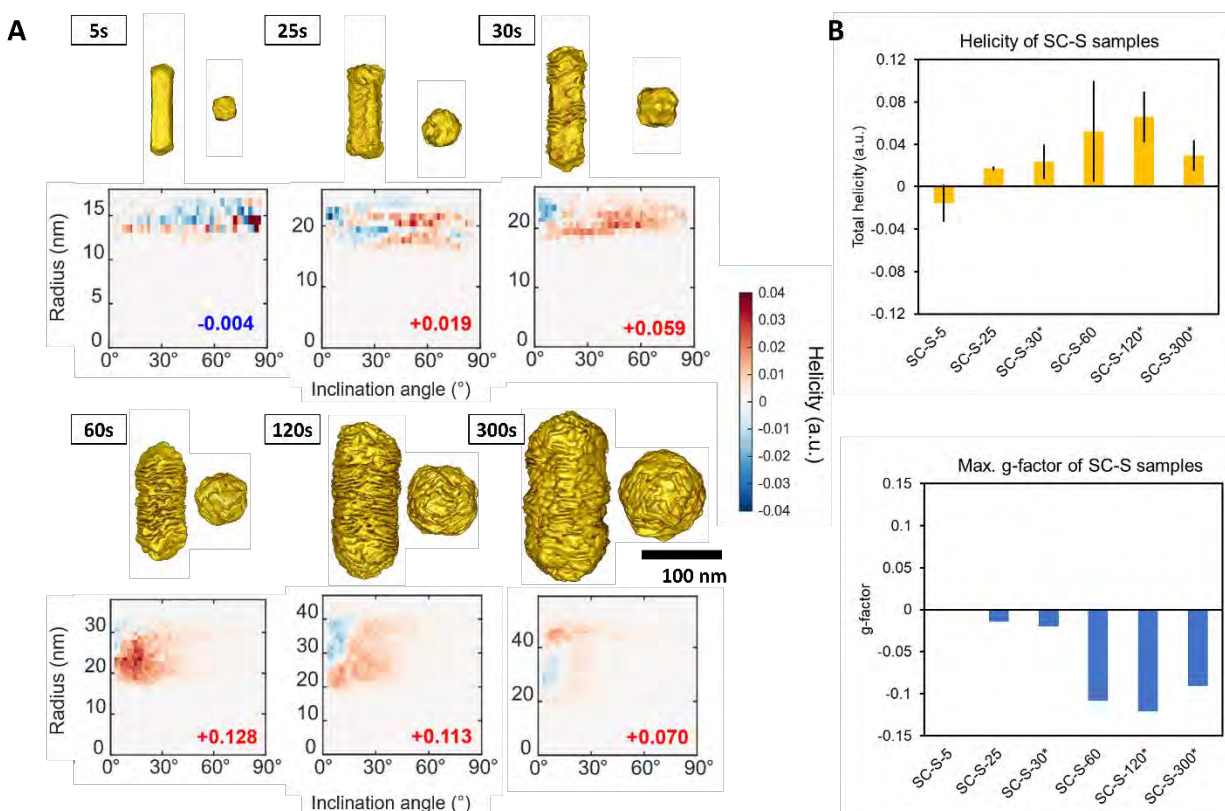


Figure 4.5. (A) Electron tomography reconstructions and associated helicity plots of a time-resolved series using NaBH_4 to cease chiral reactions induced by *S*-BINAMINE and using single-crystal achiral seeds. Electron tomography reconstructions are representative of samples at each time point. (B) Total helicity of particles from each time point in the series, and corresponding maximum dissymmetry factor of the respective colloidal samples.

4.6 Time-resolved evolution of BINAMINE chiral products (PT-AuNRs)

Upon testing this time-resolved analysis protocol on a well-documented chiral mechanism, the scope was expanded to investigate the less well understood BINAMINE-induced chiral growth on achiral pentatwinned AuNR seeds. We have previously described (see **Chapter III**) that the chiroptical response (and helicity) of chiral nanoparticles synthesized using BINAMINE and achiral pentatwinned seeds are inverted, compared to similar reactions prepared with single-crystal achiral seeds¹⁸. The mechanism for this phenomenon is unknown, but the aforementioned approach with NaBH_4 provides a useful tool with which to further investigate this phenomenon. A

similar time-resolved series as demonstrated with single-crystal achiral seeds was prepared with pentatwinned achiral seeds (**Figure 4.6**), keeping the proportions of all chemical reagents constant, including the NaBH_4 used to cease the reactions. An important detail regarding the chiroptical spectra and associated HAADF-STEM images here is the more rapid evolution of the chiroptical intensity and wrinkled surfaces on particle bodies, as compared to the series using single-crystal seeds. A much swifter chiroptical maximum is reached, from particles isolated at 30 seconds after time zero. The corresponding image at this time point shows particles with more developed wrinkling than products obtained using single-crystal seeds isolated at a similar time point. Alongside the previous observations, electron tomography reconstructions and helicity analysis provide supporting evidence for a more rapid micelle-directed evolution occurring on pentatwinned achiral seeds compared to that occurring on single-crystal achiral seeds. Deep, directional wrinkles in samples assessed at these early time points are also observed; at later time points, the wrinkles appear to lose definition and organization, in agreement with the decreased dissymmetry factor in these samples (**Figure 4.7A**). The maximum helicity (in this case, of opposite sign to the chiral products using single-crystal achiral seeds) is achieved from time points 20-60s into the reaction; this coincides well with the time at which the maximum chiroptical signature is observed (**Figure 4.7B**). Interestingly, although the total helicity of these wrinkles at its maximum is similar to that of chiral products synthesized with single-crystal achiral seeds (around ± 0.08 in both cases; achieved for PT products at 20s and for SC products at 120s), the maximum dissymmetry factor for chiral products synthesized with different seeds is less comparable (0.03 for PT products at 30s, 0.12 for SC products at 120s). The most dramatic structural difference between products yielded from single-crystal and pentatwinned seeds was found at the particle tips: working from ET reconstruction data, the tips of SC products are almost

completely rounded off during a progressing chiral reaction with BINAMINE, whereas the protruding tips of PT products persist for several minutes into a similar reaction. The influence of tip shape on the magnitude of the total helicity and dissymmetry factor of chiral products remains to be investigated in further detail.

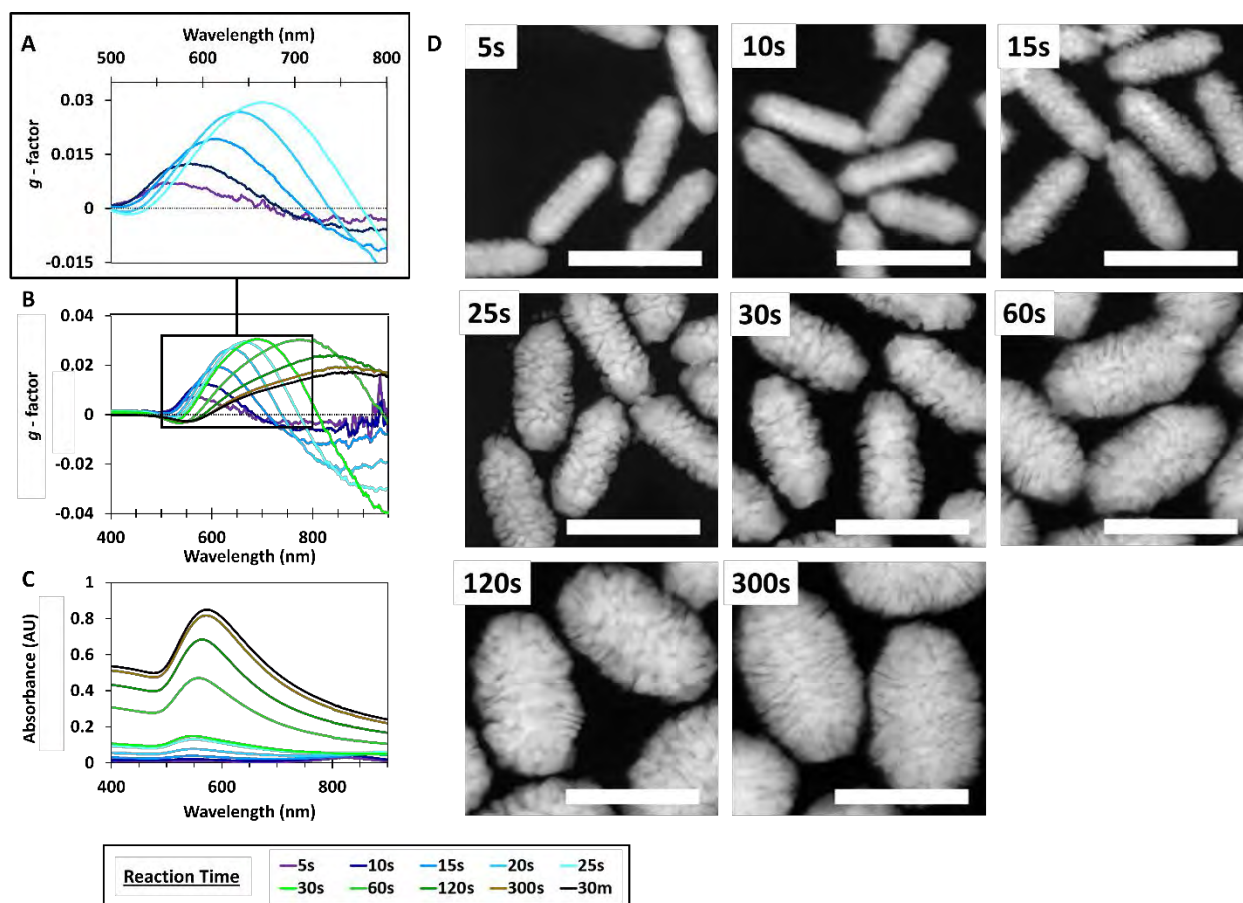


Figure 4.6. Dissymmetry factor spectra (A,B) and absorbance spectra (C) of isolated (*S*-) BINAMINE chiral products prepared with pentatwinned achiral seeds and ceased by NaBH₄ at different time intervals after the reaction was initiated. For dissymmetry factor plots, early time intervals (5s – 25s) are shown in (A), whereas the full range is shown in (B). HAADF-STEM images (bottom-right) correspond to spectra of NaBH₄-ceased chiral products; scale bars: 100 nm.

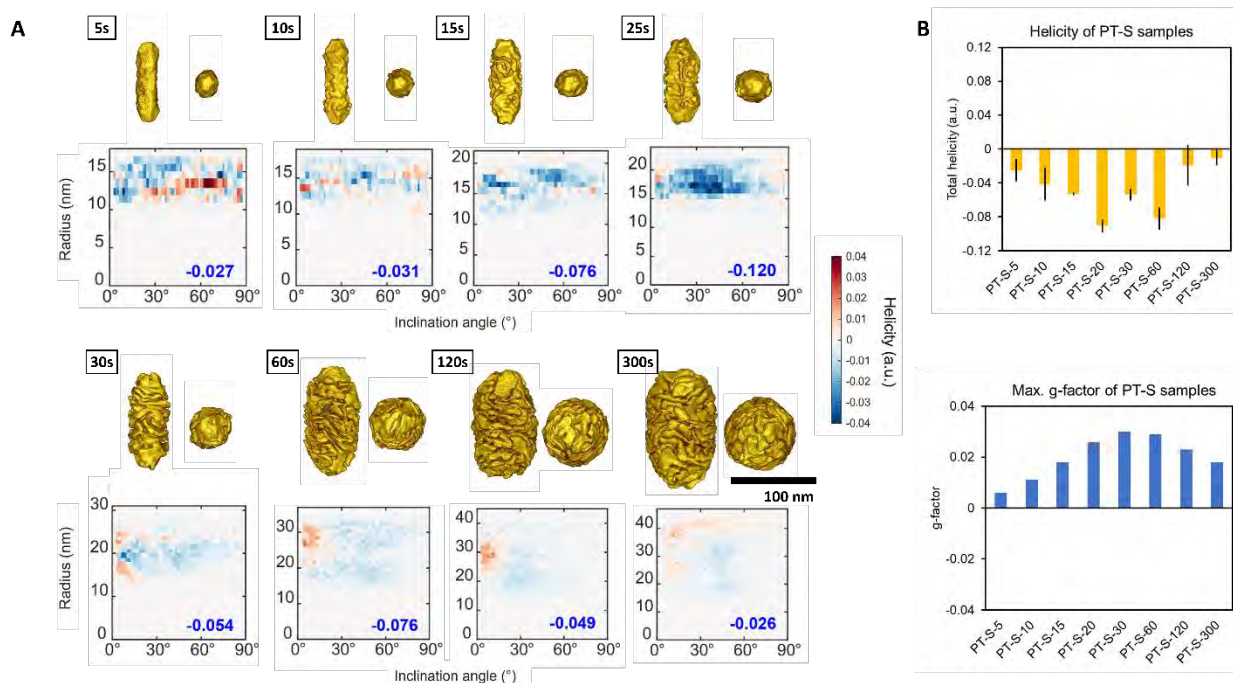


Figure 4.7. (A) Electron tomography reconstructions and associated helicity plots of a time-resolved series using NaBH_4 to cease chiral growth induced by *S*-BINAMINE on pentatwinned achiral seeds. Electron tomography reconstructions are shown for one particle representative of samples at each time point (as labeled). (B) Average total helicity of two particles from each time point in the series, and corresponding maximum dissymmetry factor of the respective colloidal samples.

4.7 Conclusions

The ability to fully characterize products at a series of time points during the course of chiral growth reactions is valuable to better understand the variety of complex mechanisms for chiral growth on nanoparticles. In this work, we verify and apply a method to cease chiral reactions in progress using NaBH_4 . This method was tested against *in situ* results from a chiral reaction prepared inside a CD instrument, to confirm the protocol works as intended and that the products obtained from each time point are comparable to those observed in real time. Treatment with NaBH_4 was found to suspend a chiral growth reaction in progress, quickly reducing the remaining

gold salts contributing to overgrowth, without affecting the larger chiral products. These products could then be isolated via centrifugation and characterized to provide a “snapshot” of the developing chiroptical signature. Products isolated from reactions ceased at different time points were found to have equivalent dissymmetry factors to those of reactions characterized *in situ*. Furthermore, products from NaBH₄-ceased reactions could be characterized by electron microscopy, an at-present insurmountable challenge *in situ*. As demonstrated with an established chiral inducer, ceasing chiral reactions with NaBH₄ may enable the comparison of the optical and structural characterization of products evolving during the course of a reaction, define property-structure relationships and better understand the underlying mechanisms for the development of particles during an overgrowth reaction. The availability of a large library of nanomaterial shapes and sizes, as well as the continued design of novel chiral inducers, increases the potential scope of this method.

4.8 References

1. Cho, N. H.; Byun, G. H.; Lim, Y.-C.; Im, S. W.; Kim, H.; Lee, H.-E.; Ahn, H.-Y.; Nam, K. T., Uniform Chiral Gap Synthesis for High Dissymmetry Factor in Single Plasmonic Gold Nanoparticle. *ACS Nano* **2020**, *14*, 3595-3602.
2. Im, S. W.; Jo, E.; Kim, R. M.; Han, J. H.; Nam, K. T., 32-Symmetric Chiral Gold Nanoplates with Near-Infrared Circular Dichroism. *Advanced Optical Materials* **2023**, *11*, 2300037.
3. Cho, N. H.; Kim, Y. B.; Lee, Y. Y.; Im, S. W.; Kim, R. M.; Kim, J. W.; Namgung, S. D.; Lee, H.-E.; Kim, H.; Han, J. H.; Chung, H. W.; Lee, Y. H.; Han, J. W.; Nam, K. T., Adenine Oligomer Directed Synthesis of Chiral Gold Nanoparticles. *Nature Communications* **2022**, *13*, 3831.
4. Cho, N. H.; Lee, H.-E.; Ahn, H.-Y.; Lee, Y. Y.; Im, S. W.; Kim, H.; Nam, K. T., Cysteine Induced Chiral Morphology in Palladium Nanoparticle. *Particle & Particle Systems Characterization* **2019**, *36*, 1900062.

5. Ahn, H.; Ahn, H.; Wy, Y.; Han, S. W., Suppressing Nanocrystal Growth with Cysteine: A Quenching Strategy for Monitoring the Evolution of Nanocrystals. *Chem. Mater.* **2023**, *35*, 10533-10541.
6. Van Gordon, K.; Baúlde, S.; Mychinko, M.; Heyvaert, W.; Obelleiro-Liz, M.; Criado, A.; Bals, S.; Liz-Marzán, L. M.; Mosquera, J., Tuning the Growth of Chiral Gold Nanoparticles Through Rational Design of a Chiral Molecular Inducer. *Nano Lett.* **2023**, *23*, 9880-9886.
7. Heyvaert, W.; Pedraza-Tardajos, A.; Kadu, A.; Claes, N.; González-Rubio, G.; Liz-Marzán, L. M.; Albrecht, W.; Bals, S., Quantification of the Helical Morphology of Chiral Gold Nanorods. *ACS Materials Letters* **2022**, *4*, 642-649.
8. Zhuo, X.; Mychinko, M.; Heyvaert, W.; Larios, D.; Obelleiro-Liz, M.; Taboada, J. M.; Bals, S.; Liz-Marzán, L. M., Morphological and Optical Transitions during Micelle-Seeded Chiral Growth on Gold Nanorods. *ACS Nano* **2022**, *16*, 19281-19292.
9. Park, K.; Drummy, L. F.; Wadams, R. C.; Koerner, H.; Nepal, D.; Fabris, L.; Vaia, R. A., Growth Mechanism of Gold Nanorods. *Chem. Mater.* **2013**, *25*, 555-563.
10. González-Rubio, G.; Mosquera, J.; Kumar, V.; Pedraza-Tardajos, A.; Llombart, P.; Solís, D. M.; Lobato, I.; Noya, E. G.; Guerrero-Martínez, A.; Taboada, J. M.; Obelleiro, F.; MacDowell, L. G.; Bals, S.; Liz-Marzán, L. M., Micelle-Directed Chiral Seeded Growth on Anisotropic Gold Nanocrystals. *Science* **2020**, *368*, 1472-1477.
11. Brust, M.; Walker, M.; Bethell, D.; Schiffrin, D. J.; Whyman, R., Synthesis of Thiol-derivatised Gold Nanoparticles in a Two-phase Liquid-Liquid system. *J. Chem. Soc., Chem. Commun.* **1994**, 801-802.
12. Gonzalez-Rubio, G.; Kumar, V.; Llombart, P.; Diaz-Nunez, P.; Bladt, E.; Altantzis, T.; Bals, S.; Pena-Rodriguez, O.; Noya, E. G.; MacDowell, L. G.; Guerrero-Martinez, A.; Liz-Marzan, L. M., Disconnecting Symmetry Breaking from Seeded Growth for the Reproducible Synthesis of High Quality Gold Nanorods. *Acs Nano* **2019**, *13*, 4424-4435.
13. Mulvaney, P.; Pérez-Juste, J.; Giersig, M.; Liz-Marzán, L. M.; Pecharromán, C., Drastic Surface Plasmon Mode Shifts in Gold Nanorods Due to Electron Charging. *Plasmonics* **2006**, *1*, 61-66.
14. Ung, T.; Liz-Marzán, L. M.; Mulvaney, P., Redox Catalysis Using Ag@SiO₂ Colloids. *The Journal of Physical Chemistry B* **1999**, *103*, 6770-6773.
15. Zhuo, X.; Vila-Liarte, D.; Wang, S.; Jimenez de Aberasturi, D.; Liz-Marzán, L. M., Coated Chiral Plasmonic Nanorods with Enhanced Structural Stability. *Chem. Mater.* **2023**, *35*, 5689-5698.

16. Chao, H.-Y.; Venkatraman, K.; Moniri, S.; Jiang, Y.; Tang, X.; Dai, S.; Gao, W.; Miao, J.; Chi, M., *In Situ* and Emerging Transmission Electron Microscopy for Catalysis Research. *Chem. Rev.* **2023**, *123*, 8347-8394.
17. Kim, J.; Kang, S.; Cheng, F.; Wang, Y.; Ye, X.; Park, J., Recent Advances in Liquid Phase Transmission Electron Microscopy of Nanoparticle Growth and Self-Assembly. *MRS Bull.* **2024**, *49*, 365-376.
18. Van Gordon, K.; Ni, B.; Girod, R.; Mychinko, M.; Bevilacqua, F.; Bals, S.; Liz-Marzán, L. M., Single Crystal and Pentatwinned Gold Nanorods Result in Chiral Nanocrystals with Reverse Handedness. *Angew. Chem. Int. Ed.* **2024**, *63*, e202403116.

Chapter V – Outlook: Engineering Hierarchical, Multi-Scale Chirality

As the field of biomimetic chiral nanoplasmonics has progressed, the library of synthesized chiral morphologies has greatly expanded. If we are to use nature as a guide, we should endeavor to emulate in synthetic structures how chirality manifests in the natural world (*e.g.* DNA, polysaccharides, and proteins), as chiral complex biomolecules comprised of chiral constituents. Although strategies abound for the assembly of such hierarchically ordered structures, most are outside the scope of this thesis, which is focused on the “bottom-up” production of inherently chiral nanomaterials. Using the research approaches developed in previous chapters, we delve here into the potential engineering of hierarchical, multi-scale chirality on colloidal nanoparticles. Ongoing projects include the use of the novel chiral inducer LipoCYS to mediate the controlled growth of helicoid-like particles, which was observed to be drastically affected by the presence of different surfactants. The production of colloidal products possessing “double-chirality” was additionally explored, by using chiral products of the chemically-induced chiral growth mechanism as seeds for a subsequent growth reaction under the micelle-directed growth mechanism. Electron tomography and helicity characterization as performed in the previous chapters were ideal tools for examination of the contrasting core-shell helical features of these products.

5.1 Introduction

The focus of the preceding chapters has been on the synthetic expression of chirality at the scale of nanoparticles: optimizing dissymmetric growth by reduction of gold salts onto achiral seeds, to produce particle geometries with an overriding directionality. However, chirality as it appears in the natural world is often of a hierarchical makeup, expressed across multiple size scales.¹ For example, β -D-glucose is the monomer of cellulose, which is a component of all plants; the cellular structure of climbing plants like okra or cucumber is an assembly of cellulose into helical microbundles, which further assemble into coiling tendrils² (see **Figure 5.1**).

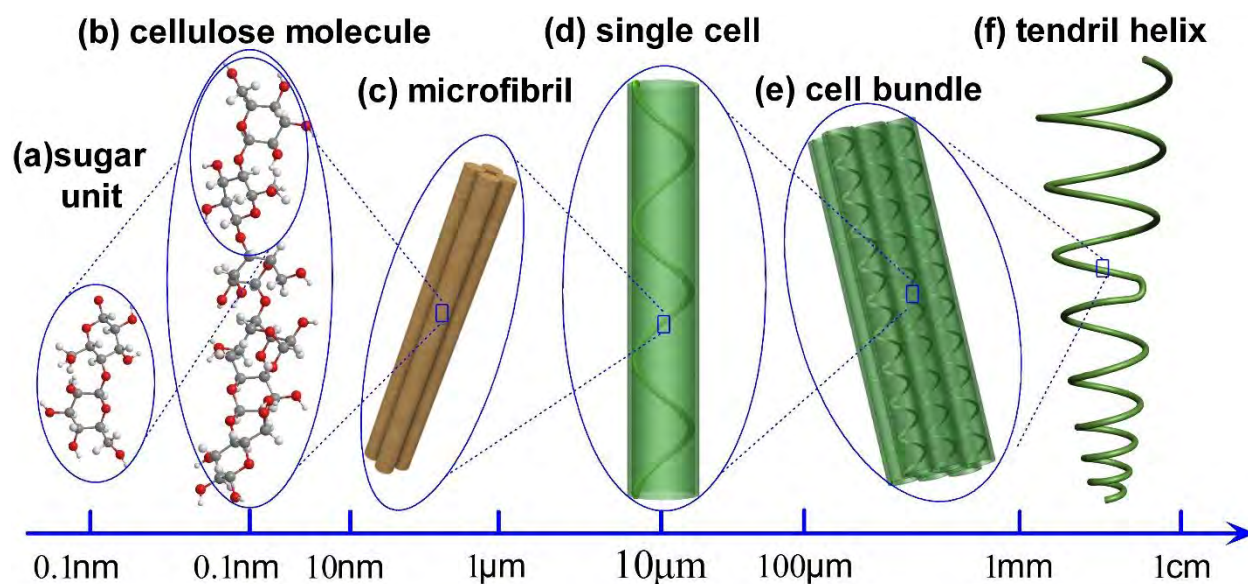


Figure 5.1. Chirality at a range of size scales presented by the compositional makeup of *Luffa acutangular* (Chinese okra). Adapted from ref. 2.

Furthermore, the spiral shells of pteropods are helical arrangements of fibers comprised of aragonite, which itself has a chiral crystalline structure.³ Across the building blocks of life,

hierarchical, multi-scale chirality appears: in the double helix of DNA, the polysaccharide chains of complex sugars, and the primary and secondary structures of proteins. A biomimetic rationale has thus motivated the production of synthetic structures with hierarchical chirality by the scientific community. A prominent example in the literature is the folding of DNA to impart secondary and tertiary structure, referred to colloquially as DNA origami.⁴⁻⁶ The predictability of nucleotide base-pairing combined with the emergence of advanced design algorithms⁷ enables the synthesis of DNA structures with extraordinary complexity, and the straightforward and precise incorporation of plasmonic nanomaterials. Owing to this latter point, these systems are ideal for the optimization of plasmonic “hot-spots” and are used primarily as SERS sensors⁸⁻¹⁰ (see **Chapter I**), but also have tremendous potential for the construction of plasmonic nanosystems with multi-scale chirality. An approach more similar to the context of the work presented in this thesis is the arrangement of smaller chiral components into hierarchically ordered particles¹¹ (**Figure 5.2**) As demonstrated by the helical micelles directing chiral growth in **Chapter III** and **Chapter IV**, the components of an arrangement with hierarchical chirality need not be entirely chiral; the achiral CTAC molecules follow the handedness of BINAMINE in a so-called “sergeants and soldiers” manner.¹²⁻¹⁴ The self-assembly of chiral structures from anisotropic constituents has been covered extensively by literature deriving from our group,^{15,16} and the factors mediating the controlled agglomeration of chiral components are similar: the presence of surfactant, chiral molecules,¹⁷ or the application of circularly polarized light,¹⁸ to be discussed in a later section.

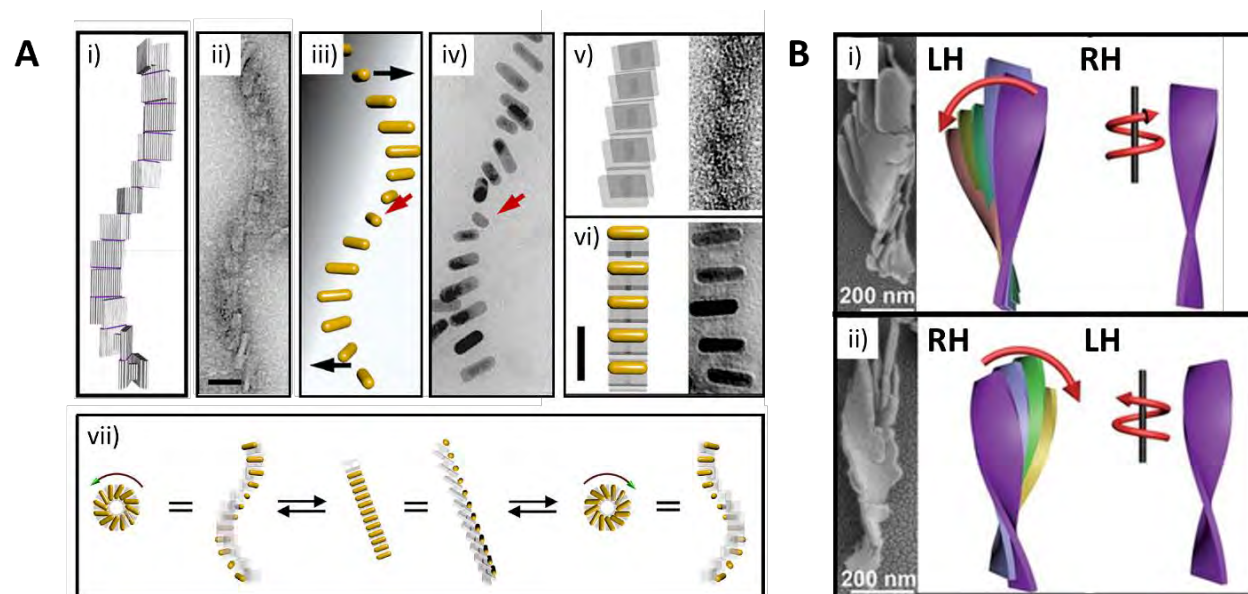


Figure 5.2. (A) DNA origami helical superstructure comprised of H-shaped components locked into a V configuration by interconnecting DNA linkers (schematic in i, TEM image in ii). Incorporated AuNRs followed the left-handed directionality of the helix (schematic in iii, TEM image in iv). In the absence of interconnecting DNA linkers, the H-shaped components assumed a relaxed achiral superstructure (schematic in v, TEM image in vi) which could be manipulated into a helical superstructure of either handedness by reintroducing different interconnecting DNA linkers (vii). Scale bars = 50 nm. (B) SEM images and schematic illustrations of hierarchically ordered particles comprised of Au nanoplatelets in the presence of *L*-cys (i) and *D*-cys (ii). Note that the handedness of the superstructures are inverted compared to the individual components. Adapted from ref. 4 and 11.

Considering that the precedent for synthesizing inherently chiral nanoparticles with hierarchical chirality is limited, a roadmap for the investigation of novel chiral morphologies and the associated growth mechanisms is laid out by the content of this thesis. In this chapter, we first consider an example of products formed with multi-scale chirality during initial investigations with LipoCYS in **Chapter II**; we then apply this chiral inducer to a protocol known to yield helicoids with multi-scale chirality (typically using cysteine or glutathione). This combinatorial approach was aimed to generating interesting nanoparticle morphologies with hierarchical chirality.

Next, following observations made in **Chapter III**, we again investigated the symmetry of the starting seeds as a variable, this time by using chemically-induced chiral products as seeds in a subsequent micelle-directed chiral reaction. Assuming that the geometrical handedness of the chiral seeds would be conserved following overgrowth, this approach presented the opportunity to form and study “double-chirality” products possessing both twisted and wrinkled chiral features.

5.2 Hierarchical chiral growth mediated by LipoCYS

The [LipoCYS]-mediated structural evolution from geometrically twisted chiral products into those possessing a wrinkled helical surface (see **Chapter II**) suggests an intermediate where both chiral features are present on the same particle. An example of this was apparent during initial experimentation using LipoCYS and achiral nanorods as the starting seeds. It was observed that the chiroptical signature was inverted for chiral products prepared in the presence of a low concentration of CTAC, compared to those synthesized when the concentration of CTAC was raised (**Figure 5.3A**). Further characterization via HAADF-STEM and electron tomography (the latter performed by Mikhail Mychinko at EMAT) revealed these products had (along with surface wrinkles) a bowed, dumbbell-like morphology from disproportionate growth occurring at the particle tips (**Figure 5.3B,C**, bottom). As discussed in the previous chapters, there may be a strong influence of protruding facet morphology on the resulting chiroptical signature; it was hypothesized that this was responsible for the inverted chiroptical signature observed in this sample. The observation of a geometrical bowing that may contribute to the chiroptical signature alongside (or in opposition to) the surface wrinkles of products formed using LipoCYS gives rationale to its use to engineer products with multi-scale chirality under certain conditions.

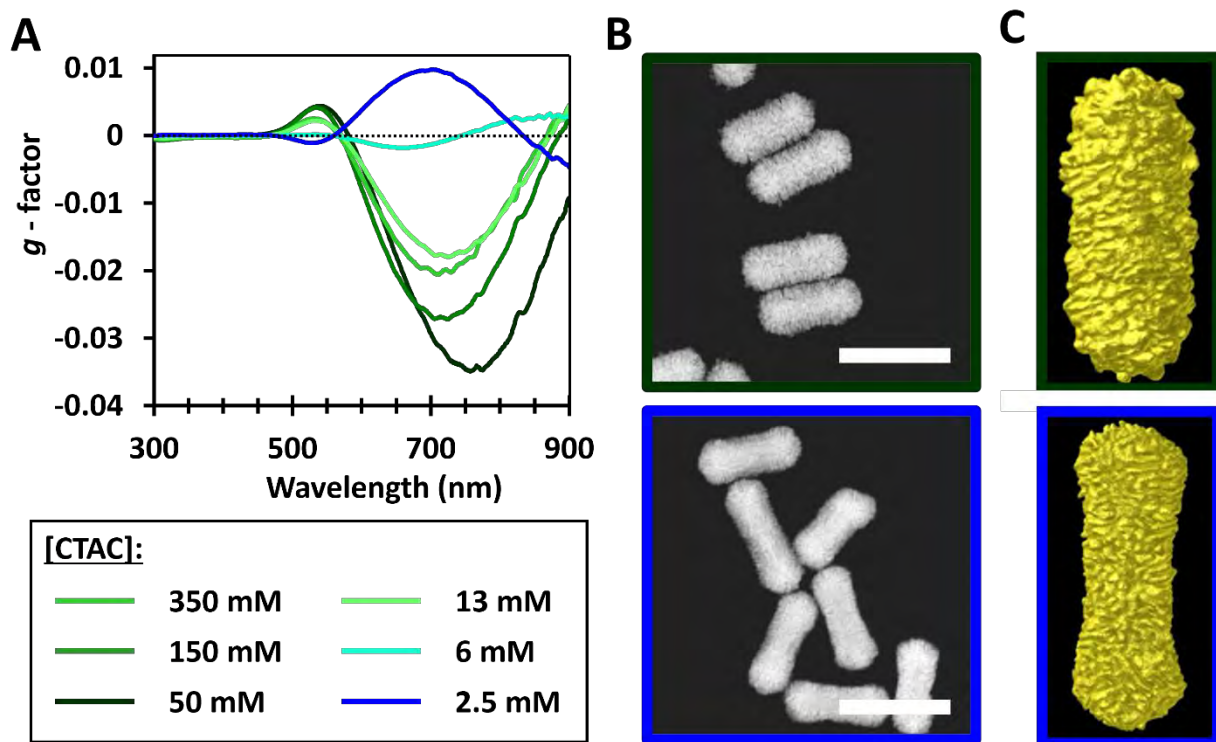


Figure 5.3. Chiroptical spectra (A) of chiral products synthesized with (*R*)-LipoCYS in the presence of a range of CTAC concentrations, as labeled (all other synthetic variables held constant). Images acquired using HAADF-STEM (B) and tomography reconstructions (C) of products with contrasting particle geometries (synthesized with 50 mM and 2.5 mM CTAC, respectively); image outlines are color-coded to match the legend of the plot. Scale bars: 200 nm. Chiral products were synthesized with 138 μM (*R*)-LipoCYS and 700 mM ascorbic acid; $[\text{Au}^{3+}]$: $[\text{Au}^0]$ was kept constant at 8.9 (185 μM and 20.8 μM , respectively).

From the literature by Prof. Nam's group at Seoul National University, we learn that helicoids synthesized in the presence of cysteine or glutathione possess chiral features with opposite handedness at the faces compared to the corners (see **Chapter I**).¹⁹⁻²¹ This is most readily apparent in Helicoid III, and is likely the cause of the enhanced intensity of its chiroptical signature compared to the other helicoids synthesized by the same group (**Figure 5.4**).^{20,22}

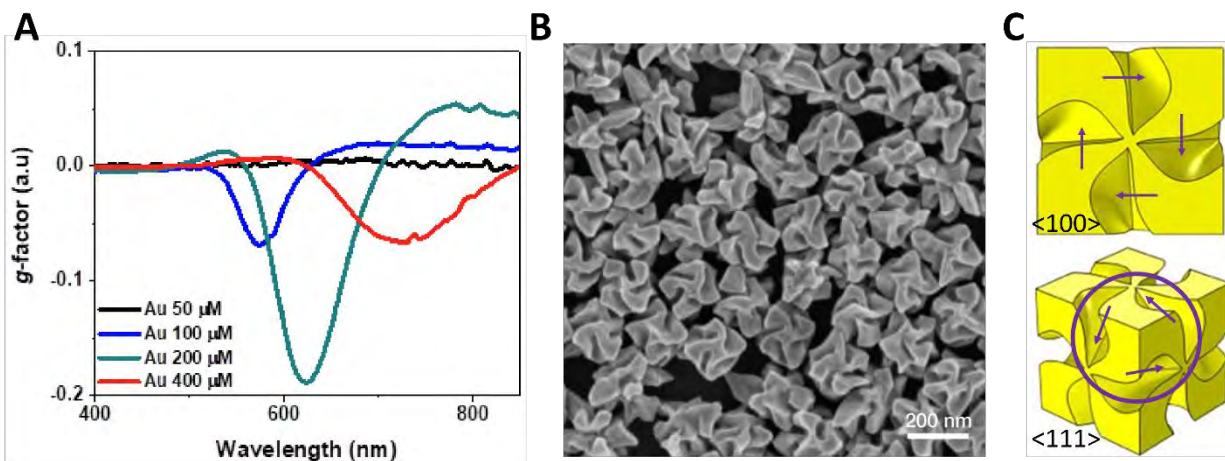


Figure 5.4. Chiroptical spectra (A) of Helicoid III synthesized with glutathione and octahedral achiral seeds at a range of Au^{3+} concentrations. An image acquired by SEM (B) and a schematic at two different viewing angles (as labeled; C) show the deep fan-like grooves in Helicoid III, which are complemented by fan-like protrusions at the corners with an opposing directionality (see arrows). Adapted from ref. 20 (© 2018 Springer Nature) and ref. 22 (© 2020 American Chemical Society).

The synthesis of helicoids using amino acids as chiral inducers has been reported to proceed more slowly²² than the chiral growth reactions discussed previously in this thesis. The reason may stem from decreased reaction temperature, a much smaller excess of ascorbic acid relative to the gold salts present in solution, and the use of CTAB as the surfactant, which has a greater affinity for gold surfaces compared to CTAC.²³ With the intent of exploring multi-scale chirality in the context of LipoCYS and helicoid-like chiral products, we used similar synthetic conditions to Helicoid III (see **Chapter VI** for details), achiral octahedral seeds, and a range of LipoCYS concentrations. Chiral products were initially evaluated using CD spectroscopy and scanning electron microscopy (SEM performed by In Han Ha at SNU). Similar to the chiral NR products resulting from LipoCYS-mediated reactions discussed in **Chapter II**, a LipoCYS concentration-dependent red-shift and intensification of the maximum chiroptical peak was observed, with a corresponding sharpening of the chiral features on the helicoid-like products (see **Figure 5.5**).

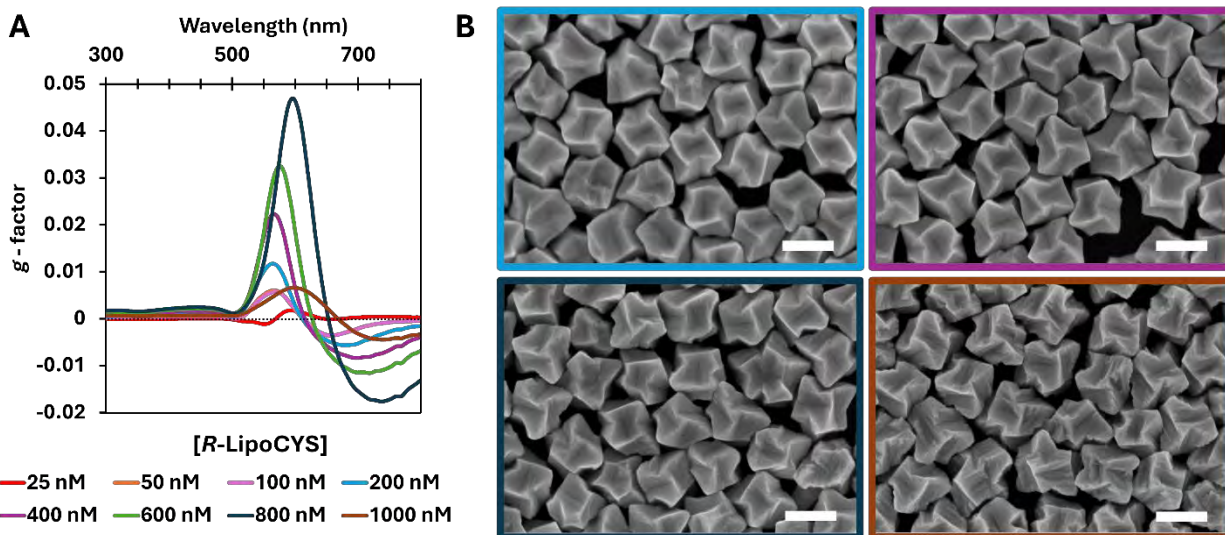


Figure 5.5. Circular dichroism (g -factor) spectra (A) and corresponding SEM images (B) for helicoid-like chiral products prepared in the presence of CTAB and different (R)-LipoCYS concentration, as labeled. Image outlines are color-coded to match the legend of the plots. Scale bars: 200 nm.

However, the effective concentration of LipoCYS for these experiments was in the nanomolar range (max $g = 0.047$ at 597 nm, from products synthesized with 800 nM LipoCYS); this opposed the range prescribed for AuNRs in **Chapter II**, which was firmly in the micromolar range (max $g = 0.066$ at 720 nm, from products synthesized with 90 μM LipoCYS). Furthermore, a steep decrease in the intensity of the maximum chiroptical peak was observed for products synthesized in the presence of 1000 nM (1 μM) LipoCYS; these particles possessed a roughened surface topography compared to the others imaged. To more closely investigate the surface features of these products, electron tomography was performed by Dr. Robin Girod and Dr. Mikhail Mychinko at the University of Antwerp (EMAT). This characterization revealed the formation of smaller features of a clear helical character that became better defined at higher concentrations of LipoCYS (see **Figure 5.6**). As the concentration of LipoCYS is increased further, these protruding features

begin to dominate the overall handedness of the particle structure, perhaps explaining their intense chiroptical signature.

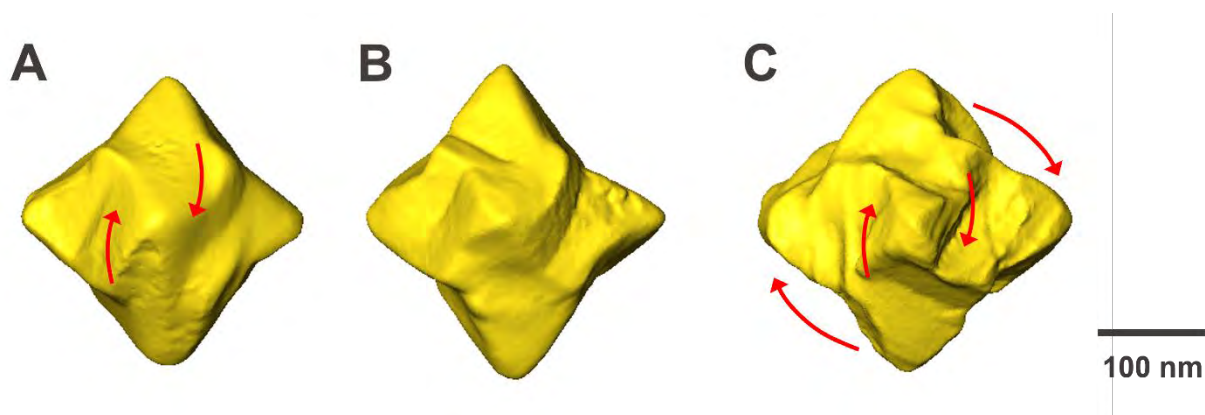


Figure 5.6. Electron tomography reconstructions of helicoid-like chiral products prepared in the presence of CTAB and different [(*R*)-LipoCYS]: 200 nM (A), 400 nM (B), and 800 nM. Note the increasingly apparent directionality of protruding facets as [LipoCYS] is raised, which envelops the directionality of the particles as a whole at higher [LipoCYS].

To study the effect of the surfactant on the products of this synthesis, a similar series of reactions were prepared with CTAC replacing CTAB (**Figure 5.7**). Though lower in intensity, the chiroptical signatures of helicoid-like products synthesized at comparable (nanomolar) concentrations of LipoCYS and in the presence of CTAC were inverted in sign (max $g = -0.006$ at 548 nm, from products synthesized with 1000 nM LipoCYS). Although a steep decrease in the intensity of the maximum chiroptical peak was also observed when the concentration of LipoCYS was increased, using a micromolar concentration of LipoCYS in the synthesis yielded rounded, roughened particles with a significant and red-shifted chiroptical signature.

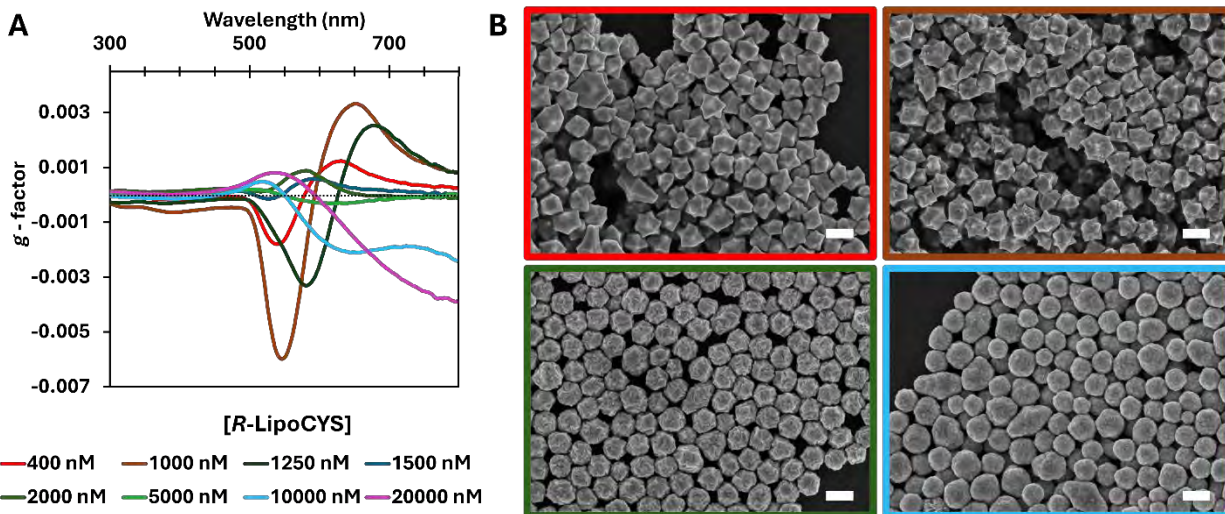


Figure 5.7. Circular dichroism (g -factor) spectra (A) and corresponding SEM images (B) for helicoid-like chiral products prepared in the presence of CTAC and different $[(R)\text{-LipoCYS}]$, as labeled. Note the higher polydispersity at high $[\text{LipoCYS}]$. Image outlines are color-coded to match the legend of the plots. Scale bars: 200 nm.

Even though it is difficult to confirm from the associated SEM image, we propose that this chiral response derives from either the complex surface texture on these particles or the polydispersity present in the sample. Electron tomography characterization of a sample synthesized using CTAC and 400 nM LipoCYS showed particles with weakly helical features and revealed the presence of different particle morphologies in the same sample, indicating that the choice of surfactant may affect the monodispersity of these products as well (see **Figure 5.8**).

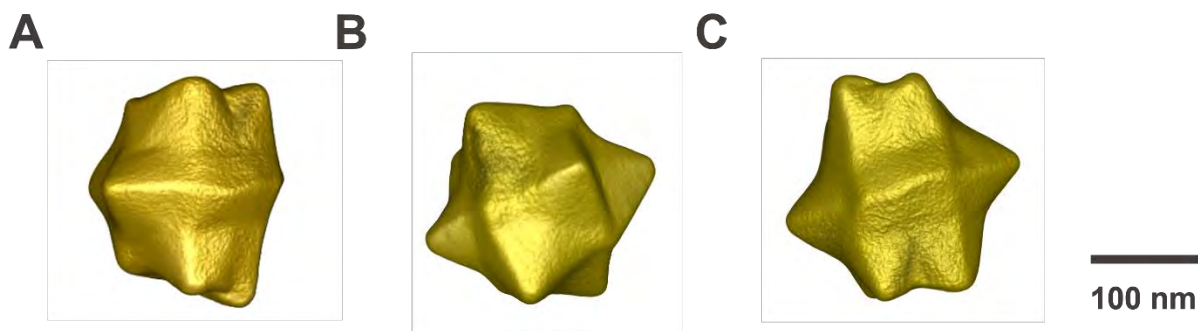


Figure 5.8. Electron tomography reconstructions of helicoid-like chiral products prepared in the presence of CTAC and 400 nM (*R*)-LipoCYS. Note the differing morphologies of particles from the same sample.

In this work, we sought to harness the potential for engineering multi-scale chirality from LipoCYS and apply it to a well-established protocol for the synthesis of helicoids with multi-scale chirality. Though products appeared helicoid-like and were found to present smaller helical features that became more prominent and encompassing as the chiroptical signature intensified, more detailed analysis of the symmetry and chirality at different scales of these products is necessary. The effects of surfactant in the context of the development of different chiral features remains to be fully understood. More investigation is warranted into chiral reaction kinetics and growth mediated by the presence of different factors, including the choice of surfactant, other chemical additives, and temperature.

5.3 “Double-chirality”: chiral growth using chiral nanoparticles as seeds

With the geometry of the starting seeds being highly influential towards the chiroptical signature of products of chiral reactions,^{24,25} and the observation that the symmetry of the starting seeds is conserved in chiral products²⁶ (see **Chapter II**), we considered the use of chiral products as seeds in a subsequent chiral growth reaction to generate particles with hierarchical chirality. To this end, different seeds and reactions were proposed, *e.g.* the use of geometrically twisted nanorods (produced using the chemically-induced mechanism) as seeds in micelle-directed chiral reactions, to give rise to products possessing core-shell chiral features (**Figure 5.9**).



Figure 5.9. Schematic of general approach to form “double-chirality” products. Starting achiral gold nanorods are first subjected to the chemically-induced chiral growth mechanism, using cystine to produce chiral products with a smooth twisted morphology. These products are then isolated and subjected to a subsequent micelle-directed chiral reaction mediated by BINAMINE, forming helical wrinkles in a “shell” that surround the smooth chiral “core”.

The synthetic details are outlined in the following: first, twisted chiral particles were produced (by Prof. Bing Ni, working at the University of Konstanz) using the stepwise chemically-mediated method detailed in **Chapter III** and **Chapter VI**. Next, these products were isolated by centrifugation and used as seeds for micelle-directed chiral reactions with both enantiomers of BINAMINE, according to the method detailed in **Chapter III** and **Chapter VI**. The concentration

of gold salts (Au^{3+}) for these reactions was kept constant at 100 μM , and different amounts of chiral seeds (Au^0) were used to test a selected range of $[\text{Au}^{3+}] : [\text{Au}^0]$ ratios; “double-chirality” products were initially evaluated by CD spectroscopy and HAADF-STEM (**Figure 5.10**). A general observation from the spectral data is that the magnitude of the peak chiroptical signature follows the directionality of the chiral seeds used (irrespective of the handedness of chiral inducer used in these reactions): positive for left-handed seeds (synthesized with *D*-cys) and negative for right-handed seeds (synthesized with *L*-cys). Also, there is a red-shift of the chiroptical signature as the $[\text{Au}^{3+}] : [\text{Au}^0]$ is increased (irrespective of the handedness of chiral seed used in these reactions), which is consistent with previous results using achiral seeds (**Chapter II**).

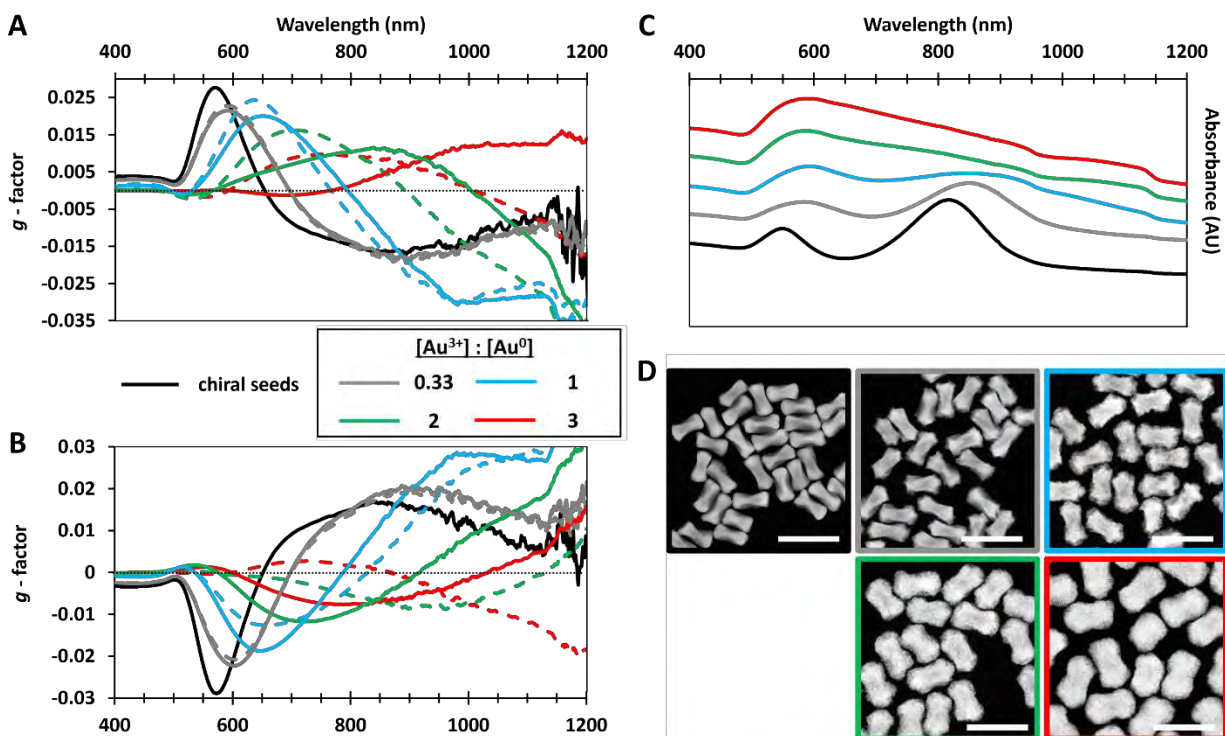


Figure 5.10. Circular dichroism (g -factor) spectra of “double-chirality” products prepared using BINAMINE, at varying $[\text{Au}^{3+}] : [\text{Au}^0]$ ratio, and left-handed (A) or right-handed (B) chiral seeds (synthesized using D -cys and L -cys, respectively). Solid and dashed lines refer to particles synthesized with S -BINAMINE and R -BINAMINE, respectively. Spectra from chiral seeds alone is indicated in black. Absorbance spectra (C) and corresponding HAADF-STEM images (D) for “double-chirality” products synthesized with left-handed chiral seeds, varying $[\text{Au}^{3+}] : [\text{Au}^0]$ ratio, and R -BINAMINE. Image outlines are color-coded to match the legend of the plots. Scale bars: 200 nm.

Characterization via HAADF-STEM of a series of these chiral products helps to confirm an intuitive conclusion from the established literature:²⁷ as the $[\text{Au}^{3+}] : [\text{Au}^0]$ ratio increases and more gold salts are available to contribute to overgrowth, the aspect ratio of the chiral products decreases, the longitudinal and transverse LSPR peaks in the absorbance spectra begin to coalesce, and as a result the chiroptical signature deriving from the wrinkled features is red-shifted (and decreased in intensity, owing to excessive growth; see **Chapter IV**). From the results using left-handed particles (synthesized using D -cystine) as seeds, a further red-shift of the chiroptical

signature is observed when *S*-BINAMINE is used at high $[\text{Au}^{3+}] : [\text{Au}^0]$ ratios than when *R*-BINAMINE is used at the same $[\text{Au}^{3+}] : [\text{Au}^0]$ ratio. Likewise, when right-handed particles (synthesized using *L*-cystine) are used as seeds, there is more red-shift of the chiroptical signature when *R*-BINAMINE is used at high $[\text{Au}^{3+}] : [\text{Au}^0]$ ratios than when *S*-BINAMINE is used, at the same $[\text{Au}^{3+}] : [\text{Au}^0]$ ratio. We can infer from these general observations that such discrepancies in peak position derive from different particle growth. We hypothesize that differences in particle growth occur because the chiral micellar template formed by BINAMINE and CTAC adsorbs more readily onto the surface of seeds of a similar handedness, promoting more organized growth during the chiral reaction. To investigate this hypothesis and explore whether the core dissymmetry of the chiral seeds is conserved after “double-chirality” reactions, we again turn to electron tomography and helicity analysis performed by Dr. Robin Girod and Dr. Mikhail Mychinko at EMAT (University of Antwerp). From 3D electron tomography reconstructions, the twist of left-handed chiral seeds (synthesized with *D*-cys) is still partially visible even after overgrowth (mediated by *R*-BINAMINE) at high $[\text{Au}^{3+}] : [\text{Au}^0]$ ratio (**Figure 5.11A**). The conservation of the chiral core geometry is even more apparent from selected orthoslices (**Figure 5.11B**).

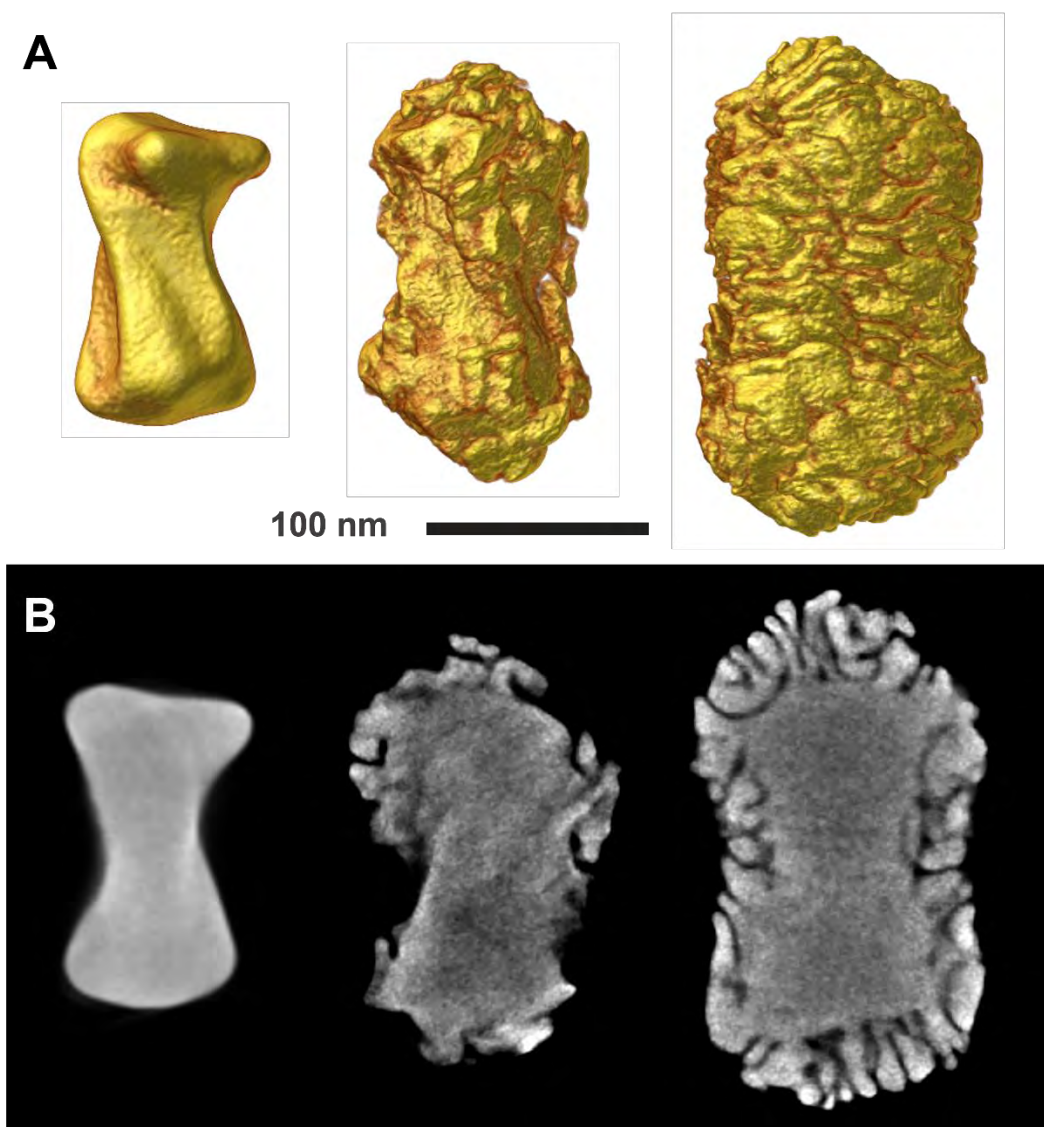


Figure 5.11. Electron tomography reconstructions (A) and selected orthoslices (B) of a left-handed chiral seed synthesized with *D*-cys (left), a left-handed chiral seed treated with *R*-BINAMINE at a $[\text{Au}^{3+}] : [\text{Au}^0] = 1$ (middle), and a left-handed chiral seed treated with *R*-BINAMINE at a $[\text{Au}^{3+}] : [\text{Au}^0] = 3$ (right).

The handedness of the core-shell geometry of “double-chirality” products was evaluated by a helicity analysis method similar to that discussed in **Chapter I**. A contrast in core-shell helicity is evident in the particles synthesized at a high $[\text{Au}^{3+}] : [\text{Au}^0]$ ratio; mostly negative helicity was observed at low radius ρ (indicating a left-handed core), whereas the handedness of the helicity at

high ρ (the shell; the helical wrinkles) is influenced by the enantiomer of BINAMINE used in the synthesis (**Figure 5.12**). As observed in previous work (see **Chapter III**), the handedness of formed helical wrinkles is opposite to that of the enantiomer of BINAMINE used; in the case of *S*-BINAMINE, right-handed wrinkles with positive helicity values are formed in the shell (at high ρ). However, the total helicity values of both particles here were found to be negative (left-handed), indicating that the handedness of the core has a greater influence than the shell on the overall helical directionality of the “double-chirality” products. This was also found to be true of “double-chirality” products synthesized at a low $[\text{Au}^{3+}] : [\text{Au}^0]$ ratio (**Figure 5.13**); the handedness of the total helicity of each product followed that of the chiral seed used. Furthermore, the helicity of the shell was observed to greatly increase when the handedness of the chiral inducer and the core match; this evidence supports the templating hypothesis mentioned above.

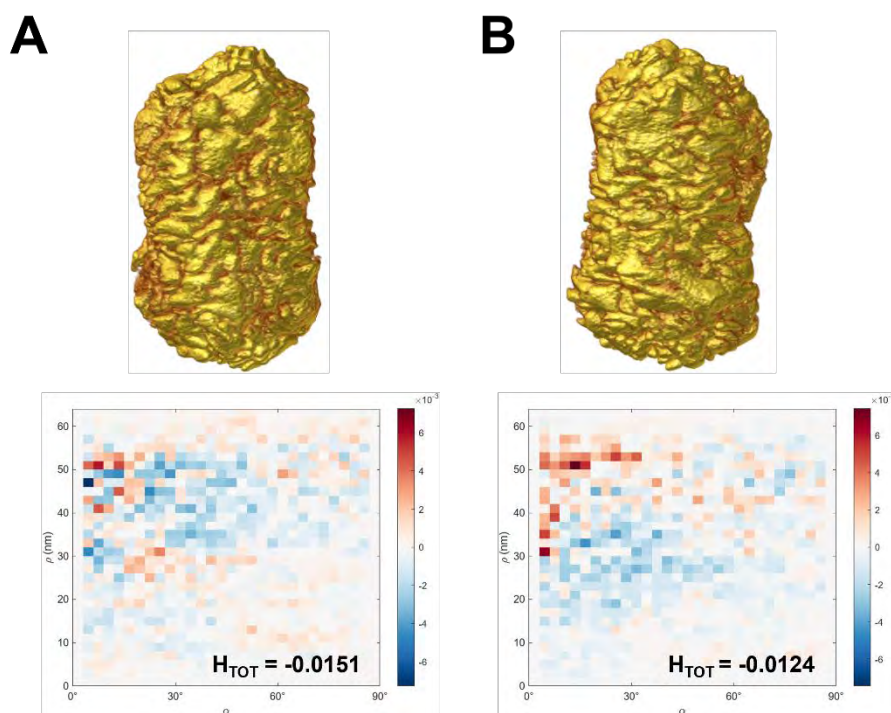


Figure 5.12. Electron tomography reconstructions (top) and corresponding helicity analysis (bottom) of a left-handed chiral seed (synthesized with *D*-cys) reacted at $[\text{Au}^{3+}] : [\text{Au}^0] = 3$, in the presence of *R*-BINAMINE (left) or *S*-BINAMINE (right).

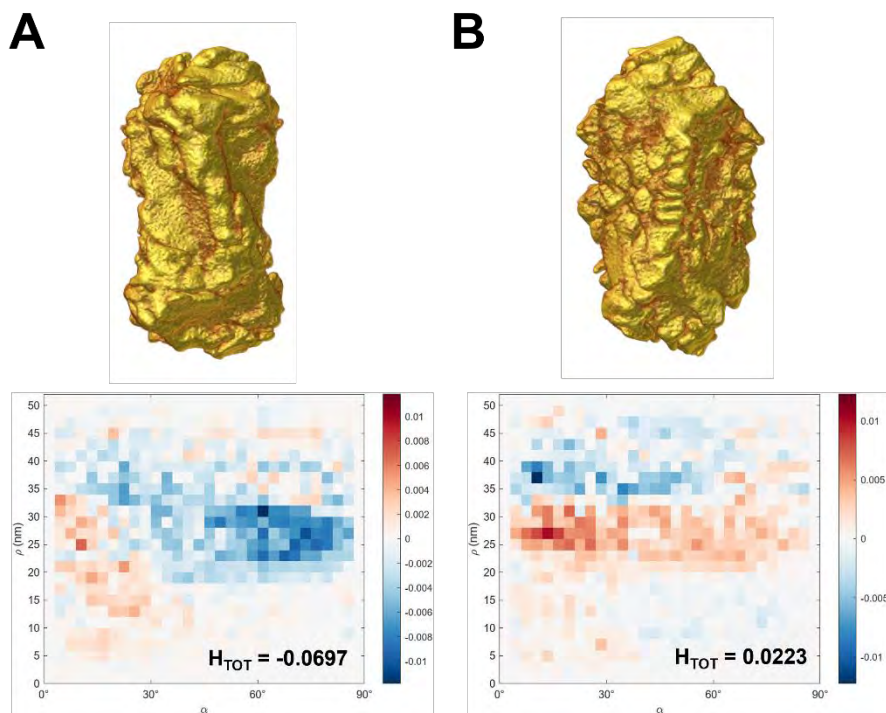


Figure 5.13. Electron tomography reconstructions (top) and corresponding helicity analysis (bottom) of left-handed (A) or right-handed (B) chiral seeds (synthesized with *D*-cys or *L*-cys, respectively) reacted at $[\text{Au}^{3+}] : [\text{Au}^0] = 1$ in the presence of *R*-BINAMINE.

The small number of particles analyzed here and the counterintuitive total helicity values prevent our conclusions from becoming definitive. Further investigation is required, using electron tomography and helicity analysis to reveal relationships between the core particle and the evolving surface tomography in “double-chirality” reactions. A focus on the intermediate structures formed, potentially enabled by the time-resolved protocol discussed in **Chapter IV**, would yield useful information in this regard.

5.4 Conclusions

In applying an abridged form of the experimental approaches featured in this thesis to the outlook, we highlight the rationale for this work in the present and future tense. Through creative use of the novel chiral inducer (LipoCYS) introduced in **Chapter II**, we synthesized helicoid-like particles with hierarchical chiral features and observed an evolving interplay between these features of different scales when different concentrations of LipoCYS were used. We also demonstrated a surfactant-dependent effect on the magnitude of the chiroptical signature of these products, which adds further depth to the synthetic toolbox used to tune the properties of chiral nanoparticles. Secondly, we carried forward a major lesson from **Chapter III**: expecting the core symmetry of a chiral seed to be conserved in a subsequent chiral reaction, we were able to reproducibly obtain core-shell particles expressing contrasting “double chirality”. Our investigation of these particles revealed important information about the relative contribution of different chiral features on particles to the overall chiroptical signature, but much more analysis is needed to make any representative conclusions. Though growth of the “shell” on these products was controlled by varying the gold salts : chiral seeds ratio, the progression of chiral growth on “double-chirality” products might be better monitored by implementing the time-resolved protocol introduced in **Chapter IV**. Future approaches to understand and optimize the production of particles expressing multi-scale chirality may permit us to progress ever so incrementally towards the synthesis of structures that more closely align with what nature so effortlessly provides.

5.5 References

1. Cho, N. H.; Guerrero-Martínez, A.; Ma, J.; Bals, S.; Kotov, N. A.; Liz-Marzán, L. M.; Nam, K. T., Bioinspired Chiral Inorganic Nanomaterials. *Nature Reviews Bioengineering* **2023**, *1*, 88-106.
2. Wang, J.-S.; Wang, G.; Feng, X.-Q.; Kitamura, T.; Kang, Y.-L.; Yu, S.-W.; Qin, Q.-H., Hierarchical Chirality Transfer in the Growth of Towel Gourd Tendrils. *Scientific Reports* **2013**, *3*, 3102.
3. Jiang, W.; Yi, X.; McKee, M. D., Chiral Biomineralized Structures and their Biomimetic Synthesis. *Materials Horizons* **2019**, *6*, 1974-1990.
4. Schreiber, R.; Luong, N.; Fan, Z.; Kuzyk, A.; Nickels, P. C.; Zhang, T.; Smith, D. M.; Yurke, B.; Kuang, W.; Govorov, A. O., Chiral Plasmonic DNA Nanostructures with Switchable Circular Dichroism. *Nature communications* **2013**, *4*, 2948.
5. Kuzyk, A.; Schreiber, R.; Fan, Z.; Pardatscher, G.; Roller, E.-M.; Högele, A.; Simmel, F. C.; Govorov, A. O.; Liedl, T., DNA-Based Self-Assembly of Chiral Plasmonic Nanostructures with Tailored Optical Response. *Nature* **2012**, *483*, 311-314.
6. Yao, G.; Li, J.; Chao, J.; Pei, H.; Liu, H.; Zhao, Y.; Shi, J.; Huang, Q.; Wang, L.; Huang, W.; Fan, C., Gold-Nanoparticle-Mediated Jigsaw-Puzzle-like Assembly of Supersized Plasmonic DNA Origami. *Angew. Chem. Int. Ed.* **2015**, *54*, 2966-2969.
7. Veneziano, R.; Ratanalert, S.; Zhang, K.; Zhang, F.; Yan, H.; Chiu, W.; Bathe, M., Designer Nanoscale DNA Assemblies Programmed from the Top Down. *Science* **2016**, *352*, 1534-1534.
8. Dass, M.; Gür, F. N.; Kołataj, K.; Urban, M. J.; Liedl, T., DNA Origami-Enabled Plasmonic Sensing. *The Journal of Physical Chemistry C* **2021**, *125*, 5969-5981.
9. Schuknecht, F.; Kołataj, K.; Steinberger, M.; Liedl, T.; Lohmueller, T., Accessible Hotspots for Single-Protein SERS in DNA-Origami Assembled Gold Nanorod Dimers with Tip-To-Tip Alignment. *Nature Communications* **2023**, *14*, 7192.
10. Mosquera, J.; Zhao, Y.; Jang, H.-J.; Xie, N.; Xu, C.; Kotov, N. A.; Liz-Marzán, L. M., Plasmonic Nanoparticles with Supramolecular Recognition. *Adv. Funct. Mater.* **2020**, *30*, 1902082.

11. Jiang, W.; Qu, Z.-b.; Kumar, P.; Vecchio, D.; Wang, Y.; Ma, Y.; Bahng, J. H.; Bernardino, K.; Gomes, W. R.; Colombari, F. M.; Lozada-Blanco, A.; Veksler, M.; Marino, E.; Simon, A.; Murray, C.; Muniz, S. R.; de Moura, A. F.; Kotov, N. A., Emergence of Complexity in Hierarchically Organized Chiral Particles. *Science* **2020**, *368*, 642-648.
12. Sang, Y.; Liu, M., Hierarchical Self-Assembly into Chiral Nanostructures. *Chem Sci* **2022**, *13*, 633-656.
13. González-Rubio, G.; Mosquera, J.; Kumar, V.; Pedraza-Tardajos, A.; Llombart, P.; Solís, D. M.; Lobato, I.; Noya, E. G.; Guerrero-Martínez, A.; Taboada, J. M.; Obelleiro, F.; MacDowell, L. G.; Bals, S.; Liz-Marzán, L. M., Micelle-Directed Chiral Seeded Growth on Anisotropic Gold Nanocrystals. *Science* **2020**, *368*, 1472-1477.
14. Ito, T. H.; Salles, A. G.; Priebe, J. P.; Miranda, P. C. M. L.; Morgon, N. H.; Danino, D.; Mancini, G.; Sabadini, E., Generation of a Chiral Giant Micelle. *Langmuir* **2016**, *32*, 8461-8466.
15. Vila-Liarte, D.; Kotov, N. A.; Liz-Marzán, L. M., Template-Assisted Self-Assembly of Achiral Plasmonic Nanoparticles into Chiral Structures. *Chemical Science* **2022**, *13*, 595-610.
16. Grzelczak, M.; Liz-Marzán, L. M.; Klajn, R., Stimuli-Responsive Self-Assembly of Nanoparticles. *Chem. Soc. Rev.* **2019**, *48*, 1342-1361.
17. Jung, I. L. J.; Lee, J.; Kwon, J.; Park, K. H.; Jung, W.; Yeom, J., Multiscale Chiral Synthesis via Self-Assembly of Achiral Nanoparticles for Next-Generation Chiral Material-Based Applications: The Role of Metal Ions as Chirality Messengers. *ACS Applied Nano Materials* **2023**, *6*, 19632-19638.
18. Kim, J.-Y.; Yeom, J.; Zhao, G.; Calcaterra, H.; Munn, J.; Zhang, P.; Kotov, N., Assembly of Gold Nanoparticles into Chiral Superstructures Driven by Circularly Polarized Light. *JACS* **2019**, *141*, 11739-11744.
19. Im, S. W.; Zhang, D.; Han, J. H.; Kim, R. M.; Choi, C.; Kim, Y. M.; Nam, K. T., Investigating Chiral Morphogenesis of Gold using Generative Cellular Automata. *Nature Materials* **2024**.
20. Lee, H.-E.; Ahn, H.-Y.; Mun, J.; Lee, Y. Y.; Kim, M.; Cho, N. H.; Chang, K.; Kim, W. S.; Rho, J.; Nam, K. T., Amino-Acid and Peptide-Directed Synthesis of Chiral Plasmonic Gold Nanoparticles. *Nature* **2018**, *556*, 360-365.

21. Lee, H.-E.; Kim, R. M.; Ahn, H.-Y.; Lee, Y. Y.; Byun, G. H.; Im, S. W.; Mun, J.; Rho, J.; Nam, K. T., Cysteine-Encoded Chirality Evolution in Plasmonic Rhombic Dodecahedral Gold Nanoparticles. *Nature Communications* **2020**, *11*, 263.
22. Cho, N. H.; Byun, G. H.; Lim, Y.-C.; Im, S. W.; Kim, H.; Lee, H.-E.; Ahn, H.-Y.; Nam, K. T., Uniform Chiral Gap Synthesis for High Dissymmetry Factor in Single Plasmonic Gold Nanoparticle. *ACS Nano* **2020**, *14*, 3595-3602.
23. Scarabelli, L.; Sánchez-Iglesias, A.; Pérez-Juste, J.; Liz-Marzán, L. M., A “Tips and Tricks” Practical Guide to the Synthesis of Gold Nanorods. *The Journal of Physical Chemistry Letters* **2015**, *6*, 4270-4279.
24. Wang, P.-p.; Yu, S.-J.; Govorov, A. O.; Ouyang, M., Cooperative Expression of Atomic Chirality in Inorganic Nanostructures. *Nature Communications* **2017**, *8*, 14312.
25. Ben-Moshe, A.; da Silva, A.; Müller, A.; Abu-Odeh, A.; Harrison, P.; Waelder, J.; Niroui, F.; Ophus, C.; Minor, A. M.; Asta, M.; Theis, W.; Ercius, P.; Alivisatos, A. P., The Chain of Chirality Transfer in Tellurium Nanocrystals. *Science* **2021**, *372*, 729-733.
26. Van Gordon, K.; Ni, B.; Girod, R.; Mychinko, M.; Bevilacqua, F.; Bals, S.; Liz-Marzán, L. M., Single Crystal and Pentatwinned Gold Nanorods Result in Chiral Nanocrystals with Reverse Handedness. *Angew. Chem. Int. Ed.* **2024**, *63*, e202403116.
27. Zhuo, X.; Mychinko, M.; Heyvaert, W.; Larios, D.; Obelleiro-Liz, M.; Taboada, J. M.; Bals, S.; Liz-Marzán, L. M., Morphological and Optical Transitions during Micelle-Seeded Chiral Growth on Gold Nanorods. *ACS Nano* **2022**, *16*, 19281-19292.

Chapter VI – Experimental Section

In this chapter, we provide detailed information on the materials and methodologies used in the preceding chapters. This includes synthetic strategies for both achiral and chiral gold nanomaterials, as well as synthetic information and characterization of the novel chiral inducer LipoCYS (synthesized by a collaborator, see **Chapter II** and following section). We also provide important background for the electron tomography characterization and helicity analysis performed by collaborators and featured throughout this thesis. Synthetic details for the multi-scale chiral products described in **Chapter V** can also be found here. To enhance clarity, we have categorized the methods by scientific field rather than adhering strictly to the sequence of chapters in which they are applied.

Synthesis of achiral nanomaterials

Chemicals

$\text{HAuCl}_4 \cdot 3\text{H}_2\text{O}$ (99.99% (metals basis)) was purchased from Alfa Aesar. AgNO_3 (>99.9%) was purchased from Roth. Cetyltrimethylammonium bromide (CTAB; 99%), cetyltrimethylammonium chloride (CTAC, *s*, >98.0%) and CTAC solution (25 wt% in H_2O), silver nitrate (AgNO_3 ; $\geq 99.0\%$), *n*-decanol (for synthesis; $\geq 99.0\%$), potassium iodide (KI, 99.5%), sodium borohydride (NaBH_4 ; 99%), citric acid monohydrate, (ACS, $\geq 99.0\%$) and ascorbic acid (AA; $\geq 99\%$) were all purchased from Sigma-Aldrich. Hydrochloric acid (HCl; ACS, ISO grade, 3% w/v) was sourced

from Scharlau. All reagents were used as received without further purification. MilliQ water was used to prepare solutions.

Methods

Synthesis of single-crystal gold nanorods (SC-AuNRs)

Single crystalline achiral AuNRs were synthesized according to a stepwise protocol adapted from the literature.^{1,2}

Preparation of gold nanoclusters (AuNCs)

To a glass vial, 5 mL of stock solution #1 (50 mM CTAB, 13.5 mM *n*-decanol) was transferred before addition of 50 μ L HAuCl₄ solution (aq., 50 mM) under constant magnetic stirring. After thorough sonication, 25 μ L AA solution (aq., 100 mM) was added under constant magnetic stirring until the solution became colorless. A 200 μ L aliquot of NaBH₄ solution (aq., 20 mM) was quickly added by rapidly depressing the plunger of the micropipettor; the solution turned a deep brown color. This last step is critical, as fast and homogenous reduction of Au(I) to Au(0) is connected to seed quality and reproducibility. Gold seeds were prepared in triplicate, and UV-vis spectra were analyzed for reproducibility and target peaks (350 and 480 nm) indicate the formation of Au seeds of around 1.5 nm, as described in the literature. AuNCs were kept at room temperature for at least one hour to ensure complete oxidation of NaBH₄, and used within four hours of synthesis.

Preparation of gold mini-rods for use as seeds in AuNR synthesis

In a glass vial, 80 mL of stock solution #1, 640 μ L of AgNO₃ solution (aq., 10 mM), and 4.4 mL

of HCl solution (aq., 1 M) were mixed before 800 μL HAuCl_4 solution (aq., 50 mM) was added under constant magnetic stirring. After thorough sonication, 1040 μL AA solution (aq., 100 mM) was added under constant magnetic stirring until the solution became colorless. 4.8 mL of the above nanocluster dispersion was added; after an overnight incubation at 25 $^\circ\text{C}$, the solution turned a brownish color. UV-vis spectra were recorded for a target LSPR peak of 734 nm, which corresponds to particle dimensions of approximately 21 nm x 7.5 nm. Initial centrifugation at 10000 g for 30 minutes was used to remove larger particles; the supernatant was then subjected to three additional rounds of centrifugation at 14500 g for 60 minutes. After each round, the supernatant was discarded and the particles resuspended in 10 mM aqueous CTAB solution.

Preparation of high aspect ratio gold nanorods (SC-AuNRs) for chiral synthesis

In a glass vial, 80 mL of stock solution #2 (50 mM CTAB, 11 mM *n*-decanol), 9.6 mL HCl solution (aq., 1 M), and 1.2 mL AgNO_3 solution (aq., 50 mM) were mixed before 800 μL HAuCl_4 solution (aq., 50 mM) was added under constant magnetic stirring. After thorough sonication, 640 μL ascorbic acid solution (aq., 100 mM) was added under constant magnetic stirring until the solution became colorless. 7 μL of cleaned gold mini-rod seeds ($[\text{Au}^0] = 29.8 \text{ mM}$) was added; after an overnight incubation at 16 $^\circ\text{C}$ in a temperature-controlled water bath, the solution turned a reddish-brown color. Synthesized nanorods were purified by three rounds of centrifugation (4250 g, 30 min); after each round, the supernatant was discarded, and the particles redispersed in 1 mM CTAC. To assist removal of CTAB and Ag^+ ions, nanorod dispersions were heated at 60 $^\circ\text{C}$ for 30 min before each round of centrifugation.

Synthesis of pentatwinned gold nanorods (PT-AuNRs)

Achiral pentatwinned AuNRs were synthesized by labmate Francisco Bevilacqua, according to a stepwise protocol adapted from the literature.^{3,4}

Preparation of pentatwinned gold seeds

To prepare pentatwinned Au seeds, a 0.05 M HAuCl₄ solution (50 μL) was added to 10 mL of 50 mM CTAC and 5 mM citric acid. After 30 minutes, a solution of a 25 mM NaBH₄ solution (250 μL) was rapidly added to the mixture, for reasons similar to those detailed in the synthesis of single-crystal nanoclusters. After a further 2 minutes, the seeds are aged for 90 min at 80 °C with stirring to induce twinning. Formation of pentatwinned seeds is indicated by the appearance of a strong LSPR peak in the linear optical spectrum around 550 nm, according to established literature.

Preparation of high aspect ratio gold nanorods (PT-AuNRs) for chiral preparations

For nanorod growth, a 0.05 M HAuCl₄ solution (125 μL) was mixed with 50 mL of 8 mM CTAB. The mixture was stored at 20 °C for at least 15 minutes, to allow for complete complexation between Au³⁺ and CTAB. After this time, a 0.1 M solution of AA (125 μL) was added, followed by 100 μL of pentatwinned Au seed dispersion ([Au³⁺] : [Au⁰] = 1.25). The reaction mixture was left undisturbed overnight, and then centrifuged at 4250 g for 10 min and washed with 10 mM CTAC thrice.

Synthesis of single-crystal octahedral gold nanoparticles (octa-AuNPs)

Achiral single-crystal octahedral AuNPs were synthesized according to a stepwise protocol adapted from the literature.^{5,6}

Preparation of CTAC-stabilized gold nanoclusters (AuNCs)

In a glass vial, 1.32 mL of 25% (w/v) CTAC was mixed with 250 μ L of a HAuCl₄ solution (0.01 M) and 8.43 mL of MilliQ-grade water; the solution was vortexed thoroughly to combine. An ice-cold NaBH₄ solution (20 mM) was prepared and 0.45 mL was quickly transferred to the above mixture, vortexing immediately for 2 minutes to quickly and completely reduce the gold salts. The solution was incubated at 30 °C for 1 hour before use.

Preparation of octahedral gold nanoparticles (octa-AuNPs)

Gold octahedrons were prepared according to established literature. 26.4 mL of 25% (w/v) CTAC was mixed with 5 mL of a HAuCl₄ solution (0.01 M), and 163 mL of MilliQ-grade water. After mixing gently by magnetic stirring, 4.4 mL of an ascorbic acid solution (40 mM) and 100 μ L of a KI solution (10 mM) were added with stirring to complete solution A. An aliquot of 995 μ L was taken from this solution, treated with 4 μ L of the solution containing CTAC-stabilized AuNCs, and immediately vortexed. Before the appearance of an intense pink color (~10 seconds), 900 μ L of the aliquot was transferred back to solution A, which was mixed via magnetic stirring for 30 seconds. The stirring was then stopped and the solution was incubated at 30 °C for 15 minutes. Gold octahedrons were isolated via two rounds of centrifugation (6708 g, 15 mins), redispersed in 3 mM CTAC, and evaluated by UV-vis spectroscopy (target LSPR peak position: 578 nm, with a tolerance of +/- 2 nm).

Synthesis of cubic single-crystal gold nanoparticles (cube-AuNPs)

Single-crystal achiral cubic AuNPs were synthesized by In Han Ha at Seoul National University according to a stepwise protocol adapted from the literature.^{5,6}

Preparation of CTAB-stabilized gold nanoclusters (AuNCs)

In a glass vial, 7.5 mL of a CTAB solution (0.1 M) was mixed with 250 μ L of a HAuCl₄ solution (0.01 M); the solution was vortexed thoroughly to combine. An ice-cold solution of NaBH₄ (10 mM) was prepared and 0.8 mL was quickly transferred to the above mixture, vortexing immediately for 2 minutes to quickly and completely reduce the gold salts. The solution was aged at room temperature for 2 hours, and diluted 1/10 into MilliQ water before use.

Preparation of gold cubic nanoparticles (cube-NPs)

Gold cubes were prepared according to established literature. 32 mL of a CTAB solution (0.2 M) was mixed with 4 mL of a HAuCl₄ solution (0.01 M) and gently stirred prior to addition (under stirring) of 19 mL of an ascorbic acid solution (0.4 M). The solution was further stirred for 30 seconds before addition of 100 μ L of the solution of CTAB-stabilized Au NCs. The solution was stirred an additional minute and then incubated at 30 °C for 15 minutes. Gold cubes were isolated via two rounds of centrifugation (6708 g, 15 min), resuspended in 1 mM CTAB, and evaluated by UV-vis spectroscopy (target LSPR peak position: 538 nm, with a tolerance of +/- 2 nm).

Synthesis of inherently chiral nanoparticles

Chemicals

HAuCl₄·3H₂O (99.99% (metals basis)), *L*-cysteine hydrochloride (*L*-cys, 99%) and *L*-Cystine hydrochloride (*L*-2cys, 98%) were purchased from Alfa Aesar. Ascorbic acid (AA) was purchased from Acros Organics. AgNO₃ (>99.9%) was purchased from Roth. (*R*)-(+)-1,1'-binaphthyl-2,2'-diamine (*R*-BINAMINE, 99%), (*S*)-(-)-1,1'-binaphthyl-2,2'-diamine (*S*-BINAMINE, 99%), cetyltrimetylammonium chloride (CTAC, >98.0%), cetyltrimethylammonium bromide (CTAB; 99%), silver nitrate (AgNO₃; ≥ 99.0%), *n*-decanol (for synthesis; ≥ 99.0%), sodium borohydride (NaBH₄; 99%), and ascorbic acid (AA; ≥ 99%) were all purchased from Sigma-Aldrich. Hydrochloric acid (HCl; ACS, ISO grade, 3% w/v) was sourced from Scharlau. All reagents were used as received without further purification. MilliQ water was used to prepare solutions. LipoCYS was synthesized according to a protocol detailed in a later section.

Methods

Seeded chiral growth in the presence of LipoCYS

Chiral products were synthesized in the presence of LipoCYS according to established literature.⁷ Chiral AuNRs were prepared in 2 mL reaction volumes at 40 °C; CTAC (or CTAB, when octahedral and cubic NPs were used as the achiral seeds) and AA concentrations were kept constant at 44 mM and 700 mM, respectively, and [Au³⁺]:[Au⁰] was kept constant at 8.9 (185 μM and 20.8 μM, respectively). For all chiral preparations, and after a 30 min incubation, chiral nanorods were centrifuged (3000 g, 10 min) and resuspended in Milli-Q water. This process was repeated twice to remove excess AA and CTAC from solution.

Estimation of relative LipoCYS concentration

Considering the average dimensions of the AuNR seeds (142 nm x 31.6 nm) and assuming a cylindrical shape, the surface area per NR would be $SA = 15665 \text{ nm}^2$ and the volume per NR $V = 111366 \text{ nm}^3$. Considering the initial AuNR seed concentration of $2.08 \times 10^{-5} \text{ mol/L}$, this would translate into $1.90476 \times 10^{12} \text{ AuNR / L}$, with a total $SA_T = 6.0 \times 10^{13} \text{ nm}^2$, in 2 mL of dispersion.

For each LipoCYS molar concentration, the number of molecules can be readily calculated as:

LipoCYS molecules = [LipoCYS] (mol/L) x vol. dispersion (L) x N_A (molecules / mol), where N_A

is the Avogadro number. Again, for 2 mL:

20 μM : 2.4×10^{16} LipoCYS molecules
45 μM : 5.4×10^{16} LipoCYS molecules
75 μM : 9.0×10^{16} LipoCYS molecules
90 μM : 1.1×10^{17} LipoCYS molecules
200 μM : 2.4×10^{17} LipoCYS molecules

As a result, the relative number of available LipoCYS molecules per nm^2 AuNR surface can be estimated as:

20 μM : 404
45 μM : 908
75 μM : 1514
90 μM : 1816
200 μM : 4036

Finally, the relative number of CTAC molecules (44 mM) per LipoCYS molecule would be:

20 μM : 2200
45 μM : 978
75 μM : 587
90 μM : 489
200 μM : 22

Seeded hierarchical chiral growth in the presence of LipoCYS

The following describes an alternative protocol using LipoCYS and octahedral seeds for the production of helicoid-like particles. Chiral products were prepared in 5.35 mL reaction volumes at 30 °C; CTAC (or CTAB) and AA concentrations were kept constant at 14.9 mM and 8.8 mM, respectively, and $[\text{Au}^{3+}] : [\text{Au}^0]$ was kept constant at 40.8 (186 μM and 4.55 μM , respectively). For all chiral preparations, and after a 2 hour incubation, chiral products were spun down (4250 g, 5 min) and resuspended in 1 mM CTAC (or CTAB). This process was repeated twice to remove excess AA and CTAC from solution.

Single-step seeded chiral growth in the presence of L-2cys

Chiral products were synthesized in the presence of cystine (*L*-2cys) in a single step, according to established literature.^{8,9} Chiral AuNRs were prepared in 2 mL reaction volumes at 40 °C; CTAC and AA concentrations were kept constant at 14.8 mM and 8.8 mM, respectively, and $[\text{Au}^{3+}] : [\text{Au}^0]$ was kept constant at 8.9 (185 μM and 20.8 μM , respectively). For all chiral preparations, and after a 30 min incubation, chiral nanorods were spun down (4250 g, 10 min) and resuspended in Milli-Q water. This process was repeated twice to remove excess AA and CTAC from solution.

Multi-step seeded chiral growth in the presence of L-2cys

Chiral products were synthesized in the presence of cystine in a stepwise manner according to established literature.^{8,9} The concentration of PT-AuNRs and SC-AuNRs was adjusted to 0.8 mM, according to the optical absorbance at 400 nm. Then 1.9 mL of CTAC solution (40 mM) was poured into a tube, followed by addition of 5 μL of HAuCl_4 (5 mM) and 0.2 mL of AA (0.1 M). The solution was sonicated for 30s. Then, 30 μL of *L*-2cys (2.5 μM) was added into the PE tube, followed by addition of 10 μL of seed solution, shaking several times and store in a water bath at

25 °C (this step is called as the first addition). After 50 min, 5 μL of HAuCl_4 (5 mM) was added into the PE tube. The addition was repeated several times, and the temperature of the water bath could also be tuned according to the growth requirements. After the 6 HAuCl_4 addition steps, the temperature of the water bath was decreased to 16 °C. After 9 additions, the PE tube was centrifuged (6000 g, 5 min) and washed twice with MilliQ-grade water. The obtained particles were dispersed in MilliQ water.

Seeded chiral growth in the presence of BINAMINE

Chiral products were synthesized in the presence of BINAMINE according to established literature.¹⁰⁻¹³ For chiral particles prepared using BINAMINE, seeds were first incubated overnight in a solution of 50 mM CTAC and 1.25 mM *R*- or *S*- BINAMINE. A typical chiral synthesis was prepared in an Eppendorf tube at a total volume of 1 mL, using 500 μM BINAMINE, 20 mM CTAC, 500 μM HAuCl_4 , 160 mM ascorbic acid, and achiral seeds (Au^0 ; 63.5 μM for **Chapter III**, 31.25 μM for **Chapter IV** and **Chapter V**). Seeds and ascorbic acid were sequentially added, and the tube was immediately shaken before leaving for 30 minutes at room temperature. Chiral particles were centrifuged at 4250 g for 10 minutes and resuspended in MILLIPORE-grade water. This process was repeated twice to separate chiral products from excess reagents and non-chiral reaction byproducts.

Time-resolved synthesis of inherently chiral nanoparticles

To cease a chiral reaction in progress, a volume of NaBH_4 is added that is equal to 1.6x the amount of gold salt present in the reaction, as dictated by literature.¹ The reaction tube is then shaken to rapidly reduce the gold salts; this is indicated by the fast appearance of a brown color in solution. Time zero is represented by when ascorbic acid is added to initiate chiral overgrowth; a given time

point in a kinetic series is represented by the time elapsed before NaBH₄ addition. Chiral particles are isolated via centrifugation at 4250 g for 10 minutes and resuspended in MilliQ grade water. This process was repeated twice to separate chiral products from excess reagents and non-chiral reaction byproducts.

Optical Characterization, Electron Tomography and Computational Analysis

Optical characterization

All circular dichroism (CD) spectra were acquired using a JASCO J-1500 CD spectrometer in CD/DC mode, measuring the differential absorption of circularly polarized light by the sample as a function of the direct current (DC) measured by the detector.

For samples measured continuously, seeded chiral growth reactions were prepared identically to the above description, but in a quartz cuvette. The CD instrument was set to capture a wavelength range between 390 and 1250 nm, at a spectral resolution (data pitch) of 20 nm and a scan rate of 5000 nm/min. Time zero is represented by the first scan of the CD instrument, which was initialized immediately after the addition of ascorbic acid to the reaction. A reinitialization time is required during scans, bringing the actual time between the starts of two consecutive scans to 25-30 s. This duration had some variability and the acquired CD spectra are therefore reported herein by their collection time by the instrument, i.e., the time at which the scan was completed.

For all other samples, CD spectra were acquired in two steps, from 300 nm to 900 nm (using a PMT detector) and from 800 nm to 1300 nm (using an InGaAs detector). Both spectra were then combined using “spectra concatenation” software from JASCO to obtain a CD spectrum from 300-

1300 nm. A Cary 50 UV Visible spectrophotometer from Agilent Technologies was used to collect UV-Vis optical spectra.

Electron tomography and helicity analysis were performed by Dr. Robin Girod, Dr. Mikhail Mychinko, Dr. Evgenii Vlasov, and Wouter Heyvaert under the supervision of Prof. Sara Bals at the NANOLab Center of Excellence (EMAT) at the University of Antwerp. Computational modelling and light simulations of chiral nanoparticles were done by Manuel Obelleiro-Liz (EM3 Works), Fernando Obelleiro (Universidade de Vigo) and José Manuel Taboada (Universidad de Extremadura).

Electron tomography

High resolution scanning transmission electron microscopy (STEM) and electron tomography experiments were performed using a “cubed” Thermo Fisher Scientific Themis Z instrument operated at 300 kV in HAADF-STEM mode. High angle annular dark field STEM (HAADF-STEM) tomography series were acquired over an angular range of $\pm 75^\circ$, with a tilt increment of 3° , and were used as an input for SIRT reconstruction using the Astra Toolbox 1.8 for MATLAB R2019A.¹⁴ Electron diffraction tomography (ED) series was acquired over an angular range of $\pm 75^\circ$, with a continuous tilting ($\sim 0.6^\circ/\text{s}$) and were reconstructed using the PETS2.0 software. Visualization of the 3D reconstructions was performed using the Amira 5.4.0 software.

Surface helicity analysis

The helical morphology of chiral AuNRs was quantitatively characterized using an updated version of our previously reported method. First, the surface of an AuNR was extracted by segmentation of the electron tomography reconstruction, by manually thresholding the reconstruction followed by denoising through several consecutive morphological opening and

closing operations. Next, the binarized data were converted to a triangulated mesh using the Thermofisher Amira 5.4.0 software. The center of mass of the resulting mesh was selected as the origin and the helical axis was determined by principal component analysis (PCA) applied to the coordinates of the vertices in the mesh. The principal component corresponds to the long axis of the NR and selected as the helical axis. Next, the normal vector of each surface element was used to determine the helical inclination angle of each surface element with respect to the helical axis. Subsequently, the helicity function $H(\alpha, \rho)$ and total helicity H_{tot} , as described in ref. 4, were calculated by integrating over the surface of the NR:

$$H(\alpha, \rho) := \frac{\iint_S \text{sign}(\alpha') \delta(\alpha - |\alpha'|) \delta(\rho - \rho') dS}{\iint_S dS}$$

$$H_{tot} := \frac{\iint_S \text{sign}(\alpha') dS}{\iint_S dS}$$

Here, α' and ρ' are the inclination angle and radius of each point on the surface, respectively. Since positive inclination angles correspond to right-handed helicity and negative inclination angles to left-handed helicity, the total helicity H_{tot} is a scalar value between -1 (perfect left-handed helicity) and +1 (perfect right-handed helicity). Similarly, the helicity function $H(\alpha, \rho)$ is a distribution indicating which handedness is prevailing at each radius from the helical axis, for each inclination angle, thus giving insights into the helical structure of a NR.

Numerical Solution of Maxwell's Equations

The M3 solver was used to perform full-wave electromagnetic simulations.¹⁵⁻¹⁷ The full-wave solutions are based on surface-integral equations (SIEs) discretized by the method of moments (MoM). In SIE-MoM, the parametrization and subsequent numerical analysis are both restricted

to the two- dimensional boundary surfaces of the particles, rather than a 3D space embedding of the material structure, which results in a drastic reduction in the number of unknowns compared with other approaches. SIE-MoM is robust against instabilities produced by rapid spatial variations of the permittivity, as is usually the case in plasmonic structures. Gold was described through its frequency-dependent complex permittivity, taken from optical measurements.^{18,19}

Nanoparticle Models

The nanorod models were designed to resemble the experimental 3D tomographic reconstructions of NPs obtained using 20, 45 and 90 μM LipoCYS. The models consist of a twisted nanorod core with square section (70 nm x 70 nm) and 170 nm in length, on which 16 or 25 helical grooves are excavated all around (for the second and third models, respectively), giving rise to 6 or 16 helical wrinkles that unfold along the lateral surfaces. The helices have two leveled and two inclined steps per pitch, with tilt angles of 60° and 30° in the inclined steps, respectively. The corresponding wrinkle widths are 8 nm and 4 nm, and the separation distances between wrinkles are 12 nm and 7 nm, respectively. Groove depths are 6 nm and 13 nm, respectively. The modeling and meshing of the models were performed with Blender 3.3, Solidworks and Hypermesh respectively. Having a high-quality, clean mesh, with a consistent aspect ratio across all elements is crucial for the results of the simulation. Mesh quality is key in obtaining accurate results and for the problem to be solved efficiently in terms of time and resources, and with fidelity to the underlying physics. Illumination was based on left- (right-) circularly polarized plane waves impinging from multiple directions. Overall responses were calculated by averaging over light incidence angles.

Synthesis of LipoCYS

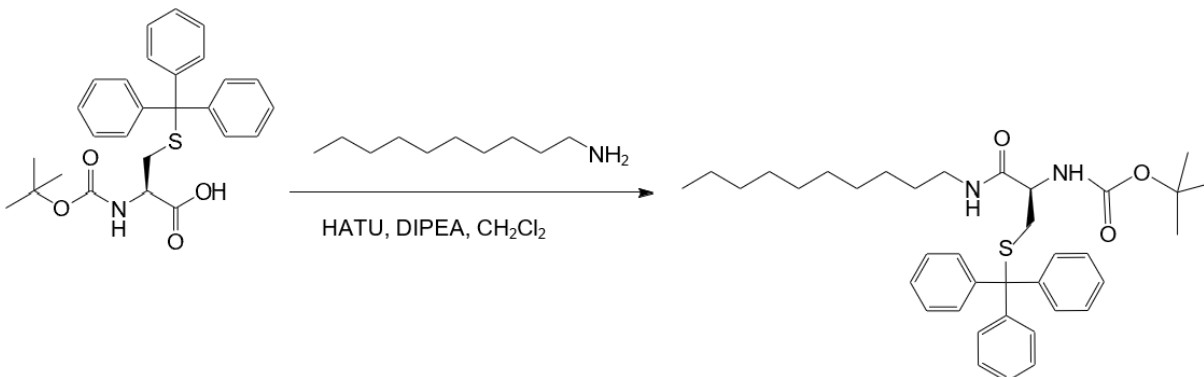
Both enantiomers of the **LipoCYS** molecule were synthesized by Sandra Baúlde under the supervision of Dr. Jesús Mosquera at the Universidade da Coruña, following a procedure reported by Neal K. Devaraj et al.²⁰

Materials

Commercially available N-Boc-(*R*)-Cys(Trt)-OH, N-Boc-(*S*)-Cys(Trt)-OH, Decan-1- amine, and triisopropylsilane (TIS) were obtained from BLD pharm. N,N- diisopropylethylamine (DIPEA), tris(2-carboxyethyl)phosphine (TCEP), and trifluoroacetic acid (TFA) were purchased from TCI. O-(7-Azabenzotriazol-1-yl)- N,N,N',N'-tetramethyluronium hexafluorophosphate (HATU) was obtained from Apollo Scientific. Dichloromethane (DCM) was acquired from Scharlau. Deuterated chloroform (CDCl₃) and methanol (CD₃OD) were obtained from Deutero GmbH. Analytical thin-layer chromatography was performed using Silicycle aluminum-backed TLC plates. Compounds that were not UV-active were visualized by dipping the plates in a ninhydrin stain. Silica gel flash chromatography was performed using Labkem silica gel (type SGEC-060-500) and HPLC purification was carried out using a Fortis C18 semipreparative column (5 μm, size: 250×10 mm) with Phase A/Phase B gradients (Phase A: H₂O with 0.1% trifluoroacetic acid; Phase B: Acetonitrile with 0.1% trifluoroacetic acid). Proton nuclear magnetic resonance (¹H NMR) and Carbon nuclear magnetic resonance (¹³C NMR) spectra were measured on Bruker AVANCE III HD 400 Nuclear Magnetic Resonance spectrometer and were referenced relating to residual proton resonances in CDCl₃ (at δ 7.24 ppm and 77.23 ppm) and CD₃OD (at δ 4.87 or 3.31 ppm and 49.15 ppm). ¹H NMR splitting patterns are assigned as singlet (s), doublet (d), triplet (t) or quartet (q). Splitting patterns that could not be readily interpreted are designated as multiplet (m).

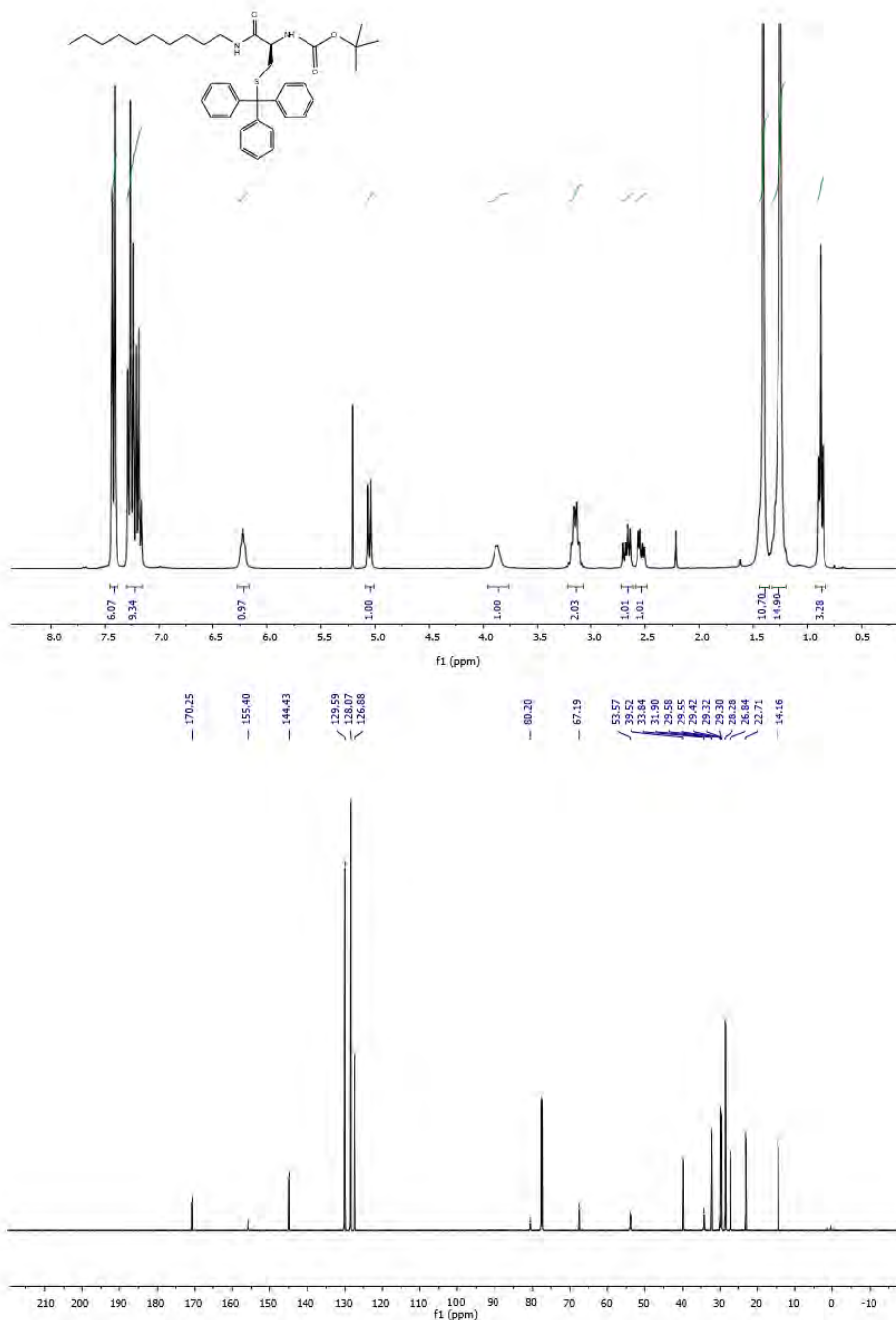
Methods

Synthesis of N-Boc-(R)-Cys(Trt)-Decan



A solution of **N-Boc-(R)-Cys(Trt)-OH** (1 g, 2.16 mmol) in CH₂Cl₂ (14.5 mL) was stirred at 0 °C for 10 min, and then HATU (820 mg, 2.16 mmol) and DIPEA (376 μL, 2.16 mmol) were successively added. After 10 min stirring at 0 °C, decan-1-amine (339 mg, 2.16 mmol) was added. After 1 h stirring at room temperature, the reaction mixture was washed with NaHCO₃(sat) (3 × 10 mL). The organic layer was dried (Na₂SO₄), filtered and concentrated, providing a yellow oil, which was purified by flash chromatography (0–3% MeOH in CH₂Cl₂), affording the expected product as a yellow oil [96%, R_f = 0.52 (1% MeOH in CH₂Cl₂)].

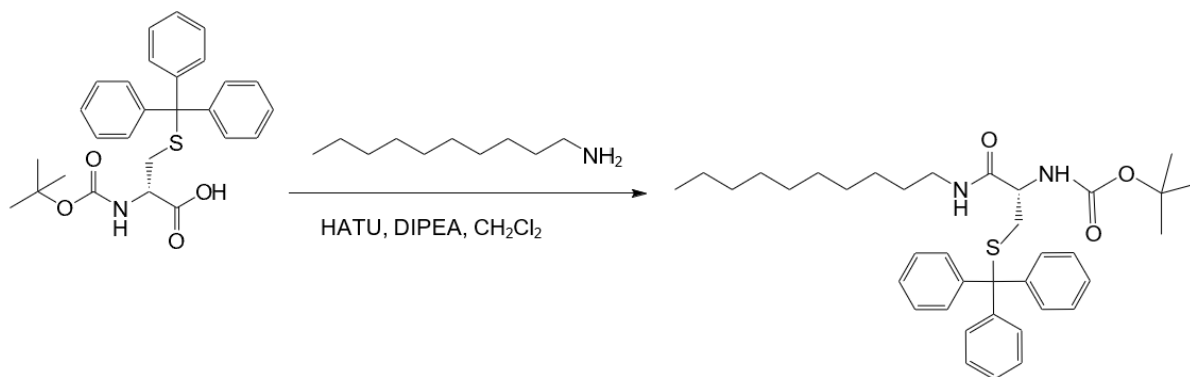
NMR Spectra of N-Boc-(R)-Cys(Trt)-Decan



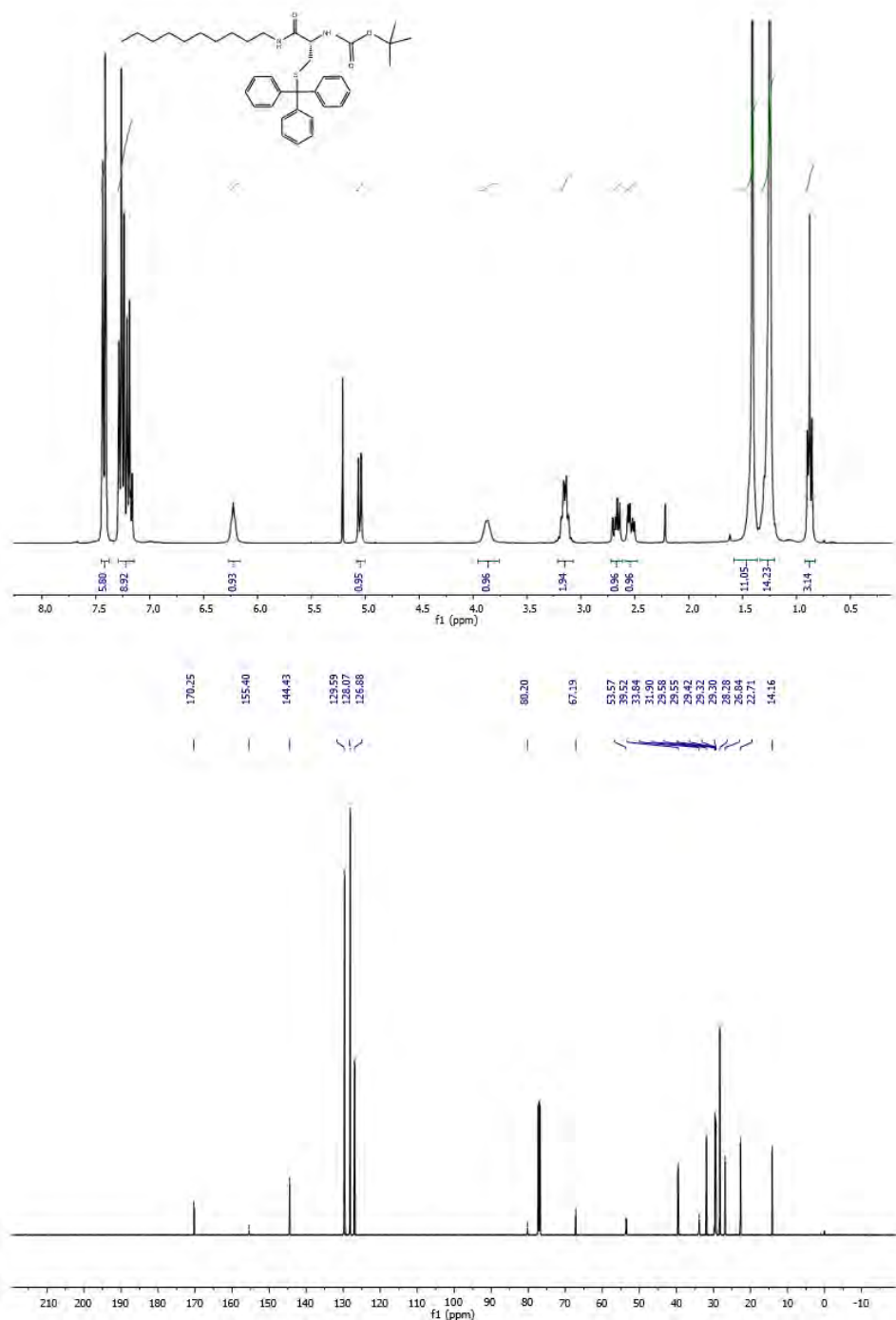
¹H NMR (300 MHz, Chloroform-*d*) δ: 7.46 – 7.36 (m, 6H), 7.30 – 7.14 (m, 9H), 6.22 (t, *J* = 5.8 Hz, 1H), 5.05 (d, *J* = 7.9 Hz, 1H), 3.87 (m, 1H), 3.19 – 3.09 (m, 2H), 2.73-2.62 (dd, *J*= 12.7, 7.1 Hz, 1H), 2.60-2.48 (dd, *J*= 12.7, 5.6 Hz, 1H), 1.39 (s, 9H, 3 x CH₃), 1.23 (s, 14H), 0.91 (t, 3H) ppm. ¹³C NMR (75 MHz, CDCl₃): δ 170.25(1C), 155.40(1C), 144.43(3C), 129.59(6CH), 128.07(6CH), 126.88(3CH), 80.20(1C), 67.19(1C), 53.57(1CH), 39.52(1CH₂), 33.84(1CH₂), 31.90(1CH₂), 29.58(1CH₂), 29.55(1CH₂), 29.42(1CH₂), 29.32(1CH₂), 29.30(1CH₂), 28.28 (3CH₃), 26.84(1CH₂), 22.71(1CH₂), 14.16 (1CH₃) ppm.

Synthesis of N-Boc-(S)-Cys(Trt)-Decan

The (S) enantiomer was prepared following the same procedure, but using **N-Boc-(S)-Cys(Trt)-OH** as a precursor.



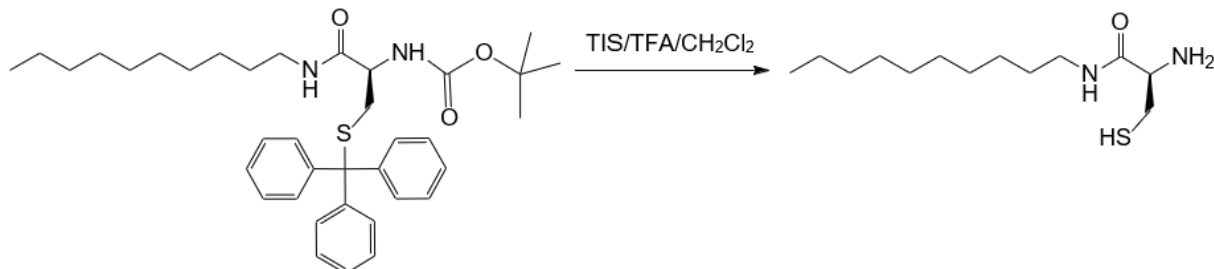
NMR Spectra of N-Boc-(S)-Cys(Trt)-Decan



¹H NMR (400 MHz, Chloroform-*d*): δ 7.48 – 7.36 (m, 6H), 7.32 – 7.12 (m, 9H), 6.23 (t, *J* = 5.8 Hz, 1H), 5.05 (d, *J* = 7.9 Hz, 1H), 3.87 (m, 1H), 3.15 (m, 2H), 2.74-2.60 (dd, *J* = 12.7, 7.1 Hz, 1H), 2.60-2.48 (dd, *J* = 12.7, 5.6 Hz, 1H), 1.41 (s, 9H, 3 x CH₃), 1.25 (s, 14H), 0.88 (m, 3H) ppm. ¹³C NMR (100 MHz, CDCl₃): δ 170.25(1C), 155.40(1C), 144.43(3C), 129.59(6CH), 128.07(6CH), 126.88(3CH), 80.20(1C), 67.19(1C), 53.57(1CH), 39.52(1CH₂), 33.84(1CH₂), 31.90(1CH₂), 29.58(1CH₂), 29.55(1CH₂), 29.42(1CH₂), 29.32(1CH₂), 29.30(1CH₂), 28.28 (3CH₃), 26.84(1CH₂), 22.71(1CH₂), 14.16 (1CH₃) ppm.

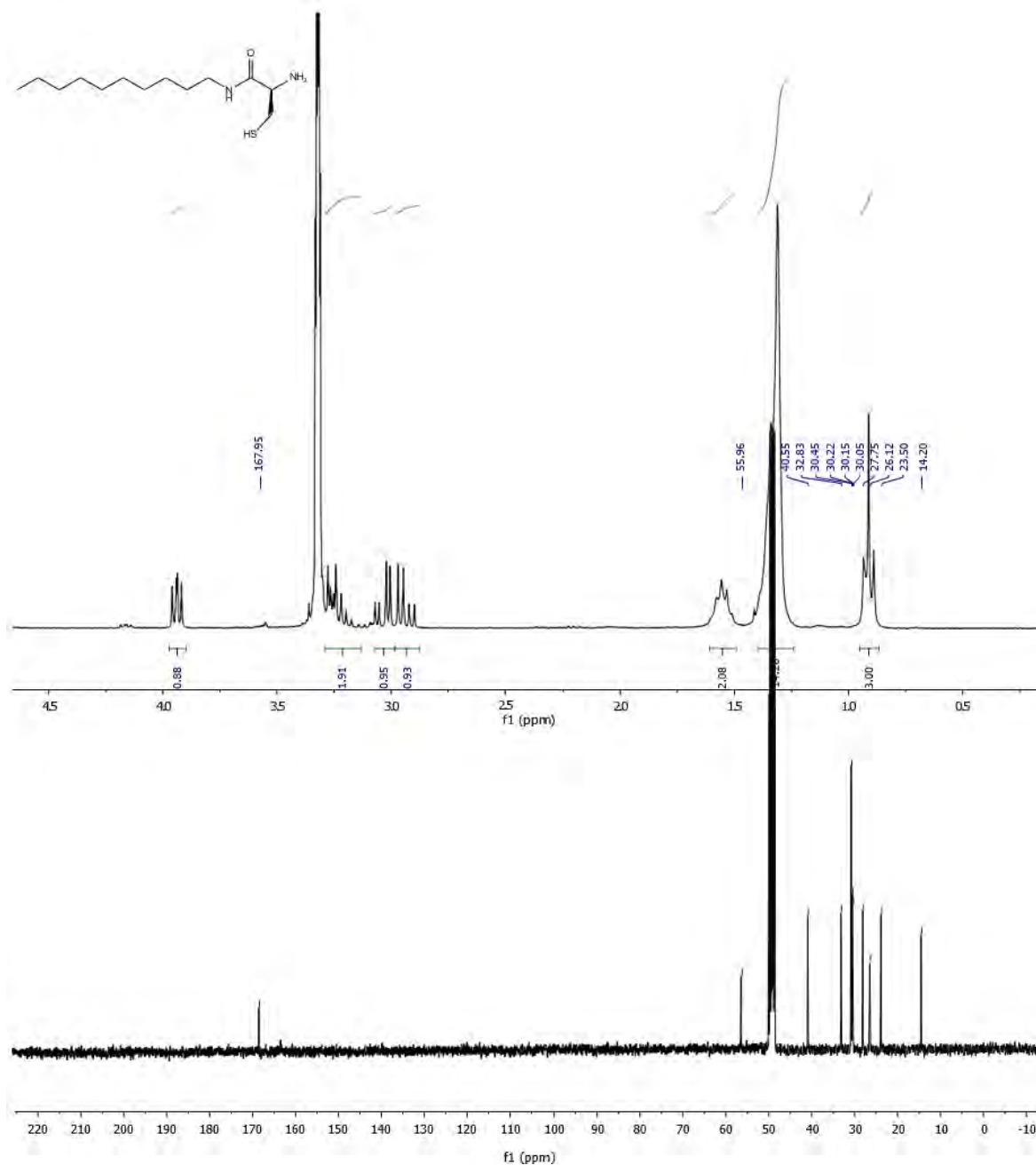
Synthesis of (R)-2-amino-N-decyl-3-mercaptopropanamide, (R)-LipoCYS

The synthesis of the (R) enantiomer of **LipoCYS** is described below.



N-Boc-(R)-Cys(Trt)-Decan (100 mg) was dissolved in 2 mL of TFA/CH₂Cl₂/TIS (225:225:50) and the mixture was stirred at room temperature for 30 min. After removal of the solvent, the residue was dried under high vacuum for 1 h. Then, the corresponding residue was diluted in milli-Q H₂O containing 1 mM of TCEP, filtered using a 0.2 μm syringe-driven filter, and the crude solution was purified by HPLC, yielding the purified compound as a colorless oil [R_T = 18 min (C18 semipreparative column, 70% Phase A in Phase B, 30 min, and then 5% Phase A in Phase B, 10 min)].

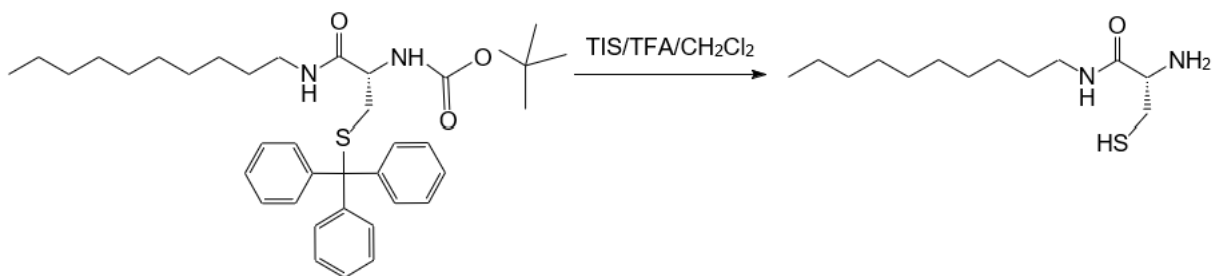
NMR Spectra of (R)-LipoCYS



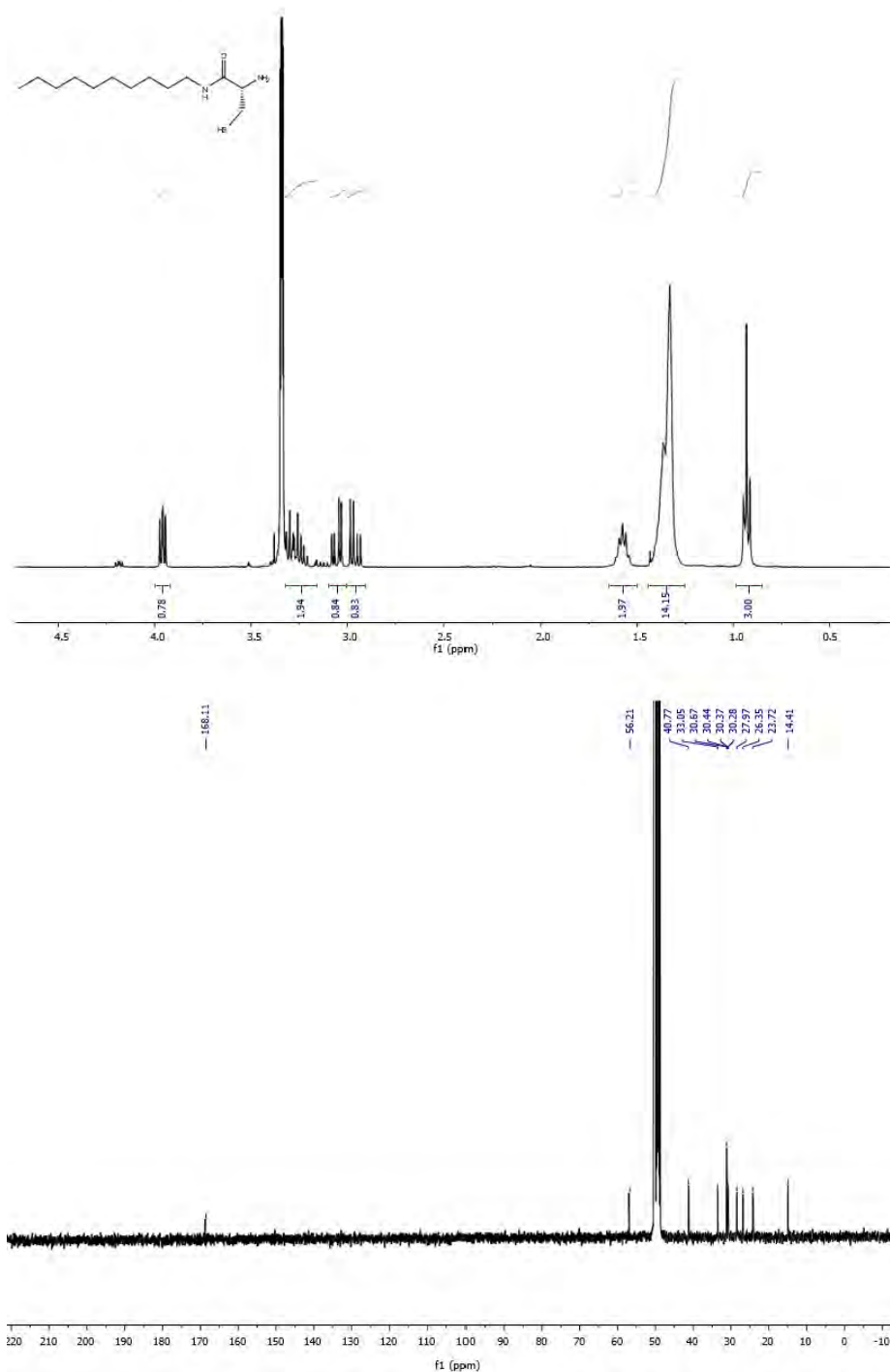
¹H NMR (400 MHz, MeOD) δ 3.97 (dd, $J=5.22, 6.88$ Hz, 1H), 3.34-3.20 (m, 2H), 3.08-2.98 (dd, $J=14.59, 6.88$ Hz, 1H) 2.98-2.88 (dd, $J=14.59, 5.22$ Hz, 1H), 1.61-1.53 (m, 2H), 1.40-1.25 (m, 14H), 0.91 (t, $J=6.9$ Hz, 3H). ¹³C NMR (100 MHz, MeOD): δ 167.95 (1C), 55.96 (1CH), 40.55 (1CH₂), 32.83 (1CH₂), 30.45 (2CH₂), 30.22 (1CH₂), 30.15 (1CH₂), 30.05 (1CH₂), 27.75 (1CH₂), 26.12 (1CH₂), 23.50 (1CH₂), 14.20 (1CH₃). HRMS (ESI⁺): m/z calculated for C₁₃H₂₇N₂O₅[M+H]⁺ 261.200, found 261.199.

Synthesis of (S)-2-amino-N-decyl-3-mercaptopropanamide, (S)-LipoCYS

The (S) enantiomer was prepared following the same procedure, but using N-Boc-(S)-Cys(Trt)-Decan as a precursor.



NMR Spectra of (S)-LipoCYS



¹H NMR (400 MHz, MeOD) δ : 3.97 (dd, $J=5.22, 6.90$ Hz, 1H), 3.34-3.17 (m, 2H), 3.09-3.00 (dd, $J=14.59, 6.90$ Hz, 1H), 3.00-2.91 (dd, $J=14.59, 5.22$ Hz, 1H) 1.62-1.50 (m, 2H), 1.44-1.25 (m, 14H), 0.93 (t, $J=6.9$ Hz, 3H) ppm. ¹³C NMR (100 MHz, CDCl₃) δ : 168.11(1C), 56.21(1CH), 40.77(1CH₂), 33.05(1CH₂), 30.67(2CH₂), 30.44(1CH₂), 30.37(1CH₂), 30.28(1CH₂), 27.97(1CH₂), 26.35(1CH₂), 23.72(1CH₂), 14.41(1CH₃) ppm. HRMS (ESI⁺): m/z calculated for C₁₃H₂₇N₂O₅[M+H]⁺ 261.200, found 261.19.

References

1. Gonzalez-Rubio, G.; Kumar, V.; Llombart, P.; Diaz-Nunez, P.; Bladt, E.; Altantzis, T.; Bals, S.; Pena-Rodriguez, O.; Noya, E. G.; MacDowell, L. G.; Guerrero-Martinez, A.; Liz-Marzan, L. M., Disconnecting Symmetry Breaking from Seeded Growth for the Reproducible Synthesis of High Quality Gold Nanorods. *Acs Nano* **2019**, *13*, 4424-4435.
2. González-Rubio, G.; Llombart, P.; Zhou, J.; Geiss, H.; Peña-Rodríguez, O.; Gai, H.; Ni, B.; Rosenberg, R.; Cölfen, H., Revisiting the Role of Seed Size for the Synthesis of Highly Uniform Sub-10 nm Length Gold Nanorods. *Chem. Mater.* **2024**, *36*, 1982-1997.
3. Sanchez-Iglesias, A.; Jenkinson, K.; Bals, S.; Liz-Marzan, L. M., Kinetic Regulation of the Synthesis of Pentatwinned Gold Nanorods below Room Temperature. *Journal of Physical Chemistry C* **2021**, *125*, 23937-23944.
4. Sánchez-Iglesias, A.; Winckelmans, N.; Altantzis, T.; Bals, S.; Grzelczak, M.; Liz-Marzán, L. M., High-Yield Seeded Growth of Monodisperse Pentatwinned Gold Nanoparticles through Thermally Induced Seed Twinning. *JACS* **2017**, *139*, 107-110.
5. Ahn, H.-Y.; Lee, H.-E.; Jin, K.; Nam, K. T., Extended Gold Nano-Morphology Diagram: Synthesis of Rhombic Dodecahedra using CTAB and Ascorbic Acid. *Journal of Materials Chemistry C* **2013**, *1*, 6861-6868.
6. Wu, H.-L.; Tsai, H.-R.; Hung, Y.-T.; Lao, K.-U.; Liao, C.-W.; Chung, P.-J.; Huang, J.-S.; Chen, I.-C.; Huang, M. H., A Comparative Study of Gold Nanocubes, Octahedra, and Rhombic Dodecahedra as Highly Sensitive SERS Substrates. *Inorg. Chem.* **2011**, *50*, 8106-8111.
7. Van Gordon, K.; Baúlde, S.; Mychinko, M.; Heyvaert, W.; Obelleiro-Liz, M.; Criado, A.; Bals, S.; Liz-Marzán, L. M.; Mosquera, J., Tuning the Growth of Chiral Gold Nanoparticles Through Rational Design of a Chiral Molecular Inducer. *Nano Lett.* **2023**, *23*, 9880-9886.
8. Van Gordon, K.; Ni, B.; Girod, R.; Mychinko, M.; Bevilacqua, F.; Bals, S.; Liz-Marzán, L. M., Single Crystal and Pentatwinned Gold Nanorods Result in Chiral Nanocrystals with Reverse Handedness. *Angew. Chem. Int. Ed.* **2024**, *63*, e202403116.
9. Ni, B.; Mychinko, M.; Gómez-Graña, S.; Morales-Vidal, J.; Obelleiro-Liz, M.; Heyvaert, W.; Vila-Liarte, D.; Zhuo, X.; Albrecht, W.; Zheng, G.; González-Rubio, G.; Taboada, J. M.; Obelleiro, F.; López, N.; Pérez-Juste, J.; Pastoriza-Santos, I.; Cölfen, H.; Bals, S.; Liz-Marzán, L. M., Chiral Seeded Growth of Gold Nanorods Into Fourfold Twisted Nanoparticles with Plasmonic Optical Activity. *Adv. Mater.* **2023**, *35*, 2208299.

10. González-Rubio, G.; Mosquera, J.; Kumar, V.; Pedraza-Tardajos, A.; Llombart, P.; Solís, D. M.; Lobato, I.; Noya, E. G.; Guerrero-Martínez, A.; Taboada, J. M.; Obelleiro, F.; MacDowell, L. G.; Bals, S.; Liz-Marzán, L. M., Micelle-Directed Chiral Seeded Growth on Anisotropic Gold Nanocrystals. *Science* **2020**, *368*, 1472-1477.
11. Heyvaert, W.; Pedraza-Tardajos, A.; Kadu, A.; Claes, N.; González-Rubio, G.; Liz-Marzán, L. M.; Albrecht, W.; Bals, S., Quantification of the Helical Morphology of Chiral Gold Nanorods. *ACS Materials Letters* **2022**, *4*, 642-649.
12. Zhuo, X.; Mychinko, M.; Heyvaert, W.; Larios, D.; Obelleiro-Liz, M.; Taboada, J. M.; Bals, S.; Liz-Marzán, L. M., Morphological and Optical Transitions during Micelle-Seeded Chiral Growth on Gold Nanorods. *ACS Nano* **2022**, *16*, 19281-19292.
13. Spaeth, P.; Adhikari, S.; Heyvaert, W.; Zhuo, X.; García, I.; Liz-Marzán, L. M.; Bals, S.; Orrit, M.; Albrecht, W., Photothermal Circular Dichroism Measurements of Single Chiral Gold Nanoparticles Correlated with Electron Tomography. *ACS Photonics* **2022**, *9*, 3995-4004.
14. van Aarle, W.; Palenstijn, W. J.; De Beenhouwer, J.; Altantzis, T.; Bals, S.; Batenburg, K. J.; Sijbers, J., The ASTRA Toolbox: A platform for advanced algorithm development in electron tomography. *Ultramicroscopy* **2015**, *157*, 35-47.
15. Solís, D. M.; Taboada, J. M.; Obelleiro, F.; Liz-Marzán, L. M.; García de Abajo, F. J., Toward Ultimate Nanoplasmonics Modeling. *ACS Nano* **2014**, *8*, 7559-7570.
16. Solís, D. M.; Taboada, J. M.; Basteiro, F. O., Surface Integral Equation-Method of Moments With Multiregion Basis Functions Applied to Plasmonics. *IEEE Transactions on Antennas and Propagation* **2015**, *63*, 2141-2152.
17. Martín, V. F.; Solís, D. M.; Jericó, D.; Landesa, L.; Obelleiro, F.; Taboada, J. M., Discontinuous Galerkin integral equation method for light scattering from complex nanoparticle assemblies. *Opt. Express* **2023**, *31*, 1034-1048.
18. Johnson, P. B.; Christy, R. W., Optical Constants of the Noble Metals. *Physical Review B* **1972**, *6*, 4370-4379.
19. Palik, E. D., *Handbook of optical constants of solids*. Academic Press, San Diego: 1985.
20. Vora, H. D.; Johnson, M.; Brea, R. J.; Rudd, A. K.; Devaraj, N. K., Inhibition of NRAS Signaling in Melanoma through Direct Depalmitoylation Using Amphiphilic Nucleophiles. *ACS Chem Biol* **2020**, *15*, 2079-2086.

Chapter VII – Conclusions

In Chapter II, we tested a novel chiral inducer, LipoCYS, intended to bridge two major chiral growth mechanisms that were the focus of this body of work. Remarkably, the chiroptical signature of products was observed to evolve and shift in both wavelength and intensity depending solely on the concentration of LipoCYS used in the chiral synthesis. Further characterization by electron tomography revealed that products synthesized with a low concentration of LipoCYS appeared like those obtained from the chemically-induced growth mechanism; at a high concentration of LipoCYS, products appeared like those obtained from the micelle-directed growth mechanism. We can infer that below a critical concentration of LipoCYS, micelles are not formed and the thiol group directly interacting with the surface of gold particles has the dominant influence over the progression of chiral growth. A future experiment using dynamic light scattering (DLS) to precisely determine the critical micelle concentration of LipoCYS seems intuitive, until we consider that the micelles, if behaving in a manner analogous to micelles comprised of BINAMINE and CTAC, may be “giant worm-like” micelles and therefore be more difficult to discriminate from spherical micelles that may also form; this measurement would be additionally complicated by the presence of surfactant.

In Chapter III, we investigated the influence of starting seed geometry for both well-established growth mechanisms by contrasting the chiral products from single-crystalline and pentatwinned achiral seeds of a high aspect ratio. The chiroptical signatures and structural handedness of chemically-induced products were observed to be inverted; the contrast between the products yielded from single-crystal and pentatwinned achiral seeds was enhanced when a stepwise addition

of gold salts was employed. This slowed growth protocol homogenized the products of single-crystal achiral seeds, and caused the products of pentatwinned achiral seeds to become more disparate in structure, even between particles of the same sample. Correctly predicting that the products from the micelle-directed mechanism would have highly regular morphologies in the form of well-defined helical wrinkles regardless of achiral seed used, these products were subjected to a finer structural analysis. From careful analysis of the wrinkle orientation about the particle surface, it was observed that chiral products formed from single-crystal achiral seeds with four-fold symmetry also had four-fold symmetry, and that chiral products formed from pentatwinned achiral seeds had a similarly preserved five-fold symmetry. This observation had large implications for the projects in the next two chapters: at once, it threw into question the intermediate morphologies formed during a micelle-directed chiral reaction, prompting a means with which to investigate, and supplied a reliable foundation for an approach to synthesize particles with multi-scale chirality.

In Chapter IV, a method using sodium borohydride was developed to cease chiral reactions in progress, enabling the study of the chiroptical and structural evolution of these products in an *approximation* of real time. Time-resolved series prepared in this way are comprised of many replicates of the same reaction allowed to progress for varying growth intervals, and not of many aliquots isolated from the same reaction. There are drawbacks to this latter approach. As the optical signature for early time points (5s, 10s of growth) was observed to be vanishingly small, aliquots taken from a single reaction at similar time points would be very difficult to characterize unless they were of a large volume. Larger aliquot volumes translate to a larger overall reaction volume, which is more difficult to reduce rapidly and homogeneously (both of which are critical to this category of chiral reaction). Using the approach as described in Chapter IV, the evolving

chiroptical signature for a chiral reaction was displayed much like a set of *in situ* measurements, and the data at equivalent time points from these two methods compared well. An advantage of our method over *in situ* characterization is the ability to isolate and characterize the products via electron microscopy and display the evolving structural features to complement the optical data. We analyzed micelle-directed growth on single-crystal and pentatwinned achiral seeds, a reaction that surprisingly yielded its maximum chiroptical signature after less than two minutes for single-crystal seeds, and less than one minute for pentatwinned seeds. The observation that the growth on pentatwinned seeds outpaces that occurring on single-crystal achiral seeds is perplexing and demands further investigation; perhaps the lack of an octahedral intermediate in the former explains the swifter transition to a wrinkled morphology, but that fails to explain the overall increase in growth on pentatwinned as opposed to single-crystal seeds. Furthermore, the growth on the tips of single-crystal and pentatwinned rods evolving differently shines a spotlight on this potentially overlooked structural feature and its disproportionate contribution to the chiroptical signature. In any case, this methodology has great potential to assist the defining of structural-optical relationships for chiral products.

In Chapter V, we first used LipoCYS in the context of a synthetic methodology using much lower concentrations of ascorbic acid and surfactant than utilized in previous chapters, designed to slowly and gently form helicoids over a time frame of hours. These products were structurally evaluated primarily by SEM, meaning that their finer chiral features were difficult to characterize. However, the chiroptical signatures of products prepared with CTAB were inverted from those prepared with CTAC, revealing yet another synthetic variable to tune in the future. While the lack of particles evaluated by electron tomography stymied our conclusions, promising corkscrew-like chiral features that grew to dominate the handedness of certain particles (as the concentration of

LipoCYS was raised) were observed. In our second approach, we used geometrically twisted yet smooth products of a chemically-induced chiral reaction as the seeds in a subsequent micelle-directed chiral reaction, geometrically twisted and wrinkled products could be formed. From the chiroptical signatures it was inferred that the growth of the micelle-directed “shell” was impacted if the handedness of the micelle (dictated by the enantiomer of the inducer) matched that of the chiral seed “core”. Further analysis of tomographic reconstructions revealed that the overall handedness of these products was dependent on the handedness of the chiral seed “core”, though further investigation is needed.

In probing chemical variables involved in the syntheses of chiral plasmonic nanomaterials such as the composition of the chiral inducer and the geometry of the starting seeds (among others), and introducing methodology to study reaction intermediates and prepare new and interesting morphologies with multi-scale chirality, we offer a broad foundation for further experimentation and projects. The design of chiral inducers beyond LipoCYS is a trove of potential for the founding and optimization of novel chiral morphologies, and honing in on the optical-structural relationships for specific chiral features (such as the particle tips / protruding facets) is key to success. The deliberate and systematic optimization of established theory combined with the ambitious application of novel techniques and computerized approaches will accelerate progression in this field.

Main conclusions:

1. LipoCYS, a novel chiral inducer incorporating features from inducers of different established chiral growth mechanisms, yielded products that evolved in structure and chiroptical signature based solely on the concentration of LipoCYS.
2. The modulation of chiral growth based solely on the concentration of novel chiral inducer LipoCYS suggests an expanded role for the design of co-surfactants when preparing nanomaterials with different chiral morphologies.
3. For seeded chiral growth reactions, the chiroptical signature was observed to invert when single-crystalline achiral nanorods were used as the starting seeds, as compared to when pentatwinned achiral nanorods were used as the starting seeds; this was demonstrated for both established chiral growth mechanisms.
4. The initial geometry present in the achiral seeds was preserved following the chiral reaction: the 4-fold symmetry of single-crystalline nanorods and the 5-fold symmetry of pentatwinned nanorods were observed in their respective chiral products.
5. Using sodium borohydride, chiral reactions in progress could be ceased, and the products from varying intervals of growth could be isolated and characterized; these time-resolved product series possessed chiroptical signatures that compared well to *in situ* measurements and could be evaluated under an electron beam, permitting complementary time-resolved structural characterization.

6. Time-resolved product series engineered using NaBH_4 help to define relationships between the observed chiroptical signature of products and their apparent chiral features, and better understand from a mechanistic standpoint the development of particles during an overgrowth reaction.

7. A pair of strategies to engineer particles with multi-scale chirality were investigated: helicoid-like particles were synthesized with LipoCYS, and chiral products were used as the starting seeds in a subsequent chiral reaction to form products with different “core-shell” chiral features.

Appendix

List of publications:

Authors: J. Sa, N. Hu, W. Heyvaert, K. Van Gordon, H. Li, L. Wang, S. Bals, L.M. Liz-Marzán, W. Ni

Title: Spontaneous Chirality Evolved at Au-Ag Interface in Plasmonic Nanorods

Journal: Chemistry of Materials

Status: Published August 21, 2023 (*Chem. Mater.* 2023, 35, 17, 6782–6789)

<https://doi.org/10.1021/acs.chemmater.3c01044>

Authors: K. Van Gordon, S. Baulde, M. Mychinko, W. Heyvaert, M. Obelleiro-Liz, A. Criado, S. Bals, L. M. Liz-Marzán, J. Mosquera

Title: Tuning the Growth of Chiral Gold Nanoparticles Through Rational Design of a Chiral Molecular Inducer

Journal: Nano Letters

Status: Published October 25, 2023 (*Nano Lett.* 2023, 23, 21, 9880–9886)

<https://doi.org/10.1021/acs.nanolett.3c02800>

Authors: K. Van Gordon, B. Ni, R. Girod, M. Mychinko, F. Bevilacqua, S. Bals, L. M. Liz-Marzán

Title: Single Crystal and Pentatwinned Gold Nanorods Result in Chiral Nanocrystals with Reverse Handedness

Journal: Angewandte Chemie

Status: Published April 22, 2024 (*Angew. Chemie* 2024, 63, 26, e202403116)

<https://doi.org/10.1002/anie.202403116>

Authors: E. Vlasov, W. Heyvaert, B. Ni, K. Van Gordon, R. Girod, J. Verbeeck, L.M. Liz-Marzan, S. Bals.

Title: High-throughput Morphological Chirality Quantification of Twisted and Wrinkled Gold Nanorods

Journal: ACS Nano

Status: Published April 26, 2024 (*ACS Nano* 2024, 18, 18, 12010-12019)

<https://doi.org/10.1021/acsnano.4c02757>

Authors: B. Ni, G. Gonzalez-Rubio, K. Van Gordon, L. M. Liz-Marzan, N. Kotov

Title: Seed-Mediated Growth and Advanced Characterization of Chiral Gold Nanorods

Journal: Advanced Materials

Status: Published October 9, 2024 (*Adv. Mat* 2024, 36, 47, 2412473)

<https://doi.org/10.1002/adma.202412473>

Authors: F. Bevilacqua, R. Girod, V. F. Martin, M. Obelleiro-Liz, G. Vinnacombe-Willson, K. Van Gordon, J. Hofkens, J. Taboada, S. Bals, L. M. Liz-Marzan.

Title: Additive-Free Synthesis of (Chiral) Gold Bipyramids from Pentatwinned Nanorods

Journal: ACS Materials Letters

Status: Published October 17, 2024 (*ACS Mat. Lett.* 2024, 6, 11, 5163-5169)

<https://doi.org/10.1021/acsmaterialslett.4c01605>

Authors: K. Van Gordon, R. Girod, L. M. Liz-Marzan, S. Bals.

Title: Structural and optical characterization of reaction intermediates during fast chiral nanoparticle growth

Journal: Nano Letters

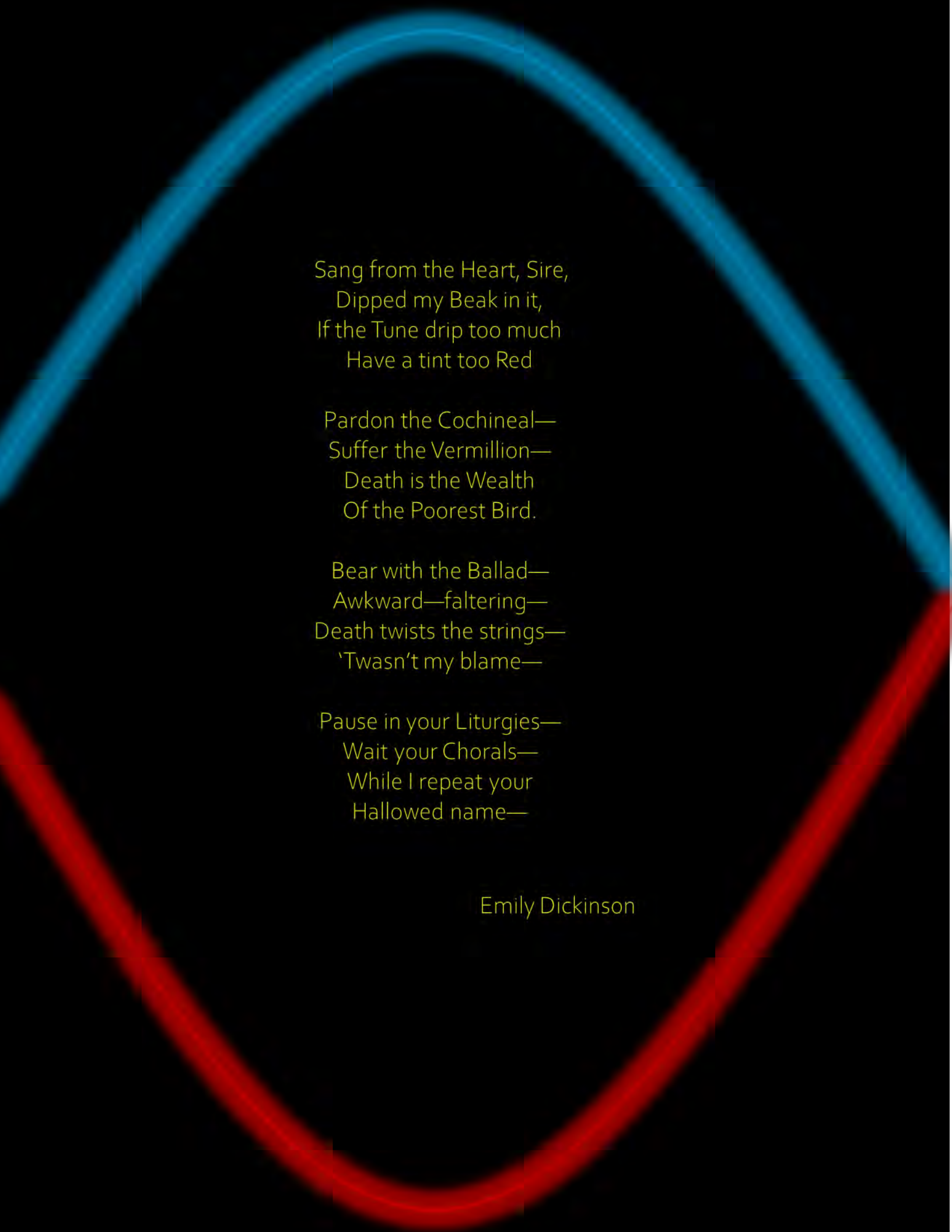
Status: Resubmitted after minor revisions

Authors: K. Van Gordon, I. Ha, J. Hyun, R. Girod, L. M. Liz-Marzan, K. T. Nam, S. Bals.

Title: The chiral synthetic toolbox: understanding inversion in helicoid-like products yielded using LipoCYS

Journal: TBD

Status: In preparation



Sang from the Heart, Sire,
Dipped my Beak in it,
If the Tune drip too much
Have a tint too Red

Pardon the Cochineal—
Suffer the Vermillion—
Death is the Wealth
Of the Poorest Bird.

Bear with the Ballad—
Awkward—faltering—
Death twists the strings—
'Twasn't my blame—

Pause in your Liturgies—
Wait your Chorals—
While I repeat your
Hallowed name—

Emily Dickinson